Mercury Stable Isotopes Identify Past and Present Mercury Sources and Cycling

by

Aaron Y. Kurz

A dissertation submitted in partial fulfillment
of the requirements for the degree of
Doctor of Philosophy
(Earth and Environmental Sciences)
in the University of Michigan
2021

Doctoral Committee:

Professor Joel D. Blum, Chair
Associate Professor Rose M. Cory
Associate Professor J. Tim Dvonch
Associate Professor Benjamin H. Passey
Associate Professor Kerri A. Pratt

Aaron Y. Kurz

kurz@umich.edu

ORCID iD: 0000-0002-6729-1223

Dedication

In loving memory of my friend, Leah Nico Z”L and my grandfather, Alvin Kurz Z”L

Acknowledgements

First and foremost, I want to thank my family for their never-ending love and support. It would have been a much tougher journey without after work dinner drop-offs from my mom to get me through the long nights in the lab or long discussions with my dad that provided perspective and comic relief. I am also lucky enough to have my sister as a lifelong best friend. Sarah has always been there for me, willing to talk and commiserate or take me to the ER and hold my hand.

I also would like to thank my wonderful fiancée, Kierstin. There is no one else in the world I would rather be with 24/7 during a pandemic. Our kitties, Mr. Kitty and Butter, have provided a constant source of joy, entertainment, and furry cuddles to make it through the long days of writing, trapped inside a studio apartment together.

I would like to graciously recognize my advisor, Joel Blum, who hired me as an undergraduate with no laboratory experience before taking me on as a PhD student. I am grateful that I was able to complete my PhD under his guidance and I truly appreciate his patience and encouragement in the process.

I would like to thank Marcus Johnson for his constant help in the laboratory, in-depth discussions regarding methods and relevant literature, and encouragement over the past seven years.

I would like to recognize my co-authors and collaborators for their scientific contributions and motivation in the publishing process. I specifically would like to thank Lynne

Gratz for her help collecting field samples in Colorado and finding me a place to stay in Colorado Springs when I lost my tent to a forest fire.

Lastly but surely not least, I would like to thank my lab mates and friends in the BIEGL lab. Sae Yun Kwon and Patrick Donovan helped train me when I started as an undergrad. Laura Motta and Spencer Washburn were wonderful mentors and great friends, providing encouragement, guidance, and collaboration at every step of the way. I would also like to acknowledge other members of the BIEGL lab during my tenure, especially Jamie Gleason and Jason Demers.

Table of Contents

List of Tables

List of Figures

Abstract

Mercury (Hg) is a neurotoxic trace metal that is globally distributed and has important implications for human health. The anthropogenic use of Hg has caused the concentration of Hg in the environment to approximately triple since ~1850. It is therefore imperative to understand the historical deposition trends and modern biogeochemical cycling of Hg to better inform future policy actions regarding the release of Hg to the environment. In this dissertation, measurements of Hg stable isotopes were applied to an environmental record of historical Hg deposition and to remote, low Hg concentration atmospheric samples to answer outstanding questions regarding both historical and modern biogeochemical conditions and processes driving Hg cycling in the environment.

To discern past sources of Hg and conditions controlling Hg isotope fractionation in the atmosphere, a sediment core from a remote, high elevation lake near Jackson, Wyoming was collected. Lake sediments were dated to understand temporal changes in the deposition of Hg to the sediments, revealing an approximate 3.8-fold increase in Hg flux from 1850 to the present. Additionally, measurements of Hg stable isotope ratios in the sediments indicated a shift in atmospheric chemical reactions over the same period. Analyses of wet precipitation and snow collected in the lake's vicinity were utilized to explain the modern Hg isotopic composition observed in the lake sediments and motivated further investigation into Hg isotope fractionation in snow.

Measurements of 12-hour atmospheric gaseous Hg samples were collected continuously for one week from two high elevation sites (Mount Bachelor, Oregon and Camp Davis,

Wyoming) with contrasting geographic characteristics to understand both the vertical gradient of Hg in the atmosphere and better understand the role of vegetation in Hg isotope fractionation in the atmosphere. Analyses of Hg isotope ratios from samples at Mount Bachelor (mountaintop site) revealed diel variation in the isotopic composition of Hg. Nightly measurements indicated a dominant influence from the free troposphere with a distinct isotopic composition. Near the end of the sampling period, the diel variation dissipated due to a nearby forest fire that came to dominate both daytime and nighttime samples. At Camp Davis (valley site), diel variation in the isotopic composition of Hg was also observed, however, the variation at this site contrasted with observations at Mount Bachelor. Nightly inversions trapping Hg in the valley at Camp Davis and the subsequent uptake of Hg from the atmosphere by vegetation explains the fractionation observed in the residual Hg.

Motivated by the analysis of Hg isotopes in snow from Lost Lake, WY, five time series of snow samples (with sampling every 12 hours for 48 hours) were collected at two sites in Michigan (Dexter and Pellston). A time series collected in Dexter during a polar vortex revealed progressively more negative odd-mass independent fractionation (MIF), similar to observations in Arctic snow. In contrast, the fractionation of Hg isotopes in all of the other snow samples progressed towards more positive odd-MIF, indicating a difference in oxidants and binding ligands associated with the Hg in snow. Finally, snow samples indicative of snowmelt were used to estimate the Hg isotopic composition of Hg deposited to mid-latitude ecosystems via snow.

As a whole, this dissertation begins to answer outstanding questions concerning processes that control the fractionation and distribution of Hg in the environment and creates a platform for future researchers to expand upon.

Chapter 1 Introduction

1.1 Mercury as a Global Pollutant

Mercury (Hg) is a neurotoxic trace metal distributed ubiquitously at Earth's surface due to both natural and anthropogenic processes. Natural sources of Hg include hydrothermal and volcanic activity and re-emission of previously deposited Hg from natural reservoirs. These natural sources, however, only account for about one third of the Hg found in Earth's atmosphere (Bagnato et al., 2015; Pirrone et al., 2010). The mining and use of Hg has a long history dating back to ~5000 B.C.E. (Emslie et al., 2015) and more recently has been used in consumer products and industrial processes. Currently, the largest sources of Hg to the atmosphere are through the combustion of coal and gold mining (Pacyna et al., 2009; Pirrone et al., 2010).

Historical inventories of Hg release from industrial processes and natural sources have been estimated through observational and modeling methods (Amos et al., 2015; Engstrom et al., 2014; Horowitz et al., 2014; Song et al., 2015; Streets et al., 2011). Natural archives such as lake sediments, peat cores, and ice cores document the historical deposition of Hg to the Earth's surface (Enrico et al., 2017; Zdanowicz et al., 2016). Through these analyses, there is a consensus that Hg deposition has increased 3-5 times since 1850. Studies have worked to elucidate the extent to which activities such as the mining of Hg in South American during the 16th century had an impact on the global Hg cycle (Cooke et al., 2013; Engstrom et al., 2014). Researchers concluded that these emissions were only recorded regionally. There is still debate, however, concerning the geographic impact of Hg released during the Gold Rush in the United States (Chellman et al., 2017; Engstrom et al., 2014; Schuster et al., 2002).

Redox cycling of Hg has important implications for the distribution and human exposure to Hg (Driscoll et al., 2013). Monomethylmercury (MMHg) poses a threat to human health and is produced in the environment via microbial activity, primarily through methylation by sulfate and iron reducing bacteria in anoxic environments (Hsu-kim et al., 2013; Janssen et al., 2016). The neurotoxicity of Hg was first recognized in Minimata, Japan in the late 1950's following a disaster in the Minimata Bay due to the industrial release of wastewater from a chemical factory (Harada, 1995). Fisherman and their families began to exhibit symptoms of severe neurological damage, leading to an investigation of the cause and a conclusion that MMHg exposure from fish consumption was responsible. Throughout the world, fish consumption continues to be the primary pathway for Hg exposure to humans (Sunderland, 2007).

Atmospheric cycling of Hg has important implications for the global distribution and deposition of Hg (Lyman et al., 2020; Selin, 2009). Hg in the atmosphere has three operationally defined species: gaseous elemental mercury (GEM or Hg^0) has an extended atmospheric lifetime of ~0.5 to 1 year, reactive gaseous mercury (RGM or $Hg^{II}_{(g)}$) and mercury bound to particles (PBM or $Hg^{II}_{(p)}$) have shorter atmospheric lifetimes and are readily stripped from the atmosphere and deposited to the Earth's surface through wet and dry deposition (Gustin et al., 2015; Lindberg and Stratton, 1998). Together, Hg^0 and $Hg^{II}_{(g)}$ are referred to as total gaseous mercury (TGM).

1.2 Mercury Isotope Systematics

Measurements of Hg isotope ratios have proved an indispensable tool in elucidation of the Hg biogeochemical cycling (Blum et al., 2014; Kwon et al., 2020; Yin et al., 2010). High precision measurements of mercury's seven stable isotopes (masses 196, 198, 199, 200, 201, 202 and 204) became possible with advancements in cold vapor multiple collector inductively

coupled mass spectrometer (CV-MC-ICP-MS) technology. The utility of Hg isotopes arises from two types of fractionation: mass dependent fractionation (MDF) and mass independent fractionation (MIF).(Yin et al., 2010) MDF occurs through reactions of nuclear mass selectivity (both kinetic and equilibrium isotope fractionation) and is reported as δ^{202}Hg in permil (‰):

$$\delta^{202}\text{Hg (‰)} = \{[(^{202}\text{Hg}/^{198}\text{Hg})_{\text{unknown}}/(^{202}\text{Hg}/^{198}\text{Hg})_{\text{NIST3133}}]\text{-}1\} \times 1000$$

MDF has been documented in a number of biotic and abiotic processes including methylation and demethylation, sorption and equilibrium reactions (Jiskra et al., 2012; Kritee et al., 2009, 2007; Rodriguez-Gonzalez et al., 2009; Wiederhold et al., 2010).

MIF occurs mainly through photochemical reactions and is reported as the deviation from the predicted fractionation from the kinetic isotope fractionation law. Blum and Bergquist (2007) calculated β values for Δ^{199}Hg, Δ^{200}Hg, Δ^{201}Hg, and Δ^{204}Hg of 0.252, 0.502, 0.752, and 1.493 respectively:

$$\Delta^{xxx}\text{Hg (‰)} = \delta^{xxx}\text{Hg} - (\delta^{202}\text{Hg} \times \beta)$$

Large magnitude MIF is thought to be related to the magnetic isotope effect, fractionating the odd-mass isotopes that have non-zero magnetic moments (masses 199 and 201) (Buchachenko, 2001). Smaller magnitude MIF is due to the nuclear volume effect during equilibrium reactions, also affecting the odd-mass isotopes (Ghosh et al., 2013). Together, observations of these MIF anomalies are referred to as odd-MIF and are represented as Δ^{199}Hg and Δ^{201}Hg. Large magnitude odd-MIF anomalies are driven by photochemical reactions including photoreduction

of aqueous Hg^{II} in the presence of dissolved organic matter (Bergquist and Blum, 2007; Rose et al., 2015; Zheng and Hintelmann, 2009) and photodemethylation of MMHg (Chandan et al., 2015) and have been observed in a number of natural materials including fish, (Bergquist and Blum, 2007) precipitation, (Gratz et al., 2010; Washburn et al., 2020) atmospheric gaseous Hg^0, (Fu et al., 2016a; Gratz et al., 2010) snow, (Sherman et al., 2010) and sediments (Cooke et al., 2013). Observations of MIF affecting the even-mass isotopes (masses 200 and 204) have also been documented in atmospherically derived samples, though the exact fractionation mechanism remains unknown (Gratz et al., 2010). It has been suggested that even-MIF occurs through UV initiated oxidation in the tropopause and was first observed in atmospheric samples of precipitation and Hg^0 (Chen et al., 2012; Gratz et al., 2010). Even-MIF is considered to be a conservative tracer, giving rise to its utility as an atmospheric source tracer (Blum and Johnson, 2017). The measurement of Hg isotopic ratios in natural media and the utility of both MDF and MIF measurements has been used extensively to better understand the Hg global biogeochemical cycle (Blum et al., 2014; Kwon et al., 2020; Sun et al., 2019; Tsui et al., 2020).

1.3 Filling in the Missing Pieces

While the Hg cycle has been studied extensively, there are still knowledge gaps concerning the isotopic characterization of Hg and the processes that fractionate Hg isotopes in the environment. These gaps include historical changes in the atmospheric fractionation of Hg isotopes, the effect of vegetation on atmospheric Hg cycling (both uptake and release of Hg from/to the atmosphere), and the Hg fractionation in snow outside of the Arctic. These processes and reactions are depicted in Figure 1.1 and are represented as part of the broader Hg biogeochemical cycle in the environment. Each chapter in this dissertation aims to fill a specific knowledge gap, which are indicated by chapter on Figure 1.1. The goal of this dissertation is to

begin to answer some of the outstanding questions regarding Hg isotope fractionation and create a platform from which future researchers may launch from to better understand and characterize the cycling of this important neurotoxin in the environment.

1.4 Application of Hg Stable Isotopes: Dissertation Narrative

Although there has been extensive work elucidating the biogeochemical cycling of Hg, many knowledge gaps remain. This dissertation utilizes the measurement of Hg stable isotopes in a number of natural sample types to better understand the historical deposition of Hg, atmospheric cycling and source identification of Hg, and the fractionation of Hg in snow at mid-latitudes coupled with the implications of this atmospheric deposition pathway to terrestrial and aquatic ecosystems.

In Chapter 2 (published in *Science of the Total Environment*) we explored the historic deposition of Hg through measurements of Hg stable isotopes in lake sediments. We identified a small lake in northwestern Wyoming with a small catchment to lake surface ratio (2.06), ideal for recording the global record of atmospheric deposition of Hg. We also collected samples of possible sources of Hg to the sediments including soil and vegetation from the catchment, Hg^0 from a nearby mountaintop, precipitation, and snow. We found that the flux of Hg began to dramatically increase circa 1850 at the beginning of the Industrial Revolution, consistent with previous observations in other lakes. Interestingly, we found that concurrent with an increase in Hg flux, values of all measured isotope ratios ($\delta^{202}Hg$, $\Delta^{199}Hg$, $\Delta^{200}Hg$ and $\Delta^{201}Hg$) trended towards higher values. Deposition of a mixture of wet precipitation and snow was used to explain the modern Hg isotopic composition, however, a global shift in atmospheric isotope fractionation was needed to explain the temporal shifts in measured ratios in the sediments.

In Chapter 3 (published in *Environmental Science and Technology*) we collected continuous 12-hour samples of Hg^0 for one week at Mount Bachelor Observatory, Oregon, where long-term monitoring and characterization of atmospheric Hg was employed to aid in the interpretation of our Hg isotopic measurements. Samples displayed diel variation in $\delta^{202}Hg$ and $\Delta^{199}Hg$ but not $\Delta^{200}Hg$, which we attributed to free tropospheric air masses measured during the night. Near the end of the sampling period, the diel variation dissipated due to the influence from a forest fire ~31 km NW of Mount Bachelor. We employed a three-endmember mixing model to identify the Hg isotopic composition of free tropospheric, regional background, and forest fire sources of Hg. In addition to the sample set collected at Mount Bachelor, we collected a similar sample set consisting of continuous 12-hour samples of Hg^0 for one week at the University of Michigan's Camp Davis in Jackson Hole, Wyoming. At this site we observed diel variation in $\delta^{202}Hg$ but not in $\Delta^{199}Hg$ or $\Delta^{200}Hg$. We attributed this pattern to nightly atmospheric inversions trapping Hg^0 in the valley and the subsequent uptake of Hg^0 by vegetation, depleting Hg from the atmosphere.

In Chapter 4 (in review for *Science of the Total Environment*) we collected a total of 5 time series of snow samples from two sites in Michigan (Dexter and Pellston) consisting of a sample of snow at the end of the snow event and samples every 12-hours over the following 48-hour period. At the Dexter site we also collected concurrent Hg^0 samples. This represents the first study to investigate the Hg isotopic fractionation in snow at mid-latitudes. We characterized the freshly fallen snow and compared it to precipitation samples from the Great Lakes region, finding a very narrow range in $\delta^{202}Hg$ values compared to precipitation, but a much larger range in $\Delta^{199}Hg$ compared to precipitation. We also used $\Delta^{199}Hg$ values and the conservative tracer $\Delta^{200}Hg$ to identify reactive surface uptake of Hg^0 in snow samples, implicating air mass origin

and trajectories in the isotopic composition of measured snow samples. At the Dexter site, we collected the first Hg isotope snow time series during a polar vortex, providing a unique opportunity to compare our observations to those of snow in Alaska. We found that the evolution of the Hg isotopic values during this time series (Δ^{199}Hg trended towards negative values) was similar to that observed in northern Alaska, which implies that halogen photooxidation of Hg plays an important role in our measured samples. All other time series displayed Δ^{199}Hg values trending to more positive values over time. A comparison of Δ^{199}Hg vs. Δ^{201}Hg in snow samples from all of the collected time series indicates that photoreduction of Hg^{II} is the dominant process controlling Hg isotopic fractionation in snow at mid-latitudes, while differences in binding ligands drives the differences in the direction and extent of fractionation. Finally, we identified two snowpack samples (vertically integrated from the top to bottom of the snowpack) as the endmember of Hg that would be incorporated into natural reservoirs upon snowmelt. This characterization has important implications for identification of Hg sources of inorganic Hg available for methylation.

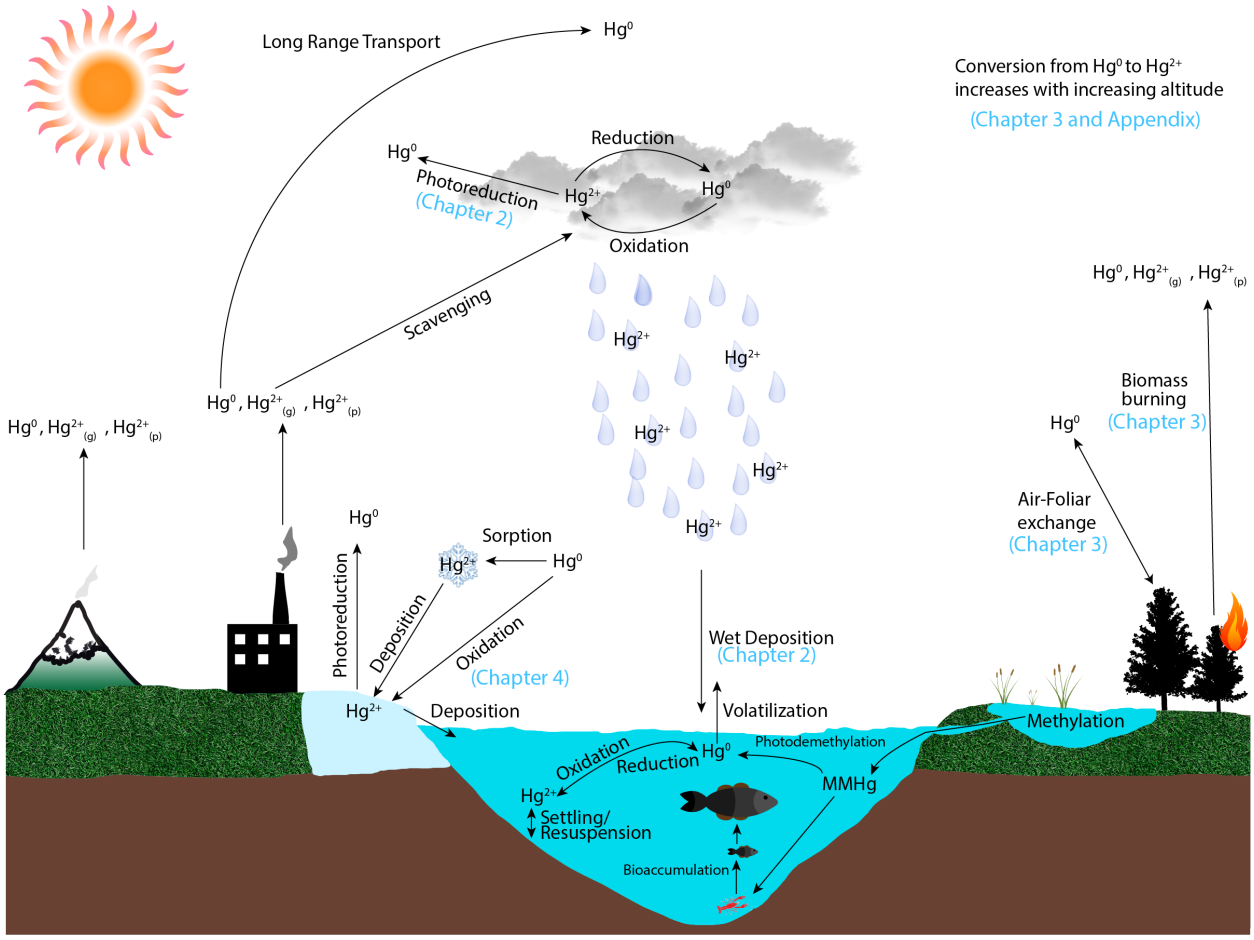

Figure 1.1 Schematic depicting the general biogeochemical cycling of Hg.

Labels in blue indicate the process and reactions of the Hg biogeochemical cycle addressed in the indicated chapter

References

Amos, H.M., Sonke, J.E., Obrist, D., Robins, N., Hagan, N., Horowitz, H.M., Mason, R.P., Witt, M., Hedgecock, I.M., Corbitt, E.S., Sunderland, E.M., 2015. Observational and modeling constraints on global anthropogenic enrichment of mercury. Environ. Sci. Technol. 49, 4036–4047. https://doi.org/10.1021/es5058665

Bagnato, E., Tamburello, G., Avard, G., Martinez-Cruz, M., Enrico, M., Fu, X., Sprovieri, M., Sonke, J.E., 2015. Mercury fluxes from volcanic and geothermal sources: an update. Geol. Soc. London, Spec. Publ. 410, 263–285. https://doi.org/10.1144/SP410.2

Bergquist, B.A., Blum, J.D., 2007. Mass-dependent and -independent fractionation of Hg isotopes by photoreduction in aquatic systems. Science (80-.). 318, 417–420. https://doi.org/10.1126/science.1148050

Blum, J.D., Sherman, L.S., Johnson, M.W., 2014. Mercury Isotopes in Earth and Environmental Sciences. Annu. Rev. Earth Planet. Sci. 42, 249–269. https://doi.org/10.1146/annurev-earth-050212-124107

Buchachenko, A.L., 2001. Magnetic Isotope Effect: Nuclear Spin Control of Chemical Reactions. J. Phys. Chem. A 105, 9995–10011. https://doi.org/10.1021/jp011261d

Chandan, P., Ghosh, S., Bergquist, B.A., 2015. Mercury isotope fractionation during aqueous photoreduction of monomethylmercury in the presence of dissolved organic matter. Environ. Sci. Technol. 49, 259–267. https://doi.org/10.1021/es5034553

Chellman, N., McConnell, J.R., Arienzo, M., Pederson, G.T., Aarons, S.M., Csank, A., 2017. Reassessment of the Upper Fremont Glacier Ice-Core Chronologies by Synchronizing of Ice-Core-Water Isotopes to a Nearby Tree-Ring Chronology. Environ. Sci. Technol. 51, 4230–4238. https://doi.org/10.1021/acs.est.6b06574

Chen, J., Hintelmann, H., Feng, X., Dimock, B., 2012. Unusual fractionation of both odd and even mercury isotopes in precipitation from Peterborough, ON, Canada. Geochim. Cosmochim. Acta 90, 33–46. https://doi.org/10.1016/j.gca.2012.05.005

Cooke, C.A., Hintelmann, H., Ague, J.J., Burger, R., Biester, H., Sachs, J.P., Engstrom, D.R., 2013. Use and legacy of mercury in the Andes. Environ. Sci. Technol. 47, 4181–4188. https://doi.org/10.1021/es3048027

Driscoll, C.T., Mason, R.P., Chan, H.M., Jacob, D.J., Pirrone, N., 2013. Mercury as a global pollutant: Sources, pathways, and effects. Environ. Sci. Technol. 47, 4967–4983. https://doi.org/10.1021/es305071v

Emslie, S.D., Brasso, R., Patterson, W.P., Carlos Valera, A., McKenzie, A., Maria Silva, A., Gleason, J.D., Blum, J.D., 2015. Chronic mercury exposure in Late Neolithic/Chalcolithic populations in Portugal from the cultural use of cinnabar. Sci. Rep. 5, 1–9.

https://doi.org/10.1038/srep14679

Engstrom, D.R., Fitzgerald, W.F., Cooke, C. a., Lamborg, C.H., Drevnick, P.E., Swain, E.B., Balogh, S.J., Balcom, P.H., 2014. Atmospheric Hg emissions from preindustrial gold and silver extraction in the Americas: A reevaluation from lake-sediment archives. Environ. Sci. Technol. 48, 6533–6543. https://doi.org/10.1021/es405558e

Enrico, M., Beek, P. Van, Souhaut, M., Sonke, J.E., 2017. Holocene Atmospheric Mercury Levels Reconstructed from Peat Bog Mercury Stable Isotopes. Environ. Sci. Technol. 51, 5899–5906. https://doi.org/10.1021/acs.est.6b05804

Fu, X., Marusczak, N., Wang, X., Gheusi, F., Sonke, J.E., 2016. Isotopic Composition of Gaseous Elemental Mercury in the Free Troposphere of the Pic du Midi Observatory, France. Environ. Sci. Technol. 50, 5641–5650. https://doi.org/10.1021/acs.est.6b00033

Ghosh, S., Schauble, E.A., Lacrampe Couloume, G., Blum, J.D., Bergquist, B.A., 2013. Estimation of nuclear volume dependent fractionation of mercury isotopes in equilibrium liquid-vapor evaporation experiments. Chem. Geol. 336, 5–12. https://doi.org/10.1016/j.chemgeo.2012.01.008

Gratz, L.E., Keeler, G.J., Blum, J.D., Sherman, L.S., 2010. Isotopic composition and fractionation of mercury in Great Lakes precipitation and ambient air. Environ. Sci. Technol. 44, 7764–7770. https://doi.org/10.1021/es100383w

Gustin, M.S., Amos, H.M., Huang, J., Miller, M.B., Heidecorn, K., 2015. Measuring and modeling mercury in the atmosphere : a critical review. Atmos. Chem. Phys. 5697–5713. https://doi.org/10.5194/acp-15-5697-2015

Harada, M., 1995. Minamata disease: Methylmercury poisoning in Japan caused by environmental pollution. Crit. Rev. Toxicol. 25, 1–24. https://doi.org/10.3109/10408449509089885

Horowitz, H.M., Jacob, D.J., Amos, H.M., Streets, D.G., Sunderland, E.M., 2014. Historical mercury releases from commercial products: Global environmental implications. Environ. Sci. Technol. 48, 10242–10250. https://doi.org/10.1021/es501337j

Hsu-kim, H., Kucharzyk, K.H., Zhang, T., Deshusses, M.A., 2013. Mechanisms Regulating Mercury Bioavailability for Methylating Microorganisms in the Aquatic Environment : A Critical Review.

Janssen, S.E., Barkay, T., Reinfelder, J.R., 2016. Fractionation of Mercury Stable Isotopes during Microbial Methylmercury Production by Iron- and Sulfate-Reducing Bacteria. https://doi.org/10.1021/acs.est.6b00854

Jiskra, M., Wiederhold, J.G., Bourdon, B., Kretzschmar, R., 2012. Solution speciation controls mercury isotope fractionation of Hg(II) sorption to goethite. Environ. Sci. Technol. 46,

6654–6662. https://doi.org/10.1021/es3008112

Kritee, K., Barkay, T., Blum, J.D., 2009. Mass dependent stable isotope fractionation of mercury during mer mediated microbial degradation of monomethylmercury. Geochim. Cosmochim. Acta 73, 1285–1296. https://doi.org/10.1016/j.gca.2008.11.038

Kritee, K., Blum, J.D., Johnson, M.W., Bergquist, B.A., Barkay, T., 2007. Mercury stable isotope fractionation during reduction of Hg(II) to Hg(0) by Mercury resistant microorganisms. Environ. Sci. Technol. 41, 1889–1895. https://doi.org/10.1021/es062019t

Kwon, S.Y., Blum, J.D., Yin, R., Tsui, M.T.K., Yang, Y.H., Choi, J.W., 2020. Mercury stable isotopes for monitoring the effectiveness of the Minamata Convention on Mercury. Earth-Science Rev. 203, 103111. https://doi.org/10.1016/j.earscirev.2020.103111

Lindberg, S.E., Stratton, W.J., 1998. Atmospheric Mercury Speciation : Concentrations and Behavior of Reactive Gaseous Mercury in Ambient Air. Environ. Sci. Technol. 32, 49–57. https://doi.org/doi:10.1021/es970546u

Lyman, S.N., Cheng, I., Gratz, L.E., Weiss-Penzias, P., Zhang, L., 2020. An updated review of atmospheric mercury. Sci. Total Environ. 707, 135575. https://doi.org/10.1016/j.scitotenv.2019.135575

Pacyna, E.G., Pacyna, J.M., Sundseth, K., Munthe, J., Kindbom, K., Wilson, S., Steenhuisen, F., Maxson, P., 2009. Global emission of mercury to the atmosphere from anthropogenic sources in 2005 and projections to 2020. Atmos. Environ. 44, 2487–2499. https://doi.org/10.1016/j.atmosenv.2009.06.009

Pirrone, N., Cinnirella, S., Feng, X., Finkelman, R.B., Friedli, H.R., Leaner, J., Mason, R., Mukherjee, A.B., 2010. Global mercury emissions to the atmosphere from anthropogenic and natural sources. Atmos. Chem. Phys. 10, 5951–5964. https://doi.org/10.5194/acp-10-5951-2010

Rodriguez-Gonzalez, P., Tessier, E., Guyoneaud, R., Monperrus, M., 2009. Species-Specific Stable Isotope Fractionation of Mercury during Hg (II) Methylation by an Anaerobic Bacteria (Desulfobulbus propionicus) under Dark Conditions. Environ. Sci. Technol. 43, 9183–9188.

Rose, C.H., Ghosh, S., Blum, J.D., Bergquist, B.A., 2015. Effects of ultraviolet radiation on mercury isotope fractionation during photo-reduction for inorganic and organic mercury species. Chem. Geol. 405, 102–111. https://doi.org/10.1016/j.chemgeo.2015.02.025

Schuster, P.F., Krabbenhoft, D.P., Naftz, D.L., Cecil, L.D., Olson, M.L., Dewild, J.F., Susong, D.D., Green, J.R., Abbott, M.L., 2002. Atmospheric mercury deposition during the last 270 years: A glacial ice core record of natural and anthropogenic sources. Environ. Sci. Technol. 36, 2303–2310. https://doi.org/10.1021/es0157503

Selin, N.E., 2009. Global Biogeochemical Cycling of Mercury: A Review. Annu. Rev. Environ. Resour. 34, 43–63. https://doi.org/10.1146/annurev.environ.051308.084314

Sherman, L.S., Blum, J.D., Johnson, K.P., Keeler, G.J., Barres, J. a., Douglas, T. a., 2010. Mass-independent fractionation of mercury isotopes in Arctic snow driven by sunlight. Nat. Geosci. 3, 173–177. https://doi.org/10.1038/ngeo758

Song, S., Selin, N.E., Soerensen, A.L., Angot, H., Artz, R., Brooks, S., Brunke, E.G., Conley, G., Dommergue, A., Ebinghaus, R., Holsen, T.M., Jaffe, D.A., Kang, S., Kelley, P., Luke, W.T., Magand, O., Marumoto, K., Pfaffhuber, K.A., Ren, X., Sheu, G.R., Slemr, F., Warneke, T., Weigelt, A., Weiss-Penzias, P., Wip, D.C., Zhang, Q., 2015. Top-down constraints on atmospheric mercury emissions and implications for global biogeochemical cycling. Atmos. Chem. Phys. 15, 7103–7125. https://doi.org/10.5194/acp-15-7103-2015

Streets, D.G., Devane, M.K., Lu, Z., Bond, T.C., Sunderland, E.M., Jacob, D.J., 2011. All-time releases of mercury to the atmosphere from human activities. Environ. Sci. Technol. 45, 10485–10491. https://doi.org/10.1021/es202765m

Sun, R., Jiskra, M., Amos, H.M., Zhang, Y., Sunderland, E.M., Sonke, J.E., 2019. Modelling the mercury stable isotope distribution of Earth surface reservoirs: Implications for global Hg cycling. Geochim. Cosmochim. Acta 246, 156–173. https://doi.org/10.1016/j.gca.2018.11.036

Sunderland, E.M., 2007. Mercury exposure from domestic and imported estuarine and marine fish in the U.S. seafood market. Environ. Health Perspect. 115, 235–242. https://doi.org/10.1289/ehp.9377

Tsui, M.T.K., Blum, J.D., Kwon, S.Y., 2020. Review of stable mercury isotopes in ecology and biogeochemistry. Sci. Total Environ. 716, 135386. https://doi.org/10.1016/j.scitotenv.2019.135386

Washburn, S.J., Blum, J.D., Motta, L.C., Bergquist, B.A., Weiss-Penzias, P., 2020. Isotopic Composition of Hg in Fogwaters of Coastal California. Environ. Sci. Technol. Lett. https://doi.org/10.1021/acs.estlett.0c00716

Wiederhold, J.G., Cramer, C.J., Daniel, K., Infante, I., Bourdon, B., Kretzschmar, R., 2010. Equilibrium mercury isotope fractionation between dissolved Hg(II) species and thiol-bound Hg. Environ. Sci. Technol. 44, 4191–4197. https://doi.org/10.1021/es100205t

Yin, R., Feng, X., Shi, W., 2010. Application of the stable-isotope system to the study of sources and fate of Hg in the environment: A review. Appl. Geochemistry 25, 1467–1477. https://doi.org/10.1016/j.apgeochem.2010.07.007

Zdanowicz, C.M., Krummel, E.M., Poulain, A.J., Yumvihoze, E., Chen, J., Strok, M., Scheer, M., Hintelmann, H., 2016. Historical variations of mercury stable isotope ratios in Arctic glacier firn and ice cores. Global Biogeochem. Cycles.

https://doi.org/10.1002/2016GB005411.Received

Zheng, W., Hintelmann, H., 2009. Mercury isotope fractionation during photoreduction in natural water is controlled by its Hg/DOC ratio. Geochim. Cosmochim. Acta 73, 6704–6715. https://doi.org/10.1016/j.gca.2009.08.016

Chapter 2 Changes in the Mercury Isotopic Composition of Sediments from a Remote Alpine Lake in Wyoming, USA

Authors: Aaron Y. Kurz, Joel D. Blum, Spencer J. Washburn, and Mark Baskaran

Citation: Kurz, A.Y., Blum, J.D., Washburn, S.J., Baskaran, M., 2019. Changes in the mercury isotopic composition of sediments from a remote alpine lake in Wyoming, USA. Sci. Total Environ. 669, 973–982. https://doi.org/10.1016/j.scitotenv.2019.03.165

Abstract: Mercury (Hg) deposition from the atmosphere has increased dramatically since 1850 and Hg isotope records in lake sediments can be used to identify changes in the sources and cycling of Hg. We collected a sediment core from a remote lake (Lost Lake, Wyoming, USA) and measured vertical variation of Hg concentration and isotopic composition as well as ^{210}Pb and ^{137}Cs activities to establish a chronology. We also analyzed vegetation and soil samples from the watershed which has a small ratio of watershed area to lake surface area (2.06). The Hg flux remains constant from ~1350 to 1850 before increasing steadily to modern values that are approximately four times pre-1850 values. The modern Hg isotopic composition preserved in the sediments is distinct from the Hg isotopic composition of pre-1850 samples with both δ^{202}Hg and Δ^{199}Hg becoming progressively more positive through time, with shifts of +0.37‰ and +0.23‰ respectively. To explain temporal changes in δ^{202}Hg, Δ^{199}Hg, and Hg concentration in the core segments, we estimated a present-day atmospheric endmember based on precipitation and snow samples collected near Lost Lake. The observed change in Hg isotopic values through time cannot be explained solely by addition of anthropogenic Hg with the isotopic composition that has been estimated by others for global anthropogenic emissions. Instead, the isotope variation

suggests that the relative importance of redox transformations, whether in the atmosphere, within the lake, or both, have changed since 1850.

2.1. Introduction

Mercury (Hg) is a neurotoxic heavy metal found ubiquitously in the atmosphere and at the Earth's surface. Mercury has a complex biogeochemical cycle and concentration measurements of both the atmosphere and lake sediments have been used extensively as a monitor of geogenic and anthropogenic inputs of Hg to the atmosphere (Zambardi et al., 2009; Tang et al., 2017; Obrist et al., 2018 and references therein). Active redox chemistry and phase changes play an important role in Hg cycling between the atmosphere and Earth's surface. Mercury released to the atmosphere has increased 3-5 fold since the onset of the Industrial Revolution (Engstrom et al., 2014; Amos et al., 2015). Substantial modern anthropogenic sources include combustion of coal and other fossil fuels, small scale artisanal gold mining, cement production, non-ferrous metal production and consumer product waste (Pacyna et al., 2009; UNEP, 2013). There are large uncertainties associated with the amount of Hg released from each of these sources, although there is a general consensus that coal combustion and artisanal scale gold mining dominate current emissions (Pacyna et al., 2009; Pirrone et al., 2010). In addition to anthropogenic sources, natural geogenic sources of Hg to the atmosphere include volcanic degassing and eruptions, and hydrothermal activity (Bagnato et al., 2015).

Mercury is emitted to the atmosphere predominantly in the form of Hg(0) and has an atmospheric residence time of ~1 yr allowing it to become globally distributed (Selin et al., 2008; Gustin et al., 2015). Hg(0) can then be photochemically oxidized to Hg(II), which is quickly removed from the atmosphere through sorption to particles and scavenging by

precipitation (Lindberg and Stratton, 1998). Hg can then be directly deposited to lake surfaces through the settling of particles and precipitation.

Lake sediment cores can in many cases reliably record Hg deposition and can provide a stratigraphic record long enough to record the transition between pre-anthropogenic and present-day global Hg deposition (Engstrom et al., 1994; Heyvaert et al., 2000; Engstrom et al., 2014). The temporal consistency in Hg deposition patterns between geographically separated lake sediment cores is suggestive of a lack of diagenetic mobility of Hg (Fitzgerald et al., 2005; Biester et al., 2007; Engstrom et al., 2014). Additionally, studies that have re-cored sites years after initial cores were collected have shown that there is often little to no post-depositional vertical migration of Hg in lake sediments, providing an intact historical deposition record (Lockhart et al., 2000; Rydberg et al., 2008; Percival and Outridge, 2013). An important component of elucidating past Hg records is the coring and analysis of sediments from lakes with small ratios of catchment area to lake surface area (Engstrom et al., 1994). This helps to ensure that the Hg signal preserved in the sedimentary layers is primarily deposited directly from the atmosphere rather than being deposited through erosional inputs of Hg from soils and vegetation of the catchment area (Engstrom et al., 1994).

Hg stable isotope measurements have emerged as a powerful tool for enhancing our understanding of Hg cycling. The usefulness of Hg isotopic ratios stems from Hg displaying both mass dependent fractionation (MDF) and two types of mass independent fractionation (MIF), even-MIF and odd-MIF (e.g. Gratz et al., 2010; Chen et al., 2012; Enrico et al, 2016). MDF can occur during both kinetic and equilibrium reactions involving Hg while MIF occurs mainly in kinetic reactions, most notably photochemically driven reactions (Yin et al., 2010). As the number of published Hg isotopic measurements has grown, a clearer understanding of the

present-day biogeochemical cycling of Hg in the environment has emerged (e.g. Blum et al., 2014).

Modern precipitation and total gaseous mercury (TGM=gaseous oxidized mercury (GOM) + gaseous elemental mercury (GEM)) isotope values have been measured at many locations throughout the world and are shown to have distinct isotopic compositions (Gratz et al., 2010; Chen et al., 2012; Sherman et al., 2012a; 2015; Demers et al., 2013; Donovan et al., 2013; Fu et al., 2016; Yu et al., 2016; Yuan et al., 2018). A number of studies have examined the isotopic composition of local Hg deposition sources in lake sediments and peat bogs (Cooke et al., 2013; Gray et al., 2013; Ma et al., 2013; Chen et al., 2016; Guédron et al., 2016), and a single study was published on Hg isotopes in a glacial ice core (Zdanowicz et al., 2016). These studies assessed local or regional Hg contamination, using down-core Hg isotopic compositions compared to younger samples to fingerprint changes due to point source or regional Hg inputs. Peat bogs have been shown to preserve past Hg isotope values predominantly of dry Hg(0) deposition (Enrico et al., 2016; 2017). Lake sediments have the potential to preserve records of Hg derived from precipitation, but many lake records are complicated by watershed erosional inputs due to typically large ratios of catchment area to lake surface area. Cooke et al. (2013) investigated the distribution of Hg used in the extraction of gold and silver in colonial South America and concluded the Hg used in this process did not enter the global cycle. Gray et al. (2013) found that coupling both Hg and Pb isotopic compositions in a sediment core contaminated by smelting processes provided a useful tool for reconstructing historical contamination from heavy metal deposition. Similarly, Ma et al. (2013) were able to trace Hg contamination in a lake sediment core proximal to a smelting facility where Hg isotopic compositions from samples dated to the time period of smelting were isotopically different than

samples either before or after this period. Finally, Chen et al. (2016) found that in a lake in Ontario, Canada, the sources of Hg to the water column and to the sediments were isotopically distinct.

A limited number of studies have been conducted in remote areas to obtain isotopic records of historical Hg deposition from the global atmospheric reservoir, at sites unaffected by direct local or regional scale Hg emissions (Yin et al., 2016; Zdanowicz et al., 2016; Enrico et al., 2017). Yin et al. (2016) observed an increasing trend in the magnitude of odd-MIF from older to younger sediment samples in two lakes located on the Tibetan Plateau. They suggested that this was due to decreased ice cover in more recent years, increasing the proportion of Hg that underwent photochemical reduction in the water column. An ice core from the eastern part of the Canadian Arctic Archipelago was analyzed for Hg isotopes and little contribution of Hg from atmospheric mercury depletion events was detected based on Hg isotopic compositions (Zdanowicz et al., 2016). Collectively these studies have provided an initial understanding of the historical isotopic composition of atmospheric Hg deposition and have documented the variability in Hg isotopic composition between temporal records in different locations globally.

In order to minimize erosional inputs and local point sources of Hg, and thus obtain a reliable measurement of past atmospheric Hg isotope values, we collected a sediment core from Lost Lake in Wyoming (Figure 2.1, 2.2). This lake has a small catchment area to lake surface area ratio and is far removed from anthropogenic activity including point sources of Hg. We hypothesized that the sediments would preserve a record of the Hg isotopic composition during the transition from a pre-anthropogenic geogenic dominated Hg signature to a coal-combustion dominated signature. By dating the sediment core (with ^{210}Pb and ^{137}Cs) and analyzing it for Hg concentrations and isotopic composition, we compare Hg deposition (both fluxes and isotopic

compositions) to previous studies in other locations. This provides an opportunity to further the understanding of historical trends in the Hg isotopic composition of lake sediments.

2.2 Materials and Methods

2.2.1 Study Site Description

Lost Lake is located in the Bridger Teton National Forest at the southwestern end of the Absaroka Mountain range in northwestern Wyoming (43°46'54.82"N, 110° 6'0.24"W) (Figure 2.1). Lost Lake is a small (0.19 km^2 surface area), perched, seepage-fed tarn with a small lake catchment to lake surface area ratio (2.06), located at an elevation of 2,889 m above sea level, and with a maximum depth of 24 m. The small catchment is predominantly forested, with Engelmann Spruce *(Picea engelmanii)* as the most prevalent species. The surficial geology is composed of Quaternary-aged landslide deposits and glacial till. The underlying bedrock is composed of the Eocene-aged Wiggins Formation, which is part of the Absaroka Volcanic Supergroup (Love and Christiansen, 1985 and references therein). The Wiggins Formation is dominantly coarse to fine-grained conglomerate and fine-grained tuff.

2.2.2 Sample Collection and Preparation

2.2.2.1 Sediment and Vegetation Sample Collection and Preparation

Lost Lake was cored in the summer of 2015 at a water depth of 21 m. The sediment core was collected using a gravity corer with an acid-cleaned acrylic tube with a diameter of 6.6 cm. The core was sectioned using a portable core extruder into 0.5-1 cm increments in the field and collected into acid-cleaned glass jars and frozen within 4 hours of collection. Samples were transported to the University of Michigan in coolers with dry ice. All samples were then stored in a freezer at -18°C and later freeze-dried. Water content was determined from the wet and dry

weights and was subsequently used to determine the porosity and mass depth for each sampled layer (e.g. Baskaran and Naidu, 1995). The sediment samples were ground with an agate mortar and pestle to a homogenous powder.

Needles from *Picea engelmannii* and O-horizon samples from the soil were collected within the small lake catchment. Soil samples had large particles removed by sieving through 2 mm nylon mesh and were subsequently homogenized. Subsamples were removed and ground in an alumina ball mill. The vegetation samples included only green needles and were also subsampled, freeze dried and ground in a ball mill.

2.2.2.2 Atmospheric TGM Sample Collection and Preparation

TGM samples were collected on July 21, 2016 (one 24 hour sample) and June 26, 2017 (two side-by-side 24 hour samples) near the peak of Rendezvous Mountain (43°35'49.84" N 110°52'13.68" W, 3185 m elevation) at the southern end of the Teton range, approximately 70km southwest of Lost Lake. Samples were collected by drawing atmospheric air at 1.8 L/min through a manifold containing 8 gold traps in series. Each gold trap was a borosilicate glass tube with an ID of 5 mm and a length of 10.2cm. The middle 4 cm of each tube was packed with 1 mm diameter borosilicate glass beads coated with gold. A pre-fired quartz filter was placed upstream of each gold trap to catch particles and prevent them from entering the gold traps. Gold traps were maintained at 50°C to prevent condensation during sample collection. Before use, gold traps were heated to remove residual Hg and performance was verified by loading 10ng of Hg onto each gold trap and subsequently desorbing the Hg directly into a cold vapor-atomic absorption spectrometer (CV-AAS) (Nippon Instruments MA-2000) to quantify recovery. Recoveries for standard reference materials (NIST-3133 and UM-Almadèn) during the desorption step ranged from 95.3 to 101.4% with an average of 97.9±2.1% (1SD, n=10).

TGM gold bead traps were dried in a stream of Ar for 1 hour and were then flash heated with a heating coil over a four minute period at 500°C. The released Hg(0) was carried by flowing Ar onto an analytical gold trap (diatomaceous earth coated with gold). All 8 gold bead traps were desorbed sequentially in the laboratory onto the same analytical gold trap. The analytical gold trap was then slowly heated to 550°C over a 3.5 hour period to release the Hg(0) which was slowly bubbled into a 1% $KMnO_4$ trap in a stream of Ar. Process standards (UM-Almadèn and NIST 3133) and process blanks were prepared in the same manner as samples. Gold bead traps were heated to remove background Hg before loading standards onto them. Recoveries for SRM during the desorption step ranged from 87.0 to 99.6% with an average of 94.0±4.7% (1SD, n=10). Identical secondary purging procedures were followed as for solid samples described above. SRM recoveries during secondary purging and trapping ranged from 92.4 to 103.2% with an average of 98.2±4.1% (1SD, n=10).

2.2.2.3 Precipitation Sample Collection and Preparation

Precipitation samples were collected on August 18th, 2016 at the Storm Peak Laboratory in Steamboat Springs Colorado (40°27'18.14" N, 106°44'40.08" W, 3213m) and July 16th, 2017 at Camp Davis in Jackson, Wyoming (43°16'55.11" N, 110°39'26.68" W, 1872m) approximately 470km SE and 70km SW of Lost Lake respectively. Precipitation collection was conducted following methods outlined in Landis and Keeler (1997). Precipitation collectors were set out prior to predicted precipitation events. Funnels were covered with clean plastic bags and secured in place. Just before the precipitation event, plastic bags were removed. All components of the sampling train were cleaned in 10% HNO_3 held at a temperature of approximately 70°C for 8 hours. Teflon bottles were deployed with 20ml of 0.8% TMG HCl to preserve samples while in the field and prevent volatile loss of Hg. After sample collection,

samples were kept cold (~ 4°C) and in the dark until shipment back to the University of Michigan. Upon arrival, samples were acidified with 0.5% TMG HCl by volume and oxidized with 1% BrCl by volume and allowed to react in a refrigerator for a minimum of 1 month.

A purge and trap method, published in Washburn et al. (2017), was used for pre-concentration of Hg in precipitation samples. Briefly, previously acidified and oxidized samples were weighed into a 2-L borosilicate media bottle. One ml of 30% hydroxylamine hydrochloride was added to the sample to destroy free halogens, the bottle was capped, shaken, and allowed to react for 30 minutes. A Teflon stir bar was added to the bottle which was placed on a stir plate. A three-hole utility cap with a Teflon face on the underside was secured on the top of the bottle. One of the holes was used for the addition of 100 ml of 10% $SnCl_2$ which was delivered to the sample using a peristaltic pump. The second hole was used to draw Hg-free clean lab air through a gold trap and through a glass frit submerged in the solution to purge reduced Hg from solution. The third hole was used to pull Hg from the headspace of the 2L bottle and into a glass trap filled with 5.5 g of 1% $KMnO_4$ solution. A process standard (UM Almaden) and process blanks were processed in tandem with samples. Standard recoveries from this process ranged from 98.0 to 108.9% with an average of 101.3±4.3% (1 SD, n=5). The two samples recovered at 85.1 and 99.2% using this processing method.

2.2.2.4 Snow Sample Collection and Preparation

Snow samples were collected on March 16, 2017 in a clearing in Bridger Teton National Forest, Wyoming (43°51’08.20” N, 110°25’22.24” W) at an elevation of 2136 m, approximately 22 km W of Lost Lake. Sample collection methods are detailed in the supplemental information (section 2.5.1.3). Snow samples were melted and subsequently processed following the procedure published previously in Washburn et al. (2018) for large volume surface water

samples. Samples were collected into 2L Teflon bottles by dipping the lip of the bottle into the snowpack until the bottom was reached. All sampling equipment was cleaned in 10% HNO_3 held at 70°C for 8 hours. Samples were then kept frozen until shipment to the University of Michigan. Upon arrival samples were filtered with a 0.45 μm filter pack (Thermo Scientific). Samples were then acidified with 0.5% HCl by volume and oxidized with 1.0% BrCl by volume. Samples were then allowed to react for a minimum of 1 month in a dark cold room at 4°C.

Hg in snow samples was processed for Hg stable isotope analyses by using an anion column separation method described in detail in Washburn et al. (2018), modified from Strok et al. (2014). Briefly, 5g of the anion exchange resin (AG1X4, Biorad, 200-400 mesh) was cleaned by weighing into an acid cleaned 40ml ICHEM vial and filling it with 4M HNO_3. The vial was alternately placed on a rocker table for 10 minutes and allowed to settle for 20 minutes before decanting and refiling with 4M HNO_3. This process was repeated five times, after which the solution was allowed to settle overnight before a final decant and refill with 4M HNO_3. Following resin cleaning, a 1.5 ml aliquot was added to a pre-cleaned glass column (22cm length, 11mm ID) with a medium porosity frit near the bottom, above the tapper to 6.35mm OD. An acid cleaned PTFE fitting was attached to the bottom of the column and connected to an acid cleaned PTFE length of tubing (6mm ID) which was connected to a peristaltic pump (Fisher Scientific GP1000). The resin that was added to the column was then prepared by pipetting 40 ml of 4M HNO_3, 80 ml DI H_2O and 80 ml of 0.1 M HCl in sequence at a flow rate of 3L/hour. Each sample bottle had 1ml of 30% hydroxylamine hydrochloride added to destroy free halogens and allowed to react for 30 minutes. The sample bottle was then attached to the top of the column with another length of acid cleaned PTFE tubing (6mm ID) inserted to the bottom of the bottle through a hole drilled in the cap of the bottle. An additional hole was drilled in the cap to

allow for Hg-free air (gold filtered) to pass into the headspace of the bottle. Samples were drawn into the top of the column at a rate of approximately 2-3.5L/hour. When all of the sample solution in the bottle was drawn into the tubing, the pump was paused momentarily while the cap was detached and the put on the next sample bottle. The pump was then restarted and the process was repeated until all sample bottles had been drawn through the column. When the final sample bottle was finished, the sample tubing was detached from the top of the of the column. The resin bed was then rinsed with 40ml of 0.1 M HCl and 80 ml of DI H_2O drawn through the column at a rate of 3L/hour. The column was then allowed to run dry before detaching the fitting at the bottom of the column. The Hg was then eluted into an acid cleaned 40 ml ICHEM vial with 10 ml of 0.05% L-cysteine prepared in a 1% sodium citrated dihydrate solution. The eluent was allowed to gravity drip into the vial. When elution was complete, 2ml of 0.2 M BrCl was added to the eluent. An aliquot (0.100 g) of this solution was then added to an acid cleaned UV vial and diluted up to a volume of 5ml with a 1% BrCl. This solution was then exposed to a UV light source for a minimum of 10 days to destroy the organic matrix before analyzing the solution for THg by CV-AFS. Process standard recoveries for this method ranged from 91.2 to 101.1% with an average of 96.6±3.3% (1 SD, n=8). The snow samples recovered at 94.0 and 94.8%.

2.2.3 Lake Sediment Radiometric Dating

Dried and ground lake sediment samples were packed into 10 ml counting vials for the assay of radionuclides (^{210}Pb, ^{226}Ra, and ^{137}Cs). The dry sample mass was small in the upper portion of the core due to high water content, and hence the top 3 cm and the 3-4 cm interval of sediment were combined into two individual samples. Samples were then measured for $^{210}Pb_{total}$,^{226}Ra and ^{137}Cs by gamma spectrometry (Baskaran, 2016). There was no peak background in the energy regions of these nuclides. The gamma ray detector was calibrated with

sediment standards (RGU-1 for ^{210}Pb and ^{226}Ra (via ^{214}Pb and ^{214}Bi at 325 keV and 609 keV, respectively), IAEA-300 for ^{137}Cs (661.6 keV)) obtained from the International Atomic Energy Agency. A vertical profile for $^{210}Pb_{xs}$ was constructed and the constant flux:constant sedimentation model was used to calculate ages for each sample (Baskaran et al., 2015). The average time represented by of each core interval is 40 years and 12 years for 0.5cm and 0.25cm intervals respectively.

The constant flux:constant sedimentation model relies on the assumption that both ^{210}Pb flux and mass accumulation rate of sediment have been constant over the time scale of interest (e.g. Sanchez-Cabeza and Ruiz-Fernandez, 2012 and references therein). These assumptions can be assessed through a plot of $^{210}Pb_{xs}$ versus depth, which should decrease exponentially. Furthermore, the relationship between ln($^{210}Pb_{xs}$) and mass depth (the total sediment mass per cross-sectional area of the core above the measured depth) should display a linear relationship (Figure 2.3), the slope of which is used to calculate ages (Sanchez-Cabeza and Ruiz-Fernandez, 2012). The lake sediment core from Lost Lake exhibited these relationships and therefore the ages determined from ^{210}Pb analyses are believed to be reliable. Additional information on the ^{137}Cs chronology and comparisons of the inventory of excess ^{210}Pb to the global fallout curve is given in the supplementary material.

It has been widely discussed that the excess ^{210}Pb-based chronology need to be validated by another independent method (Smith, 2001). In this present study, because the porosity in the upper few centimeters were very high (98.5 to 99.5%), the amount of dry mass is not sufficient for gamma counting and hence we combined top six sections of 0.5 cm layers. The penetration depth of ^{137}Cs is much deeper than the expected layer corresponding to 1952. The penetration depth of excess ^{210}Pb ($^{210}Pb_{xs}$) is about 10.5 cm (activity is 1.9% of the value in the upper 3 cm),

corresponding to 144 years while the penetration depth of ^{137}Cs is >10.5 cm, which is significantly higher than the expected value of 52 years (=2015-1963). Due to the porosity of the upper few centimeters discussed above, we did not use the ^{137}Cs vertical profile for chronology (Figure 2.4).

The calculated total inventory of $^{210}Pb_{xs}$, 18.02 dpm cm^{-2}, corresponds to a depositional flux of 0.56 dpm cm^{-2} y^{-1}, which can be compared to the long-term ^{210}Pb flux of 0.93±0.45 dpm cm^{-2} y^{-1}, reported for the 40°-50°N latitude belt (Baskaran, 2011). The lower depositional flux of ^{210}Pb is likely due to lower amount of precipitation. Although there is no long-term precipitation data for the study site, annual precipitation record at Jackson, Wyoming (43.4866°N; 110.761°W) indicates that the amount of precipitation is low, 42.8 cm, compared to Detroit, MI which is at a comparable latitude (42.33°N), where the long-term average annual precipitation is 78.7 cm. Thus, the sediment inventory of $^{210}Pb_{xs}$ seems to suggest that there is no sediment focusing and atmospheric deposition of ^{210}Pb is preserved. The inventory of ^{137}Cs, 6.15 dpm cm^{-2}, is higher than expected for similar latitude. Since most of ^{137}Cs is derived from global stratospheric fallout, it is expected to be higher in high altitude sites.

2.2.4 Sample Preparation of Solid Samples for Mercury Isotope Analysis

Approximately 500mg of each solid sample was analyzed via a combustion furnace attached to an atomic absorption spectrometer (combustion-AAS) to determine the concentration of each sample. To prepare solid samples for Hg isotopic analyses, each sample was combusted over a six-hour period by slowly heating the first stage of a two-stage combustion furnace to 750°C in a stream of Hg-free O_2 while the second stage was held at 1000°C (Biswas et al., 2008; Demers et al., 2013). The Hg(0) passed through the furnace tube and was trapped as Hg(II) in a 24 gram trap of 1% $KMnO_4$ dissolved in 10% H_2SO_4 (hereafter referred to as 1% $KMnO_4$). Trap

contents were then partially reduced with 2% (w/w) of a 30% $NH_2OH{\cdot}HCl$ solution and a small aliquot of the trap solution was analyzed for total mercury (THg) concentration via cold vapor-atomic absorption spectrometry (CV-AAS) to determine bulk concentrations and for concentration matching between samples and standards during isotope analyses.

To monitor the efficiency of combustions, procedural blanks and standard reference materials (NRCC MESS-3) were run in tandem with samples. The mean recovery of Hg from MESS-3 for the combustion process was 106.5±2.2% (1SD, n=6). Additionally, the initial concentrations determined by combustion-AAS were used to monitor efficiency of combustions. The recovery of Hg from the samples ranged from 92.1 to 106.6±2.2% with an average of 95.4±6.0% (1SD, n=26).

Post combustion for isotopic analysis, Hg concentrations were measured via CV-AAS on the 1% $KMnO_4$ solutions to determine the bulk sediment Hg concentration (THg). After analysis for THg, Hg in 1% $KMnO_4$ sample solutions was reduced to Hg(0) using 20% (w/w) $SnCl_2$ and subsequently purged and concentrated into a secondary 1% $KMnO_4$ mixture to remove potential matrix components from combustion residues (Blum and Johnson, 2017). During this process, sample recoveries ranged between 84.9 and 106.3% with an average of 98.5±5.1% (1SD, n=31). Yields of >85% have been shown to display no change in isotopic composition (Sherman et al., 2009; Fu et al., 2014).

2.2.5 Hg Isotope Analysis and Reporting of Analytical Uncertainty

For Hg isotope analysis, all samples were partially reduced using 2% (w/w) of a 30% $NH_2OH{\cdot}HCl$ solution and concentration matched (to 5% relative concentration) with NIST SRM 3133 for standard sample bracketing. They were then analyzed for isotopic composition using cold vapor sample introduction on a multiple-collector inductively coupled plasma mass

spectrometer (CV-MC-ICP-MS; Nu Instruments). Samples were reduced on-line with 2% (w/w) $SnCl_2$ and allowed to flow down a frosted glass tip gas-liquid separator. Hg(0) was swept into the MC-ICP-MS with an Ar gas stream. An internal Tl standard (NIST 987) was introduced as a dry aerosol using a desolvating nebulizer (Cetac, Aridus) and used for mass bias correction. Faraday cups were used to measure ion beams at masses 196, 198, 199, 200, 201, 202, 203, 204, 205 and 206 simultaneously (Blum and Bergquist, 2007).

Following the conventions of Blum and Bergquist (2007), we report Hg isotopic composition using delta notation as follows:

$$\delta^{xxx}Hg(‰) = \{[(^{xxx}Hg/^{198}Hg)_{unknown}/(^{xxx}Hg/^{198}Hg)_{SRM3133}]-1\} \times 1000 \quad (1)$$

where xxx is the mass of each Hg isotope between 199 and 204 amu. Isotope ratios are reported throughout using permil (‰) deviation from NIST 3133.

We used the constants from Blum and Bergquist (2007) to calculate $\Delta^{xxx}Hg$ values that can be approximated for small ranges (<10‰) in $\delta^{xxx}Hg$ by the following equations:

$$\Delta^{199}Hg = \delta^{199}Hg - (\delta^{202}Hg \times 0.2520) \quad (2)$$

$$\Delta^{200}Hg = \delta^{200}Hg - (\delta^{202}Hg \times 0.5024) \quad (3)$$

$$\Delta^{201}Hg = \delta^{201}Hg - (\delta^{202}Hg \times 0.7520) \quad (4)$$

$$\Delta^{204}Hg = \delta^{204}Hg - (\delta^{202}Hg \times 1.493) \quad (5)$$

The UM-Almadèn secondary standard was run to assess instrumental analytical uncertainty with each batch of ~10 samples. Samples were run at concentrations between 0.4 and 5 ng/g Hg. Process blanks and secondary standard reference materials were run along with unknown samples. Process combustion blanks yielded between 54.8 and 224 pg of Hg with an average of 99.8±45.7 pg (1SD, n=12). The blank therefore represents less than 2.2% of Hg in solid sample trap solutions. Process and field blanks were analyzed for Hg concentration for

TGM samples. Field blanks resulted in an average of 186±19.0 pg of Hg (1SD, n=2) while process blanks resulted in an average of 85.8±17.5 pg of Hg (1SD, n=2). The field blanks are more representative of the blank for each sample, but still represent <5% of Hg in TGM trap solutions. Process blanks for the purge and trap method yielded 28.0±8.0 pg of Hg (1 SD, n=2), representing less than 0.2% of Hg in precipitation samples. Process blanks for the anion column exchange method were 128.5±16.4 pg of Hg (1 SD, n=3), representing less than 2.0% of Hg in snow samples.

Analytical uncertainty is calculated using analyses of UM-Almadèn and secondary standards run in tandem with samples for isotopic analysis. Internal lab reproducibility is calculated as 2SD of the mean Hg isotopic composition of UM-Almadèn during each analytical session. External reproducibility is calculated as 2SE using the average Hg isotopic composition of procedural standards matched to sample type; NRCC MESS-3 for solid samples, NIST 3133 and UM Almadèn for TGM samples, NIST 1575a for vegetation samples, and UM Almadèn for precipitation and snow samples (Table 2.1). Calculated Hg isotopic values for NRCC MESS-3 were within uncertainty of previously reported values (Blum and Johnson, 2017 and references therein). We report analytical uncertainty for each isotopic ratio as the highest estimated value of either procedural standards or UM Almadèn. For solid samples, we report analytical uncertainty as 2SD of the mean Hg isotopic composition of UM Almadèn as follows: ±0.09‰ for δ^{202}Hg, ±0.02‰ for Δ^{199}Hg, ±0.04‰ for Δ^{200}Hg, ±0.04‰ for Δ^{201}Hg, and ±0.07‰ Δ^{204}Hg (n=11). TGM samples are reported with the same analytical uncertainty for Hg isotopic ratios as above, except for Δ^{199}Hg which we report as 2SE of the NIST 3133 process standard with a value of ±0.05‰ (n=7). Analytical uncertainty for vegetation samples are reported as 2SE of the mean Hg isotopic composition of NIST 1575a as follows: ±0.09‰ for δ^{202}Hg, ±0.04‰ for Δ^{199}Hg, ±0.09‰ for

Δ^{200}Hg, ±0.08‰ for Δ^{201}Hg, and ±0.14‰ Δ^{204}Hg (n=3). Analytical uncertainty for precipitation samples is reported with the same δ^{202}Hg and Δ^{204}Hg as solid samples, all others are reported as the 2SE of the mean Hg isotopic composition of the process UM Almadèn standards processed by purge and trap as follows: ±0.16‰ for Δ^{199}Hg, ±0.07‰ for Δ^{200}Hg, and ±0.14‰ for Δ^{201}Hg (n=2). Snow samples are reported with the same analytical uncertainty as solid samples for δ^{202}Hg, all others are reported as the 2SE of process UM Almadèn standards processed by the anion exchange column method as follows: ±0.09‰ for Δ^{199}Hg, ±0.10‰ for Δ^{200}Hg, ±0.06‰ for Δ^{201}Hg, and ±0.10‰ Δ^{204}Hg (n=8).

2.2.6 Statistics

Statistical tests used in this paper are independent two sample t-tests with equal variance unless otherwise noted. Linear regressions are calculated using the York regression method (York, 1968).

2.3. Results and Discussion

2.3.1 Mercury Flux and Industrial Enrichment

Analyses of ^{210}Pb activity with depth were used to calculate an average mass accumulation rate in Lost Lake of 5.72±0.37 mg cm^{-2} yr^{-1}. This sedimentation rate along with THg concentrations at each depth were subsequently used to calculate Hg fluxes to Lost Lake sediments. THg ranges from 16.2 to 20.8 ng/g in pre-1850 sediments before increasing to a maximum concentration of 98.55 ng/g in 2014. The pre-1850 Hg flux to Lost Lake averaged 2.3±0.1 µg m^{-2} yr^{-1} (1 SD, n=15) (Figure 2.5). A sharp increase in Hg deposition began in about 1850 and increased to 9.1 µg m^{-2} yr^{-1} 1960. From 1960 to 1983 Hg flux decreased to 8.3 µg m^{-2} yr^{-1}, which may be related to a lagged response in the decrease in U.S. coal production and

consumption between 1957 and 1963. However, from 1960 to 1983, U.S. production and consumption of coal steadily increased by approximately 85% (U.S. Energy Information Administration, 2011). Hg flux then increased from 1984 to 2005, to the maximum value observed in the core of 12.5 μg m^{-2} yr^{-1}. A decline in Hg flux from 2005 to 2014 of 12.5 to 11.1 μg m^{-2} yr^{-1} is consistent with declines in recent anthropogenic loading of Hg to the atmosphere (Zhang et al., 2015). For comparison, at five Mercury Deposition Network sites throughout the Rocky Mountain Region from southern Colorado to northern Montana that collect precipitation and quantify "wet" Hg deposition (NADP, 2018), yearly Hg fluxes from 2004 to 2017 range from 3.0 μg m^{-2} yr^{-1} to 16.0 μg m^{-2} yr^{-1}. The modern depositional flux of Hg (commonly defined as 1990-2014 [Engstrom et al., 2014 and references therein]) (1990-2014) that we estimate from Lost Lake sediments (11.5±1.0 μg m^{-2} yr^{-1} [1 SD, n=3]) falls within the range of Hg deposition values measured at regional Mercury Deposition Network Sites.

To calculate an anthropogenic-derived enrichment factor, we subtract the pre-1850 Hg flux from the average Hg flux for modern samples and then divide by the pre-1850 average Hg flux, which yields an industrial enrichment factor of 3.8 for Lost Lake. This calculated enrichment factor is consistent with other historical records in remote lake sediments reported in the literature which range from 2.2 to 7.8 (Swain et al., 1992; Engstrom et al., 1994; Kamman and Engstrom, 2002; Engstrom et al., 2014 and references therein).

2.3.2 Discussion of Upper Fremont Glacier Record

A previous study suggested that Hg used in the gold amalgamation process during the California Gold Rush (circa 1850) might be present in historical records of Hg in the Rocky Mountain Region (Schuster et al., 2002). Two ice cores were investigated from the Upper Fremont Glacier (UFG) in the Wind River Range in Wyoming, approximately 83 km SE of Lost

Lake, revealing a spike in THg thought to be consistent with the timing of the California Gold Rush (Schuster et al., 2002). Other historical records proximal to California (mainly lake sediment records) do not show the THg spike and this has called into question whether Hg used during the California Gold Rush was deposited regionally (Van Metre and Fuller, 2009; Engstrom et al., 2014). Van Metre and Fuller (2009) suggest that the differences seen in the UFG record is due to photoreduction near the top of the ice core correspondent with warming temperatures. Additionally, a new study using an improved ice core dating approach provided an updated timescale for the UFG ice core (Chellman et al., 2017). This effectively shifts the ice core ages to younger values by up to 80 years, causing the spike in THg originally thought to be from the California Gold Rush to be aligned with early 20th century industrial emissions. The Hg record preserved in the sediments of Lost Lake, like other proximal sediment cores, does not show a spike in Hg flux that corresponds to the California Gold Rush, but 1850 is the time when Hg fluxes began to increase from pre-anthropogenic background values (Figure 2.5).

2.3.3 Hg Isotopes in Lost Lake Sediments

Values of δ^{202}Hg in Lost Lake sediments range from -1.06±0.09 to -0.40±0.09‰ (n=29) (Figure 2.6). In pre-1850 samples, the average value for δ^{202}Hg is -0.89±0.13‰ (1 SD, n=15) with values ranging from -1.06±0.09 to -0.64±0.09‰. δ^{202}Hg values show a marked increase from the pre-1850 average to the post-1850 average of -0.52±0.09‰ (1 SD, n=14). These two time periods display average values that are significantly different ($p<0.001$, t-statistic=-8.67, $n_1=15$, $n_2=14$). This difference is suggestive of a change in atmospheric Hg sources and/or fractionation processes occurring between these two depositional periods.

Values of Δ^{199}Hg in Lost Lake sediments range from -0.10±0.02‰ to 0.45±0.02‰ (n=29) throughout the sediment core (Figure 2.6). Pre-1850 samples show limited variation,

ranging from -0.10±0.02‰ to 0.04±0.02‰ (n=15) and have an average Δ^{199}Hg value of -0.02±0.04‰ (1 SD, n=15). Post-1850 Δ^{199}Hg values are much higher with an average value of 0.25±0.10‰ (1 SD, n=14). As with δ^{202}Hg values, these two time periods have average Δ^{199}Hg values that are significantly different ($p<0.001$, t-statistic=-9.07, $n_1=15$, $n_2=14$). Δ^{201}Hg values display a similar range of values as Δ^{199}Hg and additionally match the temporal trend observed for Δ^{199}Hg. When all sediment core samples are plotted on a Δ^{199}Hg vs. Δ^{201}Hg diagram, a York regression (York, 1968) yields a slope of 1.06±0.05 (Figure 2.7), which is consistent with the 1:1 relationship suggested by Bergquist and Blum (2007) as evidence for aqueous photoreduction of Hg(II) and loss of Hg(0).

Δ^{200}Hg values range from 0.05±0.04‰ to 0.19±0.04‰ (n=29) (Figure 2.6), with a pre-1850 average of 0.11±0.03‰ (1 SD, n=15) and a post-1850 average of 0.14±0.04‰ (1 SD, n=14). Similarly, Δ^{204}Hg values vary from pre to post-1850 samples, ranging from -0.28±0.07‰ to -0.12±0.07‰ (n=29) with an average value of -0.21±0.04‰ (1 SD, n=29). The average Δ^{200}Hg/Δ^{204}Hg ratio is -0.59, which is similar to an average ratio of about -0.5 observed in other studies of atmospherically derived Hg (Blum and Johnson, 2017 and references therein). Although there is slight variation in even-MIF between pre-1850 and post-1850 samples, the consistent positive sign of Δ^{200}Hg and negative sign of Δ^{204}Hg are the same as observed in modern precipitation measurements (Chen et al., 2012; Demers et al., 2013; Sherman et al., 2015; Blum and Johnson et al., 2017; Yuan et al., 2018). Even-MIF has been proposed to be a conservative tracer for UV initiated oxidation of Hg in the tropopause (Chen et al., 2012). While the exact mechanism for even-MIF is uncertain, the Δ^{204}Hg and Δ^{200}Hg values throughout the entire sediment core provide evidence for a constant even-MIF fractionation mechanism from the pre-1850 period to the present.

2.3.4 Atmospheric Hg Deposition Pathways to Lost Lake

There are several possible depositional pathways by which Hg can enter lake sediments, including wet deposition directly to the lake's surface, dry deposition to the lake's surface, and uptake of Hg(0) and Hg(II) by vegetation in the catchment with subsequent transport to the lake via soil erosion. To assess which pathway(s) are dominant in Lost Lake, we compare the isotopic composition of lake sediments to measurements of TGM, vegetation and organic soils, and both previously published and new Hg isotope values for precipitation from North America. Two samples of snow were collected in the vicinity of Lost Lake and analyzed for Hg isotopes. The average isotopic composition for these two samples was δ^{202}Hg=-0.36±0.18‰, Δ^{199}Hg=1.96±0.20‰, Δ^{200}Hg=0.12±0.00‰ and Δ^{204}Hg=-0.40±0.03‰ (±1SD, n=2). Precipitation samples were also collected for Hg isotopic measurements in the region of Lost Lake. One sample collected at Camp Davis, WY displayed the following isotopic composition: δ^{202}Hg=-0.06±0.09‰, Δ^{199}Hg=0.45±0.16‰, Δ^{200}Hg=0.23±0.07‰ and Δ^{204}Hg=-0.33±0.07‰. Another precipitation sample was collected at a high elevation site much farther away but also in the Rocky Mountain Region at Storm Peak, CO and yielded similar precipitation sample values: δ^{202}Hg=0.17±0.09‰, Δ^{199}Hg=0.95±0.16‰, Δ^{200}Hg=0.23±0.07‰ and Δ^{204}Hg=-0.35±0.07‰. Average North American precipitation values from sites in the Great Lakes Region, Florida, and California that are not directly impacted by point source Hg emissions are -0.41±0.48‰, 0.36±0.27‰, and 0.23±0.17‰ for δ^{202}Hg, Δ^{199}Hg and Δ^{200}Hg respectively (±1 SD, n=70) (Gratz et al., 2010; Chen et al., 2012; Sherman et al., 2012a; 2015; Demers et al., 2013; Donovan et al., 2013). The precipitation values reported from this study in the Rocky Mountains are statistically similar to samples collected at many other locations in North America that are not directly impacted by anthropogenic sources ($p>0.13$ for all isotope values $n_1=70$, $n_2=2$, independent two

sample t-test with equal variance and Mann-Whitney U test). The precipitation samples reported in this study are also statistically indistinguishable from modern sediment samples in Lost Lake ($p>0.14$ for all isotope values, $n_1=2$, $n_2=3$, Mann-Whitney U test).

Based on the MDF and both the odd and even MIF observed in snow and precipitation samples, it appears that a combination of these two Hg sources is the most likely dominant modern source of Hg to Lost Lake sediments (Figure 2.8). According to the estimates from the Mercury Deposition Network monitoring sites in the Rocky Mountain region, deposition via precipitation (late June to early September) accounts for 39-77% of total wet deposition of Hg throughout the year (NADN, 2018). We can calculate an endmember, that when added to pre-1850 sediments would yield the Hg isotopic composition observed in modern Lost Lake sediments. This endmember would require 75% precipitation and 25% snow derived Hg and is plotted on Figure 2.7. Additionally, Figure 2.9 depicts 1/[Hg] vs. 199 and 202, displaying a strong linear relationship ($r^2=0.85$, 0.74 respectively). This provides additional evidence for mixing of two sources, in this case pre-1850 Hg with modern snow and precipitation.

Mercury isotopic studies of precipitation throughout North America shows there is considerable variation in MDF but all analyses have positive odd MIF (Gratz et al., 2010; Chen et al., 2012; Sherman et al., 2012a; 2015; Demers et al., 2013; Donovan et al., 2013) (Figure 2.8). Another consistent signal in all precipitation analyses is the occurrence of even MIF, with all precipitation samples displaying positive Δ^{200}Hg and negative Δ^{204}Hg. While the mechanism causing even MIF is unknown, precipitation-derived samples are the only type of sample in which this even MIF signature is observed. The consistent positive Δ^{200}Hg and negative Δ^{204}Hg throughout the entire core of Lost Lake sediments is strong additional evidence that precipitation derived Hg is the dominant source of Hg to Lost Lake.

Our isotopic measurements of atmospheric TGM at Rendezvous Mountain display negative odd-MIF (Δ^{199}Hg=-0.27±0.01‰, Δ^{201}Hg=-0.23±0.03‰, 1SD, n=3), and both negative and positive even-MIF (Δ^{200}Hg=-0.07±0.01‰, Δ^{204}Hg=0.12±0.02‰, 1SD, n=3). This isotopic composition is consistent with other measurements of TGM globally at locations not impacted by local Hg sources (Gratz et al., 2010; Demers et al., 2013; Demers et al., 2105; Fu et al., 2016; Obrist et al., 2017). Vegetation collected from the catchment of Lost Lake displayed isotope values of δ^{202}Hg=-2.89±0.09‰, Δ^{199}Hg=-0.23±0.04‰ and Δ^{201}Hg=-0.30±0.08‰. TGM that enters the stomata of leaves and accumulates in foliage and then soil retains the negative Δ^{199}Hg and Δ^{201}Hg but undergoes MDF, leading to a ~2.5‰ decrease in δ^{202}Hg between vegetation and TGM (Demers et al., 2013; Enrico et al., 2016; Zheng et al., 2016; Obrist et al., 2017). This phenomenon is documented at Lost Lake where we observe a difference of -2.61‰ in δ^{202}Hg between regional TGM and vegetation sampled from Lost Lake. O-horizon soils from the catchment of Lost Lake are isotopically similar to vegetation, but with somewhat higher δ^{202}Hg of -1.69±0.09‰ as compared to vegetation. In other studies, this shift has been explained by mixing of litterfall with underlying mineral soil or with precipitation, or abiotic, photochemical, and microbial reduction of Hg(II), thus shifting δ^{202}Hg to more positive values in organic soils as compared to δ^{202}Hg values in vegetation (Demers et al., 2013; Jiskra et al., 2015; Zheng et al., 2016). Based on both MDF and MIF observations in TGM, soil, and vegetation these possible sources of Hg don't appear to dominate Hg deposition to Lost Lake sediments. If these Hg sources were dominant, we would expect to see slightly negative odd-MIF and more negative MDF than is observed in the lake sediments. It appears that because Lost Lake has a very small watershed to lake surface area ratio, other inputs do not mask the precipitation derived signal as is the case in many other lakes.

2.3.5 Pre-1850 Atmospheric Hg

Prior to 1850, Hg originating from volcanic and hydrothermal (geogenic) emissions was the dominant source of "new" Hg inputs to the Earth surface system. Re-emission to the atmosphere of Hg previously deposited to Earth surface reservoirs, including the oceans and soils also contributed to the total atmospheric Hg burden (Mason et al., 1994; Biester et al., 2007; Selin et al., 2008). The average δ^{202}Hg value of Lost Lake pre-Industrial samples is -0.89±0.13‰ (1 SD, n=15), which is not statistically different from the average value for TGM measured from three passively degassing volcanoes in Italy and Indonesia (-0.76±0.22‰, 1SD, n=9) (Zambardi et al., 2009; R. Sun et al., 2016), providing evidence for a dominant atmospheric source of Hg of geogenic origin ($p=0.074$, t-statistic=-1.87, $n_{volcanic}=9$, $n_{sediments}=15$). Additionally, geogenic-derived Hg exhibits near 0‰ MIF, which is consistent with measurements made in pre-1850 samples in Lost Lake. While we argue that geogenic emissions are the dominant source of "new" Hg to Lost Lake sediments, this statement comes with the caveat that there are a limited number of direct volcanic emission measurements from a limited number of sites and therefore, this source needs additional characterization to be definitively attributable as the dominant source of Hg to the pre-1850 Lost Lake sediments. Additionally, Hg released from volcanoes may undergo redox reactions in the atmosphere, causing possible isotopic fractionation of Hg prior to deposition to lake surfaces and obscuring the initial isotopic composition.

The proximity of Yellowstone National Park (YNP) to Lost Lake could represent a source of regional Hg due to the volatilization of Hg from the large active hydrothermal system (Hall et al., 2006; King et al., 2006; Sherman et al., 2009). Hall et al. (2006) measured Hg concentrations at sites within YNP but far from hydrothermal features and emission plumes and suggested that these values reflected global background concentrations. In close proximity to

hydrothermal features, Hg(0) concentrations were elevated above background. To assess if these anomalies were a significant source of Hg(0) to areas outside YNP, Hall et al (2006) used a Gaussian plume model to estimate Hg(0) fluxes. They concluded that Hg(0) was quickly dispersed and concentrations were diluted such that the YNP source did not significantly contribute Hg outside of YNP (Hall et al., 2006). Based on these conclusions Hg derived from the hydrothermal system in YNP is not considered to be a significant source of Hg to Lost Lake, and if there are minor contributions they would be expected to be relatively constant over time.

Forest fires in the area could have influenced the isotopic composition measured in Lost Lake sediments. However, this process would be expected to conserve the negative MIF signature measured in vegetation (average Δ^{199}Hg=-0.24±0.09‰, Δ^{201}Hg=-0.26±0.10‰ [1SD, n=48]) (Tsui et al., 2012; Demers et al., 2013; Zheng et al., 2016; Obrist et al., 2017; Ku et al., 2018), which is more negative than measurements made in all Lost Lake sediments. Additions of Hg from wildfires would be intermittent and limited in temporal scale, and the impact of such additions are difficult to verify due to the lack of charcoal found in any of the sediment layers.

2.3.6 Changing Atmospheric Composition of Hg During the Industrial Period

The trend in Δ^{199}Hg and δ^{202}Hg observed in Lost Lake sediments from 1850 to the present could be attributable to the following scenarios: 1) a change in sources of new Hg to the atmosphere beginning in ~1850 which have more positive Δ^{199}Hg and δ^{202}Hg values than pre-1850 geogenic inputs, 2) a change in atmospheric reductant composition resulting in increased photochemical reduction of Hg(II) in precipitation in the atmosphere, or 3) an increase in photochemical reduction of Hg(II) within the water column of Lost Lake, prior to deposition of Hg to the sediments.

2.3.6.1 Shifting Sources of Hg to the Atmosphere

At the onset of the Industrial Revolution, Hg sources to the atmosphere began to shift from dominantly geogenic to dominantly anthropogenic emissions (Streets et al., 2011; Horowitz 2014; Amos et al., 2015; Bagnato et al., 2015; R. Sun et al., 2016). R. Sun et al. (2016) used published Hg isotope data of source materials, coupled with Hg emission inventories to model the historic Hg isotopic composition of Hg(0), Hg(II) and particulate bound mercury (Hg(p)) emissions. Their model estimates a 0.44‰ increase in δ^{202}Hg and a 0.02‰ decrease in Δ^{199}Hg of THg from 1850 to the present. The positive shift in δ^{202}Hg agrees with the shift observed in Lost Lake sediments of +0.37‰ from pre-1850 to post-1850 samples. However, the negative shift predicted for Δ^{199}Hg is in the opposite direction of the +0.23‰ shift observed in Lost Lake sediments. R. Sun et al. (2016) pointed out that there were major changes in sources of Hg emissions with shifts from Hg(0) emissions from liquid Hg used in metal extraction and smelting in the late 1800's to increased emissions from coal combustion in the mid 1900's. This shift in sources drives the isotopic changes modeled by R. Sun et al. (2016) during this time interval.

Neither a shift in Hg source from volcanic to anthropogenic emissions nor a change in the Δ^{199}Hg of the dominant anthropogenic Hg sources to the atmosphere are reflected in the measured Δ^{199}Hg in Lost Lake. Volcanic emissions do not show significant odd-MIF (Δ^{199}Hg =0.05±0.06‰, 1 SD, n=9) (Zambardi et al., 2009; R. Sun et al., 2016) and globally averaged anthropogenic emissions are modeled to range from -0.01 to -0.04‰ in Δ^{199}Hg from 1850 to 2010 (R. Sun et al., 2016). If we assume these values are representative of global Hg emissions of geogenic and anthropogenic Hg respectively, this shift in Δ^{199}Hg to more negative values due to a changing Hg source is not in accordance with the positive shift of 0.23‰ for Δ^{199}Hg observed in Lost Lake sediments. Additionally, other Hg deposition records from remote lake

sediments (Cooke et al., 2013; Guédron et al., 2016; Yin et al., 2016), and peat cores (Enrico et al., 2017) also show a positive shift in odd MIF from pre-1850 to post-1850 samples. The lack of correlation between modeled odd MIF emissions values and measured values in Lost Lake sediments implies that if the modeled Hg isotopic values are correct, the temporal change in Hg isotopic composition measured in Lost Lake sediments are likely to be process-driven fractionation rather than source-driven.

2.3.6.2 Changing Hg Isotope Fractionation

Redox reactions that occur in the atmosphere can influence the isotopic composition of Hg in atmospherically derived samples (Gratz et al., 2010; Chen et al., 2012; Demers et al., 2013; Enrico et al., 2016; Zheng et al., 2016). To explore the role Hg oxidation reactions play in Hg isotope fractionation, G. Sun et al. (2016) performed gas-phase Hg oxidation experiments involving atomic Cl and Br. Experimental results of Hg oxidation reactions with Cl yielded a $\Delta^{199}Hg/\Delta^{201}Hg$ slope of 1.64±0.30, and oxidation reactions with Br yielded $\Delta^{199}Hg/\Delta^{201}Hg$ slope of 1.89±0.18. In addition to oxidation, aqueous photoreduction of Hg(II) bound to dissolved organic matter (DOM) has been shown to induce odd-MIF with a $\Delta^{199}Hg/\Delta^{201}Hg$ ratio of about 1.00±0.02 and a $\Delta^{199}Hg/\delta^{202}Hg$ ratio of 1.15±0.07 (Bergquist and Blum, 2007). When this characteristic isotope ratio was initially observed in precipitation, Gratz et al. (2010) proposed that it was caused by photochemical reduction of Hg(II) to Hg(0) in droplets or on ice crystals containing DOM in the atmosphere. Because this process results in causing a characteristic $\Delta^{199}Hg/\Delta^{201}Hg$ ratio, photochemical reduction of Hg(II) has been called upon as the driver of the positive odd-MIF observed in precipitation-derived samples (Blum et al., 2014 and references therein). In our study, when all of the Lost Lake sediment samples are regressed using a York regression (York, 1968), they yield a $\Delta^{199}Hg/\Delta^{201}Hg$ slope of 1.06±0.05 (Figure 2.7) and a

$\Delta^{199}Hg/\delta^{202}Hg$ slope of 1.07±0.10 (Figure 2.10). These results most closely match those of photoreduction experiments, leading us to conclude that this process could be driving the changes in isotopic composition in Lost Lake sediments.

During the Industrial period (1850 to present), the increase in fossil fuel combustion has released byproducts into the atmosphere (e.g. DOM), effectively increasing the reduction capacity of the atmosphere (Baken et al., 2011; Stubbins et al., 2012). Concurrently, there has been a 3 to 5-fold increase in Hg(0) in the atmosphere. Ligands important in oxidation and reduction reactions of Hg such as Br and S attached to DOM could have increased the proportion of Hg that is photochemically reduced in the atmosphere prior to deposition to Lost Lake. This phenomenon could explain the observed changes in MDF and odd MIF signals along the characteristic aqueous photoreduction slopes as discussed above.

Yin et al. (2016) attributed a generally increasing $\Delta^{199}Hg$ signal from 1990 to the present in two Tibetan lakes to decreased ice cover and thus, increased photoreduction within the lakes. In Lost Lake, $\Delta^{199}Hg$ values begin to increase significantly starting around 1850, which is far in advance of significant warming trends (Briffa, 2000), suggesting that the phenomenon observed by Yin et al. (2016) may not occur at Lost Lake. A very remote equatorial lake, El Junco, located on the Galapagos Islands, displays a similar trend in $\Delta^{199}Hg$ to what we observe in Lost Lake (Cooke et al., 2013) This suggests that the increasing $\Delta^{199}Hg$ may be a global trend rather than a local one due to ice cover. Additionally, we argue that the dominant source of Hg to Lost Lake sediments is from precipitation and snow, which carries a much higher magnitude odd-MIF signal than the observed composition of pre-1850 lake sediments. This suggests that the photoreduction is occurring in precipitation droplets (Gratz et al., 2010) prior to deposition to the lake surface. However, we cannot rule out the possibility that in-situ fractionation in the water

column, related to decreasing ice cover and increasing surface water exposure to sunlight for a greater part of each year, led to the observed increasing MIF trend. The single published ice core study from the Canadian Arctic indicates that there has been no change in the isotopic composition of precipitation from pre-1850 to post-1850. However, as stated by the authors, it is likely that the Hg isotopic signal observed in these samples is dominated by local marine sources rather than preserving a global signal (Zdanowicz et al., 2016).

We suggest that based on the characteristic slopes of $\Delta^{199}Hg/\Delta^{201}Hg$ and $\Delta^{199}Hg/\delta^{202}Hg$ observed in Lost Lake sediments, that the increasing trend in both MDF and MIF from 1850 to present is likely due to changes in the fraction of Hg(II) that is photochemically reduced prior to deposition to lake sediments, either within precipitation droplets or within the lake water column. This implies the proportion of Hg(II) in precipitation and/or within the water column that is photochemically reduced prior to deposition to Lost Lake sediments has increased as the concentration of Hg in the atmosphere has increased since 1850. We use the measured shift in $\Delta^{199}Hg$ and experimental fractionation experiments (Bergquist and Blum, 2007) to estimate that about 20% of Hg(II) was photochemically reduced and lost as Hg(0).

2.4 Conclusions

Lost Lake is far from any point sources of Hg and the small catchment area to lake surface area ratio makes it an ideal location to document temporal changes in Hg deposition. Lake sediments reveal an increase in Hg loading to the lake sediments by a factor of 3.8 from pre-1850 to modern samples. This is concurrent with a positive shift both MDF and odd MIF recorded in the sediments but there is a significant and unchanging record of even MIF. Comparing the values in the lake sediments to geogenic emissions and modeled anthropogenic

emissions, the change in dominant emissions sources from pre-1850 (geogenic) to post-1850 (anthropogenic) cannot account for the temporal shift observed in Lost Lake.

We conclude that the temporal change in the Hg isotopic composition in Lost Lake sediments is due instead to an increase in the proportion of Hg(II) that is photochemically reduced either in precipitation droplets prior to deposition to the lake surface, in the water column of Lost Lake, or a combination of both. Increases in Hg photoreduction have been caused by the presence of higher levels of other anthropogenic atmospheric pollutants (for instance DOM) or a decrease in annual ice cover. Further work will be needed to elucidate whether the changes in Hg isotope fractionation occurred in the atmosphere or the lake, but it is clear that remote small-catchment lakes provide important records of environmental change in high elevation locations.

Funding

This research did not receive any specific grant from funding agencies in the public, commercial, or not-for-profit sectors.

Acknowledgements

We thank Marcus Johnson for his skillful assistance in operating the CV-MC-ICP-MS and both Don Zak and Kyle Meyer for their generous help in the field.

Table 2.1 Summary of Hg stable isotope values for standards and reference materials.

For UM Almadèn, n1 denotes the number of isotope measurements and n2 denotes the number of analytical sessions. For reference materials, n1 denotes the number of process replicates and n2 represents the number of isotope measurements.

Reference Material	n1	n2	$\delta^{204}Hg$	2SD	$\delta^{202}Hg$	2SD	$\delta^{201}Hg$	2SD	$\delta^{200}Hg$	2SD	$\delta^{199}Hg$	2SD	$\Delta^{204}Hg$	2SD	$\Delta^{201}Hg$	2SD	$\Delta^{200}Hg$	2SD	$\Delta^{199}Hg$	2SD
UM-Almadèn (this study)	65	11	-0.85	0.17	-0.57	0.09	-0.48	0.08	-0.28	0.08	-0.17	0.04	-0.01	0.07	-0.05	0.04	0.00	0.04	-0.02	0.02
Mess-3	16	33	-3.35	0.07	-2.25	0.05	-1.73	0.04	-1.13	0.04	-0.57	0.02	0.01	0.03	-0.04	0.01	0.00	0.02	0.00	0.02
NIST 1575a	3	3	-2.22	0.19	-1.48	0.09	-1.47	0.11	-0.76	0.09	-0.67	0.03	-0.01	0.14	-0.36	0.08	-0.02	0.09	-0.30	0.04
NIST 3133 TGM Proc. Ref.	7	7	0.08	0.12	0.02	0.08	0.01	0.06	0.00	0.03	0.03	0.05	0.05	0.05	-0.01	0.04	0.00	0.02	0.02	0.05
UM-Almadèn TGM Proc. Ref.	2	2	-0.79	0.04	-0.53	0.00	-0.47	0.04	-0.26	0.03	-0.20	0.10	0.00	0.04	-0.07	0.04	0.00	0.03	-0.07	0.10
UM-Almadèn Precipitation Proc. Ref.	2	2	-0.74	0.04	-0.45	0.02	-0.39	0.15	-0.20	0.08	-0.14	0.17	-0.06	0.06	-0.04	0.14	0.03	0.07	-0.03	0.16
UM-Almadèn Snow Proc. Ref.	8	23	-0.84	0.2	-0.53	0.07	-0.45	0.10	-0.28	0.08	-0.16	0.10	-0.05	0.10	-0.05	0.06	-0.01	0.10	-0.03	0.09

Table 2.2 Summary of THg and Hg isotopic ratios for all samples collected.

*Concentration expressed in ng/m^3. **Concentration expressed in ng/L

Sample	^{210}Pb Date	Mid-Section Depth	Concentration	δ^{204}Hg	δ^{202}Hg	δ^{201}Hg	δ^{200}Hg	δ^{199}Hg	Δ^{204}Hg	Δ^{201}Hg	Δ^{200}Hg	Δ^{199}Hg
	Year	cm	ng/g	‰	‰	‰	‰	‰	‰	‰	‰	‰
Lost Lake 00-03	2014	1.5	98.55	-0.96	-0.46	-0.02	-0.06	0.34	-0.28	0.32	0.17	0.45
Lost Lake 03-04	2000	3.5	96.22	-0.84	-0.40	0.09	-0.01	0.34	-0.24	0.39	0.19	0.44
Lost Lake 4.25	1990	4.25	77.08	-0.95	-0.47	-0.06	-0.12	0.25	-0.25	0.30	0.12	0.37
Lost Lake 4.75	1983	4.75	68.54	-1.16	-0.60	-0.21	-0.18	0.21	-0.27	0.24	0.12	0.36
Lost Lake 5.25	1976	5.25	71.16	-1.02	-0.54	-0.22	-0.14	0.14	-0.21	0.18	0.13	0.28
Lost Lake 5.75	1968	5.75	71.62	-0.92	-0.47	-0.12	-0.11	0.13	-0.22	0.23	0.13	0.25
Lost Lake 6.25	1960	6.25	74.58	-1.19	-0.67	-0.30	-0.20	0.09	-0.19	0.20	0.14	0.26
Lost Lake 7.25	1942	7.25	67.84	-1.05	-0.53	-0.33	-0.18	0.05	-0.25	0.07	0.09	0.18
Lost Lake 7.75	1930	7.75	59.96	-0.85	-0.40	-0.25	-0.08	0.08	-0.25	0.05	0.13	0.18
Lost Lake 8.25	1922	8.25	49.86	-0.81	-0.42	-0.22	-0.09	0.08	-0.18	0.10	0.12	0.18
Lost Lake 8.75	1912	8.75	44.25	-1.02	-0.56	-0.31	-0.17	0.00	-0.19	0.11	0.11	0.14
Lost Lake 9.25	1901	9.25	39.68	-1.07	-0.56	-0.35	-0.15	0.01	-0.23	0.07	0.14	0.15
Lost lake 10	1876	10	31.35	-1.09	-0.57	-0.35	-0.14	0.06	-0.23	0.08	0.15	0.21
Lost Lake 11	1851	11	24.55	-1.22	-0.69	-0.45	-0.16	-0.05	-0.19	0.07	0.18	0.13
Lost Lake 12	1817	12	19.82	-1.36	-0.76	-0.67	-0.26	-0.20	-0.23	-0.10	0.12	-0.01
Lost Lake 13	1788	13	19.35	-1.65	-1.00	-0.80	-0.45	-0.25	-0.16	-0.05	0.05	0.00
Lost Lake 14	1761	14	18.56	-1.31	-0.75	-0.64	-0.31	-0.23	-0.20	-0.08	0.07	-0.05
Lost Lake 15	1733	15	18.20	-1.59	-0.91	-0.84	-0.32	-0.27	-0.23	-0.16	0.13	-0.04
Lost Lake 16	1701	16	20.46	-1.27	-0.72	-0.66	-0.25	-0.23	-0.19	-0.12	0.11	-0.05
Lost Lake 17	1670	17	19.20	-1.66	-0.98	-0.86	-0.40	-0.32	-0.20	-0.13	0.09	-0.08
Lost Lake 18	1640	18	20.46	-1.12	-0.64	-0.58	-0.20	-0.12	-0.16	-0.10	0.12	0.04
Lost Lake 19	1607	19	18.80	-1.74	-1.00	-0.84	-0.36	-0.21	-0.25	-0.09	0.14	0.04
Lost Lake 20	1572	20	20.77	-1.71	-1.06	-0.90	-0.41	-0.26	-0.12	-0.10	0.12	0.00
Lost Lake 21	1539	21	19.75	-1.70	-0.98	-0.80	-0.39	-0.30	-0.25	-0.07	0.10	-0.06
Lost Lake 22	1503	22	19.86	-1.65	-1.01	-0.92	-0.41	-0.36	-0.14	-0.16	0.09	-0.10
Lost Lake 23	1471	23	18.71	-1.36	-0.77	-0.68	-0.26	-0.19	-0.22	-0.10	0.13	0.00
Lost Lake 24	1435	24	18.86	-1.59	-0.97	-0.91	-0.35	-0.31	-0.15	-0.18	0.14	-0.06
Lost Lake 25	1401	25	19.28	-1.53	-0.86	-0.84	-0.32	-0.21	-0.24	-0.19	0.11	0.00
Lost Lake 26	1362	26	16.24	-1.58	-0.93	-0.83	-0.37	-0.26	-0.20	-0.13	0.10	-0.03
Lost Lake Soil			219.00	-2.63	-1.69	-1.64	-0.81	-0.73	-0.10	-0.37	0.04	-0.31
Lost Lake Vegetation			5.67	-4.44	-2.89	-2.47	-1.42	-0.96	-0.13	-0.30	0.03	-0.23

Rendezvous Mountain TGM_2016			0.93*	0.43	0.20	-0.05	0.02	-0.19	0.13	-0.20	-0.09	-0.24
Rendezvous Mountain TGM_2017_1			0.89*	0.65	0.34	0.00	.011	-0.19	0.13	-0.26	-0.07	-0.28
Rendezvous Mountain TGM_2017_2			0.89*	0.54	0.30	0.00	.008	-0.22	0.09	-0.23	-0.07	-0.29
Camp Davis Precipitation			6.90**	-0.42	-0.06	0.46	0.20	0.43	-0.33	0.51	0.23	0.45
Storm Peak Precipitation			18.62**	-0.09	0.17	1.07	0.32	0.99	-0.35	0.94	0.23	0.95
Lost Lake Snow_ 1			0.23**	-0.72	-0.23	1.71	0.00	2.05	-0.38	1.88	0.11	2.11
Lost Lake Snow_ 2			0.22**	-1.15	-0.49	1.24	-0.13	1.70	-0.42	1.61	0.12	1.82

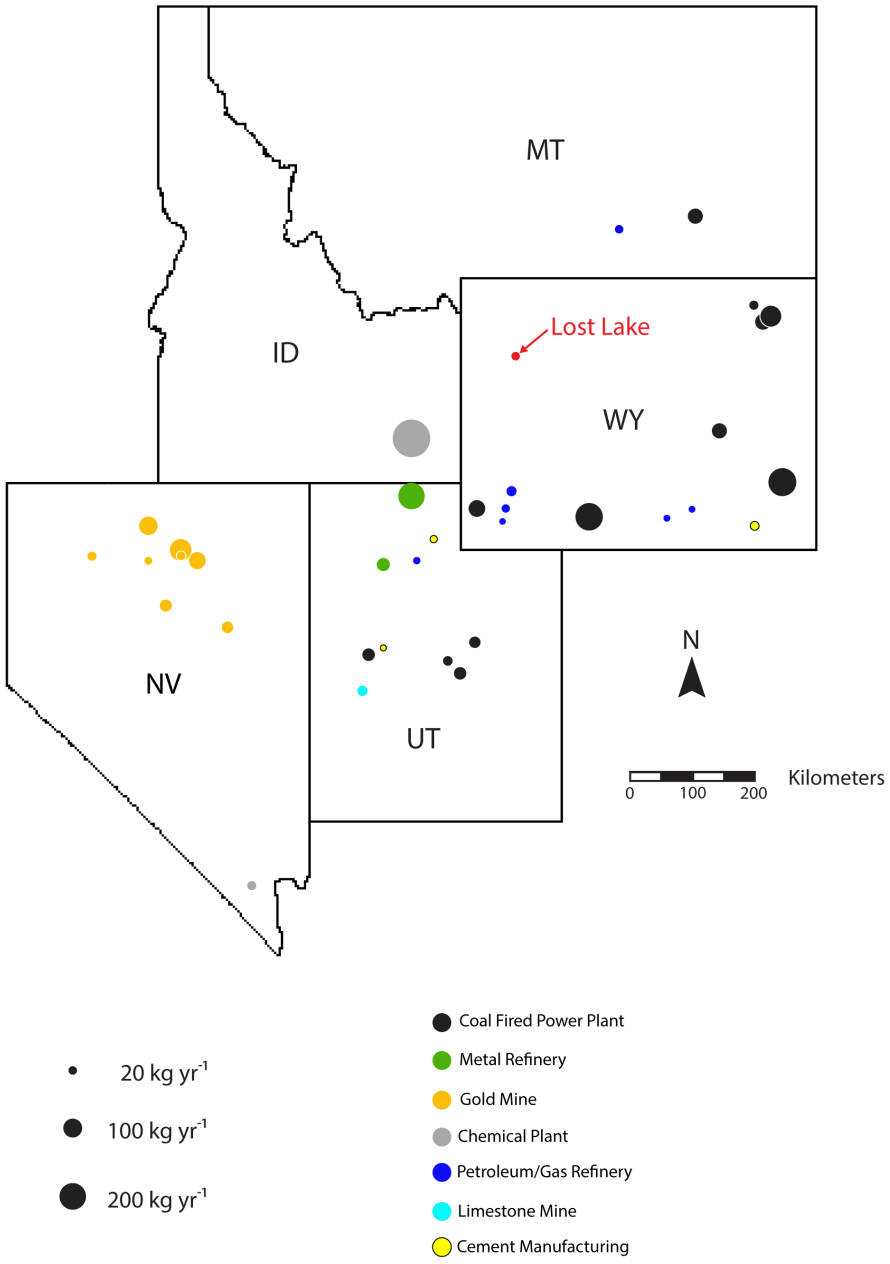

Figure 2.1 Location of Lost Lake in Wyoming, USA with respect to local and regional sources of industrial mercury.

Symbol size is scaled based on reported annual emission of Hg (U.S. Environmental Protection Agency, 2014).

Figure 2.2 Air photo of Lost Lake and associated watershed.

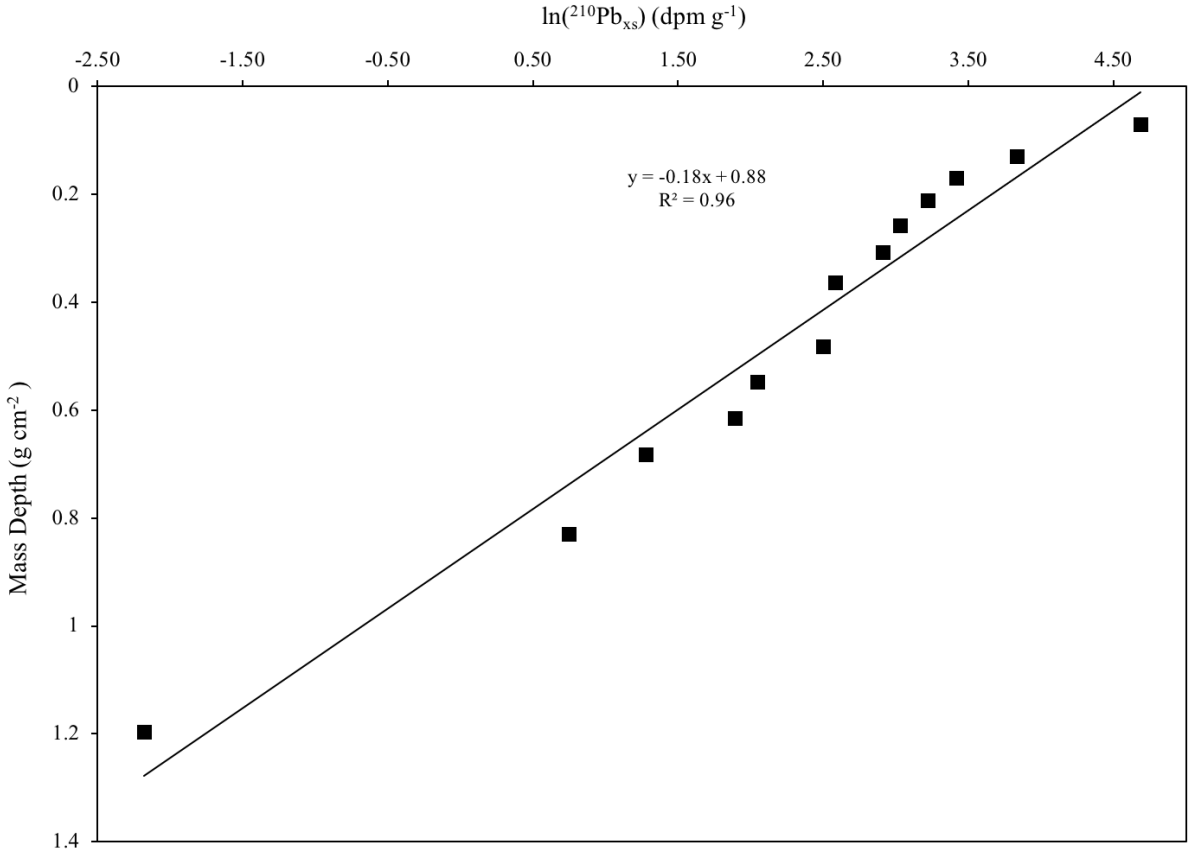

Figure 2.3 Plot of ln($^{210}Pb_{xs}$) versus mass depth (the total sediment mass per cross-sectional area of the core above the measured depth).

The calculated linear regression slope is subsequently used to calculate the sedimentation rate in Lost Lake.

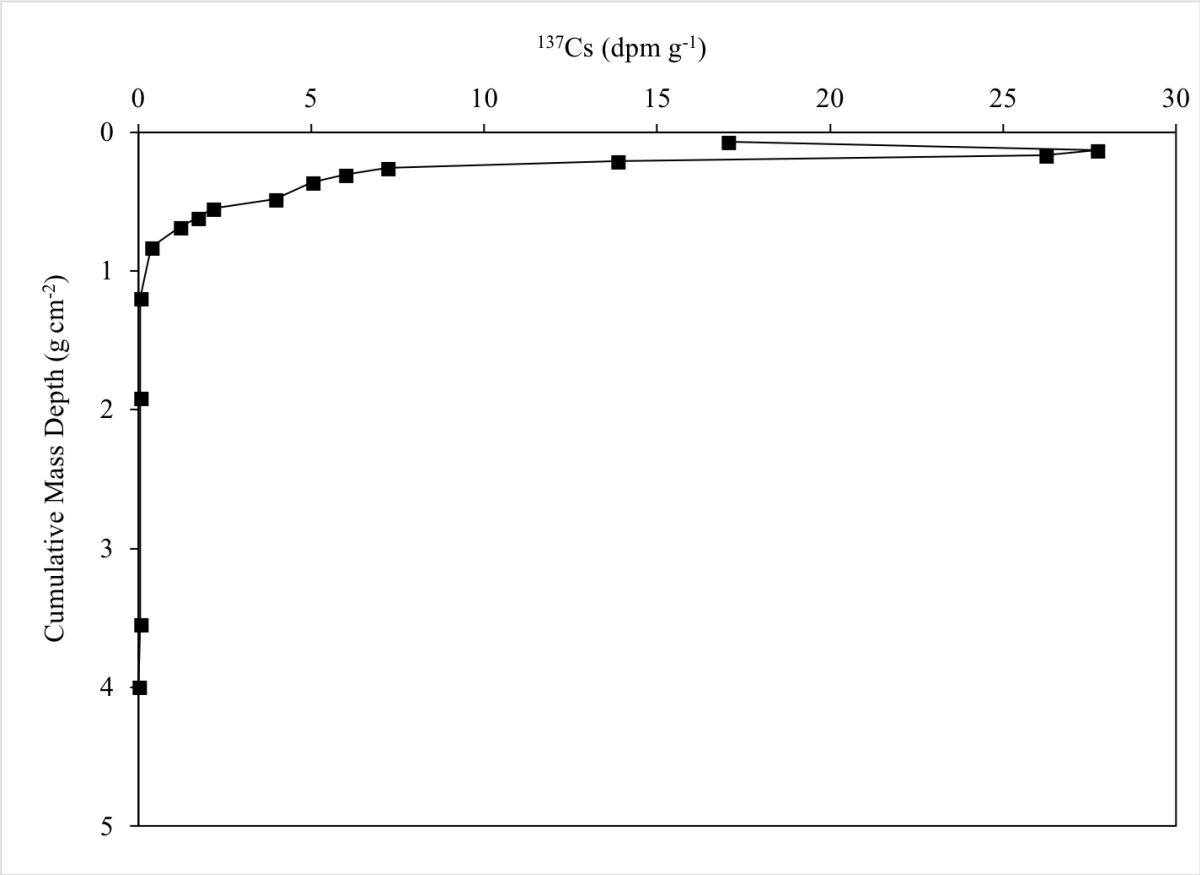

Figure 2.4 Plot of ^{137}Cs versus Cumulative Mass Depth.

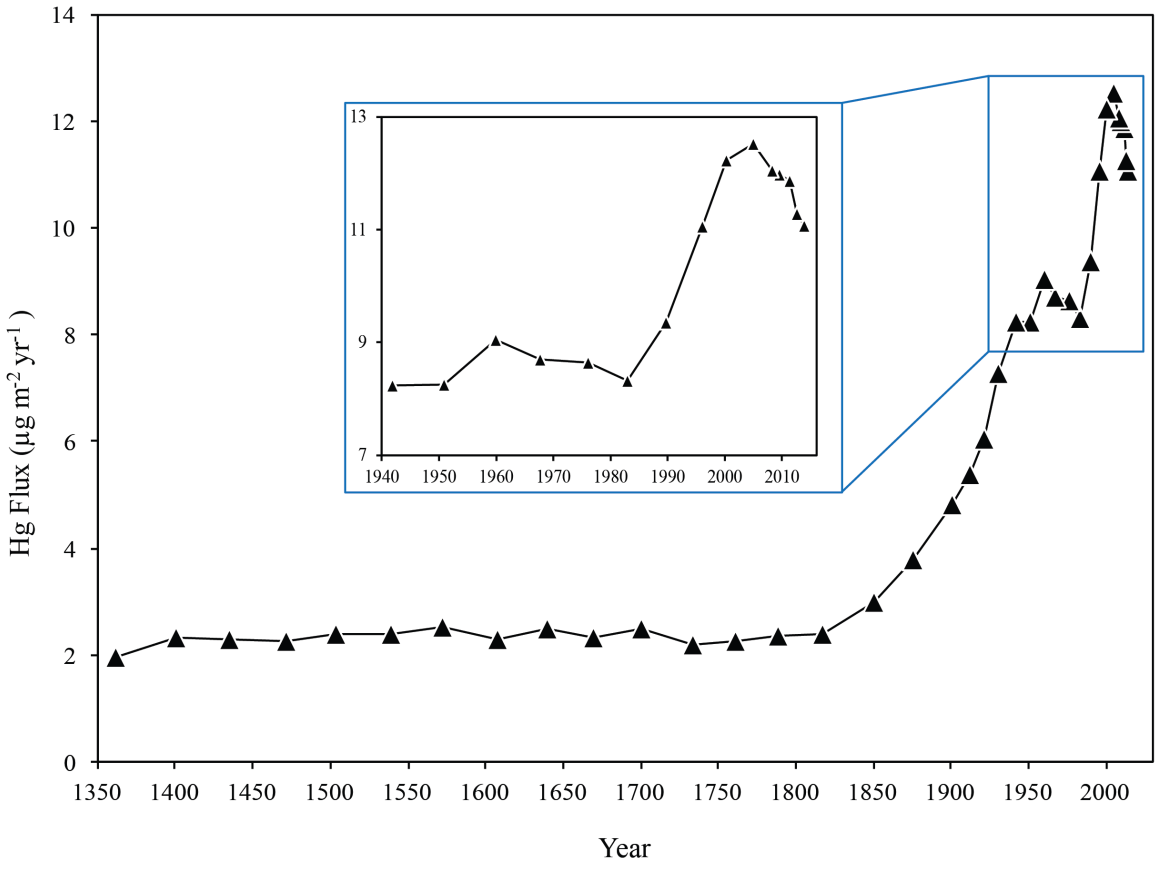

Figure 2.5 Flux of THg to Lost Lake sediments over time.

Insert provides enhanced view of modern changes in THg flux of Hg to Lost Lake.

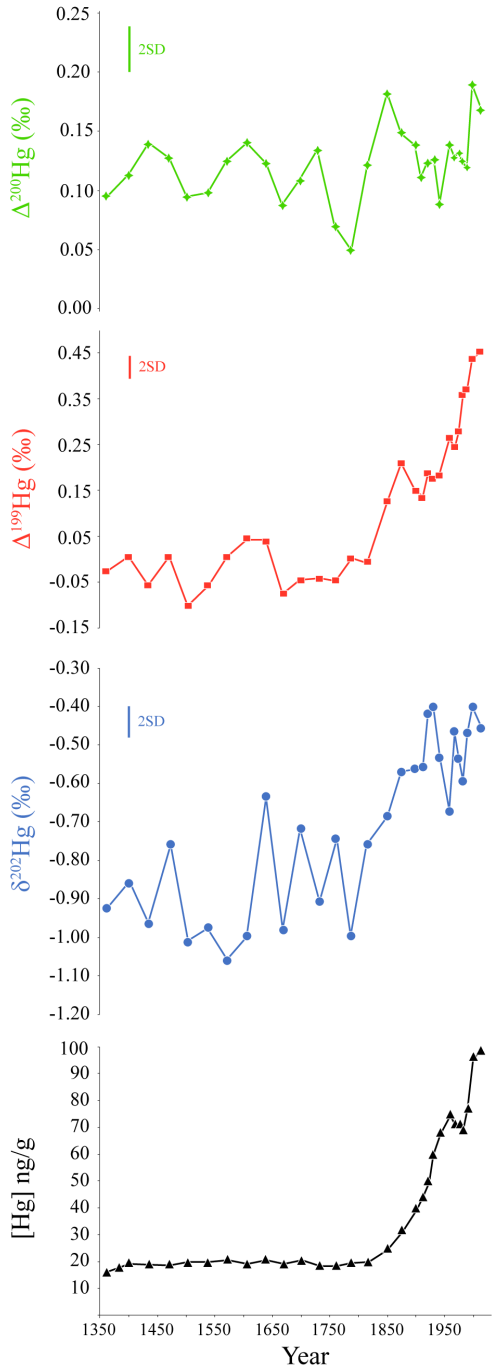

Figure 2.6 Change in Hg concentration, δ^{202}Hg, Δ^{199}Hg and Δ^{200}Hg in Lost Lake sediment core over time.

Each parameter is on its own y-axis while sharing the same x-axis.

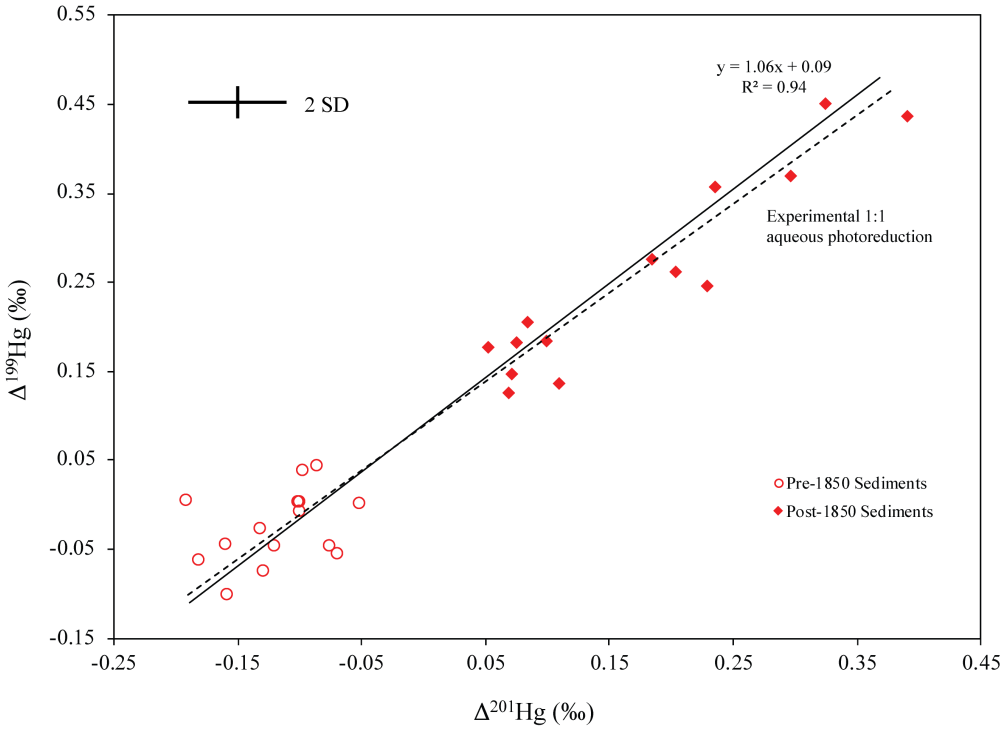

Figure 2.7 Comparison of Δ^{201}Hg to Δ^{199}Hg.

York regression yields slope of 1.06±0.05 (solid line), which is within error of approximate 1:1 ratio (dashed line) and consistent with aqueous photochemical reduction of Hg in the atmosphere (Bergquist and Blum, 2007).

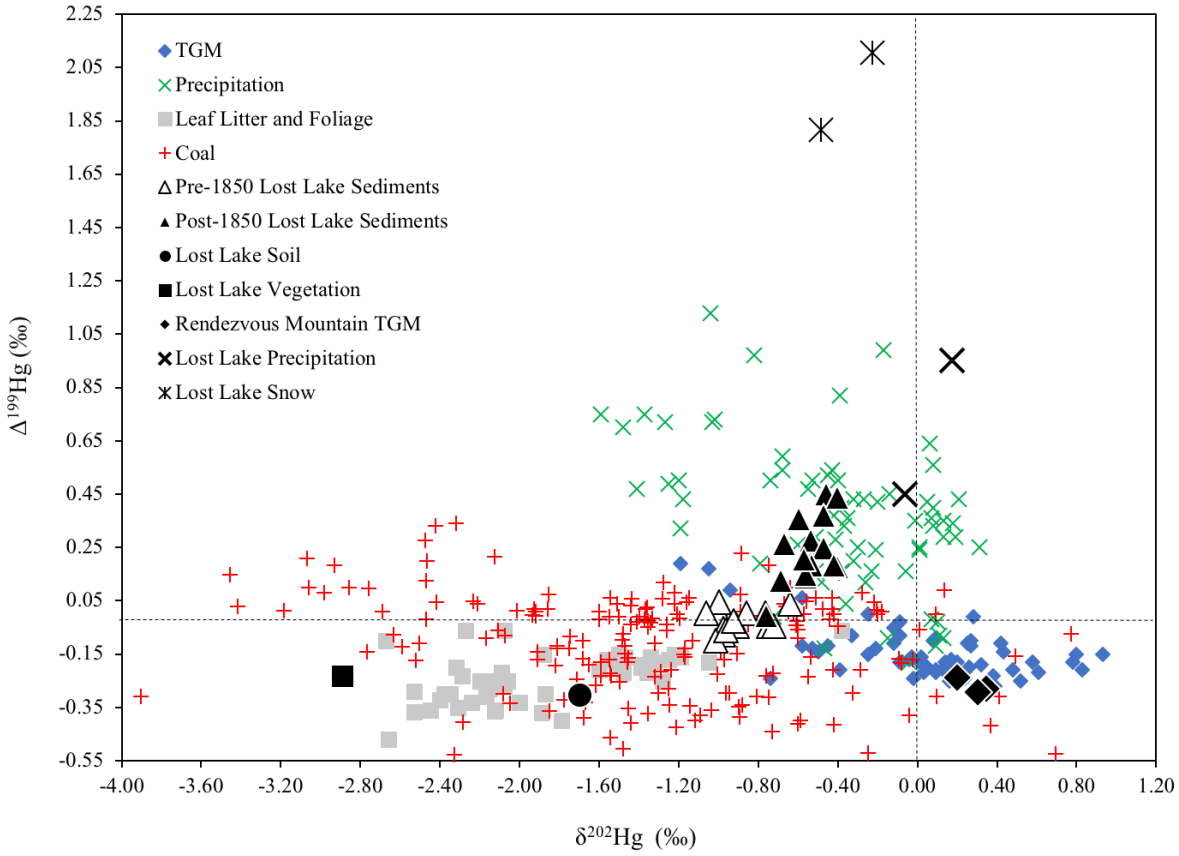

Figure 2.8 Plot of $\delta^{202}Hg$ versus $\Delta^{199}Hg$ for possible sources of Hg to Lost Lake from current literature.

Black dashed lines represent zero values for $\delta^{202}Hg$ and $\Delta^{199}Hg$. TGM (blue diamonds) [Gratz et al., 2010; Sherman et al., 2010; Demers et al., 2013; Donovan et al., 2013, Yin et al., 2013; Fu et al., 2016; Yu et al., 2016], North American Precipitation (green X's) [Gratz et al., 2010; Chen et al., 2012; Sherman et al., 2012a; 2015; Demers et al., 2013; Donovan et al., 2013], Leaf Litter and Foliage (grey squares) [Das et al; 2012; Tsui et al., 2012; Demers et al., 2013; Zheng et al., 2016], World coal deposits (Biswas et al., 2008; Lefticariu et al., 2011; Sherman et al., 2012a; Sun et al., 2013;2014) (red +), Pre-1850 Lost Lake sediments (black outlined triangles), +), Post-1850 Lost Lake sediments (black triangles), Lost Lake Soil (black circle), Lost Lake Vegetation (black square), Rendezvous Mountain TGM (black diamond), Lost Lake Precipitation (black x) and Lost Lake Snow (black x with vertical line).

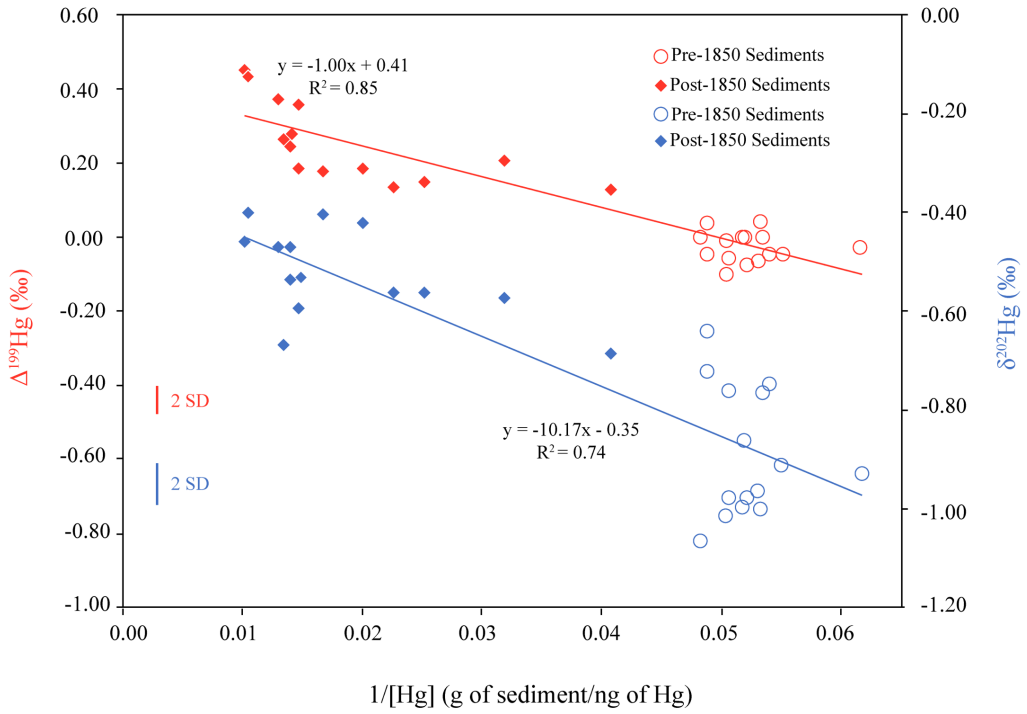

Figure 2.9 1/[Hg] vs. Δ^{199}Hg on the primary y-axis and δ^{202}Hg on the secondary y-axis.

Strong linear relationships indicate mixing of two different Hg sources, in this case pre-1850 Hg and modern precipitation and snow.

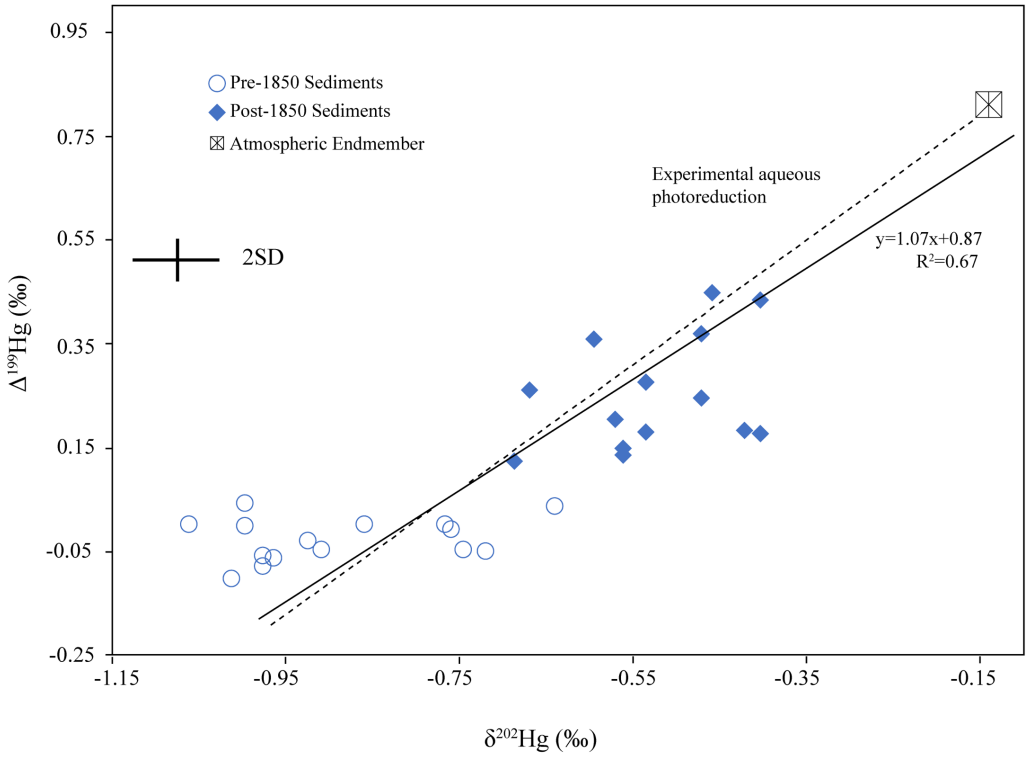

Figure 2.10 Plot of $\delta^{202}Hg$ vs. $\Delta^{199}Hg$ in Lost Lake sediments (blue circles).

York regression yields slope of 1.07±0.10 (solid line), which is similar to experimental photoreduction slope of 1.2 (dashed line). Calculated atmospheric endmember (75% precipitation, 25% snow) (square with x) displays possible endmember associated with changing photoreduction over time.

References

Amos, H.M., Sonke, J.E., Obrist, D., Robins, N., Hagan, N., Horowitz, H.M., Mason, R.P., Witt, M., Hedgecock, I.M., Corbitt, E.S., Sunderland, E.M. (2015). Observational and modeling constraints on global anthropogenic enrichment of mercury. *Environmental Science and Technology*, *49*(7), 4036–4047. https://doi.org/10.1021/es5058665

Bagnato, E., Tamburello, G., Avard, G., Martinez-Cruz, M., Enrico, M., Fu, X., Sprovieri, M., Sonke, J.E. (2015). Mercury fluxes from volcanic and geothermal sources: an update. *Geological Society, London, Special Publications*, *410*(1), 263–285. https://doi.org/10.1144/SP410.2

Baken, S.; Degryse, F.; Verheyen, L.; Merckx, R.; Smolders, E. Metal complexation properties of freshwater dissolved organic matter are explained by its aromaticity and by anthropogenic ligands. *Environ. Sci. Technol.* **2011**, *45* (7), 2584–2590 DOI: 10.1021/es103532a.

Baskaran, M. Po-210 and Pb-210 As Atmospheric Tracers and Global Atmospheric Pb-210 Fallout: A Review. *J. Environ. Radioact.* **2011**, *102* (5), 500–513 DOI: 10.1016/j.jenvrad.2010.10.007.

Baskaran, M; Naidu, A. S. (1995). Cs isotopes into continental shelf 210Pb-derived chronology and the fluxes of 210Pb and 137Cs isotopes into continental shelf sediments sediments, East Chukchi Sea, Alaskan Arctic. *Geochimica et Cosmochimica Acta*, *59*(21), 4435–4448.

Baskaran, M., Miller, C. J., Kumar, A., Andersen, E., Hui, J., Selegean, J. P., Creech, C.T., Barkach, J. (2015). Sediment accumulation rates and sediment dynamics using five different methods in a well-constrained impoundment : Case study from Union Lake , Michigan. *Journal of Great Lakes Research*, *41*(2), 607–617. http://doi.org/10.1016/j.jglr.2015.03.013

Baskaran, M. (2016). *Radon: A Tracer for Geological, Geophysical and Geochemical Studies*.

Bergquist, B.A., & Blum, J.D. (2007). Mass-dependent and -independent fractionation of Hg isotopes by photoreduction in aquatic systems. *Science*, *318*(5849), 417–420. https://doi.org/10.1126/science.1148050

Biester, H., Bindler, R., Martinez-Cortizas, A., & Engstrom, D.R. (2007). Modeling the past atmospheric deposition of mercury using natural archives. *Environmental Science and Technology*, *41*(14), 4851–4860. https://doi.org/10.1021/es0704232

Biswas, A., Blum, J.D., Bergquist, B.A., Keeler, G. J., & Xie, Z. (2008). Natural mercury isotope variation in coal deposits and organic soils. *Environmental Science and Technology*, *42*(22), 8303–8309. https://doi.org/10.1021/es801444b

Blum, J.D., & Bergquist, B.A. (2007). Reporting of variations in the natural isotopic composition of mercury. *Analytical and Bioanalytical Chemistry*, *388*(2), 353–359. https://doi.org/10.1007/s00216-007-1236-9

Blum, J. D., Sherman, L. S., & Johnson, M. W. (2014). Mercury Isotopes in Earth and Environmental Sciences. *Annual Review of Earth and Planetary Sciences*, *42*(1), 249–269. http://doi.org/10.1146/annurev-earth-050212-124107

Blum, J.D., & Johnson, M.W. (2017). Recent Developments in Mercury Stable Isotope Analysis, *Rev. Mineral. Geochem., 82*(July 2013), 733–757.

Briffa, K. R. Annual climate variability in the Holocene: Interpreting the message of ancient trees. *Quat. Sci. Rev.* **2000**, *19* (1–5), 87–105 DOI: 10.1016/S0277-3791(99)00056-6.

Chellman, N., McConnell, J.R., Arienzo, M., Pederson, G.T., Aarons, S.M., & Csank, A. (2017). Reassessment of the Upper Fremont Glacier Ice-Core Chronologies by Synchronizing of Ice-Core-Water Isotopes to a Nearby Tree-Ring Chronology. *Environmental Science and Technology*, *51*(8), 4230–4238. https://doi.org/10.1021/acs.est.6b06574

Chen, J., Hintelmann, H., Feng, X., & Dimock, B. (2012). Unusual fractionation of both odd and even mercury isotopes in precipitation from Peterborough, ON, Canada. *Geochimica et Cosmochimica Acta*, *90*, 33–46. https://doi.org/10.1016/j.gca.2012.05.005

Chen, J., Hintelmann, H., Zheng, W., Feng, X., Cai, H., Wang, Z., Yuan, S., Wang, Z. (2016). Isotopic evidence for distinct sources of mercury in lake waters and sediments. *Chemical Geology*, *426*, 33–44. https://doi.org/http://dx.doi.org/10.1016/j.chemgeo.2016.01.030

Cooke, C.A., Hintelmann, H., Ague, J.J., Burger, R., Biester, H., Sachs, J.P., & Engstrom, D.R. (2013). Use and legacy of mercury in the Andes. *Environmental Science and Technology*, *47*(9), 4181–4188. https://doi.org/10.1021/es3048027

Das, R.; Bizimis, M.; Wilson, A. M. Tracing mercury seawater vs. atmospheric inputs in a pristine SE USA salt marsh system: Mercury isotope evidence. *Chem. Geol.* **2013**, *336*, 50–61 DOI: 10.1016/j.chemgeo.2012.04.035.

Demers, J.D., Blum, J.D., & Zak, D.R. (2013). Mercury isotopes in a forested ecosystem: Implications for air-surface exchange dynamics and the global mercury cycle. *Global Biogeochemical Cycles*, *27*(1), 222–238. https://doi.org/10.1002/gbc.20021

Demers, J.D., Sherman, L.S., Blum, J.D., Marsik, F.J., & Dvonch, J.T. (2015). Coupling atmospheric mercury isotope ratios and meteorology to identify sources of mercury impacting a coastal urban-industrial region near Pensacola, Florida, USA. *Global Biogeochemical Cycles*, *29*(10), 1689–1705. https://doi.org/10.1002/2015GB005146

Donovan, P.M., Blum, J.D., Yee, D., Gehrke, G.E., & Singer, M.B. (2013). An isotopic record of mercury in San Francisco Bay sediment. *Chemical Geology*, *349–350*, 87–98. https://doi.org/10.1016/j.chemgeo.2013.04.017

Engstrom, D.R., Swain, E.B., Henning, T.A., Brigham, M.E., & Brezonik, P.L. (1994). Environmental chemistry of lakes and reservoirs. *Environmental Chemistry of Lakes and Reservoirs*, 33–66.

Engstrom, D.R., Fitzgerald, W.F., Cooke, C.A., Lamborg, C. H., Drevnick, P. E., Swain, E.B., Balogh, S.S., Balcom, P.H. (2014). Atmospheric Hg emissions from preindustrial gold and silver extraction in the Americas: A reevaluation from lake-sediment archives. *Environmental Science and Technology*, *48*(12), 6533–6543. https://doi.org/10.1021/es405558e

Enrico, M., Roux, G. Le, Marusczak, N., Heimbürger, L.E., Claustres, A., Fu, X., Sun, R., Sonke, J.E. (2016). Atmospheric Mercury Transfer to Peat Bogs Dominated by Gaseous Elemental Mercury Dry Deposition. *Environmental Science & Technology*, acs.est.5b06058. https://doi.org/10.1021/acs.est.5b06058

Enrico, M., Roux, G. Le, Heimburger, L., Van, P., Souhaut, M., Chmeleff, J., & Sonke, J.E. (2017). Holocene atmospheric mercury levels reconstructed from peat bog mercury stable isotopes. *Environmental Science & Technology, 51* (11), 5899–5906.

Fitzgerald, W.F., Engstrom, D.R., Lamborg, C.H., Tseng, C.M., Balcom, P.H., & Hammerschmidt, C.R. (2005). Modern and historic atmospheric mercury fluxes in northern Alaska: Global sources and arctic depletion. *Environmental Science and Technology*, *39*(2), 557–568. https://doi.org/10.1021/es049128x

Foucher, D., & Hintelmann, H. (2009). Tracing Mercury Contamination from the Idrija Mining Region (Slovenia) to the Gulf of Trieste Using Hg Isotope Ratio Measurements. *Environmental Science & Technology*, *43*(1), 33–39. https://doi.org/10.1021/es801772b

Fu, Xuewe; Heimburger, Lars-Eric; Sonke, J. E. (2014). Collection of atmospheric gaseous mercury for stable isotope analysis using iodine- and chlorine-impregnated activated carbon traps. *Journal of Analytical Atomic Spectrometry*, *29*, 841–852. http://doi.org/10.1039/c3ja50356a

Fu, X., Marusczak, N., Wang, X., Gheusi, F., & Sonke, J.E. (2016). Isotopic Composition of Gaseous Elemental Mercury in the Free Troposphere of the Pic du Midi Observatory, France. *Environmental Science and Technology*, *50*(11), 5641–5650. https://doi.org/10.1021/acs.est.6b00033

Gratz, L.E., Keeler, G.J., Blum, J.D., & Sherman, L.S. (2010). Isotopic composition and fractionation of mercury in Great Lakes precipitation and ambient air. *Environmental Science and Technology*, *44*(20), 7764–7770. https://doi.org/10.1021/es100383w

Gray, J.E., Pribil, M.J., Van Metre, P.C., Borrok, D.M., & Thapalia, A. (2013). Identification of contamination in a lake sediment core using Hg and Pb isotopic compositions, Lake Ballinger, Washington, USA. *Applied Geochemistry*, *29*, 1–12. https://doi.org/10.1016/j.apgeochem.2012.12.001

Guedron, S., Amouroux, D., Sabatier, P., Desplanque, C., Develle, A.L., Barre, J., Feng, C., Guiter, F., Arnaud, F., Reyss, J.L., Charlet, L. (2016). A hundred year record of industrial and urban development in French Alps combining Hg accumulation rates and isotope composition in sediment archives from Lake Luitel. *Chemical Geology*, *431*, 10–19. https://doi.org/10.1016/j.chemgeo.2016.03.016

Gustin, M.S., Amos, H.M., Huang, J., Miller, M.B., & Heidecorn, K. (2015). Measuring and modeling mercury in the atmosphere: a critical review, *Atmos. Chem. Phys.,* 5697–5713. https://doi.org/10.5194/acp-15-5697-2015

Hall, B.D., Olson, M.L., Rutter, A.P., Frontiera, R.R., Krabbenhoft, D.P., Gross, D.S., Yuen, M., Rudolph, T.M., Schauer, J. J. (2006). Atmospheric mercury speciation in Yellowstone National Park, *Sci. Total Environ., 367*, 354–366. https://doi.org/10.1016/j.scitotenv.2005.12.007

Heyvaert, A.C., Reuter, J.E., Slotton, D.G., & Goldman, C.R. (2000). Paleolimnological reconstruction of historical atmospheric lead and mercury deposition at Lake Tahoe, California - Nevada. *Environmental Science and Technology*, *34*(17), 3588–3597. https://doi.org/10.1021/es991309p

Horowitz, H.M., Jacob, D.J., Amos, H.M., Streets, D.G., & Sunderland, E.M. (2014). Historical mercury releases from commercial products: Global environmental implications. *Environmental Science and Technology*, *48*(17), 10242–10250. https://doi.org/10.1021/es501337j

Jiskra, M., Wiederhold, J. G., Skyllberg, U., Kronberg, R.-M., Hajdas, I., & Kretzschmar, R. (2015). Mercury Deposition and Re-emission Pathways in Boreal Forest Soils Investigated with Hg Isotope Signatures. *Environmental Science & Technology*, *49*(12), 7188–7196. http://doi.org/10.1021/acs.est.5b00742

Kamman, N.C., & Engstrom, D.R. (2002). Historical and present fluxes of mercury to Vermont and New Hampshire lakes inferred from ^{210}Pb dated sediment cores. *Atmospheric Environment*, *36*(10), 1599–1609. https://doi.org/10.1016/S1352-2310(02)00091-2

King, S.A., Behnke, S., Slack, K., Krabbenhoft, D.P., Nordstrom, D.K., Burr, M.D., & Striegl, R. G. (2006). Mercury in water and biomass of microbial communities in hot springs of Yellowstone National Park, USA, *Applied Geochemisry, 21*, 1868–1879. https://doi.org/10.1016/j.apgeochem.2006.08.004

Ku, P., Tsui, M. T.-K., Nie, X., Chen, H., Hoang, T. C., Blum, J. D., Dahlgren, R.A., Chow, A. T. (2018). Origin, Reactivity, and Bioavailability of Mercury in Wildfire Ash.

Environmental Science & Technology, acs.est.8b03729. http://doi.org/10.1021/acs.est.8b03729

Landis, M. S., & Keeler, G. J. (1997). Critical evaluation of a modified automatic wet-only precipitation collector for mercury and trace element determinations. *Environmental Science and Technology*, *31*(9), 2610–2615. http://doi.org/10.1021/es9700055

Lefticariu, L., Blum, J.D., & Gleason, J.D. (2011). Mercury isotopic evidence for multiple mercury sources in coal from the Illinois basin. *Environmental Science and Technology*, *45*(4), 1724–1729. https://doi.org/10.1021/es102875n

Lindberg, S. E., & Stratton, W. J. (1998). Atmospheric Mercury Speciation: Concentrations and Behavior of Reactive Gaseous Mercury in Ambient Air. *Environmental Science and Technology*, *32*(1), 49–57. http://doi.org/doi:10.1021/es970546u

Lockhart, W.L., Macdonald, R.W., Outridge, P.M., & Wilkinson, P. (2000). Tests of the fidelity of lake sediment core records of mercury deposition to known histories of mercury contamination, *Sci. Total Environ.,* 171–180.

Love, J.D., Christiansen, A.C. (1985) Geologic Map of Wyoming. *U.S. Geologic Survey*

Ma, J., Hintelmann, H., Kirk, J.L., & Muir, D.C.G. (2013). Mercury concentrations and mercury isotope composition in lake sediment cores from the vicinity of a metal smelting facility in Flin Flon, Manitoba. *Chemical Geology*. https://doi.org/10.1016/j.chemgeo.2012.10.037

Mason, R., Fitzgerald, W., & Morel, F. (1994). The biogeochemical cycling of elemental mercury: Anthropogenic influences. *Geochimica et Cosmochimica Acta*, *58*(15), 3191–3198. http://doi.org/10.1016/0016-7037(94)90046-9

National Atmospheric Deposition Program (NRSP-3). **2017**. *NADP Program Office Illinois State Water Survey, University of Illinois, Champaign, IL 61820.*

Obrist, D., Agnan, Y., Jiskra, M., Olson, C.L., & Dominique, P. (2017). Tundra uptake of atmospheric elemental mercury drives Arctic mercury pollution. *Nature Publishing Group*, *547*(7662), 201–204. https://doi.org/10.1038/nature22997

Obrist, D., Kirk, J. L., Zhang, L., Sunderland, E. M., Jiskra, M., & Selin, N. E. (2018). A review of global environmental mercury processes in response to human and natural perturbations: Changes of emissions, climate, and land use. *Ambio*, *47*(2), 116–140. http://doi.org/10.1007/s13280-017-1004-9

Pacyna, E. G.; Pacyna, J. M.; Sundseth, K.; Munthe, J.; Kindbom, K.; Wilson, S.; Steenhuisen, F.; Maxson, P. Global emission of mercury to the atmosphere from anthropogenic sources in 2005 and projections to 2020. *Atmos. Environ.* **2009**, *44* (20), 2487–2499 DOI: 10.1016/j.atmosenv.2009.06.009.

Percival, J. B., & Outridge, P. M. (2013). A test of the stability of Cd, Cu, Hg, Pb and Zn pro fi les over two decades in lake sediments near the Flin Flon Smelter, Manitoba , Canada. *Science of the Total Environment, The*, *454–455*, 307–318. https://doi.org/10.1016/j.scitotenv.2013.03.011

Pirrone, N., Cinnirella, S., Feng, X., Finkelman, R. B., Friedli, H. R., Leaner, J., Mason, R., Mukherjee, A. B. (2010). Global mercury emissions to the atmosphere from anthropogenic and natural sources. *Atmospheric Chemistry and Physics*, *10*, 5951–5964. http://doi.org/10.5194/acp-10-5951-2010

Rydberg, J., Gälman, V., Renberg, I., & Mart, A. (2008). Assessing the Stability of Mercury and Methylmercury in a Varved Lake Sediment Deposit, *Environ. Sci. Technol., 42*(12), 4391–4396.

Sanchez-Cabeza, J.A., Ruiz-Fernandez, A. C. (2012). ^{210}Pb sediment radiochronology: An integrated formulation and classification of dating models, *Geochemica et Cosmochimica Acta, 82*, 183–200. https://doi.org/10.1016/j.gca.2010.12.024

Schuster, P.F., Krabbenhoft, D.P., Naftz, D.L., Cecil, L.D., Olson, M.L., Dewild, J.F., Susong, D.D., Green, J.R., Abbott, M. L. (2002). Atmospheric mercury deposition during the last 270 years: A glacial ice core record of natural and anthropogenic sources. *Environmental Science and Technology*, *36*(11), 2303–2310. https://doi.org/10.1021/es0157503

Selin, N.E., Jacob, D.J., Yantosca, R.M., Strode, S., & Jaegle, L. (2008). Global 3-D land-ocean-atmosphere model for mercury: Present-day versus preindustrial cycles and anthropogenic enrichment factors for deposition, *Global Biogeochemical Cycles, 22*(Ii), 1–13. https://doi.org/10.1029/2007GB003040

Sherman, L.S., Blum, J.D., Nordstrom, D.K., Mccleskey, R.B., Barkay, T., & Vetriani, C. (2009). Mercury isotopic composition of hydrothermal systems in the Yellowstone Plateau volcanic field and Guaymas Basin sea-floor rift. *Earth and Planetary Science Letters*, *279*(1–2), 86–96. https://doi.org/10.1016/j.epsl.2008.12.032

Sherman, L.S., Blum, J.D., Johnson, K.P., Keeler, G.J., Barres, J.A., & Douglas, T.A. (2010). Mass-independent fractionation of mercury isotopes in Arctic snow driven by sunlight. *Nature Geoscience*, *3*(3), 173–177. https://doi.org/10.1038/ngeo758

Sherman, L.S., Blum, J.D., Keeler, G.J., Demers, J.D., & Dvonch, J.T. (2012a). Investigation of Local Mercury Deposition from a Coal-Fired Power Plant Using Mercury Isotopes, *Environmental Science & Technology,* 382–390.

Sherman, L. S., Blum, J. D., Douglas, T. A., & Steffen, A. (2012b). Frost flowers growing in the Arctic ocean-atmosphere-sea ice-snow interface: 2. Mercury exchange between the atmosphere, snow, and frost flowers. *Journal of Geophysical Research Atmospheres*, *117*(3), 1–10. http://doi.org/10.1029/2011JD016186

Sherman, L.S., Blum, J.D., Dvonch, J.T., Gratz, L.E., & Landis, M.S. (2015). The use of Pb, Sr, and Hg isotopes in Great Lakes precipitation as a tool for pollution source attribution. *Science of the Total Environment*, *502*, 362–374. https://doi.org/10.1016/j.scitotenv.2014.09.034

Smith, C.N., Kesler, S.E., & Blum, J.D. (2005). Mercury isotope fractionation in fossil hydrothermal systems, *Geology,* (10), 825–828. https://doi.org/10.1130/G21863.1

Smith, C.N., Kesler, S.E., Blum, J.D., & Rytuba, J.J. (2008). Isotope geochemistry of mercury in source rocks, mineral deposits and spring deposits of the California Coast Ranges, USA, *Earth and Planetary Science Letters, 269*, 399–407. https://doi.org/10.1016/j.epsl.2008.02.029

Smith, J. N. Why Should We Believe ^{210}Pb Sediment Geochronologies? *J. Environ. Radioact.* **2001**, *55* (2001), 121–123.

Sonke, J.E., Schäfer, J., Chmeleff, J., Audry, S., Blanc, G., & Dupré, B. (2010). Sedimentary mercury stable isotope records of atmospheric and riverine pollution from two major European heavy metal refineries. *Chemical Geology*, *279*(3–4), 90–100. https://doi.org/10.1016/j.chemgeo.2010.09.017

Stetson, S.J., Gray, J.E., Wanty, R.B., & Macalady, D.L. (2009). Isotopic variability of mercury in ore, mine-waste calcine, and leachates of mine-waste calcine from areas mined for mercury. *Environmental Science and Technology*, *43*(19), 7331–7336. https://doi.org/10.1021/es9006993

Streets, D.G., Devane, M.K., Lu, Z., Bond, T.C., Sunderland, E.M., & Jacob, D.J. (2011). All-time releases of mercury to the atmosphere from human activities. *Environmental Science and Technology*, *45*(24), 10485–10491. https://doi.org/10.1021/es202765m

Štrok, M., Baya, P. A., & Hintelmann, H. (2015). The mercury isotope composition of Arctic coastal seawater. *Comptes Rendus - Geoscience*, *347*(7–8), 368–376. http://doi.org/10.1016/j.crte.2015.04.001

Stubbins, A.; Hood, E.; Raymond, P. A.; Aiken, G. R.; Sleighter, R. L.; Hernes, P. J.; Butman, D.; Hatcher, P. G.; Striegl, R. G.; Schuster, P.; (2012) Anthropogenic aerosols as a source of ancient dissolved organic matter in glaciers. *Nat. Geosci. 5* (3), 198–201 DOI: 10.1038/ngeo1403.

Sun, G., Sommar, J., Feng, X., Lin, C.-J., Ge, M., Wang, W., Yin, R., Fu, X., Shang, L. (2016) Mass-Dependent and -Independent Fractionation of Mercury Isotope during Gas-Phase Oxidation of Elemental Mercury Vapor by Atomic Cl and Br. *Environ. Sci. Technol.* acs.est.6b01668 DOI: 10.1021/acs.est.6b01668.

Sun, R., Heimbürger, L., Sonke, J.E., Liu, G., Amouroux, D., & Berail, S. (2013). Mercury stable isotope fractionation in six utility boilers of two large coal-fired power plants. *Chemical Geology*, *336*, 103–111. https://doi.org/10.1016/j.chemgeo.2012.10.055

Sun, R., Sonke, J.E., Heimbu, L., Belkin, H. E., Liu, G., Shome, D., Cukrowska, E., Liousse, C., Pekrovsky, O.S., Streets, D. G. (2014). Mercury Stable Isotope Signatures of World Coal Deposits and Historical Coal Combustion Emissions. *Environmental Science and Technology,* 48 (13) 7660-7668

Sun, R., Streets, D.G., Horowitz, H.M., Amos, H.M., Liu, G., Perrot, V., Toutain, J.P., Hintelmann, H., Sunderland, E.M., Sonke, J.E. (2016). Historical (1850 – 2010) mercury stable isotope inventory from anthropogenic sources to the atmosphere, *Elementa,* 1–15. https://doi.org/10.12952/journal.elementa.000091

Swain, E. B., Engstrom, D.R., Brigham, M.E., Henning, T.A., & Brezonik, P.L. (1992). Increasing rates of atmospheric mercury deposition in midcontinental North America. *Science, 257*(5071), 784–787. https://doi.org/10.1126/science.257.5071.784

Tang, S.; Feng, C.; Feng, X.; Zhu, J.; Sun, R.; Fan, H.; Wang, L.; Li, R.; Mao, T.; Zhou, T. (2017) Stable isotope composition of mercury forms in flue gases from a typical coal-fired power plant, Inner Mongolia, northern China. *J. Hazard. Mater. 328*, 90–97 DOI: 10.1016/j.jhazmat.2017.01.014.

Tsui, M.T.K., Blum, J.D., Kwon, S.Y., Finlay, J.C., Balogh, S.J., & Nollet, Y.H. (2012). Sources and transfers of methylmercury in adjacent river and forest food webs. *Environmental Science and Technology*, *46*(20), 10957–10964. https://doi.org/10.1021/es3019836

UN Environ. Program. (UNEP). 2013. Global Mercury Assessment, Inter-Organ. Program Sound Manag. Chem., Geneva

U.S. Energy Information Administration. Annual Energy Review, 1949 through 2011

U.S. Environmental Protection Agency (USEPA) (2014), National Emission Inventory (NEI). [Available at https://www.epa.gov/air-emissions-inventories/2014-national-emissions-inventory-nei-data, Accessed January 2018.]

Van Metre, Peter C.; Fuller, C. C. (2009). Dual-Core Mass-Balance Approach for Evaluating Mercury and 210 Pb Atmospheric Fallout and Focusing to Lakes. *Environmental Science and Technology*, (42), 26–32.

Washburn, S. J., Blum, J. D., Demers, J. D., Kurz, A. Y., & Landis, R. C. (2017). Isotopic Characterization of Mercury Downstream of Historic Industrial Contamination in the South River, Virginia. *Environmental Science & Technology*, acs.est.7b02577. http://doi.org/10.1021/acs.est.7b02577

Washburn, S. J., Blum, J. D., Kurz, A. Y., & Pizzuto, J. E. (2018). Spatial and temporal variation in the isotopic composition of mercury in the South River, VA. *Chemical Geology*, *494*(July), 96–108. http://doi.org/10.1016/j.chemgeo.2018.07.023

Yin, R., Feng, X., Shi, W. Applied Geochemistry Application of the stable-isotope system to the study of sources and fate of Hg in the environment: A review. *Appl. Geochemistry* **2010**, *25* (10), 1467–1477 DOI: 10.1016/j.apgeochem.2010.07.007.

Yin, R., Feng, X., Meng, B. Stable mercury isotope variation in rice plants (Oryza sativa L.) from the Wanshan mercury Mining District, SW China. *Environ. Sci. Technol.* **2013**, *47* (5), 2238–2245 DOI: 10.1021/es304302a.

Yin, R., Feng, X., Hurley, J.P., Krabbenhoft, D.P., Lepak, R.F., Kang, S., Yang, H., Li, X. (2016). Historical Records of Mercury Stable Isotopes in Sediments of Tibetan Lakes. *Scientific Reports*, *6*, 23332. https://doi.org/10.1038/srep23332

York, D. (1968). Least squares fitting of a straight line with correlated errors. *Earth and Planetary Science Letters*, *5*, 320–324.

Yu, B., Fu, X., Yin, R., Zhang, H., Wang, X., Lin, C.-J., Wu, C., Zhang, Y., He, N., Fu, P., Wang, Z., Shang, L., Sommar, J., Sonke, J.E., Maurice, L., Guinot, B., Feng, X. (2016). Isotopic composition of atmospheric mercury in China: New evidence for source and transformation processes in air and in vegetation. *Environmental Science & Technology*. https://doi.org/10.1021/acs.est.6b01782

Yuan, S., Chen, J., Cai, H., Yuan, W., Wang, Z., Huang, Q., Liu, Y., Wu, X. (2018). Science of the Total Environment Sequential samples reveal significant variation of mercury isotope ratios during single rainfall events. *Science of the Total Environment*, *624*, 133–144. https://doi.org/10.1016/j.scitotenv.2017.12.082

Zambardi, T., Sonke, J.E., Toutain, J.P., Sortino, F., & Shinohara, H. (2009). Mercury emissions and stable isotopic compositions at Vulcano Island (Italy). *Earth and Planetary Science Letters*, *277*(1–2), 236–243. https://doi.org/10.1016/j.epsl.2008.10.023

Zdanowicz, C.M., Krummel, E.M., Poulain, A.J., Yumvihoze, E., Chen, J., Strok, M., Scheer, M., Hintelmann, H. (2016). Historical variations of mercury stable isotope ratios in Arctic glacier firn and ice cores. *Global Biogeochemical Cycles*. 30(9) 1324-1347. https://doi.org/10.1002/2016GB005411.Received

Zhang, Y., Jacob, D.J., Horowitz, H. M., Chen, L., Amos, H.M., Krabbenhoft, D.P., Slemr, F., St. Louis, F.L., Sunderland, E. M. (2015). Observed decrease in atmospheric mercury explained by global decline in anthropogenic emissions, *Proc. Natl. Acad. Sci., 113*(x), 1–6. https://doi.org/10.1073/pnas.1516312113

Zheng, W., Hintelmann, H. Isotope Fractionation of Mercury during Its Photochemical Reduction by Low-Molecular-Weight Organic Compounds. *J. Phys. Chem. A* **2010**, *114* (12), 4246–4253.

Zheng, W., Obrist, D., Weis, D., & Bergquist, B.A. (2016). Mercury isotope compositions across North American forests. *Global Biogeochemical Cycles*, 1475–1492. https://doi.org/10.1002/2015GB005323.Received

Chapter 3 Contrasting Controls on the Diel Isotopic Variation of Hg^0 at Two High Elevation Sites in the Western United States

Authors: Aaron Y. Kurz[1*], Joel D. Blum[1], Lynne E. Gratz[2], and Daniel A. Jaffe[3]

Citation: Kurz, A.Y., Blum, J.D., Gratz, L.E., Jaffe, D.A., 2020. Contrasting Controls on the Diel Isotopic Variation of Hg0 at Two High Elevation Sites in the Western United States. Environ. Sci. Technol. 54, 10502–10513. https://doi.org/10.1021/acs.est.0c01918

Abstract: The atmosphere is a significant global reservoir for mercury (Hg) and its isotopic characterization is important to understand sources, distribution, and deposition of Hg to the Earth's surface. To better understand Hg isotope variability in the remote background atmosphere, we collected continuous 12-hr Hg^0 samples for one week from two high elevation sites, Camp Davis, Wyoming (valley) and Mount Bachelor, Oregon (mountaintop). Samples collected at Camp Davis displayed strong diel variation in $\delta^{202}Hg$ values of Hg^0, but not in $\Delta^{199}Hg$ or $\Delta^{200}Hg$ values. We attribute this pattern to nightly atmospheric inversions trapping Hg in the valley and the subsequent nighttime uptake of Hg by vegetation which depletes Hg from the atmosphere. At Mount Bachelor, samples displayed diel variation in both $\delta^{202}Hg$ and $\Delta^{199}Hg$, but not $\Delta^{200}Hg$. We attribute this pattern to differences in the vertical distribution of Hg in the atmosphere as Mount Bachelor received free tropospheric air masses on certain nights during the sampling period. Near the end of the sampling period at Mount Bachelor, the observed diel pattern dissipated due to the influence of a nearby forest fire. The processes governing the Hg isotopic fractionation differ across sites depending on mixing, topography, and vegetation cover.

3.1. Introduction

Mercury (Hg) is a trace metal found ubiquitously at Earth's surface and in its atmosphere and is of concern to human health. Human activities such as combustion of fossil fuels and mining of mercury and gold have increased atmospheric Hg concentrations globally and altered the natural chemistry and cycling of Hg in the environment (Kurz et al., 2019; Mason et al., 1994; Obrist et al., 2018). Active redox chemistry controls transitions between the different chemical species of Hg, which determines the cycling behavior and fate of Hg in the atmosphere.

Atmospheric Hg has three operationally-defined species: gaseous elemental mercury (GEM; Hg^0), gaseous oxidized mercury (GOM; $Hg^{II}_{(g)}$) and particulate bound mercury (PBM; $Hg^{II}_{(p)}$). Together, GEM and GOM are defined as total gaseous mercury (TGM). Hg^0 is thought to be the dominant form of Hg in the atmosphere comprising >95% of the global pool (Lindberg and Stratton, 1998). Hg^0 is relatively non-reactive, and has an atmospheric residence time of ~1 year (Slemr et al., 2015; William H and Munthe, 1998). Hg^0 can undergo oxidation reactions and become $Hg^{II}_{(g)}$ which is thought to have an atmospheric residence time on the order of days to weeks (Ariya et al., 2008; Subir et al., 2012). $Hg^{II}_{(g)}$ can also adsorb to particles and is then defined as $Hg^{II}_{(p)}$ which also has an atmospheric residence time of days to weeks (Subir et al., 2012).

The isotopic composition of atmospheric Hg pools has not been well-studied due to the low concentrations of Hg species and the difficulties of sample collection. The large volumes of air needed to obtain enough Hg for isotopic analysis leads to most individual samples being integrated over time periods of 24 hours to two weeks of continuous collection (Demers et al., 2015; Fu et al., 2016a). The lack of sampling and isotopic analysis of atmospheric Hg leaves a large knowledge gap in the specific reactions that govern Hg cycling in the atmosphere (Kwon

and Selin, 2016). Recent advancements in multiple collector inductively coupled plasma mass spectrometry (MC-ICP-MS) allow for high precision measurements of mercury's seven stable isotopes (Blum and Bergquist, 2007). Both experimental studies and environmental measurements have shed light on mercury cycling and the reactions and pathways that control Hg isotopic fractionation (Obrist et al., 2018).

The measurement of Hg stable isotope ratios is a powerful tool due to the fact that mercury displays both mass dependent fractionation (MDF) as well as mass independent fractionation (MIF).(Yin et al., 2010) MDF is controlled by both biotic and abiotic reactions including methylation, demethylation, photoreduction and equilibrium reactions (Kritee et al., 2009, 2008; Wiederhold et al., 2010). MIF is mainly controlled by reactions involving photochemistry (Chandan et al., 2015; Rose et al., 2015). The identification of these two types of fractionation aids in tracing Hg through the environment and enhancing understanding of changes in Hg speciation (Demers et al., 2013, 2015; Gratz et al., 2010; S. Yuan et al., 2018).

Most atmospheric Hg isotopic measurements have been made at ground level and at low elevation but those studies made aloft have revealed that there is an altitudinal gradient of mercury concentration in the atmosphere and that there is also a shift from Hg^0 to $Hg^{II}_{(g)}$ dominance with increasing altitude (Slemr et al., 2016; Talbot et al., 2007). This has led to speculation that the Hg species composition of the stratosphere could be different than that of the troposphere and that there may be a difference between the planetary boundary layer (PBL) and the free troposphere (FT). Along with a difference in Hg species throughout the atmospheric vertical column, there is also thought to be a difference in the isotopic composition of Hg (Chen et al., 2012). The Hg isotopic composition measured in airmasses is affected by the origin and trajectory. Measurements of Hg stable isotopes in atmospheric species allows for differentiation

between point source, regional or background sources of Hg (Demers et al., 2015; Fu et al., 2016a; Gratz et al., 2010). Additionally, recent studies have used the fractionation imparted on airmasses by the uptake of Hg from the atmosphere by vegetation to understand the Hg isotopic composition of sampled TGM (Demers et al., 2015, 2013; Enrico et al., 2016). Most recently Huang et al. (2019) collected 12-hr PBM samples in Beijing, China. These authors found that day samples with increased exposure to sunlight had higher odd-MIF, which they attributed to *in situ* photoreduction (Huang et al., 2019). Huang et al. (2019) represents the first measurements of day vs. night samples for Hg isotopes in atmospheric samples. Jiskra et al. (2019) used integrated 12-hour samples of TGM at Toolik Lake Field Station in Alaska to assess differences between day and night samples. These authors found a difference in MDF between day and night samples and attributed this difference to the uptake and reemission of Hg from vegetation (Jiskra et al., 2019). This body of work provides an important start to understanding the different local and regional processes, reactions, and conditions that influence the isotopic composition of atmospheric Hg species.

To assess diel variations in Hg^0 isotopic composition and further characterize the global atmospheric Hg pool, we collected continuous 12-hour Hg^0 samples over a seven-day period in the summer of 2019 at the University of Michigan Camp Davis Geological Field Station (Camp Davis), a forested high elevation site in the Hoback Mountains in Western Wyoming (Figure 3.1). Here, we expected the uptake of Hg by vegetation to dominate the diel variation in Hg^0. We additionally conducted a similar sampling campaign at Mount Bachelor Observatory near Bend, Oregon during the summer of 2017 (Figure 3.1). This high elevation site is far from any point source of Hg and often receives free tropospheric air masses on a nightly basis (Swartzendruber et al., 2006). We hypothesized that there would be isotopic variation in both MDF and MIF

between day and night samples due to differences in the vertical distribution of Hg in the atmosphere. We expected differences in vegetation cover, meteorology, mixing, and redox chemistry to drive different diel patterns between the two high elevation study sites. This provides an opportunity to better understand the processes controlling Hg isotopic composition at high elevation sites and further characterize the isotopic composition of mercury's vertical distribution in the atmosphere.

3.2. Methods

3.2.1 Study Sites

Camp Davis (CD), is located in a valley in the Hoback Mountain Range in Western Wyoming at an elevation of 1872m above sea level (43°16′55.11″ N, 110°39′26.68″ W). CD is situated at the base of Mt. Ann, whose peak is ~2270m above sea level, on Quaternary aged alluvium. The Hoback River flows through the valley ~1 km north of the sampling site. The sampling location is at the edge of a forest with lodgepole pine (*pinus contorta*) and Douglas fir (*pseudotsuga menziesii;* the dominant species). During the sampling period, temperatures ranged from 3°C to 28°C and sky conditions remained mostly clear with some intermittent clouds. Here we collected 12-hr Hg^0 samples continually for one week (total of 13 samples) from June 26th to July 3rd 2019.

The second, high elevation sample site, the Mount Bachelor Observatory (MBO) is located on the leeward side of a dormant volcano (2734m above sea level) located in the Cascade Range approximately 30 km southwest of Bend, Oregon (43°58'39.19" N, 121°41'9.66" W). The site location is approximately 500m above the tree line and 200 km east of the Pacific Ocean coastline and frequently receives FT air masses during the night (Swartzendruber et al., 2006; Weiss-Penzias et al., 2006). During the sampling period, temperatures ranged from

approximately 8°C to 14°C. Sky conditions remained clear throughout the sampling period. The surrounding valleys began to fill with smoke from the nearby Milli forest fire beginning on August 19th through the end of the sampling period. Here we collected 12-hr Hg^0 samples continually for one week (total of 13 samples) from August 15th to August 22nd 2017. MBO has been in operation since 2004, measuring atmospheric constituents such as CO, aerosol scattering, and Hg species as well as other basic meteorological parameters (Jaffe et al., 2005; Weiss-Penzias et al., 2006). Through these measurements, MBO has been well characterized meteorologically and characteristic concentrations of atmospheric constituents have been measured during events such as forest fires, airmasses dominated by long range pollution transport from Asia, and free tropospheric air masses (Ambrose et al., 2011; Finley et al., 2009; Jaffe et al., 2005; Swartzendruber et al., 2006). We can compare this long-term characterization with measurements taken during our sampling campaign to assess impacts of the nearby forest fires and to estimate when FT air masses may have dominated our samples.

3.2.2 Hg^0 Sample Collection and Preparation

Our method of Hg^0 sample collection has been previously described in Demers et al. (2013) and Kurz et al. (2019). Briefly, atmospheric air was drawn through a manifold with 8 gold bead traps in parallel at a rate of 1.8 liters per minute per gold trap (14.4 liters per minute total). Upstream of each gold trap, a filter housing was outfitted with a pre-fired quartz filter to prevent particulates from accumulating on the gold bead traps. Gold bead traps were wrapped with heat tape and kept at a constant temperature of 50°C to prevent water condensation during sample collection. A dry test meter (Schlumberger, Gallus 2000) connected in the sampling train was used to measure the volume of air drawn through the manifold. Air volumes were corrected

to standard temperature and pressure using the method outlined by the Environmental Protection Agency Compendium Method IO-2.4.

We acknowledge that there may be some influence of $Hg^{II}_{(g)}$ in the samples collected in this study; however, the difference in the isotopic composition between Hg^0 and Hg^{II} (GOM + PBM) has been shown to be significant in previous studies (Fu et al., 2016a, 2018; Huang et al., 2019). The upstream quartz filter in our sampling stream prevents $Hg^{II}_{(p)}$ from accumulating on the gold bead traps, though the extent to which $Hg^{II}_{(g)}$ is excluded from our samples is unclear. Thus, based on the Hg isotopic composition of the measured samples in this study as compared to previously collected samples that have been demonstrated to be dominantly Hg^0, (Fu et al., 2016a, 2018) we believe that our samples are dominated by Hg^0.

After sample collection and in the laboratory at the University of Michigan, each of the 8 gold bead traps in a sample were individually heated to 500°C over a four-minute period to desorb the Hg and re-trap it on a single analytical gold trap (diatomaceous earth coated with gold). The analytical gold trap was then heated in a step-wise manner from 25°C to 550°C over a 3.5-hour period. The released Hg was carried in a stream of argon and bubbled through a 24 g liquid trap containing a solution of 1% $KMnO_4$ dissolved in 10% H_2SO_4 (hereafter referred to as 1% $KMnO_4$). Samples were then partially reduced with 2% (w/w) of a 30% $NH_2OH{\cdot}HCl$ solution and an aliquot was measured for total mercury (THg) via cold vapor atomic fluorescence spectroscopy (CV-AFS).

A second sample purification step was performed with all samples which included sample reduction with 20% (w/w) $SnCl_2$ and subsequent purge and trap into a fresh 5.5g liquid trap of 1% $KMnO_4$. This step was performed to remove residual contaminants that may have been transferred from the heated gold bead traps and that might potentially produce matrix

effects during analysis. For determination of final sample THg, samples were partially reduced with 2% (w/w) of a 30% $NH_2OH{\cdot}HCl$ solution and an aliquot was measured for THg via CV-AFS. Overall sample recoveries during processing ranged from 91.0 to 103.0% with an average recovery of 96.1±4.1% (1 SD, n=26). Process standards consisting of UM-Almadèn were loaded onto gold bead traps by reducing prepared standards with 20% $SnCl_2$ which was subsequently pumped through one gold bead trap at a time at a flow rate of 0.5 L/min, while simultaneously monitoring breakthrough via atomic absorption spectroscopy. These process standards, consisting of 8 gold bead traps loaded with UM-Almadèn in the manner described above, were used to evaluate gold bead trapping efficiency and to monitor quantitative recovery of Hg during processing. UM-Almadèn process standards were processed in tandem with samples and had recoveries ranging from 92.9 to 98.9% with an average of 96.3±2.3% (1 SD, n=6).

3.2.3 Mercury Isotope Analyses

Hg isotope analyses were conducted at the University of Michigan using a cold vapor multiple collector inductively coupled plasma mass spectrometer (CV-MC-ICP-MS) (Nu Plasma). Prior to analyses, samples were partially reduced with 2% (w/w) of a 30% $NH_2OH{\cdot}HCl$ solution. Samples were prepared to match the concentration of the NIST 3133 standard (within 5% relative concentration) for standard sample bracketing. Samples were introduced into the instrument using continuous flow cold vapor generation and the Hg in solution was reduced to Hg^0 with the introduction of a 2% $SnCl_2$ solution. The Hg^0 was introduced into the CV-MC-ICP-MS in a stream of Ar along with a dry aerosol Tl standard (NIST 987) produced by a desolvating nebulizer and used for mass bias correction.

We report Hg isotopic compositions using delta notation, in units of permil (‰), as follows:

$$\delta^{xxx}Hg(‰) = \{[(^{xxx}Hg/^{198}Hg)_{unknown}/(^{xxx}Hg/^{198}Hg)_{NIST\ 3133}]-1\} \times 1000$$

where xxx represents the Hg isotope of 199, 200, 201, or 204 amu (Blum and Bergquist, 2007).

MIF is the deviation from the calculated MDF based on the kinetic isotope effect and is reported using capital delta notation. Blum and Bergquist (2007) calculated beta constants that can be used to calculate MIF of less than ±10‰:

$$\Delta^{xxx}Hg = \delta^{xxx}Hg - (\delta^{202}Hg \times \beta)$$

xxx represents the Hg isotope mass (199, 200, 201, 204) and the β represents the calculated constant (0.252, 0.502. 0.752, 1.492 respectively) (Blum and Bergquist, 2007).

UM-Almadèn was run as a secondary standard with each set of samples to asses analytical uncertainty. Results for UM-Almadèn measurements are presented in Table 3.1 and are similar to long term measurements in both the University of Michigan lab and others (Blum and Johnson, 2017). Hg^0 samples were run at concentrations between 1.56 and 4.28 ng/g. Secondary reference materials were prepared in the same manner as samples and run at the same concentration as unknown samples. Process Hg^0 blanks yielded between 62.2 and 198 pg of Hg with an average of 113.9±46.3 pg (1 SD, n=6) while field Hg^0 blanks yielded between 115.5 and 453.5 pg of Hg with an average of 217.3±135.9 pg (1 SD, n=5). Field blanks are more representative of the blank associated with collecting Hg^0 samples and represent <5% of Hg in the lowest concentration sample collected.

Analytical errors associated with sample analyses for isotopes are calculated as 2 standard deviations (SD) of the secondary UM-Almadèn standard measurements or 2 standard errors (SE) of process standard measurements depending on whichever is larger. The MBO sample set was analyzed in August of 2018 and the CD sample set was analyzed in October of 2019. In October of 2018, we experienced a two-fold increase in sensitivity in our CV-MC-ICP-

MS due to the introduction of a modified phase separator design. We therefore calculate our analytical errors separately for each sample set (Table 3.1). For Hg^0 samples collected at MBO, we use the 2SE associated with our process UM-Almadèn measurements from 2018 to assign analytical uncertainty to these samples for all isotope ratios except for $\Delta^{199}Hg$ as follows: ±0.10‰ for $\delta^{202}Hg$, ±0.10‰ for $\Delta^{204}Hg$, ±0.05‰ for $\Delta^{201}Hg$, and ±0.05‰ for $\Delta^{200}Hg$. For $\Delta^{199}Hg$ we use the 2SD associated with UM-Almadèn measurements from 2018 which is ±0.05‰. For Hg^0 samples collected at CD, we use the 2SD associated with our UM-Almadèn measurements from 2019 to assign analytical uncertainty to these samples for all isotope ratios except for $\Delta^{200}Hg$ as follows: ±0.06‰ for $\delta^{202}Hg$, ±0.03‰ for $\Delta^{204}Hg$, ±0.03‰ for $\Delta^{201}Hg$, and ±0.08‰ for $\Delta^{199}Hg$. For $\Delta^{200}Hg$ we use the 2SE associated with process UM-Almadèn measurements from 2019 which is ±0.06‰.

3.2.4 Ancillary Atmospheric Chemistry Measurements at MBO

During the sampling period at MBO, CO and CO_2 were measured using a Picarro G2502 Cavity Ring-Down Spectrometer. Relative humidity (RH) was measured with a Campbell Scientific HMP 45C RH probe. Aerosol scattering (σ_{sp}) was measured at 3 different wavelengths (450, 550, and 700nm) with an integrating nephelometer (TSI, Inc. Model 3563). Finally, particle mass was measured using a Grimm Technologies Model EDM 180 Optical Particle Counter (OPC). These measurements are described in previous publications (Ambrose et al., 2011; Fischer et al., 2011; Swartzendruber et al., 2008; Zhang and Jaffe, 2017).

3.2.5 Atmospheric Transport

HYbrid Single-Particle Lagrangian Integrated Trajectory (HYSPLIT) models were run to assess air mass origin for samples collected at both CD and MBO. The National Oceanic and Atmospheric Administration (NOAA) HYSPLIT model was run using the archived High-

Resolution Rapid Refresh (HRRR) data with a grid resolution of 3 km x 3 km. Back trajectories with 24-hr durations were calculated every 12 hours at the mid-time of each sample with starting heights of 500, 1000, and 1500 m above ground level. The 24-hr duration of back trajectories was chosen to provide a representative regional transport of Hg prior to each sample. Additionally, stability plots using the HRRR data set were generated to assess atmospheric stability and boundary layer heights during the sampling periods (Rolph et al., 2017; Stein et al., 2015).

3.2.6 Statistical Tests

All statistical tests employed in this study are independent two sample t-tests with equal variance at the 95% confidence interval and were calculated using RStudio (Version 1.2.5001, © 2009-2019 RStudio, Inc.). All t-test results are presented in Table 3.2. All regressions were done using the York regression (York, 1968) and were also calculated using RStudio.

3.3. Results and Discussion

3.3.1 Camp Davis THg Concentrations and Isotopic Compositions of Hg^0

CD Hg^0 sample THg concentrations range from 0.81 to 1.22 ng/m^3 over the entire sampling period. Samples collected during the day were characterized by higher average THg (1.06±0.14 ng/m^3, 1SD, n=6) compared to those collected at night (0.94±0.11 ng/m^3, 1SD, n=7) (Figure 3.2A), though these averages are not statistically different. The maximum THg concentration was recorded on July 1st (1.22 ng/m^3) and the lowest THg concentration was recorded on the night of June 29th (0.81 ng/m^3). The relative difference between the maximum and minimum measured THg concentrations was 34%. Modeled air mass back trajectories for day and night samples indicated a regionally consistent origin before reaching CD (Figure 3.3).

This suggests a constant, dominant source of Hg^0 to the sampling site that is representative of regional Hg sources.

While the reported THg of Hg^0 samples are lower than Northern Hemisphere background Hg^0, (Sprovieri et al., 2018; Temme et al., 2007; Weigelt et al., 2015) they are similar to THg concentrations measured in forested areas where similar diel patterns in Hg^0 concentrations have been observed (Fu et al., 2016b; Kellerhals et al., 2003; Poissant et al., 2008). These diel patterns have been attributed to differences in source, meteorology, uptake by vegetation, photo reduction/oxidation rate, and dry deposition (Fu et al., 2016b; Kellerhals et al., 2003; Poissant et al., 2008). The discussion below provides information concerning the use of Hg stable isotopes in elucidating the dominant processes causing diel variations in Hg^0.

In the CD sample set we recorded higher values of $\delta^{202}Hg$ during the night (average $\delta^{202}Hg$=0.94±0.13‰, 1SD, n=7) with a maximum value of 1.10±0.06‰ and lower values during the day (average $\delta^{202}Hg$=0.56±0.05‰, 1SD, n=6) with a minimum value of 0.51±0.06‰ (Figure 3.4). Day and night samples at CD are statistically different (Table 3.2).

Measurement of odd-MIF has proven to be a powerful tool in elucidating chemical transformations of Hg in the environment. Due to the fact that MIF of the odd mass Hg isotopes is mainly caused by photochemical reactions, measurements of $\Delta^{199}Hg$ and $\Delta^{201}Hg$ can help identify fractionation processes and trace Hg sources. Daytime Hg^0 measurements of $\Delta^{199}Hg$ and $\Delta^{201}Hg$ yielded average values of -0.31±0.07‰ and -0.27±0.07‰ respectively (1SD, n=6) (Figure 3.4). Nighttime samples yielded average values of -0.23±0.08‰ and -0.26±0.11‰ respectively (1SD, n=7). The averages between day and night samples are not statistically different for $\Delta^{199}Hg$ or $\Delta^{201}Hg$ (Table 3.2). While there is no consistent pattern in MIF values between day and night samples, there is a range of 0.28‰ between the highest and lowest

recorded Δ^{199}Hg values during the sampling period. Additionally, there are days where daytime Δ^{199}Hg values are significantly lower than those of the previous or following night (June 27th, and 28th, and July 2nd) (Figure 3.4). The absence of a strong diel pattern in the odd-MIF of Hg^0 suggests that while there may be some influence from photochemical processes, other processes may also influence Hg concentration and isotopic variation.

3.3.2 Processes Driving Diel Variation in Hg^0 Isotopic Composition at Camp Davis

We identify four possible processes that control the diel variation of the Hg isotopic composition of Hg^0 measured at CD: 1) uptake of Hg^0 by vegetation 2) deposition of Hg^0 to soil, 3) photoreduction of Hg^{II} and subsequent reemission of Hg^0 from vegetation and/or soil, and 4) downward mixing of overlying air (Fu et al., 2016b; Jiskra et al., 2019, 2018; Poissant et al., 2008).

Uptake of Hg^0 by Vegetation. Using a mixing model described below (Eq 1), we calculate the δ^{202}Hg value of the Hg that is lost from the atmosphere at night to be approximately -2.51‰:

$$\delta^{202}Hg_{day} = \delta^{202}Hg_{night} \times f_{night} + \delta^{202}Hg_{lost} \times f_{lost} \quad (1)$$

$$1 = f_{night} + f_{lost}$$

$$f_{lost} = 1 - [THg]_{night} / [THg]_{day}$$

where $\delta^{202}Hg_{day}$ is the average daytime δ^{202}Hg of Hg^0 measured at Camp Davis, $\delta^{202}Hg_{night}$ is the average nighttime δ^{202}Hg of Hg^0 measured at Camp Davis, $\delta^{202}Hg_{lost}$ is the calculated δ^{202}Hg that is lost from the system, f_{lost} is the fraction of total Hg lost from the system, $[THg]_{night}$ is the measured concentration of nighttime Hg^0 measured at Camp Davis, and $[THg]_{night}$ is the measured concentration of nighttime Hg^0 measured at Camp Davis. This value is similar to the

δ^{202}Hg measurements of vegetation previously made in the region (-2.89‰) (Kurz et al., 2019). Multiple environmental studies have documented a shift in atmospheric δ^{202}Hg values associated with vegetation uptake of Hg^0, where the MDF between Hg^0 and vegetation ranges from approximately -2.89‰ to -2.40‰ (Demers et al., 2013; Enrico et al., 2016; W. Yuan et al., 2018). This fractionation process has been shown to have both regional and global implications for the isotopic composition of Hg^0 in the atmosphere (Demers et al., 2013; Fu et al., 2019; Jiskra et al., 2018).

CD is located in a valley in the Hoback Range and exhibits local scale meteorology characteristic of mountain valleys. Stability plots generated using NOAAS's HRRR model indicate that during each night of the sampling campaign, atmospheric inversions occurred, creating a moderately stable to extremely stable (Pasquill atmospheric stability class) boundary layer in the valley with a depth of approximately 50 to 100m (Figure 3.5A). These conditions are consistent with the documented trapping of chemical constituents, such as ozone and carbonyl sulfide, within the boundary layer and their depletion by chemical reactions or by vegetation uptake (Talbot et al., 2005; Wehr et al., 2017). Hg^0 is an additional atmospheric constituent that is similarly trapped within the boundary layer resulting in diel variations in THg and Hg isotopic composition (Fu et al., 2016b; Jiskra et al., 2019; Kellerhals et al., 2003; Poissant et al., 2008; W. Yuan et al., 2018). During the day, solar radiation warms the ground, creating slightly to moderately unstable atmospheric conditions with a boundary layer depth of approximately 3000m (Figure 3.5B). This allows overlying air to mix downwards and to resupply Hg^0 to the valley. As a result of this behavior, the daytime samples display lower δ^{202}Hg and higher THg than those measured at night.

Hg^0 atmospheric THg concentrations in forests have been shown to be anticorrelated with light intensity, displaying minimum THg concentrations just before sunrise and maximum THg concentrations in the afternoon (Fu et al., 2016b; Jiskra et al., 2019, 2018; Kellerhals et al., 2003; Mao et al., 2008; Poissant et al., 2008). This is proposed to be a balance between vegetation uptake and reemission and is documented by Hg flux measurements in forested areas (Fu et al., 2016b; Kellerhals et al., 2003; Poissant et al., 2008). We suggest that the lower Hg^0 THg concentrations and more positive δ^{202}Hg observed in the nighttime samples are characteristic of vegetation uptake of Hg^0, where the light isotopes are preferentially taken up by vegetation, leaving the residual Hg^0 in the atmosphere with heavier δ^{202}Hg values (Jiskra et al., 2019).

Deposition of Hg^0 to Soil. Demers et al. (2013) found that as atmospheric air flowed through or interacted with surface soils, light isotopes were preferentially adsorbed or oxidized and removed from the atmosphere, leaving the residual Hg^0 pool with lower THg and higher δ^{202}Hg values. This process is thought to be similar to that of uptake of Hg^0 by vegetation and drives the MDF of Hg^0 in the atmosphere in the same direction. This process could contribute to the diel variation in THg and δ^{202}Hg, enhancing the effects of vegetation uptake on the residual atmospheric Hg^0 pool.

Photochemical Reduction of Hg^{II}. Experimental work on Hg isotopes has revealed diagnostic odd-MIF ratios that can be useful in identifying dominant redox reactions. Bergquist and Blum (2007) found that when Hg^{II} is photoreduced in the presence of DOM in an aqueous solution, the reactant is imparted with a $\Delta^{199}Hg/\Delta^{201}Hg$ ratio of 1.00±0.02 (Bergquist and Blum, 2007). Similarly, Sun et al. (2016) performed gas-phase experiments where they oxidized gaseous Hg with Cl and Br radicals. These reactions produced $\Delta^{199}Hg/\Delta^{201}Hg$ ratios of 1.64±0.30 and 1.89±0.18 with the two different oxidants respectively (G. Sun et al., 2016). When either all

of the CD data or only the nighttime samples are regressed using a York regression, (York, 1968) we calculate slopes of 0.31±0.23 and 0.19±0.28 which are both significantly lower than either oxidation or reduction experiments and do not indicate statistical significance (r^2=0.34, p>0.3 and r^2=0.22, p>0.2 respectively). However, when only the daytime data are regressed, we obtain a $\Delta^{199}Hg/\Delta^{201}Hg$ slope of 0.82±0.34 (r^2=0.90, p<0.1), which overlaps with the experimental slope for Hg^{II} photoreduction. The difference in slope between the regressions of all CD samples, only nighttime samples and only daytime samples indicates a relative increase in the influence of photochemical reduction on the odd-MIF signatures during the day (Figure 3.6). This suggests that during the day, photoreduction of Hg^{II} plays a more important role in controlling Hg speciation than at night and could account for the differences in $\Delta^{199}Hg$ between the day and night samples of June 27th, and 28th, and July 2nd. The variation in the difference in $\Delta^{199}Hg$ values may be due to the magnitude of photoreduction and subsequent reemission of Hg^0, though cannot be fully explained through variations in photoreduction.

Three-Endmember Mixing Model. Previous studies have utilized three-endmember mixing models to identify Hg source contributions in measured samples (Donovan et al., 2014; Washburn et al., 2018). Here we present a three-endmember mixing model that can account for the isotopic variation in samples collected at CD. In Figure 3.7, we present a plot of $\delta^{202}Hg$ vs. $\Delta^{199}Hg$ on the panel (A) and 1/THg vs. $\Delta^{199}Hg$ on panel (B). We identify the three isotopic endmembers as follows:

Hg Reemitted from Vegetation. Daytime samples fall along a mixing line between an endmember with high THg, low $\delta^{202}Hg$, and intermediate $\Delta^{199}Hg$ and an endmember with intermediate THg, intermediate $\delta^{202}Hg$ and low $\Delta^{199}Hg$. We identify the high THg endmember as Hg^0 that has been reemitted from vegetation through photoreduction of Hg^{II}. Yuan et al (2018)

demonstrated that the isotopic composition of Hg^0 reemitted from vegetation is more negative in $\delta^{202}Hg$ and more positive in $\Delta^{199}Hg$ than ambient air with an offset of approximately -2.21‰ and +0.45‰ for $\delta^{202}Hg$ and $\Delta^{199}Hg$, respectively (W. Yuan et al., 2018). This is consistent with photoreduction of Hg^{II} bound to reduced sulfur ligands (Zheng and Hintelmann, 2010). Our samples do not display the same magnitude of difference between ambient air and reemitted Hg^0, but this is expected because the experimental setup of Yuan et al (2018) was designed to isolate the reemitted Hg^0 from other processes (W. Yuan et al., 2018).

Unknown Low $\Delta^{199}Hg$ endmember. Previous studies have proposed that MIF occurring in the upper atmosphere (upper troposphere/lower stratosphere) can impart more negative MIF signatures on Hg^0 due to the increased exposure to UV radiation (Chen et al., 2012). At sunrise as thermal convection begins in the valley at CD, there may be some downward mixing of overlying air into the valley with more negative $\Delta^{199}Hg$ values. However, mixing between the free troposphere and the planetary boundary layer would be expected to be minimal at CD. Additionally, the more negative $\Delta^{199}Hg$ values could be due to photoreduction of Hg bound to O/N functional groups, driving odd-MIF to more negative values compared with photoreduction from reduced sulfur ligands (Zheng and Hintelmann, 2010). The relatively small number of samples collected makes it difficult to confidently identify this endmember.

Hg Modified by Uptake of Hg^0 by Vegetation. During the nighttime, samples are influenced by an endmember with low THg, high $\delta^{202}Hg$ and high $\Delta^{199}Hg$. We identify this endmember as Hg^0 that has been modified by uptake into vegetation. As discussed earlier, uptake of Hg^0 by vegetation dominates during the nighttime hours in forested areas and preferentially takes up the light isotopes from the atmosphere. While the mechanism is unclear, Yuan et al (2018) found that Hg^0 modified by the uptake of vegetation displays more positive $\delta^{202}Hg$ and

more positive Δ^{199}Hg as compared to ambient air, which is consistent with the pattern we see for nighttime samples. Additionally, Fu et al (2019) attributed the shift in δ^{202}Hg and Δ^{199}Hg toward more positive values in Hg^0 collected during summer months to increased vegetation activity as compared to winter months. We propose that while the Hg^0 samples collected during the summer months are day and night integrations, they are somewhat analogous to our nighttime samples where increased uptake of Hg^0 by vegetation drives the isotopic composition towards more positive δ^{202}Hg and Δ^{199}Hg values.

While these three Hg endmembers can be generally identified by their distinct isotopic composition and THg, we highlight the need for additional sampling and experimental work to identify the fractionation mechanism that alters the isotopic composition of Hg^0 through the process of uptake by vegetation. Field measurements could consist of 12-hr simultaneous Hg isotopic measurements at ground level, directly below the canopy and above the canopy. Additionally, simultaneous quantification and isotopic characterization of vegetation and soil fluxes could provide more insight into the relative contribution of each of the above processes.

3.3.3 Even-MIF at Camp Davis

Another useful tracer for identifying atmospheric Hg sources and/or transport distances is even-MIF. The fractionation process imparting even-MIF signatures on Hg is not well understood but it has been suggested to be related to photo-initiated oxidation occurring in the upper troposphere or lower stratosphere (Chen et al., 2012). Multiple studies of atmospheric Hg samples reveal that samples with Hg dominantly in the oxidized form (Hg^{II}) display positive Δ^{200}Hg (average=0.16±0.13‰, 1SD, n=188) (Chen et al., 2012; Demers et al., 2013; Donovan et al., 2013; Gratz et al., 2010; Huang et al., 2018; Kritee et al., 2017; Sherman et al., 2012, 2015; Wang et al., 2015; S. Yuan et al., 2018) while samples with Hg dominantly in the reduced form

(Hg^0) display near zero or slightly negative $\Delta^{200}Hg$ (average=-0.06±0.05‰, 1SD, n=154) (Demers et al., 2015, 2013; Fu et al., 2018, 2016a; Gratz et al., 2010; Rolison et al., 2013; Sherman et al., 2010; Yamakawa et al., 2017; Yu et al., 2016). Hg^0 measured at CD reveals an average $\Delta^{200}Hg$ value of -0.09±0.03‰ (1SD, n=6) for daytime samples and -0.07±0.03‰ (1SD, n=7) for nighttime samples (Figure 3.8). CD samples reveal no statistical variation between day and night samples throughout the entire sampling period for $\Delta^{200}Hg$ (Table 3.2). Our measured $\Delta^{200}Hg$ values are consistent with all previously reported Hg^0 measurements (Table 3.2) (Demers et al., 2015, 2013; Fu et al., 2018, 2016a; Gratz et al., 2010; Rolison et al., 2013; Sherman et al., 2010; Yamakawa et al., 2017; Yu et al., 2016).

3.3.4 Mount Bachelor THg Concentrations and Atmospheric Characterization

Hg^0 THg concentrations measured at MBO display slightly higher values (though not significantly different) during the day (average=1.56±0.19 ng/m^3, 1SD, n=6) than at night (average=1.47±0.27 ng/m^3, 1SD, n=7) (Figure 3.2B). Near the end of the sampling period during the night of August 20th, the pattern reversed and THg concentrations were higher during the night than during the day. Starting on August 13th, 2017, a forest fire, named the Milli Fire, ignited approximately 31 km NW of MBO and grew in size through the sampling period. The origin of air masses between day and night samples and throughout the entire sampling period suggest a dominant regional origin of airmasses to the MBO sampling site (Figure 3.9). The back trajectories also indicate that the modeled air masses passed over the site of the Milli fire and, therefore, this added source of Hg may have become dominant near the end of the sampling period as discussed below. When we compare daytime THg concentrations, prior to the time when fire impacted the samples, to nighttime THg concentrations during the same time period, we find a statistically significant difference (Table 3.2).

Identification of FT air masses. Previous studies have used approaches of both direct measurements and modeling to understand the vertical profile of Hg species in the atmosphere. It has been proposed that while overall THg decreases with increasing altitude, there is also a decrease in Hg^0 THg concentrations with increasing altitude due to an increase in Hg oxidation and sorption of $Hg^{II}_{(g)}$ to atmospheric particles, which is known to increase with decreasing temperature (Lyman and Jaffe, 2012; Murphy et al., 2006; Rutter and Schauer, 2007). Since MBO receives FT air masses at night, we hypothesize that the lower Hg^0 concentration measurements observed in the nighttime MBO samples are due to air masses from higher in the atmosphere exhibiting a shift in Hg speciation from Hg^0 to Hg^{II} (Gratz et al., 2015; Swartzendruber et al., 2006). This hypothesis is further supported by measurements of CO and the aerosol scattering coefficient (Figure 3.10). Based on previous long-term measurements, it is well known that FT air masses at MBO are characterized by CO concentrations below 150ppbv with concurrent aerosol scattering values <20 Mm^{-1} between 2000 and 0800 hours local time (Ambrose et al., 2011; Reidmiller et al., 2010; Weiss-Penzias et al., 2007, 2006). Using these thresholds to identify periods when FT air masses dominate, we identify the nights of August 15th through 18th as periods of influence from FT air masses. During each of these nights, there also appears to be some influence from the forest fires between 2000 hours and 0200-0400 hours, keeping CO concentrations slightly elevated above 150ppbv before decreasing below this threshold in the early morning hours. These nightly samples also display 4 of the 6 lowest Hg^0 THg concentrations measured during the sampling campaign (1.16 to 1.47 ng/m^3).

Identification of Forest Fire influence at MBO. Beginning during the day on August 19th, daytime CO concentrations consistently exceeded 400 ppbv with concurrent aerosol scattering values of >200 Mm^{-1}. Unlike earlier in the sampling period, CO concentrations and

aerosol scattering values did not return to background values during the nighttime but rather stayed elevated above 140 ppbv and 50 Mm^{-1} respectively. We suggest that these elevated values are consistent with direct impact from the nearby forest fire. Due to the proximity of the Milli fire to MBO, it is likely that the smoke was transported to the sampling site within the PBL. From August 19th through the end of the sampling period, CO concentrations and aerosol scattering values did not reflect FT air masses during the nighttime but rather the transport of smoke plumes from the nearby forest fires which came to dominate the Hg transported to MBO. Additionally, we use the relationship of THg concentration to CO concentration to characterize the change in Hg sources. As CO was measured continuously and Hg isotope samples are integrated over 12 hours, we calculated 12-hour average CO concentrations for comparison over the same time period as Hg samples were collected. We find that the [THg]/[CO] ratio significantly decreased from before the forest fire dominated the samples to when the samples were influenced by the fire (Table 3.2). This change in Hg source was more significant when comparing nighttime samples prior to fire influence to nighttime samples dominated by Hg from the forest fire (Table 3.2). Further discussion on this hypothesis that incorporates observed variations in the Hg isotopic composition of samples is provided below.

3.3.5 Isotopic Characterization of Hg^0 at Mount Bachelor

We observed diel variation in δ^{202}Hg values at MBO, however, the offset from each day to night throughout the sampling campaign was inconsistent and disappeared later in the sampling campaign due to the wildfire impact. Average δ^{202}Hg values throughout the entire sampling period during the day were 0.34±0.19‰ (1SD, n=6) while nighttime average δ^{202}Hg values were 0.58±0.16‰ (1SD, n=7) (Figure 3.11). When comparing δ^{202}Hg values between day and night samples we find that they are statistically different (Table 3.2). Throughout the entire

sampling period, δ^{202}Hg values decrease from 0.60±0.10‰ on the first night of sampling, August 15th, to 0.36±0.10‰ on the final night of sampling, August 21st.

Similar to δ^{202}Hg, we observed diel variation in odd-MIF with more negative values at night (average Δ^{199}Hg=-0.35±0.09‰, average Δ^{201}Hg=-0.30±0.12‰, 1SD, n=7) than during the day (average Δ^{199}Hg=-0.22±0.03‰, average Δ^{201}Hg=-0.17±0.07‰, 1SD, n=6) (Figure 3.11). Daytime and nighttime samples are statistically different from each other for both Δ^{199}Hg and Δ^{201}Hg (Table 3.2). Similar to the variation in δ^{202}Hg observed at MBO, the variation in odd-MIF between day and night samples at MBO disappeared starting on August 19th through the end of the sampling period.

Photochemical reduction of Hg^{II}. The ratios of Δ^{199}Hg to Δ^{201}Hg were determined for all MBO samples, only nighttime samples, and only daytime samples. A York regression was used with calculated slopes of 0.24±0.12 ($p<0.01$), 0.08±0.21 ($p<0.01$) and 0.03±0.36 ($p>0.6$), respectively. While the relationships between Δ^{199}Hg and Δ^{201}Hg are significant for all MBO samples and nighttime samples, the calculated slopes are much lower than those for any known reaction including photochemical reduction of Hg^{II}. The calculated slopes probably result from a mixture of different reactions and source mixing, though based on the calculated slopes, we can rule out *in situ* photochemical reduction of Hg^{II} as the dominant reaction driving the observed variation in odd-MIF at MBO.

Three-Endmember Mixing Model. At MBO, the full range in the isotopic composition of Hg^0 samples collected can be accounted for through a three-endmember mixing model (Figure 3.12). Ancillary atmospheric measurements (CO and particle scattering) allowed us to identify the influence of distinct air masses and we now extrapolate that to the isotopic composition of Hg^0.

Free Tropospheric endmember. On the nights of August 15th-August 18th, we identified influence from the free troposphere. The composition of Hg^0 in the free troposphere has intermediate THg (1.32±0.13 ng/m^3, 1SD, n=3), high $\delta^{202}Hg$ (0.68±0.07‰, 1SD, n=3) and low $\Delta^{199}Hg$ (-0.41±0.05‰, 1SD, n=3). As previously discussed, Hg in the upper atmosphere may experience increased exposure to UV radiation, causing more MIF (Chen et al., 2012). The direction of odd-MIF is determined by the binding ligands (Zheng and Hintelmann, 2010). More negative $\Delta^{199}Hg$ values in Hg^0 as observed during FT influence at MBO are indicative of photoreduction of Hg^{II} from O/N functional groups. Additionally, we report what we believe to be the most negative $\Delta^{199}Hg$ and $\Delta^{201}Hg$ values ever measured in Hg^0 (with values of -0.46±0.05‰ and -0.50±0.05‰ respectively) on the night of August 18th when MBO was receiving air masses from the FT.

Regional Background endmember. Prior to influence from the nearby forest fire, samples collected during the day have intermediate THg (1.15±0.04 ng/m^3, 1SD, n=3), intermediate $\delta^{202}Hg$ (0.48±0.10‰, 1SD, n=3) and high $\Delta^{199}Hg$ (-0.22±0.05‰, 1SD, n=3). This endmember is most likely representative of regional Hg sources transported to MBO in the PBL that may be influenced by fractionation processes during transport, obscuring the initial isotopic composition of the source. Tang et al (2017) demonstrated that the $\delta^{202}Hg$ of Hg^0 emitted from coal fired power plants can be enriched in $\delta^{202}Hg$ by up to ~2.5‰ as compared to the isotopic composition of feed coal with no associated MIF. While dependent on the initial isotopic composition, Hg^0 emissions from coal fired power plants was estimated to have a $\delta^{202}Hg$ value of 0.54±0.25‰, (1SD, n=5), which is consistent with the $\delta^{202}Hg$ value of the identified regional background endmember (Tang et al., 2017). Coal from the US has an average $\Delta^{199}Hg$ of -0.10±0.13‰ (1SD, n=27), (R. Sun et al., 2016) which overlaps with the identified endmember. However, additional

studies have identified smaller differences between $\delta^{202}Hg$ of feed coal and emitted Hg^0 (Sun et al., 2014). Additionally, atmospheric fractionation processes such as the uptake of Hg^0 by vegetation could fractionate the isotopes, obscuring the initial isotopic composition of released Hg^0 during transport to MBO.

Fire endmember. As discussed above, from August 19th through the end of the sampling period the isotopic composition of Hg^0 at MBO was influenced by the nearby Milli forest fire. We identify the forest fire endmember based on daytime measurements of Hg^0 impacted by the Milli fire as high THg (1.59±0.21 ng/m^3, 1SD, n=3), low $\delta^{202}Hg$ (0.20±0.16‰, 1SD, n=3), and high $\Delta^{199}Hg$ (-0.23±0.02‰, 1SD, n=3). The isotopic composition of Hg in vegetation and litter has characteristically low $\delta^{202}Hg$ and negative $\Delta^{199}Hg$ (avg. $\delta^{202}Hg$ = -2.56±0.64‰ and avg. $\Delta^{199}Hg$ -0.31±0.13‰, 1 SD, n=156) (Demers et al., 2013; Enrico et al., 2016; Jiskra et al., 2015; Wang et al., 2017; Yu et al., 2016; Zhang et al., 2013; Zheng et al., 2016) and it is assumed that when vegetation is combusted, the light isotopes are preferentially released and MIF is conserved. The combustion of vegetation/litter does not have the associated MDF identified for coal combustion as the fractionation occurs due to the use of emissions control devices (Tang et al., 2017). Ku et al (2018) suggest that burning conditions - including O_2 availability, temperature and burning duration - can affect Hg^0 volatilization in forest fires. This could account for some of the variability in $\delta^{202}Hg$ of Hg^0 observed at MBO in samples impacted by the Milli fire as conditions changed through the sampling period. This variability could also be attributed to mixing with the other identified endmembers.

3.3.6 Even-MIF at Mount Bachelor

Samples collected at MBO during the daytime had an average $\Delta^{200}Hg$ value of -0.09±0.02‰ (1SD, n=6) and those collected during the nighttime had an average $\Delta^{200}Hg$ value of

-0.11±0.05‰ (1SD, n=7) (Figure 3.13). There was no statistically significant variation in Δ^{200}Hg values between day and night samples (Table 3.2). To further assess differences between Δ^{200}Hg values in the FT and the PBL, we compare Δ^{200}Hg values in nighttime samples prior to the forest fire's influence to Δ^{200}Hg values in daytime samples prior to the forest fire's influence (Table 3.2). Based on these relationships, we conclude there is no statistical difference in even-MIF between FT air masses and PBL air masses measured at MBO. Furthermore, when we compare the average Δ^{200}Hg values from MBO to all published Hg^0/TGM data from other locations worldwide, we find a statistical difference (Table 3.2), however, none of our individual measured values are outside the range of previously measured values (Demers et al., 2015, 2013; Fu et al., 2018, 2016a; Gratz et al., 2010; Rolison et al., 2013; Sherman et al., 2010; Yamakawa et al., 2017; Yu et al., 2016). The difference between our measured Δ^{200}Hg values and those from previous studies may indicate that the high elevation of our study site captures lower Δ^{200}Hg values on average compared with samples collected at lower elevations.

Chen et al. (2012) documented extremely high positive Δ^{200}Hg values in precipitation (where Hg is expected to be dominated by Hg^{II}) reaching a maximum of 1.24‰. These authors attributed these high positive even-MIF values to photo-initiated oxidation in the tropopause. If high magnitude positive even-MIF is produced in Hg^{II} in the tropopause, we would expect there to be a residual pool of Hg^0 with more negative even-MIF. Since we found no statistical variation in Δ^{200}Hg values in Hg^0 between FT and PBL air masses, we suggest that large-magnitude (negative Δ^{200}Hg for Hg^0 and positive Δ^{200}Hg for Hg^{II}) even-MIF may not be imparted on samples through reactions in the tropopause or it is also possible that events that mix Hg with large-magnitude even-MIF are stochastic and therefore these values are only rarely captured in measured samples.

Acknowledgements

The authors thank Marcus Johnson for his guidance and help in operating the CV-MC-ICP-MS. The authors gratefully acknowledge the NOAA Air Resources Laboratory (ARL) for the provision of the HYSPLIT transport and dispersion model and READY website (https://www.ready.noaa.gov) used in this publication.

Table 3.1 Summary of Hg isotopic compositions for standard and reference materials.

For UM Almadèn, n1 denotes the number of isotope measurements and n2 denotes the number of analytical sessions. For reference materials, n1 denotes the number of process replicates and n2 represents the number of isotope measurements.

	n1	n2	$\delta^{204}Hg$	2SD	$\delta^{202}Hg$	2SD	$\delta^{201}Hg$	2SD	$\delta^{200}Hg$	2SD	$\delta^{199}Hg$	2SD	$\Delta^{204}Hg$	2SD	$\Delta^{201}Hg$	2SD	$\Delta^{200}Hg$	2SD	$\Delta^{199}Hg$	2SD
2018 Results																				
UM-Almadèn (this study)	8	1	-0.82	0.03	-0.52	0.06	-0.44	0.01	-0.26	0.04	-0.16	0.03	-0.04	0.07	-0.04	0.04	0.00	0.01	-0.03	0.05
UM-Almadèn Hg^0 Proc. Ref.	9	3	-0.65	0.21	-0.44	0.10	-0.37	0.05	-0.22	0.03	-0.13	0.01	0.01	0.10	-0.04	0.05	0.01	0.05	-0.02	0.03
2019 Results																				
UM-Almadèn (this study)	12	1	-0.84	0.07	-0.56	0.06	-0.46	0.02	-0.26	0.08	-0.14	0.03	0.00	0.03	-0.04	0.03	0.02	0.04	0.01	0.08
UM-Almadèn Hg^0 Proc. Ref.	3	3	-0.66	0.04	-0.46	0.02	-0.36	0.02	-0.22	0.05	-0.13	0.07	0.02	0.02	-0.02	0.01	0.01	0.06	-0.02	0.08

Table 3.2 Compilation of all t-test results for statistical tests calculated in this study.

Avg. 1 and avg. 2 are the averages for each of the two compared datasets, respectively. n1 and n2 are the number of data points in each of the two compared datasets, respectively.

Data Type	Comparison	p-value	t-statistic	Avg. 1	n1	Avg. 2	n2
$\delta^{202}Hg$	Night vs. day @ CD	<0.001	-0.686	0.94‰	7	0.56‰	6
$\Delta^{199}Hg$	Night vs. day @ CD	0.79	-0.27	-0.23‰	7	-0.31‰	6
$\Delta^{201}Hg$	Night vs. day @ CD	0.086	-1.88	-0.26‰	7	-0.27‰	6
$\Delta^{200}Hg$	Night vs. day @ CD	0.12	-1.66	-0.07‰	7	-0.09‰	6
$\Delta^{200}Hg$	CD vs. all published TGM	0.13	1.53	-0.08‰	13	-0.06‰	154
[THg]	Night (pre-fire) vs. Day (pre-fire) @ MBO	0.04	-2.70	1.33 ng/m^3	4	1.54 ng/m^3	4
[THg]/[CO]	Pre vs. post fire @ MBO	0.009	3.30	0.012	5	0.004	6
[THg]/[CO]	Night (pre-fire) vs. Day (post-fire) @ MBO	0.001	8.01	0.013	3	0.004	3
$\delta^{202}Hg$	Night vs. day @ MBO	0.031	-2.47	0.58‰	7	0.34‰	6
$\delta^{202}Hg$	Pre vs. post-fire @ MBO	0.013	2.97	0.6‰	7	0.33‰	6
$\Delta^{199}Hg$	Night vs. day @ MBO	0.012	2.97	-0.35‰	7	-0.22‰	6
$\Delta^{201}Hg$	Night vs. day @ MBO	0.037	2.36	-0.3‰	7	-0.17‰	6

Δ^{200}Hg	Night vs. day @ MBO	0.23	1.28	-0.11‰	7	-0.09‰	6
Δ^{200}Hg	Night (pre-fire) vs. day (pre-fire) @ MBO	0.44	-0.84	-0.11‰	4	-0.08‰	4
Δ^{200}Hg	MBO vs. all published TGM	0.001	3.23	-0.10‰	13	-0.06‰	154

Table 3.3 Sample THg and Hg stable isotope data for all TGM samples analyzed in this study.

Hg isotope values are expressed in per mille (‰).

Sample	Site	Collection Date	Night/Day	THg (ng/m^3)	$\delta^{204}Hg$	$\delta^{202}Hg$	$\delta^{201}Hg$	$\delta^{200}Hg$	$\delta^{199}Hg$	$\Delta^{204}Hg$	$\Delta^{201}Hg$	$\Delta^{200}Hg$	$\Delta^{199}Hg$
CD _06_26_19_PM	CD	6/26/19	Night	0.98	1.57	0.88	0.48	0.37	0.01	0.26	-0.19	-0.07	-0.21
CD _06_27_19_AM	CD	6/26/19	Day	1.00	1.00	0.59	0.19	0.19	-0.15	0.13	-0.25	-0.10	-0.30
CD _06_27_19_PM	CD	6/27/19	Night	0.85	1.73	0.98	0.56	0.41	0.08	0.27	-0.18	-0.08	-0.17
CD _06_28_19_AM	CD	6/27/19	Day	0.89	1.07	0.58	0.08	0.19	-0.23	0.20	-0.36	-0.11	-0.38
CD _02_28_19_PM	CD	6/28/19	Night	0.87	1.57	0.94	0.39	0.39	-0.01	0.17	-0.32	-0.09	-0.25
CD _06_29_19_AM	CD	6/28/19	Day	0.92	1.14	0.64	0.10	0.19	-0.24	0.19	-0.38	-0.13	-0.40
CD _06_29_19_PM	CD	6/29/19	Night	0.81	1.94	1.10	0.35	0.47	-0.12	0.31	-0.48	-0.08	-0.39
CD _06_30_19_AM	CD	6/29/19	Day	1.17	0.88	0.51	0.15	0.16	-0.17	0.11	-0.24	-0.09	-0.30
CD _06_30_19_PM	CD	6/30/19	Night	1.14	1.10	0.70	0.27	0.28	-0.07	0.05	-0.26	-0.08	-0.25
CD _07_01_19_AM	CD	6/30/19	Day	1.22	0.92	0.53	0.20	0.21	-0.08	0.13	-0.20	-0.05	-0.21
CD _07_01_19_PM	CD	7/1/19	Night	1.00	1.61	1.03	0.61	0.47	0.04	0.07	-0.17	-0.05	-0.22
CD _07_02_19_AM	CD	7/1/19	Day	1.16	0.94	0.51	0.17	0.18	-0.15	0.18	-0.21	-0.07	-0.28
CD _07_02_19_PM	CD	7/2/19	Night	0.96	1.68	0.98	0.52	0.48	0.12	0.23	-0.21	-0.01	-0.12
MBO_08_15_17_PM	MBO	8/15/17	Night	1.47	1.19	0.60	0.21	0.25	-0.23	0.29	-0.24	-0.05	-0.38
MBO_08_16_17_AM	MBO	8/16/17	Day	1.59	1.00	0.57	0.17	0.18	-0.08	0.14	-0.26	-0.11	-0.22

MBO_08_16_17_PM	MBO	8/16/17	Night	1.35	1.20	0.70	0.15	0.28	-0.18	0.16	-0.38	-0.07	-0.35
MBO_08_17_17_AM	MBO	8/17/17	Day	1.53	1.05	0.51	0.22	0.19	-0.13	0.29	-0.16	-0.07	-0.26
MBO_08_17_17_PM	MBO	8/17/17	Night	1.16	1.34	0.77	0.07	0.24	-0.25	0.20	-0.50	-0.14	-0.45
MBO_08_18_17_AM	MBO	8/18/17	Day	1.50	0.70	0.38	0.20	0.10	-0.07	0.14	-0.08	-0.08	-0.16
MBO_08_18_17_PM	MBO	8/18/17	Night	1.33	1.22	0.66	0.16	0.17	-0.29	0.23	-0.34	-0.17	-0.46
MBO_08_19_17_AM	MBO	8/19/17	Day	1.67	0.17	0.03	-0.07	-0.05	-0.21	0.12	-0.10	-0.07	-0.22
MBO_08_19_17_PM	MBO	8/19/17	Night	1.38	1.08	0.63	0.15	0.20	-0.10	0.14	-0.32	-0.12	-0.26
MBO_08_20_17_AM	MBO	8/20/17	Day	1.83	0.61	0.34	0.04	0.06	-0.15	0.11	-0.21	-0.11	-0.23
MBO_08_20_17_PM	MBO	8/20/17	Night	1.84	0.78	0.38	0.08	0.11	-0.20	0.22	-0.21	-0.08	-0.30
MBO_08_21_17_AM	MBO	8/21/17	Day	1.26	0.61	0.24	-0.01	0.04	-0.19	0.25	-0.19	-0.08	-0.25
MBO_08_21_17_PM	MBO	8/21/17	Night	1.73	0.77	0.36	0.15	0.02	-0.12	0.23	-0.12	-0.16	-0.21

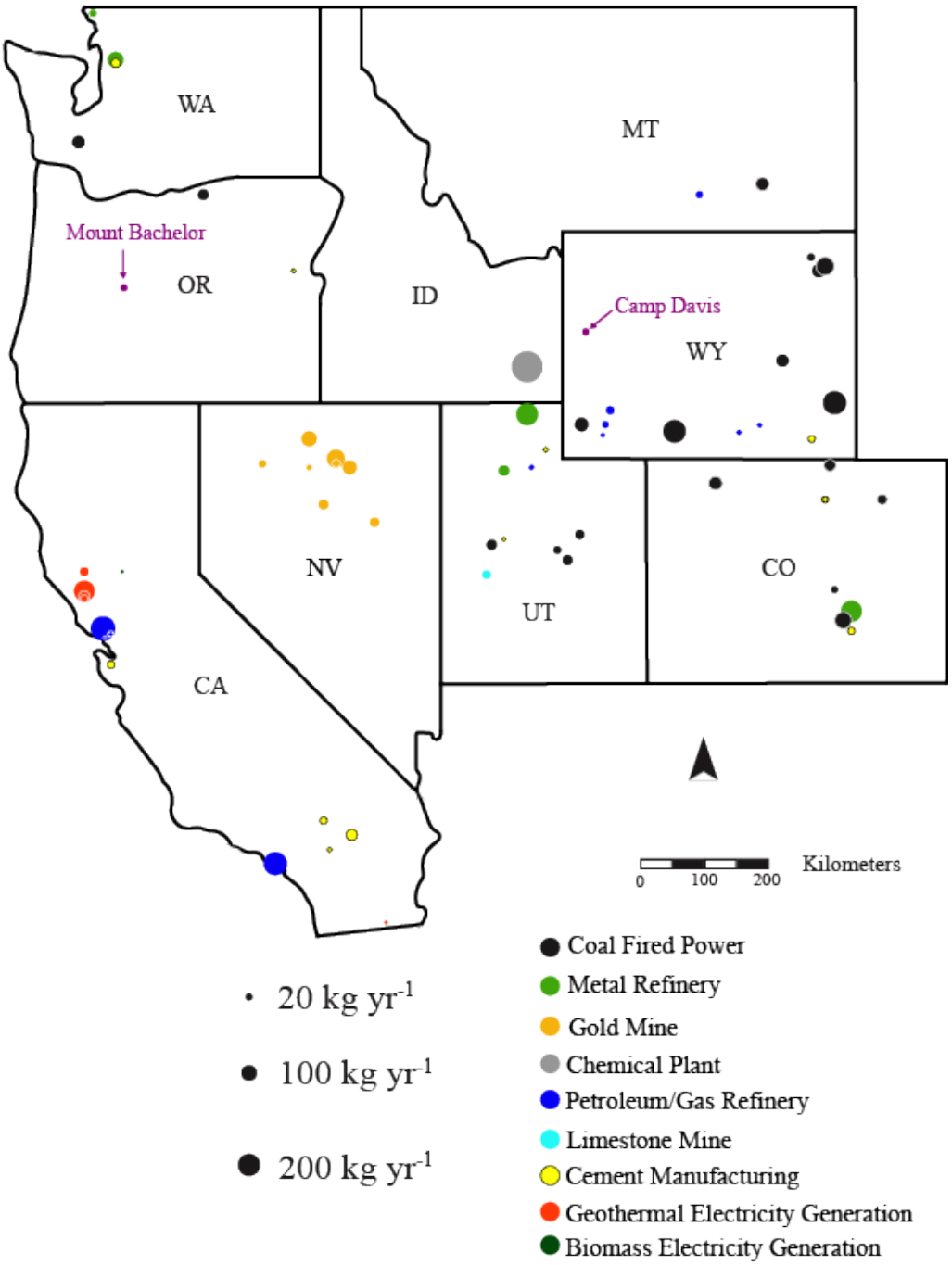

Figure 3.1 Location of Camp Davis in Wyoming and Mount Bachelor in Oregon, USA with respect to local and regional sources of industrial mercury.

Symbol size is scaled based on reported annual emission of Hg (USEPA, 2017). Figure adapted from Kurz et al. (2019).

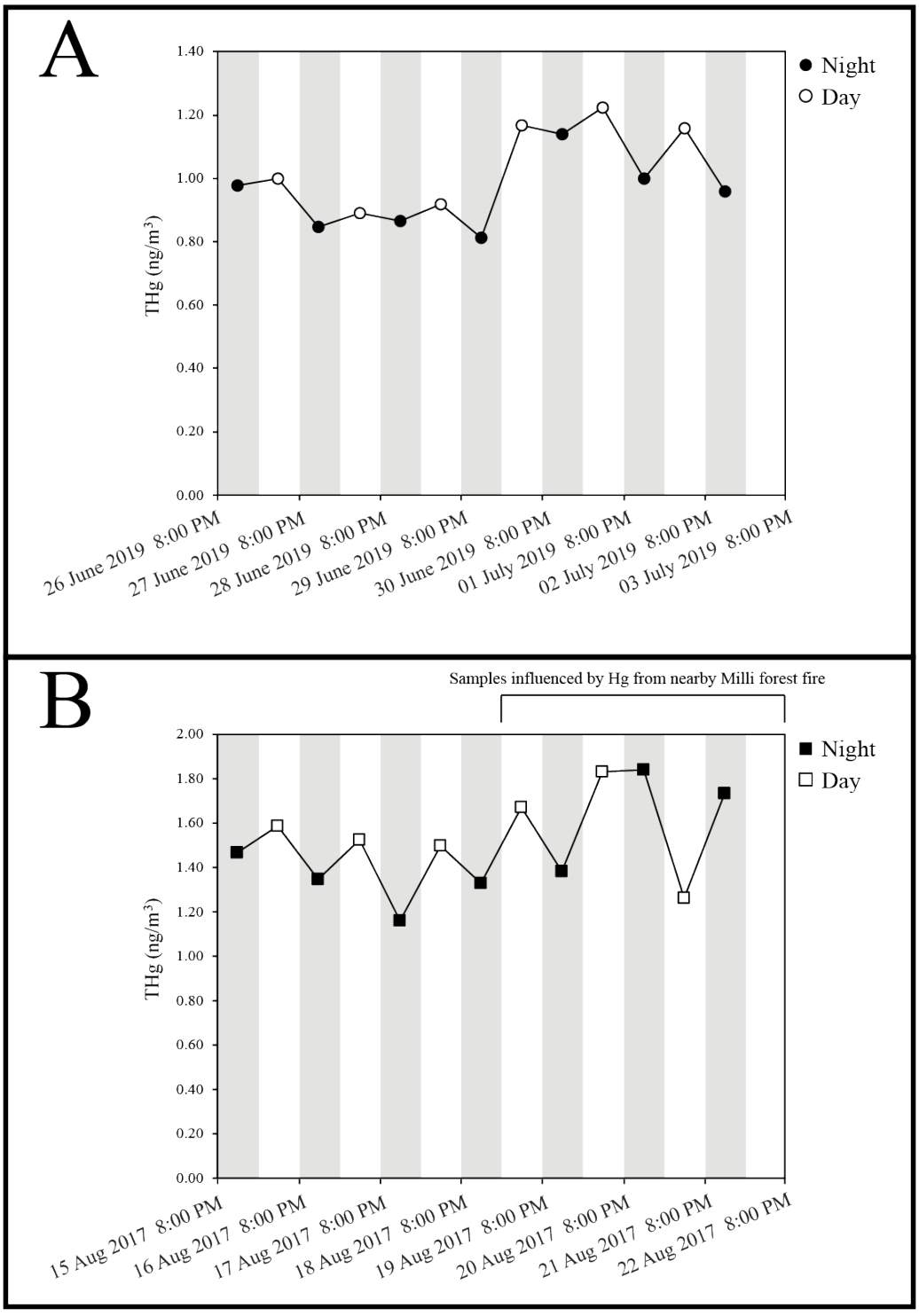

Figure 3.2 THg concentrations of measured Hg^0 samples at A) Camp Davis and B) Mount Bachelor.

Vertical grey shading represents nighttime periods and white represents daytime. Open symbols represent daytime measurements while closed symbols are nighttime measurements.

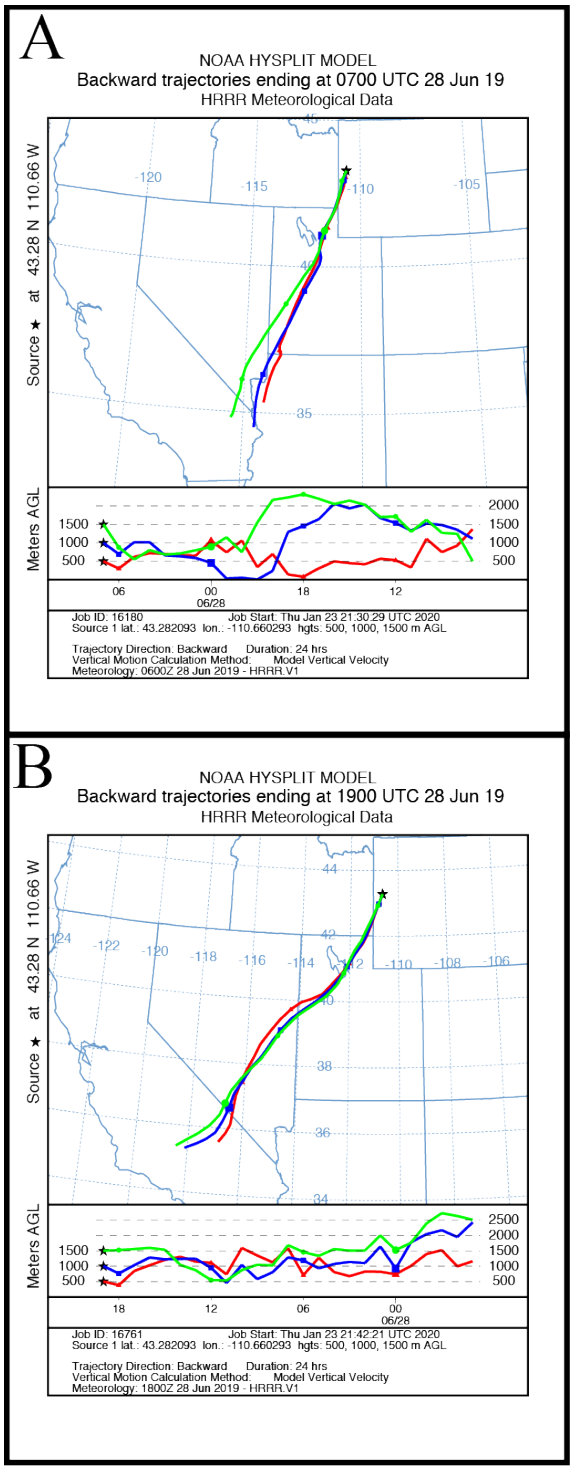

Figure 3.3 HYSPLIT back-trajectories from Camp Davis, WY.

Panel A) 24-hour back-trajectory representative of nightly air mass origins during sampling. Panel B) 24-hour back-trajectory representative of daily air mass origins during sampling. Local time at Camp Davis (Mountain Daylight Time) is equivalent to UTC-6:00 hours.

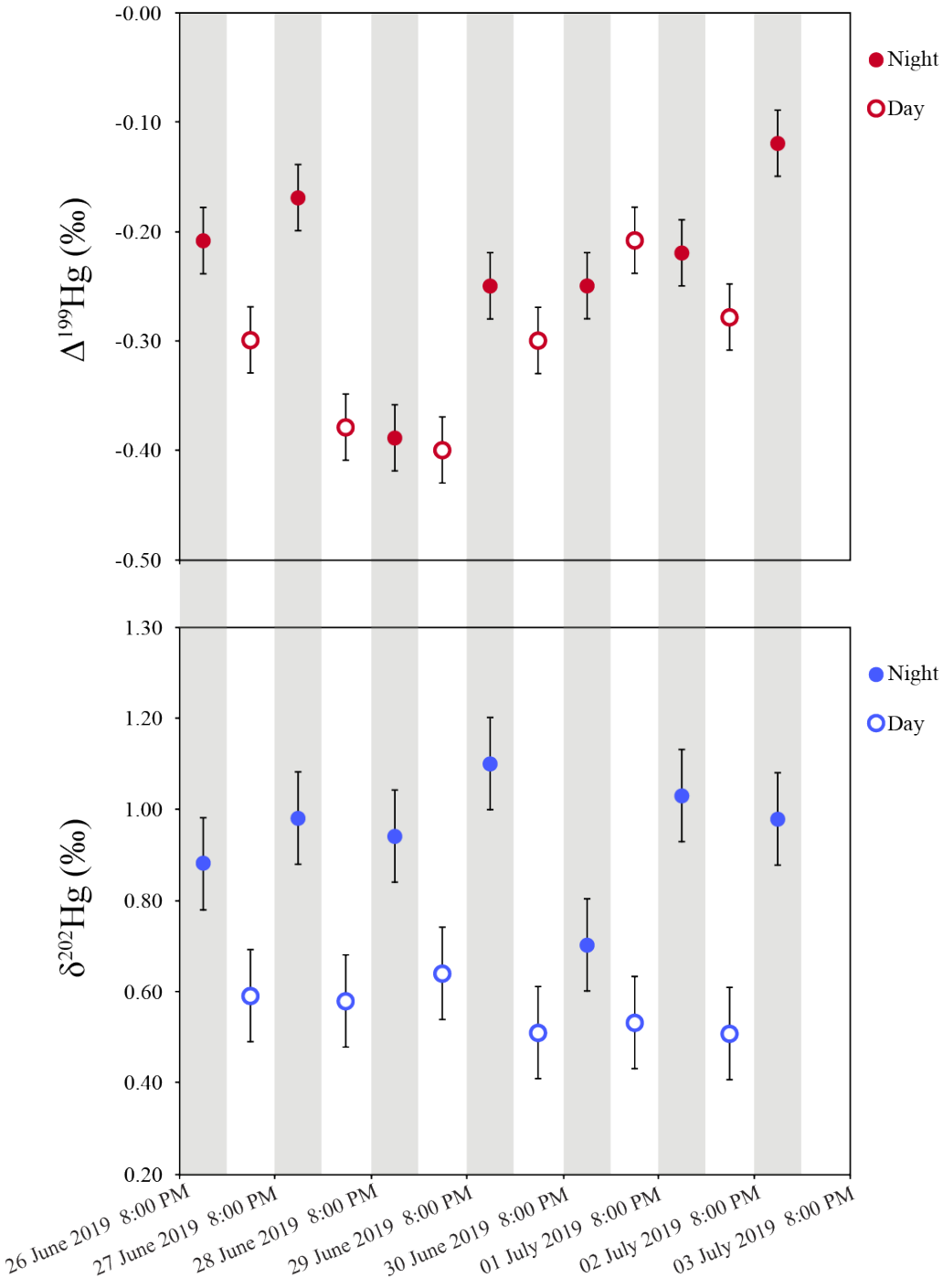

Figure 3.4 Camp Davis Hg isotope data plotted with δ^{202}Hg and Δ^{199}Hg on separate y-axes while sharing time on the x-axis.

Vertical grey shading represents nighttime periods and white represents daytime. Black bars represent analytical error (2SD).

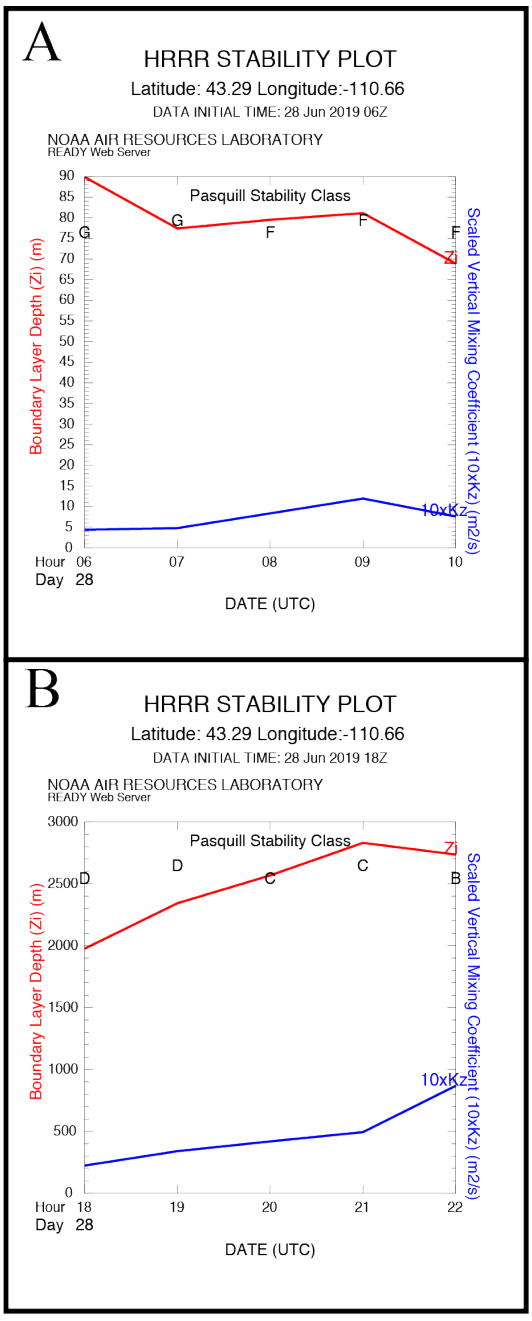

Figure 3.5 Stability plots from Camp Davis, WY.

Panel A) Boundary layer depth and stability representative of nightly conditions during sampling. Panel B) Boundary layer depth and stability representative of daily conditions during sampling. Local time at Camp Davis (Mountain Daylight Time) is equivalent to UTC-6:00 hours.

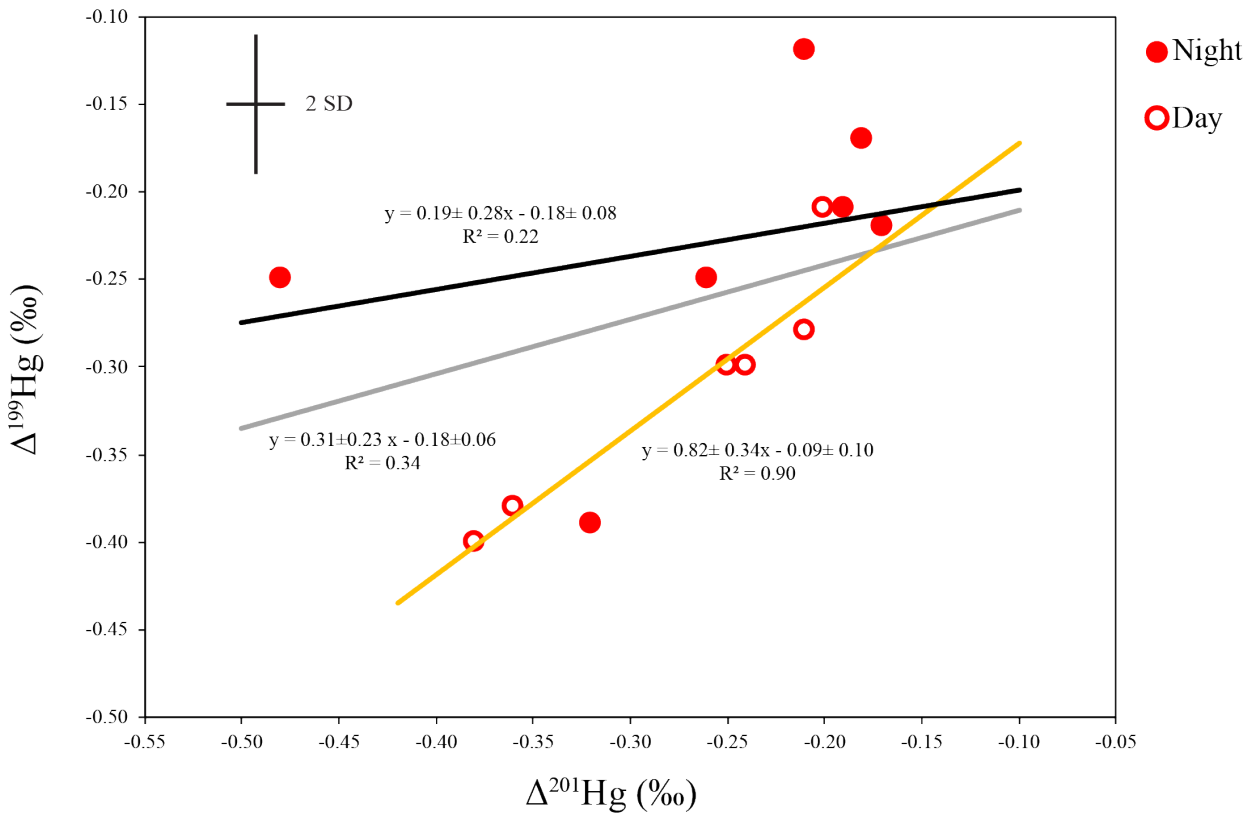

Figure 3.6 Plot of Δ^{199}Hg vs. Δ^{201}Hg measured in Hg^0 samples at Camp Davis.

The solid grey line is a York regression of all Camp Davis Hg^0 samples, the solid black line is a York regression of only nighttime Camp Davis samples, and the solid orange line is a York regression of only daytime samples.

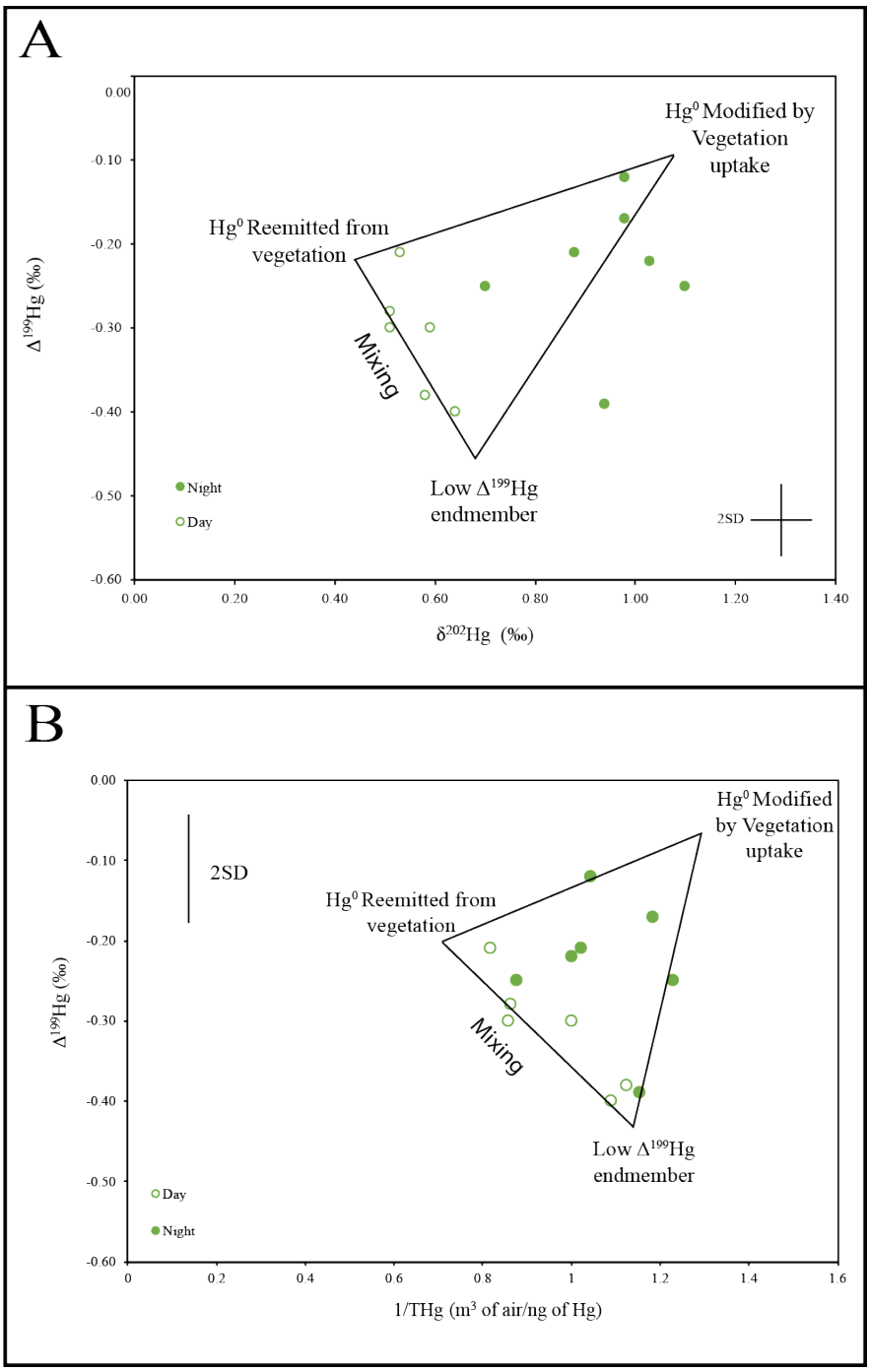

Figure 3.7 Three-endmember isotopic mixing model for Hg^0 at Camp Davis.

Panel A) displays $\delta^{202}Hg$ vs. $\Delta^{199}Hg$ values and panel B) displays 1/THg vs. $\Delta^{199}Hg$. On both panels, black lines represent mixing between isotopic endmembers. Representative analytical uncertainty for isotope measurements is presented on each panel as 2SD.

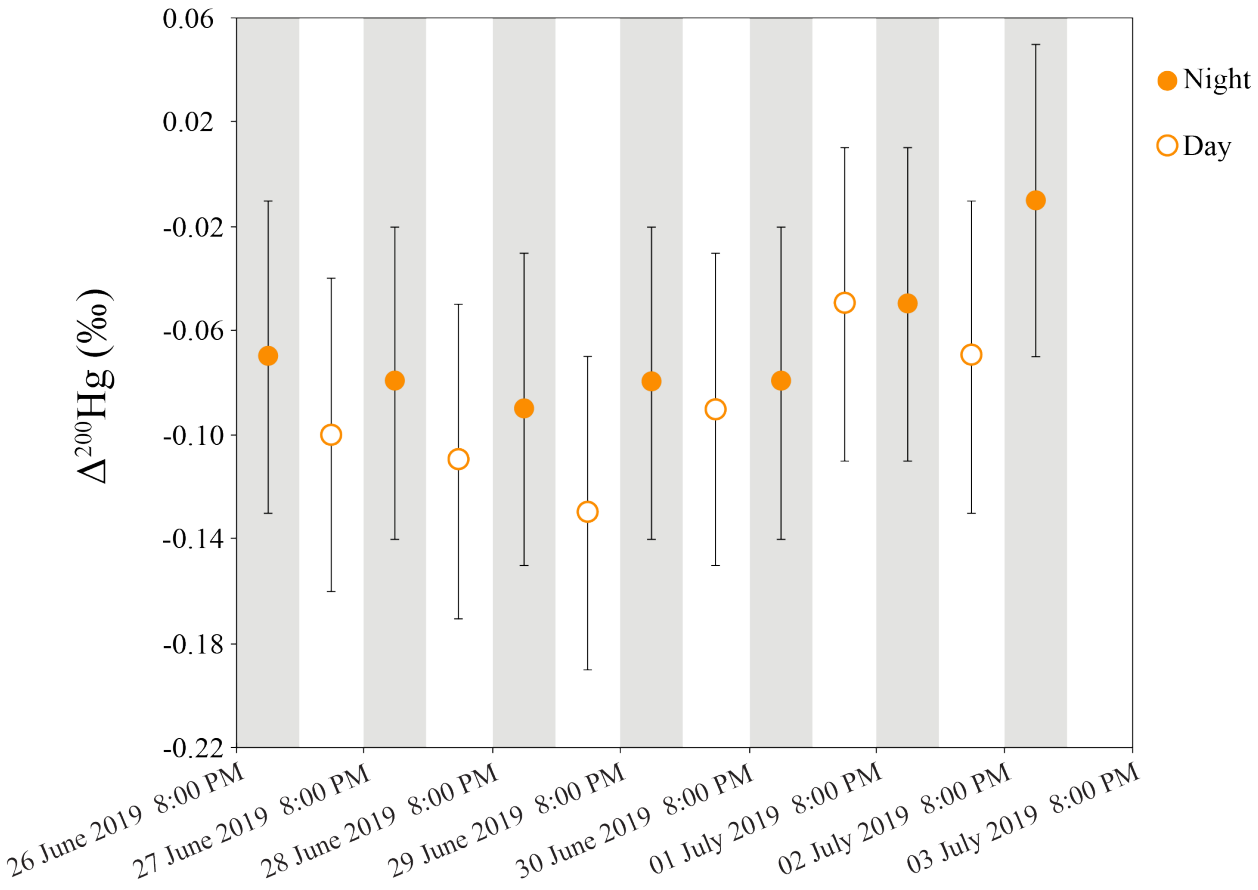

Figure 3.8 Camp Davis Δ^{200}Hg data measured from June 26th, 2019 to July 3rd, 2019.

Vertical grey shading represents nighttime periods and white represents daytime. Black bars represent analytical error (2SD). There is little variation in even-MIF outside of analytical uncertainty and day and night samples are not statistically different.

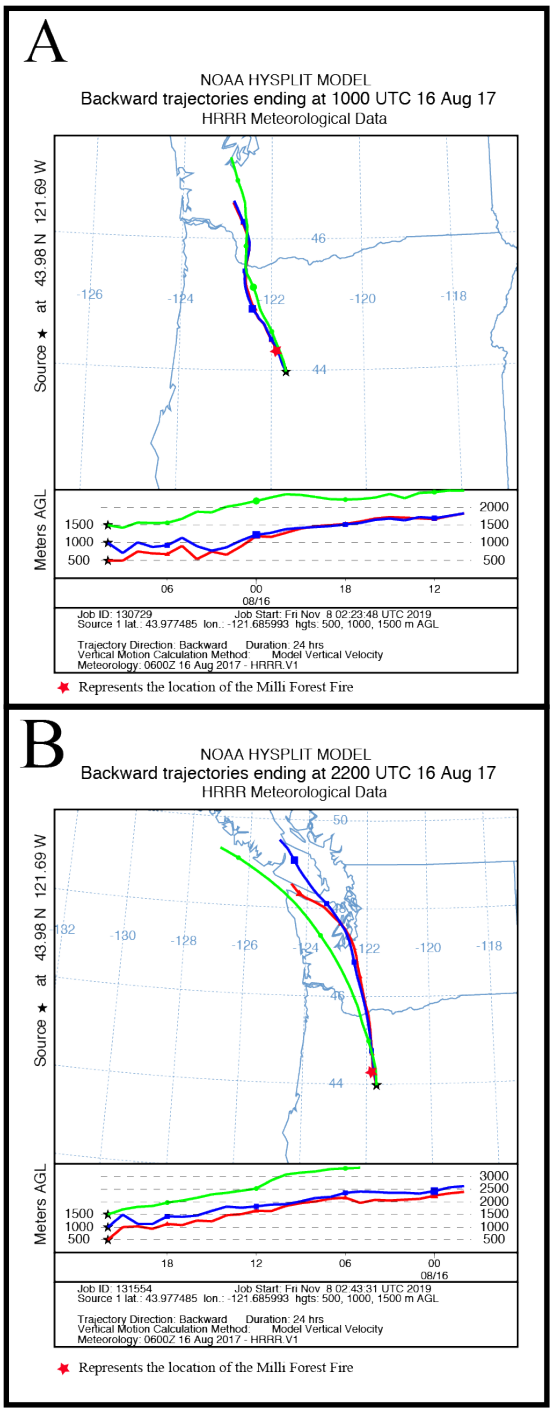

Figure 3.9 HYSPLIT back-trajectories from Mount Bachelor, OR.

Panel A) 24-hour back-trajectory representative of nightly air mass origins during sampling. Panel B) 24-hour back-trajectory representative of daily air mass origins during sampling. The red star represents the location of the Milli Forest fire. Local time at Mount Bachelor (Pacific Daylight Time) is equivalent to UTC-7:00 hours.

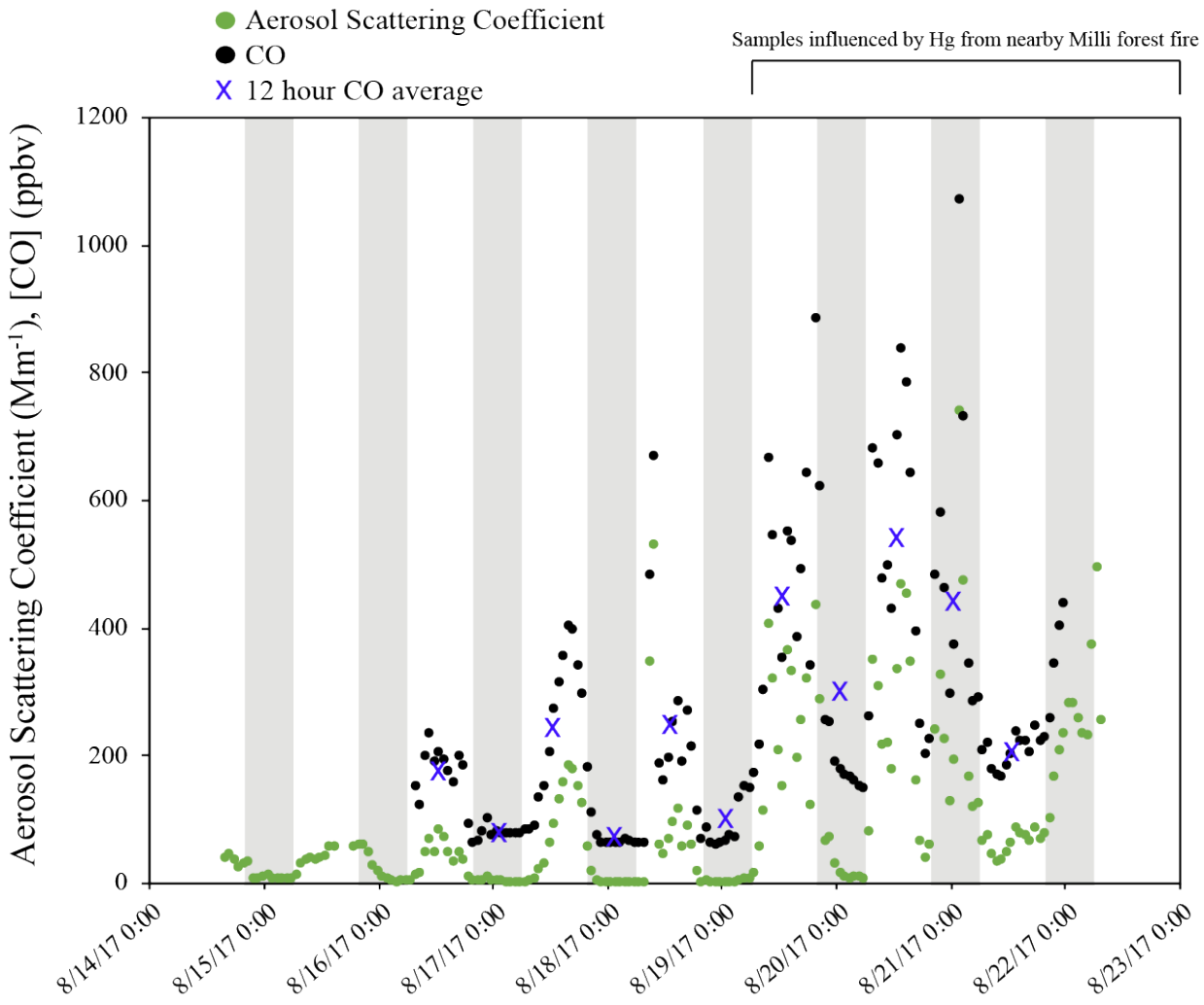

Figure 3.10 Aerosol scattering coefficient (Mm^{-1}) (green circles) and [CO] (ppbv) (black circles) as measured during the sampling campaign at MBO.

Blue X represent 12 hour [CO] averages. Vertical grey shading represents nighttime periods and white represents daytime. Samples collected on August 19th through the end of the sampling period are dominated by Hg from the nearby Milli forest fire.

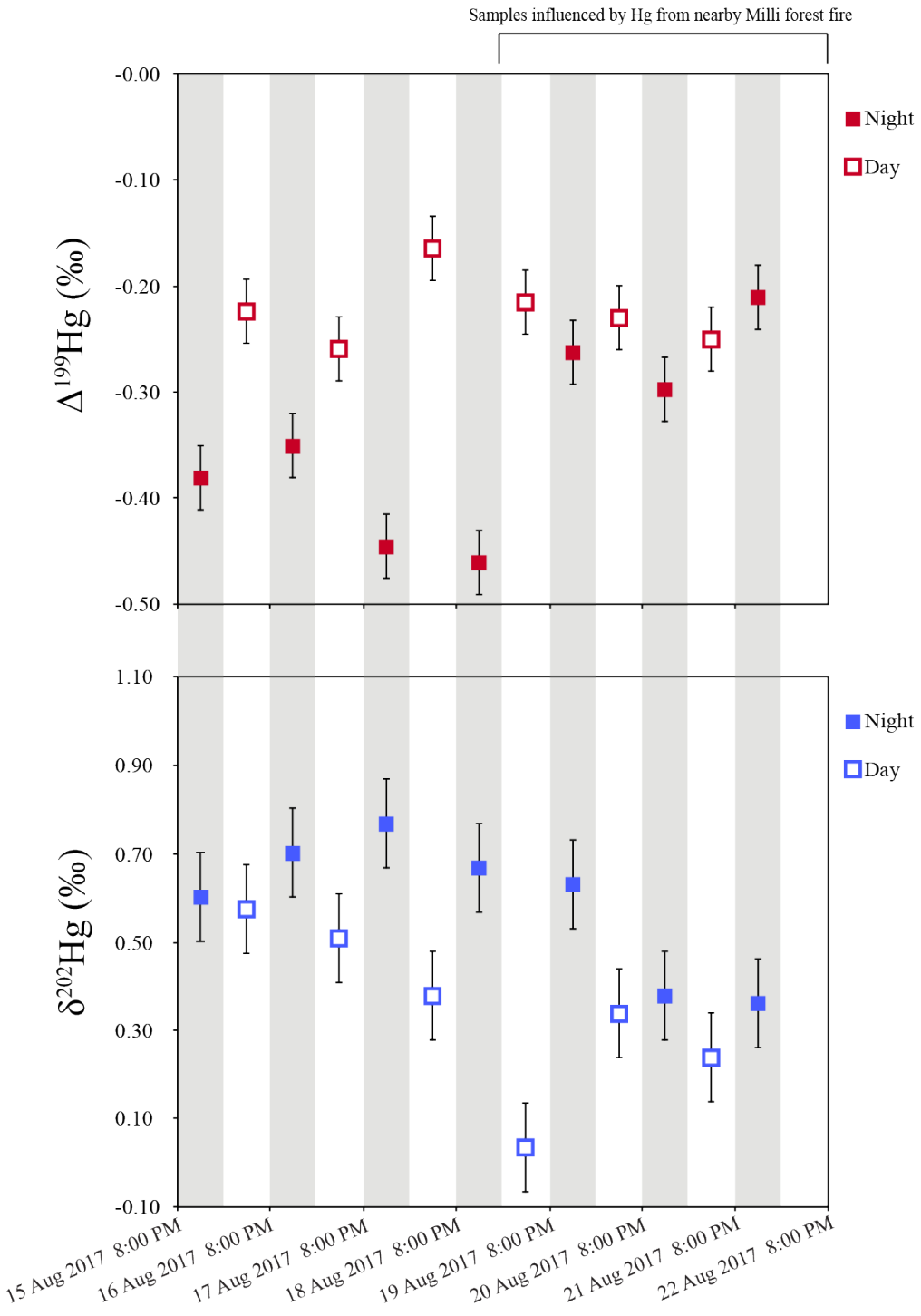

Figure 3.11 Mount Bachelor Hg isotope data plotted with δ^{202}Hg and Δ^{199}Hg on separate y-axes while sharing time on the x-axis.

Vertical grey shading represents nighttime periods and white represents daytime. Black bars represent analytical error (2SD). Samples collected on August 19th through the end of the sampling period are dominated by Hg from the nearby Milli forest fire.

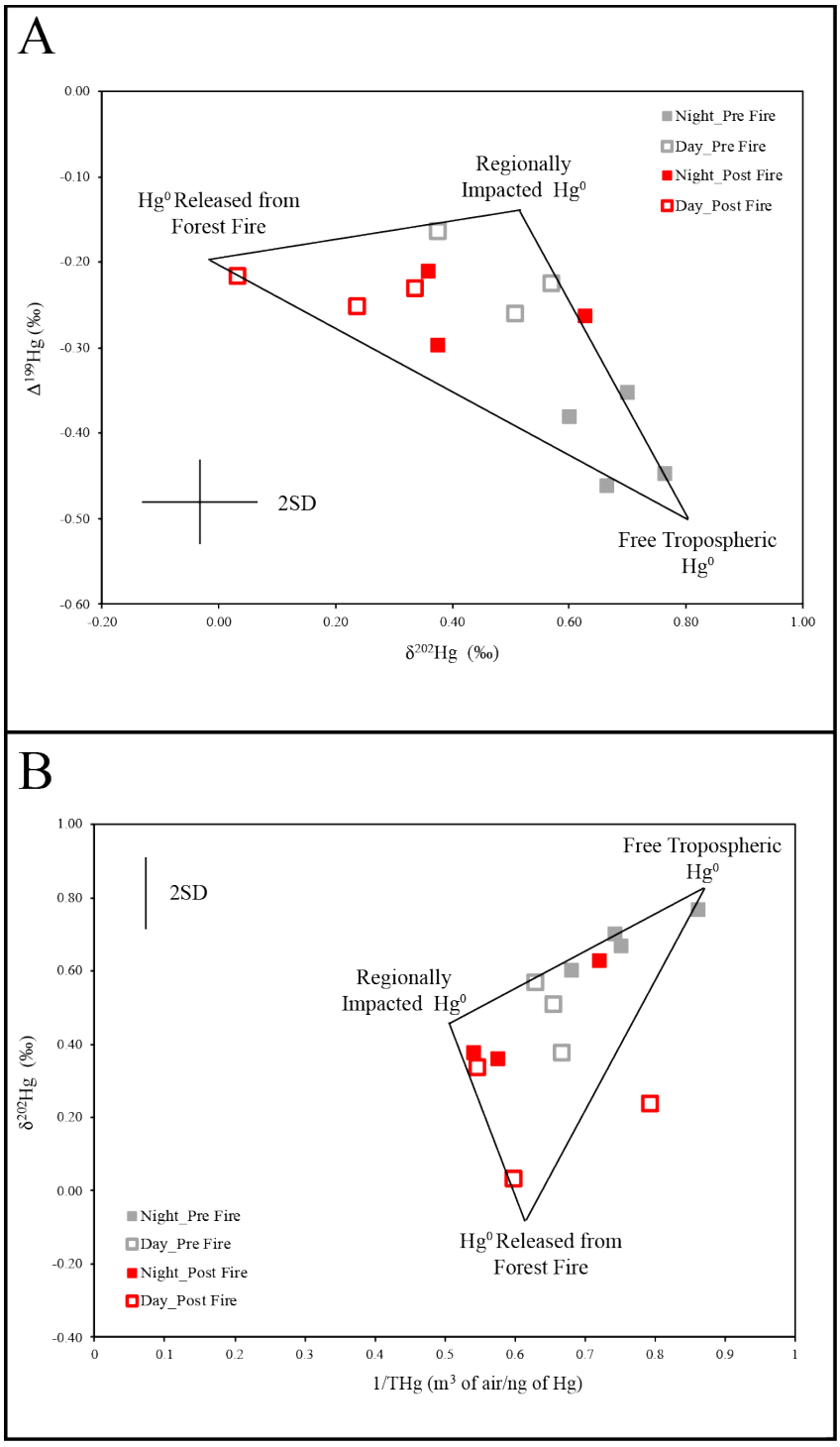

Figure 3.12 Three-endmember isotopic mixing model for Hg^0 at Camp Davis.

Panel A) displays $\delta^{202}Hg$ vs. $\Delta^{199}Hg$ values and panel B) displays 1/THg vs. $\delta^{202}Hg$. On both panels, black lines represent mixing between isotopic endmembers. Representative analytical uncertainty for isotope measurements is presented on each panel as 2SD.

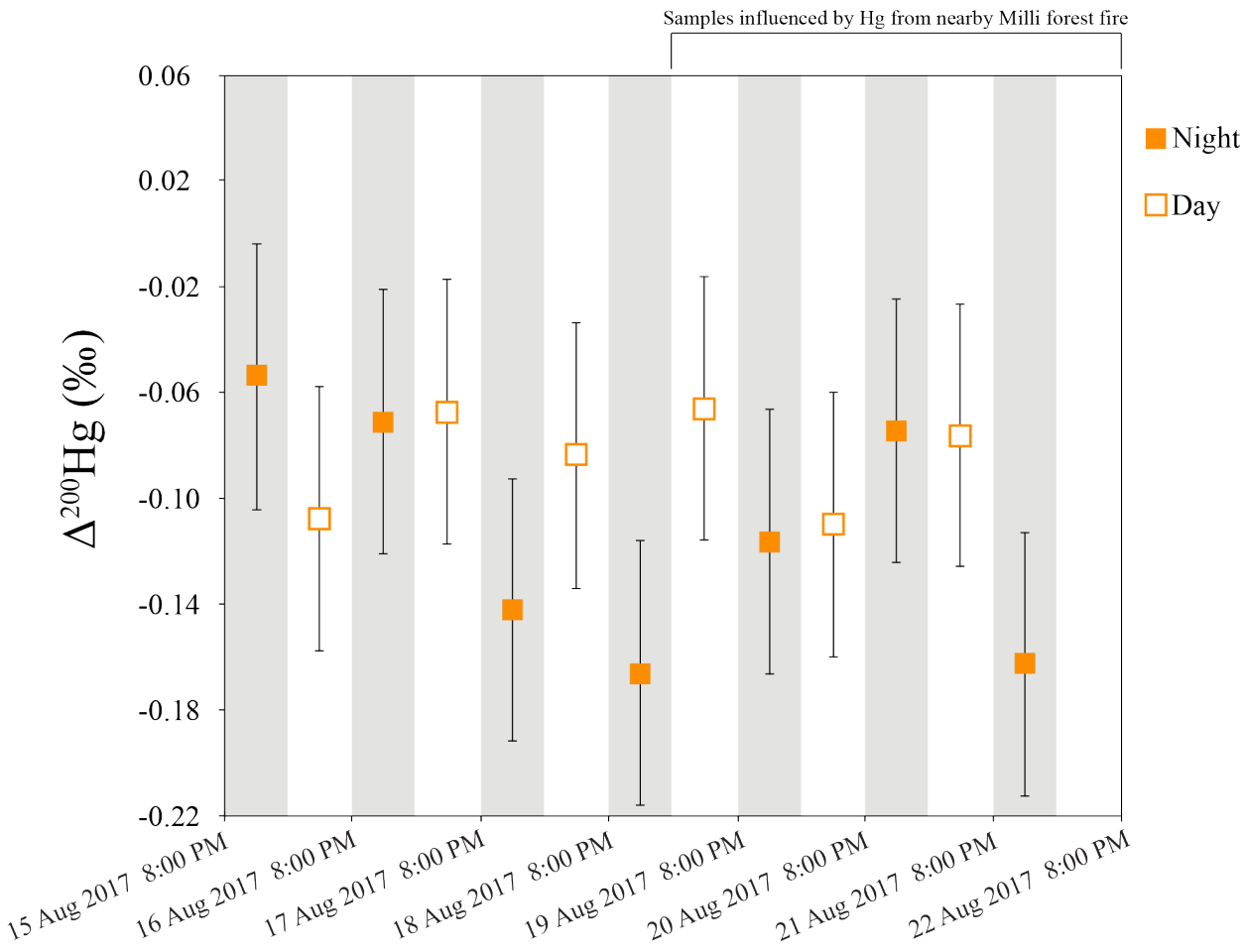

Figure 3.13 Mount Bachelor Δ^{200}Hg data measured from Aug 15th, 2019 to Aug 22nd, 2019.

Vertical grey shading represents nighttime periods and white represents daytime. Black bars represent analytical error (2SD). There is little variation in even-MIF outside of analytical uncertainty and day and night sample averages are not statistically different. Samples collected on August 19th through the end of the sampling period are dominated by Hg from the nearby Milli forest fire.

References

Ambrose, J.L., Reidmiller, D.R., Jaffe, D.A., 2011. Causes of high O3 in the lower free troposphere over the Pacific Northwest as observed at the Mt. Bachelor Observatory. Atmos. Environ. 45, 5302–5315. https://doi.org/10.1016/j.atmosenv.2011.06.056

Ariya, P.A., Skov, H., Grage, M.M.L., Goodsite, M.E., 2008. Gaseous Elemental Mercury in the Ambient Atmosphere: Review of the Application of Theoretical Calculations and Experimental Studies for Determination of Reaction Coefficients and Mechanisms with Halogens and Other Reactants, Advances in Quantum Chemistry. Elsevier Masson SAS. https://doi.org/10.1016/S0065-3276(07)00204-3

Bergquist, B.A., Blum, J.D., 2007. Mass-dependent and -independent fractionation of Hg isotopes by photoreduction in aquatic systems. Science (80-.). 318, 417–420. https://doi.org/10.1126/science.1148050

Blum, J.D., Bergquist, B.A., 2007. Reporting of variations in the natural isotopic composition of mercury. Anal. Bioanal. Chem. 388, 353–359. https://doi.org/10.1007/s00216-007-1236-9

Blum, J.D., Johnson, M.W., 2017. Recent Developments in Mercury Stable Isotope Analysis. Rev. Mineral. Geochemistry 82, 733–757.

Chandan, P., Ghosh, S., Bergquist, B.A., 2015. Mercury isotope fractionation during aqueous photoreduction of monomethylmercury in the presence of dissolved organic matter. Environ. Sci. Technol. 49, 259–267. https://doi.org/10.1021/es5034553

Chen, J., Hintelmann, H., Feng, X., Dimock, B., 2012. Unusual fractionation of both odd and even mercury isotopes in precipitation from Peterborough, ON, Canada. Geochim. Cosmochim. Acta 90, 33–46. https://doi.org/10.1016/j.gca.2012.05.005

Demers, J.D., Blum, J.D., Zak, D.R., 2013. Mercury isotopes in a forested ecosystem: Implications for air-surface exchange dynamics and the global mercury cycle. Global Biogeochem. Cycles 27, 222–238. https://doi.org/10.1002/gbc.20021

Demers, J.D., Sherman, L.S., Blum, J.D., Marsik, F.J., Dvonch, J.T., 2015. Coupling atmospheric mercury isotope ratios and meteorology to identify sources of mercury impacting a coastal urban-industrial region near Pensacola, Florida, USA. Global Biogeochem. Cycles 29, 1689–1705. https://doi.org/10.1002/2015GB005146

Donovan, P.M., Blum, J.D., Demers, J.D., Gu, B., Brooks, S.C., Peryam, J., 2014. Identification of multiple mercury sources to stream sediments near Oak Ridge, TN, USA. Environ. Sci. Technol. 48, 3666–3674. https://doi.org/10.1021/es4046549

Donovan, P.M., Blum, J.D., Yee, D., Gehrke, G.E., Singer, M.B., 2013. An isotopic record of mercury in San Francisco Bay sediment. Chem. Geol. 349–350, 87–98. https://doi.org/10.1016/j.chemgeo.2013.04.017

Enrico, M., Roux, G. Le, Marusczak, N., Heimbürger, L.-E., Claustres, A., Fu, X., Sun, R., Sonke, J.E., 2016. Atmospheric Mercury Transfer to Peat Bogs Dominated by Gaseous Elemental Mercury Dry Deposition. Environ. Sci. Technol. 50, 2405–2412. https://doi.org/10.1021/acs.est.5b06058

Finley, B.D., Swartzendruber, P.C., Jaffe, D.A., 2009. Particulate mercury emissions in regional wildfire plumes observed at the Mount Bachelor Observatory. Atmos. Environ. 43, 6074–

6083. https://doi.org/10.1016/j.atmosenv.2009.08.046

Fischer, E. V., Perry, K.D., Jaffe, D.A., 2011. Optical and chemical properties of aerosols transported to Mount Bachelor during spring 2010. J. Geophys. Res. Atmos. 116, 1–13. https://doi.org/10.1029/2011JD015932

Fu, X., Marusczak, N., Wang, X., Gheusi, F., Sonke, J.E., 2016a. Isotopic Composition of Gaseous Elemental Mercury in the Free Troposphere of the Pic du Midi Observatory, France. Environ. Sci. Technol. 50, 5641–5650. https://doi.org/10.1021/acs.est.6b00033

Fu, X., Yang, X., Tan, Q., Ming, L., Lin, T., Lin, C.-J., Li, X., Feng, X., 2018. Isotopic Composition of Gaseous Elemental Mercury in the Marine Boundary Layer of East China Sea. J. Geophys. Res. Atmos. 123, 7656–7669. https://doi.org/10.1029/2018JD028671

Fu, X., Zhang, H., Liu, C., Zhang, H., Lin, C.J., Feng, X., 2019. Significant Seasonal Variations in Isotopic Composition of Atmospheric Total Gaseous Mercury at Forest Sites in China Caused by Vegetation and Mercury Sources. Environ. Sci. Technol. 53, 13748–13756. https://doi.org/10.1021/acs.est.9b05016

Fu, X., Zhu, W., Zhang, H., Sommar, J., Yu, B., Yang, X., Wang, X., Lin, C.J., Feng, X., 2016b. Depletion of atmospheric gaseous elemental mercury by plant uptake at Mt. Changbai, Northeast China. Atmos. Chem. Phys. 16, 12861–12873. https://doi.org/10.5194/acp-16-12861-2016

Gratz, L.E., Ambrose, J.L., Jaffe, D.A., Shah, V., Jaeglé, L., Stutz, J., Festa, J., Spolaor, M., Tsai, C., Selin, N.E., Song, S., Zhou, X., Weinheimer, A.J., Knapp, D.J., Montzka, D.D., Flocke, F.M., Campos, T.L., Apel, E., Hornbrook, R., Blake, N.J., Hall, S., Tyndall, G.S., Reeves, M., Stechman, D., Stell, M., 2015. Oxidation of mercury by bromine in the subtropical Pacific free troposphere. Geophys. Res. Lett. 42, 494–502. https://doi.org/10.1002/2015GL066645.Received

Gratz, L.E., Keeler, G.J., Blum, J.D., Sherman, L.S., 2010. Isotopic composition and fractionation of mercury in Great Lakes precipitation and ambient air. Environ. Sci. Technol. 44, 7764–7770. https://doi.org/10.1021/es100383w

Huang, Q., Chen, J., Huang, W., Reinfelder, J.R., Fu, P., Yuan, S., 2019. Diel variation in mercury stable isotope ratios records photoreduction of PM2.5-bound mercury. Atmos. Chem. Phys. 19, 315–325.

Huang, S., Sun, L., Zhou, T., Yuan, D., Du, B., Sun, X., 2018. Natural stable isotopic compositions of mercury in aerosols and wet precipitations around a coal-fired power plant in Xiamen, southeast China. Atmos. Environ. 173, 72–80. https://doi.org/10.1016/j.atmosenv.2017.11.003

Jaffe, D., Prestbo, E., Swartzendruber, P., Weiss-Penzias, P., Kato, S., Takami, A., Hatakeyama, S., Kajii, Y., 2005. Export of atmospheric mercury from Asia. Atmos. Environ. 39, 3029–3038. https://doi.org/10.1016/j.atmosenv.2005.01.030

Jiskra, M., E. Sonke, J., Agnan, Y., Helmig, D., Obrist, D., 2019. Insights from mercury stable isotopes on terrestrial-atmosphere exchange of Hg(0) in the Arctic tundra. Biogeosciences 16, 4051–4064. https://doi.org/10.5194/bg-16-4051-2019

Jiskra, M., Sonke, J.E., Obrist, D., Bieser, J., Ebinghaus, R., Myhre, C.L., Pfaffhuber, K.A., Wängberg, I., Kyllönen, K., Worthy, D., Martin, L.G., Labuschagne, C., Mkololo, T.,

Ramonet, M., Magand, O., Dommergue, A., 2018. A Vegetation control on seasonal variations in global atmospheric mercury concentrations. Nat. Geosci. 11, 244–251. https://doi.org/10.1038/s41561-018-0078-8

Jiskra, M., Wiederhold, J.G., Skyllberg, U., Kronberg, R.-M., Hajdas, I., Kretzschmar, R., 2015. Mercury Deposition and Re-emission Pathways in Boreal Forest Soils Investigated with Hg Isotope Signatures. Environ. Sci. Technol. 49, 7188–7196. https://doi.org/10.1021/acs.est.5b00742

Kellerhals, M., Beauchamp, S., Belzer, W., Blanchard, P., Froude, F., Harvey, B., McDonald, K., Pilote, M., Poissant, L., Puckett, K., Schroeder, B., Steffen, A., Tordon, R., 2003. Temporal and spatial variability of total gaseous mercury in Canada: Results from the Canadian Atmospheric Mercury Measurement Network (CAMNet). Atmos. Environ. 37, 1003–1011. https://doi.org/10.1016/S1352-2310(02)00917-2

Kritee, K., Barkay, T., Blum, J.D., 2009. Mass dependent stable isotope fractionation of mercury during mer mediated microbial degradation of monomethylmercury. Geochim. Cosmochim. Acta 73, 1285–1296. https://doi.org/10.1016/j.gca.2008.11.038

Kritee, K., Blum, J.D., Barkay, T., 2008. Mercury Stable Isotope Fractionation during Reduction of Hg (II) by Different Microbial Pathways Mercury Stable Isotope Fractionation during Reduction of Hg (II) by Different Microbial Pathways. Environ. Sci. Technol. 42, 9171–9177. https://doi.org/10.1021/es801591k

Kritee, K., Motta, L.C., Blum, J.D., Tsui, M.T.-K., Reinfelder, J.R., 2017. Photomicrobial Visible Light-Induced Magnetic Mass Independent Fractionation of Mercury in a Marine Microalga. ACS Earth Sp. Chem. acsearthspacechem.7b00056. https://doi.org/10.1021/acsearthspacechem.7b00056

Kurz, A.Y., Blum, J.D., Washburn, S.J., Baskaran, M., 2019. Changes in the mercury isotopic composition of sediments from a remote alpine lake in Wyoming , USA. Sci. Total Environ. 669, 973–982. https://doi.org/10.1016/j.scitotenv.2019.03.165

Kwon, S.Y., Selin, N.E., 2016. Uncertainties in Atmospheric Mercury Modeling for Policy Evaluation. Curr. Pollut. Reports 2, 103–114. https://doi.org/10.1007/s40726-016-0030-8

Lindberg, S.E., Stratton, W.J., 1998. Atmospheric Mercury Speciation : Concentrations and Behavior of Reactive Gaseous Mercury in Ambient Air. Environ. Sci. Technol. 32, 49–57. https://doi.org/doi:10.1021/es970546u

Lyman, S.N., Jaffe, D.A., 2012. Formation and fate of oxidized mercury in the upper troposphere and lower stratosphere. Nat. Geosci. 5, 114–117. https://doi.org/10.1038/ngeo1353

Mao, H., Talbot, R.W., Sigler, J.M., Sive, B.C., Hegarty, J.D., Mao, H., Talbot, R.W., Sigler, J.M., Sive, B.C., Seasonal, J.D.H., Mao, H., Talbot, R.W., Sigler, J.M., Sive, B.C., Hegarty, J.D., 2008. Seasonal and diurnal variations of Hg ° over New England. Atmos. Chem. Phys. 8, 1403–1421.

Mason, R., Fitzgerald, W., Morel, F., 1994. The biogeochemical cycling of elemental mercury: Anthropogenic influences. Geochim. Cosmochim. Acta 58, 3191–3198. https://doi.org/10.1016/0016-7037(94)90046-9

Murphy, D.M., Hudson, P.K., Thomson, D.S., Sheridan, P.J., Wilson, J.C., 2006. Observations of mercury-containing aerosols. Environ. Sci. Technol. 40, 3163–3167.

https://doi.org/10.1021/es052385x

Obrist, D., Kirk, J.L., Zhang, L., Sunderland, E.M., Jiskra, M., Selin, N.E., 2018. A review of global environmental mercury processes in response to human and natural perturbations: Changes of emissions, climate, and land use. Ambio 47, 116–140. https://doi.org/10.1007/s13280-017-1004-9

Poissant, L., Pilote, M., Yumvihoze, E., Lean, D., 2008. Mercury concentrations and foliage/atmosphere fluxes in a maple forest ecosystem in Québec, Canada. J. Geophys. Res. Atmos. 113, 1–12. https://doi.org/10.1029/2007JD009510

Reidmiller, D.R., Jaffe, D.A., Fischer, E. V., Finley, B., 2010. Nitrogen oxides in the boundary layer and free troposphere at the Mt. Bachelor Observatory. Atmos. Chem. Phys. 10, 6043–6062. https://doi.org/10.5194/acp-10-6043-2010

Rolison, J.M., Landing, W.M., Luke, W., Cohen, M., Salters, V.J.M., 2013. Isotopic composition of species-specific atmospheric Hg in a coastal environment. Chem. Geol. 336, 37–49. https://doi.org/10.1016/j.chemgeo.2012.10.007

Rolph, G., Stein, A., Stunder, B., 2017. Real-time Environmental Applications and Display sYstem: READY. Environ. Model. Softw. 95, 210–228. https://doi.org/10.1016/j.envsoft.2017.06.025

Rose, C.H., Ghosh, S., Blum, J.D., Bergquist, B.A., 2015. Effects of ultraviolet radiation on mercury isotope fractionation during photo-reduction for inorganic and organic mercury species. Chem. Geol. 405, 102–111. https://doi.org/10.1016/j.chemgeo.2015.02.025

Rutter, A.P., Schauer, J.J., 2007. The effect of temperature on the gas-particle partitioning of reactive mercury in atmospheric aerosols. Atmos. Environ. 41, 8647–8657. https://doi.org/10.1016/j.atmosenv.2007.07.024

Sherman, L.S., Blum, J.D., Dvonch, J.T., Gratz, L.E., Landis, M.S., 2015. The use of Pb, Sr, and Hg isotopes in Great Lakes precipitation as a tool for pollution source attribution. Sci. Total Environ. 502, 362–374. https://doi.org/10.1016/j.scitotenv.2014.09.034

Sherman, L.S., Blum, J.D., Johnson, K.P., Keeler, G.J., Barres, J. a., Douglas, T. a., 2010. Mass-independent fractionation of mercury isotopes in Arctic snow driven by sunlight. Nat. Geosci. 3, 173–177. https://doi.org/10.1038/ngeo758

Sherman, L.S., Blum, J.D., Keeler, G.J., Demers, J.D., Dvonch, J.T., 2012. Investigation of local mercury deposition from a coal-fired power plant using mercury isotopes. Environ. Sci. Technol. 46, 382–390. https://doi.org/10.1021/es202793c

Slemr, F., Angot, H., Dommergue, A., Magand, O., Barret, M., Weigelt, A., Ebinghaus, R., Brunke, E.G., Pfaffhuber, K.A., Edwards, G., Howard, D., Powell, J., Keywood, M., Wang, F., 2015. Comparison of mercury concentrations measured at several sites in the Southern Hemisphere. Atmos. Chem. Phys. 15, 3125–3133. https://doi.org/10.5194/acp-15-3125-2015

Slemr, F., Weigelt, A., Ebinghaus, R., Kock, H.H., Bödewadt, J., Brenninkmeijer, C.A.M., Rauthe-Schöch, A., Weber, S., Hermann, M., Becker, J., Zahn, A., Martinsson, B., 2016. Atmospheric mercury measurements onboard the CARIBIC passenger aircraft. Atmos. Meas. Tech. 9, 2291–2302. https://doi.org/10.5194/amt-9-2291-2016

Sprovieri, F., Pirrone, N., Bencardino, M., Amore, F.D., Carbone, F., Cinnirella, S., Mannarino,

V., Landis, M., Weigelt, A., Brunke, E., Labuschagne, C., Munthe, J., Wängberg, I., Artaxo, P., Morais, F., De, H., 2018. Atmospheric mercury concentrations observed at ground-based monitoring sites globally distributed in the framework of the GMOS network. Atmos. Chem. Phys. 16, 11915–11935. https://doi.org/10.5194/acp-16-11915-2016.Atmospheric

Stein, A.F., Draxler, R.R., Rolph, G.D., Stunder, B.J.B., Cohen, M.D., Ngan, F., 2015. Noaa's hysplit atmospheric transport and dispersion modeling system. Bull. Am. Meteorol. Soc. 96, 2059–2077. https://doi.org/10.1175/BAMS-D-14-00110.1

Subir, M., Ariya, P.A., Dastoor, A.P., 2012. A review of the sources of uncertainties in atmospheric mercury modeling II. Mercury surface and heterogeneous chemistry - A missing link. Atmos. Environ. 46, 1–10. https://doi.org/10.1016/j.atmosenv.2011.07.047

Sun, G., Sommar, J., Feng, X., Lin, C.-J., Ge, M., Wang, W., Yin, R., Fu, X., Shang, L., 2016. Mass-Dependent and -Independent Fractionation of Mercury Isotope during Gas-Phase Oxidation of Elemental Mercury Vapor by Atomic Cl and Br. Environ. Sci. Technol. 50, 9232–9241. https://doi.org/10.1021/acs.est.6b01668

Sun, R., Sonke, J.E., Heimbu, L., Belkin, H.E., Liu, G., Shome, D., Cukrowska, E., Liousse, C., Pokrovsky, O.S., Streets, D.G., 2014. Mercury Stable Isotope Signatures of World Coal Deposits and Historical Coal Combustion Emissions. Environ. Sci. Technol. 43, 7660–7668.

Sun, R., Sonke, J.E., Liu, G., 2016. Biogeochemical controls on mercury stable isotope compositions of world coal deposits: A review. Earth-Science Rev. 152, 1–13. https://doi.org/10.1016/j.earscirev.2015.11.005

Swartzendruber, P.C., Chand, D., Jaffe, D.A., Smith, J., Reidmiller, D., Gratz, L., Keeler, J., Strode, S., Jaeglé, L., Talbot, R., 2008. Vertical distribution of mercury, CO, ozone, and aerosol scattering coefficient in the Pacific Northwest during the spring 2006 INTEX-B campaign. J. Geophys. Res. Atmos. 113, 1–15. https://doi.org/10.1029/2007JD009579

Swartzendruber, P.C., Jaffe, D.A., Prestbo, E.M., Weiss-Penzias, P., Selin, N.E., Park, R., Jacob, D.J., Strode, S., Jaeglé, L., 2006. Observations of reactive gaseous mercury in the free troposphere at the Mount Bachelor Observatory. J. Geophys. Res. Atmos. 111, 1–12. https://doi.org/10.1029/2006JD007415

Talbot, R., Mao, H., Scheuer, E., Dibb, J., Avery, M., 2007. Total depletion of Hg ° in the upper troposphere – lower stratosphere. Geophys. Res. Lett. 34, 1–5. https://doi.org/10.1029/2007GL031366

Talbot, R., Mao, H., Sive, B., 2005. Diurnal characteristics of surface level O3 and other important trace gases in New England. J. Geophys. Res. D Atmos. 110, 1–16. https://doi.org/10.1029/2004JD005449

Tang, S., Feng, C., Feng, X., Zhu, J., Sun, R., Fan, H., Wang, L., Li, R., Mao, T., Zhou, T., 2017. Stable isotope composition of mercury forms in flue gases from a typical coal-fired power plant, Inner Mongolia, northern China. J. Hazard. Mater. 328, 90–97. https://doi.org/10.1016/j.jhazmat.2017.01.014

Temme, C., Blanchard, P., Steffen, A., Banic, C., Beauchamp, S., Poissant, L., Tordon, R., Wiens, B., 2007. Trend, seasonal and multivariate analysis study of total gaseous mercury data from the Canadian atmospheric mercury measurement network (CAMNet). Atmos.

Environ. 41, 5423–5441. https://doi.org/10.1016/j.atmosenv.2007.02.021

U.S. Environmental Protection Agency (USEPA) National Emission Inventory (NEI). https://www.epa.gov/air-emissions-inventories/2017-national-emissions-inventory-nei-data (Accessed February 3rd, 2020).

Wang, X., Luo, J., Yin, R., Yuan, W., Lin, Che-jen, Sommar, J., Feng, X., Wang, H., Lin, Cynthia, 2017. Using Mercury Isotopes To Understand Mercury Accumulation in the Montane Forest Floor of the Eastern Tibetan Plateau. Environ. Sci. Technol. 51, 801–809. https://doi.org/10.1021/acs.est.6b03806

Wang, Z., Chen, J., Feng, X., Hintelmann, H., Yuan, S., Cai, H., Huang, Q., Wang, S., Wang, F., 2015. Mass-dependent and mass-independent fractionation of mercury isotopes in precipitation from Guiyang, SW China. Comptes Rendus - Geosci. 347, 358–367. https://doi.org/10.1016/j.crte.2015.02.006

Washburn, S.J., Blum, J.D., Kurz, A.Y., Pizzuto, J.E., 2018. Spatial and temporal variation in the isotopic composition of mercury in the South River , VA. Chem. Geol. 494, 96–108. https://doi.org/10.1016/j.chemgeo.2018.07.023

Wehr, R., Commane, R., Munger, J.W., Barry Mcmanus, J., Nelson, D.D., Zahniser, M.S., Saleska, S.R., Wofsy, S.C., 2017. Dynamics of canopy stomatal conductance, transpiration, and evaporation in a temperate deciduous forest, validated by carbonyl sulfide uptake. Biogeosciences 14, 389–401. https://doi.org/10.5194/bg-14-389-2017

Weigelt, A., Ebinghaus, R., Manning, A.J., Derwent, R.G., Simmonds, P.G., Spain, T.G., Jennings, S.G., Slemr, F., 2015. Analysis and interpretation of 18 years of mercury observations since 1996 at Mace Head, Ireland. Atmos. Environ. 100, 85–93. https://doi.org/10.1016/j.atmosenv.2014.10.050

Weiss-Penzias, P., Jaffe, D., Swartzendruber, P., Hafner, W., Chand, D., Prestbo, E., 2007. Quantifying Asian and biomass burning sources of mercury using the Hg/CO ratio in pollution plumes observed at the Mount Bachelor observatory. Atmos. Environ. 41, 4366–4379. https://doi.org/10.1016/j.atmosenv.2007.01.058

Weiss-Penzias, P., Jaffe, D.A., Swartzendruber, P., Dennison, J.B., Chand, D., Hafner, W., Prestbo, E., 2006. Observations of Asian air pollution in the free troposphere at Mount Bachelor Observatory during the spring of 2004. J. Geophys. Res. 111, 1–15. https://doi.org/10.1029/2005JD006522

Wiederhold, J.G., Cramer, C.J., Daniel, K., Infante, I., Bourdon, B., Kretzschmar, R., 2010. Equilibrium mercury isotope fractionation between dissolved Hg(II) species and thiol-bound Hg. Environ. Sci. Technol. 44, 4191–4197. https://doi.org/10.1021/es100205t

William H and Munthe, J.S., 1998. Atmospheric Mercury - An Overview. Atmos. Environ. 32, 809–822.

Yamakawa, A., Moriya, K., Yoshinaga, J., 2017. Determination of isotopic composition of atmospheric mercury in urban-industrial and coastal regions of Chiba, Japan, using cold vapor multicollector inductively coupled plasma mass spectrometry. Chem. Geol. 448, 84–92. https://doi.org/10.1016/j.chemgeo.2016.11.010

Yin, R., Feng, X., Shi, W., 2010. Application of the stable-isotope system to the study of sources

and fate of Hg in the environment: A review. Appl. Geochemistry 25, 1467–1477. https://doi.org/10.1016/j.apgeochem.2010.07.007

York, D., 1968. Least squares fitting of a straight line with correlated errors. Earth Planet. Sci. Lett. 5, 320–324.

Yu, B., Fu, X., Yin, R., Zhang, H., Wang, X., Lin, C.-J., Wu, C., Zhang, Y., He, N., Fu, P., Wang, Z., Shang, L., Sommar, J., Sonke, J.E., Maurice, L., Guinot, B., Feng, X., 2016. Isotopic composition of atmospheric mercury in China: New evidence for source and transformation processes in air and in vegetation. Environ. Sci. Technol. 50, 9262–9269. https://doi.org/10.1021/acs.est.6b01782

Yuan, S., Chen, J., Cai, H., Yuan, W., Wang, Z., Huang, Q., Liu, Y., Wu, X., 2018. Sequential samples reveal significant variation of mercury isotope ratios during single rainfall events. Sci. Total Environ. 624, 133–144. https://doi.org/10.1016/j.scitotenv.2017.12.082

Yuan, W., Sommar, J., Lin, C., Wang, X., Li, K., Liu, Y., Zhang, H., Lu, Z., Wu, C., Feng, X., 2018. Stable Isotope Evidence Shows Re-emission of Elemental Mercury Vapor Occurring after Reductive Loss from Foliage. Environ. Sci. Technol. 53, 651–660. https://doi.org/10.1021/acs.est.8b04865

Zhang, H., Yin, R., Feng, X., Sommar, J., Anderson, C.W.N., Sapkota, A., Fu, X., Larssen, T., 2013. Atmospheric mercury inputs in montane soils increase with elevation: Evidence from mercury isotope signatures. Sci. Rep. 3. https://doi.org/10.1038/srep03322

Zhang, L., Jaffe, D.A., 2017. Trends and sources of ozone and sub-micron aerosols at the Mt. Bachelor Observatory (MBO) during 2004–2015. Atmos. Environ. 165, 143–154. https://doi.org/10.1016/j.atmosenv.2017.06.042

Zheng, W., Hintelmann, H., 2010. Isotope Fractionation of Mercury during Its Photochemical Reduction by Low-Molecular-Weight Organic Compounds. J. Phys. Chem. A 114, 4246–4253.

Zheng, W., Obrist, D., Weis, D., Bergquist, B.A., 2016. Mercury isotope compositions across North American forests. Biogeochem. Cycles 30, 1475–1492. https://doi.org/10.1002/2015GB005323.Received

Chapter 4 Isotopic Composition of Hg Deposited via Snow into mid-latitude Ecosystems

Authors: Aaron Y. Kurz[1,*], Joel D. Blum[1], Marcus W. Johnson[1], Knute Nadelhoffer[2], and Donald R. Zak[2,3]

Abstract: Atmospheric deposition of mercury (Hg) to terrestrial and aquatic ecosystems has significant implications for human and animal exposure. Measurements of Hg isotopic composition can be utilized to trace sources of Hg, but outside of the Arctic, there has been very little Hg isotopic characterization of snow. To better understand deposition pathways at mid-latitudes, we collected five time series of snowfall at two sites (Dexter, Michigan and Pellston, Michigan) to investigate the Hg isotopic composition of snowfall, how it changes after deposition, and how it compares to wet precipitation. The Hg isotopic composition of a subset of fresh snow samples revealed the influence of reactive surface uptake of atmospheric Hg^0. The first time series collected at Dexter occurred during a polar vortex, demonstrating Hg isotopic fractionation dynamics similar to those in Arctic snow, with increasingly negative $\Delta^{199}Hg$ as snow aged with exposure to sunlight. All other time series revealed an increase in $\Delta^{199}Hg$ as snow aged, with values reaching up to 3.5‰. This characterization of Hg isotopes in snow reveals the strong influence of oxidants and binding ligands in snow that mediate Hg isotope fractionation. Additionally, isotopic characterization of Hg in snow deposited to natural ecosystems at mid-latitudes allows for better understanding of atmospheric mercury sources that are deposited to lakes and forests and that may become available for methylation and transfer to the food web.

4.1 Introduction

Mercury (Hg) is a globally distributed heavy metal that can bioaccumulate in aquatic ecosystems leading to high levels in fish, causing human health concerns. In its most toxic and bioaccumulative form (monomethylmercury: MMHg), Hg poses a threat to the neurological health of humans and other animals (Driscoll et al., 2013). Currently, the release of Hg to the atmosphere is dominated by anthropogenic emissions through coal combustion and artisanal gold mining, followed by natural releases from volcanoes and geothermal activity (Horowitz et al., 2014). Since the onset of the Industrial Revolution, the deposition of Hg from the atmosphere has approximately tripled (Engstrom et al., 2014).

The biogeochemical cycling of Hg in the atmosphere is of importance due to the long atmospheric lifetime of Hg^0 (approximately 1 to 2 years), which allows it to be globally distributed (Gustin et al., 2015). Gaseous oxidized mercury ($Hg^{2+}_{(g)}$) and Hg bound to particles ($Hg^{2+}_{(p)}$) are short-lived and readily deposited to the Earth's surface through both wet and dry deposition (Horowitz et al., 2017). These Hg species are operationally defined based on collection methods.

Advancements in multiple collector-inductively coupled plasma-mass spectrometry allow for the high precision measurement of Hg stable isotopes in environmental samples. Building on what is now over a decade of analyses, Hg isotopic characterization has contributed to the understanding and assessment of global biogeochemical cycling of Hg (e.g. Blum et al., 2014; Kwon et al., 2020; Yin et al., 2010). The utility of Hg isotopes stems from Hg displaying both mass dependent fractionation (MDF) and mass independent fractionation (MIF). MDF is driven by physiochemical reactions such as methylation and demethylation of Hg, sorption of Hg, and equilibrium reactions (Jiskra et al., 2012; Kritee et al., 2009, 2007; Rodriguez-Gonzalez et al.,

2009; Wiederhold et al., 2010). MIF is separated into two categories: MIF of odd mass isotopes (odd-MIF) and MIF of even mass isotopes (even-MIF). Odd-MIF is mainly driven by aqueous photochemical reactions (Bergquist and Blum, 2007; Chandan et al., 2015; Rose et al., 2015; Zheng and Hintelmann, 2010), while the mechanism causing even-MIF remains uncertain, but is hypothesized to be related to photo-initiated oxidation of Hg^0 in the upper atmosphere (Chen et al., 2012).

Atmospheric deposition of Hg to terrestrial and aquatic ecosystems is an important component of the biogeochemical cycle of Hg and must be quantified to fully understand the implications of Hg deposition in forests and lakes and for bioaccumulation of Hg in fish, which is the most common pathway for human exposure (Hammerschmidt and Fitzgerald, 2006; Sunderland, 2007). A significant number of studies have characterized the Hg isotopic composition of wet precipitation at mid-latitudes, an important source of Hg to ecosystems (Chen et al., 2012; Demers et al., 2013; Donovan et al., 2013; Gratz et al., 2010; Huang et al., 2018; Sherman et al., 2012, 2015; Wang et al., 2016; Washburn et al., 2020; Yuan et al., 2015). The isotopic composition of Hg that enters ecosystems via snow, unlike wet precipitation, may be significantly impacted through chemical reactions after deposition to the land surface but prior to incorporation into terrestrial or aquatic ecosystems at the time of snowmelt (Douglas and Blum, 2019; Obrist et al., 2017; Sherman et al., 2010).

Previous investigations of Hg dynamics in snow have indicated that cycling within the snowpack and exchange with the atmosphere are complex processes. Most often, studies have focused on polar regions though Hg dynamics in snow at mid-latitudes is particularly important due to the proximity of Hg emissions sources to densely populated areas. Faïn et al. (2013) investigated Hg concentration dynamics in the snowpack in the Colorado Rocky Mountains

through vertical measurements of Hg^0 within and above the snowpack. The authors found that diurnal cycles of near-surface Hg^0 concentrations had distinct maxima coinciding with peak solar radiation. Additionally, Hg^0 concentrations in the upper snow layers remained elevated as compared to ambient concentrations even during the night, indicating nighttime production of Hg^0 (Faïn et al., 2013). In the Arctic, Hg can be quickly and quantitatively stripped from the atmosphere in coastal regions and deposited to the snowpack (Steffen et al., 2008). Subsequent photochemical reactions can release much of the Hg in the snowpack back to the atmosphere (Douglas et al., 2008). This process is referred to as an atmospheric mercury depletion event (AMDE). This phenomenon was first discovered using Hg concentration measurements (Schroeder et al., 1998) but there has since been characterization of the Hg isotope fractionation that occurs during these events (Douglas and Blum, 2019; Obrist et al., 2017; Sherman et al., 2010). The Hg isotopic analysis of snow during AMDEs displays unprecedented negative values for odd-MIF (Sherman et al., 2010).

Although Hg concentrations are normally quite low in snow, making it difficult to separate Hg for isotopic analysis, AMDEs deposit large amounts of Hg making Hg isotope analyses less challenging. This explains in part why most Hg isotopic measurements in snow have been performed on samples from the Arctic. To date, only one study has measured snow at mid-latitudes, and it was a mixture of rain and snow collected on a rooftop in Peterborough, Canada (Chen et al., 2012). In contrast to AMDE snow in Alaska, Chen et al. (2012) reported positive odd-MIF in snow. Further investigation of Hg isotopes during AMDEs has confirmed geographic variability by collecting snow along a 200 km transect from the northern Alaskan coast to Toolik Field Station on the North Slope of Alaska (Obrist et al., 2017). Results from the transect demonstrated that the odd-MIF anomalies dissipate progressively with distance inland

(Obrist et al., 2017). Douglas and Blum (2019) conducted a study to investigate the isotopic composition of Hg that is incorporated into terrestrial and aquatic ecosystems on the Arctic coast of Alaska. Through analysis of Hg isotopes in snow, meltwater, and tundra vegetation, the authors found that meltwater did not reflect the isotopic composition of AMDE snow but did have a similar isotopic composition to vegetation (Douglas and Blum, 2019). Finally, Wang et al (2019) made direct measurements of Br near Utqiagvik, Alaska during AMDEs and provided a quantitative assessment of the role of Br in the Hg oxidation process, concluding that bromine chemistry near the Arctic coast drives quantitative oxidation and removal of Hg^0 from the atmosphere, depositing Hg^{2+} to the snowpack. (Wang et al., 2019). The final Hg isotopic composition incorporated into natural reservoirs through snowmelt, however, is highly fractionated compared to the snow deposited during AMDEs.

The present study investigates the Hg isotopic composition of snow at mid-latitudes. Our objectives were twofold: i) to investigate the progressive fractionation of the Hg isotopic composition in snow from the time of deposition and through subsequent exposure to sunlight, and ii) to characterize the Hg isotopic variation in fresh snow during long duration (48+ hour) snow events. To accomplish our objectives, we collected five separate time series of snow and associated filtered (0.45μm) atmospheric particles at two different sites in Lower Michigan: Dexter, MI and the University of Michigan Biological Station (UMBS) in Pellston, MI (Figure 4.1). Snow samples were collected directly after snow fall and then every 12 hours for a 48-hour period. At the sample site in Dexter, MI, we also collected 12-hour gaseous Hg^0 samples for the duration of the snow collection period. This sampling campaign allows us to characterize the Hg isotopic composition of snow at mid-latitudes during long duration snow events and allows us the opportunity to further elucidate the mechanisms driving the isotopic fractionation of Hg in

snow as it is deposited and as it ages. Furthermore, understanding of the isotopic composition of Hg in snow after exposure to sunlight aids in predicting the isotopic composition of Hg entering terrestrial and aquatic ecosystems during snowmelt.

4.2 Methods

4.2.1 Sample Sites

Two sample sites were chosen for this study. The first was in a rural area in Dexter Township, Michigan (42°25'0.11"N, 83°54'6.84"W) approximately 20 km NW of Ann Arbor, MI. This sample site has been employed for over a decade to collect Hg samples in different media including precipitation and Hg^0. Additionally, this site is used by the Environmental Protection Agency (EPA) as one of the Clean Air Status and Trends Network sites to monitor atmospheric chemical constituents. Here, we collected snow samples in an open field at the end of three snow deposition events. Snow samples were then continually collected every 12 hours for a 48-hour time period after the initial sample collection. Gaseous atmospheric Hg^0 samples of 12-hour duration were collected concurrently with snow and changed every 12 hours to monitor changes in Hg isotopic composition. Each 48-hour period constitutes one time series, and three time series were collected at the Dexter site. The first time series (DTS_1) collection began at sundown (5:45pm EST) on January 28th, 2019 and proceeded until January 30th at sundown (5:45pm EST). This time series was collected during a polar vortex, when a large area of cold, low pressure air expanded southward, bringing airmasses from the Arctic region (Butler et al., 2020; Schoeberl et al., 1992). The second time series (DTS_2) collection began on February 18th, 2019 at sunrise (7:30am EST) and proceeded until February 20th at sunrise (7:30am EST). In addition to the collection of the final surface snow sample during the second time series, a sample was collected from the top to the bottom of the snowpack and is referred to as a

"snowpack" sample. The third time series (DTS_3) collection began on February 27th, 2019 at sundown (6:20pm EST) and proceeded until March 1st at sundown (6:20pm EST). The final snow sample was not collected on March 1st at sundown because all of the snow had melted.

The second snow collection site is located at UMBS in Pellston, Michigan (45°33'41.40"N, 84°40'45.64"W). The UMBS site has been a part of the Mercury Deposition Network (MDN) since 2013, where precipitation samples have been collected for Hg concentration analysis. A similar sampling scheme as that in Dexter was employed in Pellston; however, Hg^0 sampling was not feasible. A total of two time series were collected in Pellston. The first time series (PTS_1) collection began on February 13th, 2019 at sunrise (7:45am EST) and proceeded through February 15th at sunrise (7:45am EST). Each sample in this time series was treated as a fresh snow sample as it continuously snowed through this time interval. This time series (PTS_1) was therefore used to characterize the Hg isotopic variation of fresh snow during a long duration snow event. The second time series (PTS_2) collection began on February 15th, 2019 at sundown (6:10pm EST) and proceeded until February 17th at sunrise (7:40am EST). At the time of the final surface snow collection, a snowpack sample was also collected. The initially deposited snow sample for this time series was not retained.

4.2.2 Sample Collection

4.2.2.1 Hg^0 Collection

To collect Hg^0, ambient air was pulled through a manifold outfitted with 8 gold-coated bead traps in parallel at a rate of 1.8 L/gold trap for 12 hours (Kurz et al., 2020). A quartz filter was placed upstream of each gold bead trap to prevent particles from accumulating on the gold traps. Gold traps were wrapped in heat tape and kept at a temperature of 50°C to prevent condensation. A dry test meter (Schlumberger, Gallus 2000) connected in the sampling train was

used to measure the volume of air drawn through the manifold. For comparison with previously published Hg^0 samples, air volumes were corrected to standard temperature and pressure using the method outlined by the EPA Compendium Method IO-2.4. After sample collection, gold bead traps were wrapped in Teflon tape, triple bagged and stored in a clean cooler. Samples were then transported to the University of Michigan for processing.

4.2.2.2 Snow Collection

Snow samples were collected from the top 5 cm of the snowpack. In addition, one entire snowpack sample (vertically integrated) was collected at each site from the top to the base of the snowpack. Collection was carried out with acid cleaned plastic scoops. Samples were collected into 20 L Teflon bags with Teflon closures. Teflon bags were cleaned with a 10% HNO_3 solution prior to collection. For sufficient sample volume, 2 Teflon bags were filled for each sample. Teflon bags containing snow samples were placed in individual coolers and transported to the University of Michigan where they were stored in a freezer (-20°C) until processing.

4.2.3 Sample Processing

4.2.3.1 Hg^0 Sample Processing

In the laboratory at the University of Michigan, each Hg^0 sample consisting of 8 gold bead traps was heated to 500°C over a 4-minute period and carried in a stream of gold filtered argon to a single analytical gold trap (diatomaceous earth coated in gold). The analytical gold trap was subsequently heated in a stepwise manner to 550°C over a 3.5-hour period. Desorbed Hg was carried in a stream of gold filtered argon and bubbled through a trap containing 24g of 1% $KMnO_4$ solution dissolved in 10% H_2SO_4, hereafter referred to as 1% $KMnO_4$. Samples were analyzed for total mercury (THg) via cold vapor atomic fluorescence spectroscopy (CV-AFS) to

determine the initial Hg concentration. A secondary processing step was performed on Hg^0 samples where each sample was partially reduced with a 30% solution of hydroxylamine hydrochloride equal to 2% of the sample weight. Samples were then reduced with 20% $SnCl_2$ and bubbled through a fresh 1% $KMnO_4$ solution with a volume of 5.5g. This step was performed to remove potential matrix interferences and pre-concentrate samples prior to isotopic analyses. Samples were again analyzed for THg by CV-AFS and recoveries ranged from 96.1 to 103.6% with an average of 99.0±2.0 (1SD, n=12). UM Almaden was reduced with 20% $SnCl_2$ and loaded onto gold bead traps and processed in the same manner as Hg^0 samples for quality control. UM Almaden recoveries ranged from 96.9 to 100.7% with an average of 98.5±1.7% (1SD, n=4).

4.2.3.2 Snow Sample Processing

Snow samples were removed from the freezer and allowed to melt at room temperature. Samples were then filtered through 0.45 μm cellulose nitrate filters (Thermo Scientific) and transferred into pre-cleaned 1 L Pyrex bottles. Individual snow samples consisted of between 3 and 16 L of melted snow. Each bottle was brought to 1% BrCl and sealed tightly before being placed on a hotplate and heated to 90°C. Bottles were left on the hot plate for one week to allow for oxidation of Hg and break down of organic material that could create matrix effects during analyses. After one week on the hotplate, each individual bottle was analyzed for THg via CV-AFS. To quantify matrix effects, 4 separate aliquots from each bottle were analyzed for THg consisting of 1 ml, 2 ml, 4 ml and 2 ml + 25 pg spike of the Hg standard reference material NIST 3133.

Snow samples were concentrated using an anion exchange resin method adapted from Štrok et al (2014) and previously described in Washburn et al (2018) (Štrok et al., 2014;

Washburn et al., 2018). Prior to sample processing, 5 g of AG 1x4 resin (Biorad, 200-400 mesh) was weighed into a 40 ml glass ICHEM vial. The vial was then filled with 4M trace metal grade HNO_3 and placed on a rocker table to mix for 10 minutes. The vial was then vigorously shaken and allowed to sit for 20 minutes while the resin settled. The vial was then decanted and refiled with 4M HNO_3. The above steps were repeated 5x and then the vial was allowed to sit overnight before a final decanting.

For sample processing, 1.5 ml of resin was pipetted into a clean column. The bottom of the column was attached to a peristaltic pump (Fisher Scientific GP1000) to draw liquid through the column. To prepare the resin, reagents were pumped through the resin as follows: 40 ml of 4M HNO_3, 80 ml of deionized water (DI), and 80 ml of 0.1M HCl. Once the resin was prepared, each sample (up to 16L) was pumped through the column at a flowrate of 2 to 3.5 L/h. After the final bottle of each sample was completed, reagents were again pumped through the resin as follows: 40 ml of 0.1M HCl followed by 80 ml of DI. The peristaltic pump was detached from the column and a clean 40ml vial was placed beneath the column. A solution of 0.5% L-cysteine dissolved in 1% sodium citrate was used as the eluent. Ten ml of the L-cysteine solution was added to the column and allowed to gravity drip into the 40 ml vial, eluting the sample. After 30 minutes, the remaining solution was evacuated from the column into the vial using a 5-ml pipettor before adding concentrated bromine chloride to the vial equal to 2% of the sample weight. Samples were analyzed for THg via CV-AFS and recoveries from the anion exchange column process were calculated and had an average of 95.2±6.1% (1SD, n=25). UM Almaden standards prepared and processed through the anion exchange column had an average recovery of 97.0±4.1% (1SD, n=4).

Similar to Hg^0 processing, concentrated snow Hg samples were partially reduced with 30% hydroxylamine hydrochloride prior to reduction with 20% $SnCl_2$ and transferred into a fresh 5.5 g trap of 1% $KMnO_4$. Samples were then analyzed for THg by CV-AFS and sample recoveries were calculated yielding an average recovery of 96.0±5.0% (1SD, n=25).

4.2.3.3 Particulate Sample Processing

The particles retained from the filtering of snow samples were processed and analyzed for Hg isotopic composition following methods previously described in Demers et al (2013). Briefly, the cellulose nitrate filters loaded with retained particles were placed into a two-stage combustion furnace. The first furnace was ramped to 750°C over a 6-hour period with the second furnace held at 1000°C. Hg-free O_2 carried the released Hg and it was then bubbled through a 24 g trap of 1% $KMnO_4$. Due to the small amount of Hg, we were unable to analyze an aliquot of each sample via combustion followed by atomic absorption spectrometry. To monitor combustion efficiency, Montana soil (NIST 2711) was prepared, combusted, and analyzed for THg via CV-AFS. Combustion recoveries for Montana soil ranged from 99.2 to 103.0% with an average of 101.5±1.8% (1SD, n=4). Following combustions, samples were partially reduced with 30% hydroxylamine hydrochloride prior to THg analysis by CV-AFS. Samples were then subjected to a secondary transfer as described above into a fresh 1% $KMnO_4$ trap. Recovery of samples ranged from 90.3 to 99.5% with an average of 97.0±2.1% (1SD, n=24).

4.2.4 Sample Hg Isotope Analysis

Samples were analyzed for Hg isotopic composition via cold vapor multiple collector inductively coupled mass spectrometry (CV-MC-ICP-MS, Nu Plasma, Nu Instruments). Sample solutions were partially reduced with 30% hydroxylamine hydrochloride at 2% of the sample

weight and diluted to 0.18 to 4.98 ng Hg/g sample solution with a similarly reduced 1% $KMnO_4$ solution. Hg was introduced into the mass spectrometer by reducing samples with 2% $SnCl_2$ in a liquid-gas separator and the Hg^0 was subsequently swept into the instrument in a stream of argon. Simultaneously, a thallium standard (NIST 997) used for mass bias correction was introduced into the gas-liquid separator as a dry aerosol. Strict sample-standard bracketing was employed using NIST 3133 matched to sample concentrations ±5%.

Mercury stable isotope compositions are reported in permil (‰) using delta notation ($\delta^{xxx}Hg$) relative to NIST 3133 (eq. 1). Mass dependent fractionation is denoted as $\delta^{202}Hg$ based on the $^{202}Hg/^{198}Hg$ ratio. Mass dependent fractionation is reported using capital delta notation ($\Delta^{xxx}Hg$; eq. 2), which is based on the deviation from the expected mass dependent fractionation using the kinetic fractionation law. For values <10‰, Blum and Bergquist (2007) calculated β values for $\Delta^{199}Hg$, $\Delta^{200}Hg$, $\Delta^{201}Hg$, and $\Delta^{204}Hg$ of 0.252, 0.502, 0.752, and 1.493 respectively (Blum and Bergquist, 2007).

$$\delta^{xxx}Hg\ (‰) = \{[(^{xxx}Hg/^{198}Hg)_{unknown}/(^{xxx}Hg/^{198}Hg)_{NIST3133}]-1\} \times 1000 \quad (1)$$

$$\Delta^{xxx}Hg\ (‰) = \delta^{xxx}Hg - (\delta^{202}Hg \times \beta) \quad (2)$$

For each sample type, field blanks and process blanks were collected to characterize the blank contributions. For particulate and snow samples, we used field blanks (one from each site) which are higher than the process blanks and therefore a more conservative representation of the blank. Particulate field blanks yielded an average of 108.2±9.0 pg (1SD, n=2), while snow field blanks yielded an average of 173.4±18.4 pg (1SD, n=2). Hg^0 field blanks and process blanks were similar for THg and were therefore combined to calculate an average blank of 91.9±6.8 pg

(1SD, n=3). For the lowest concentration sample analyzed, blanks contribute less than 5% of THg and therefore are considered negligible.

Due the variable concentration of samples analyzed on the CV-MC-ICP-MS and the variable magnitude of analytical errors associated with samples analyzed at a given concentration, we assign analytical errors to samples as follows. Analytical error for each isotope ratio is assigned based on the larger value of the 2SD of the secondary reference material UM Almaden or the 2SE of process reference materials prepared alongside samples. We binned these samples incrementally with the following ranges: 0-0.5ppb, 0.5-1ppb, 1-2ppb, 2-3ppb, 3-4ppb and 4-5ppb (Table 4.1). Samples run between 0.18 and 0.5 ppb are assigned the 2SE of Montana soil for all isotope values except for δ^{202}Hg as follows: 0.46‰, 0.13‰, 0.16‰, and 0.16‰ for Δ^{204}Hg, Δ^{201}Hg, Δ^{200}Hg, and Δ^{199}Hg respectively. Analytical uncertainty for δ^{202}Hg is calculated as the 2SE of UM Almaden process standards: 0.21‰. Samples run between 0.5 and 1.0 are assigned the 2SD of Almaden for all isotope ratios as follows: 0.19‰, 0.13‰, 0.12‰, 0.03‰, and 0.14‰ for δ^{202}Hg, Δ^{204}Hg, Δ^{201}Hg, Δ^{200}Hg, and Δ^{199}Hg respectively. Samples run at concentrations between 1 and 2 ppb are assigned the 2SE of process Almaden for all isotope ratios except Δ^{204}Hg as follows: 0.15‰, 0.06‰, 0.06‰, and 0.06‰ for δ^{202}Hg, Δ^{201}Hg, Δ^{200}Hg, and Δ^{199}Hg respectively. For Δ^{204}Hg, samples are assigned the 2SD of Almaden with a value of 0.15‰. Samples run at concentrations between 2 and 3 ppb are assigned the 2SE of Montana soil as follows: 0.10‰, 0.07‰, 0.06‰, 0.12‰, and 0.11‰ for δ^{202}Hg, Δ^{204}Hg, Δ^{201}Hg, Δ^{200}Hg, and Δ^{199}Hg respectively. Samples run between 3 and 4 ppb are assigned the 2SD of Almaden as follows: 0.13‰, 0.12‰, 0.05‰, 0.06‰, and 0.05‰ for δ^{202}Hg, Δ^{204}Hg, Δ^{201}Hg, Δ^{200}Hg, and Δ^{199}Hg respectively. Samples run between 4 and 5 ppb are assigned the 2SE of Montana soil for all isotope ratios except for δ^{202}Hg and Δ^{199}Hg as follows: 0.06‰, 0.02‰, and 0.04 for Δ^{204}Hg,

Δ^{201}Hg, and Δ^{200}Hg respectively. For δ^{202}Hg and Δ^{199}Hg, samples are assigned the 2SD of Almaden with values of 0.10‰ and 0.04‰ respectively.

4.2.5 Atmospheric Transport

HYbrid Single-Particle Lagrangian Integrated Trajectory (HYSPLIT) models were run to assess air mass origin for all snow samples collected at both the Dexter and Pellston sampling sites. The National Oceanic and Atmospheric Administration (NOAA) HYSPLIT model was run using archived North American Meteorology (NAM) data with a grid resolution of 12 km x 12 km. Back trajectories with 72-hr durations were calculated every 12 hours at the mid-time of each sample with starting heights of 500, 1000, and 1500 m above ground level. The 72-hr duration of back trajectories was chosen to provide a comprehensive assessment of the origin of each air mass. Back trajectories for each fresh snow sample are displayed in Figure 4.1.

4.2.6 Statistical Analyses

Sample means of THg and all isotopic compositions were compared using t-tests with equal variance at the 95% confidence interval. Regression analyses comparing Hg isotopic compositions were calculated using a York regression (York, 1968). RStudio (Version 1.2.5001, © 2009-2019 RStudio, Inc.) was employed for all statistical analyses.

4.3 Results and Discussion

For discussion of snow samples, we categorize samples as ***fresh snow*** (the first sample deposited for each time series and all of PTS_1), ***aging snow***, and ***final snow*** (the two snowpack samples). As PTS_1 consists only of fresh snow and the PTS_2 fresh snow sample was not retained, these data are not discussed in terms of aging but are included in their respective categories of fresh, aging, and final snow. We frame our discussion based on the difference in

Hg isotopic composition between freshly fallen snow and aged snow, and we explore the processes and mechanisms that may control changes in THg, MDF, odd-MIF, and even-MIF measured in snow. For brevity, we use Δ^{199}Hg to discuss the magnitude of odd-MIF and Δ^{200}Hg to discuss the magnitude of even-MIF. Finally, we discuss the implications of the isotopic composition of Hg deposited to terrestrial and aquatic ecosystems based on the snowpack samples that we analyzed.

4.3.1 Air Mass Back Trajectories

The back trajectory for DTS_1 indicates the air mass originated over the Pacific Ocean off the west coast of Canada before it traveled southeast across Canada (Figure 4.1). The air mass then crossed the US border over Montana and generally traveled southeast before arriving at the Dexter sampling site. The DTS_2 airmass originated over continental Canada, southwest of Hudson Bay, and then traveled southeast before it arrived at the Dexter sampling site. The DTS_3 air mass had a similar origin and trajectory to that of DTS_2. The air masses for PTS_1_1, PTS_1_2 and PTS_1_3 all had similar origins and trajectories. They originated to the northeast of the sampling site, over Quebec, Canada, just south of the Hudson Strait and traveled over Lake Superior before they arrived at the Pellston sampling site. The PTS_1_4 airmass originated over the southern tip of Hudson Bay and traveled southwest over the north shore of Lake Superior before it traveled southeast to the Pellston sampling site. Finally, the PTS_1_5 airmass originated over Idaho and traveled to the southeast over Tennessee before it turned northward and arrived at the Pellston sampling site.

4.3.2 THg in Snow

Measured THg in snow samples are listed in Table 4.2 and plotted versus time since snowfall on Figure 4.2A and Figure 4.2E for the Dexter and Pellston sites, respectively. Snow

from DTS_1 and DTS_2 was deposited with THg of 0.90 and 0.55 ng/L, respectively. DTS_1 was relatively invariant in THg for the first 36 hours, after which it increased to 1.75 ng/L at the 48 hour sampling. DTS_2 decreased steadily in THg to 0.60 ng/L at 48 hours. Finally, DTS_3 was deposited with THg of 1.6 ng/L and generally decreased to 1.1 ng/L in the final sample collected at 36 hours. PTS_1 fresh snow ranged from 0.63 to 1.17 ng/L, whereas PTS_2 snow measured at 12 hours had THg of 1.28 ng/L, decreased to 0.85 ng/L at 24 hours and then increased to 1.14 ng/L at 36 hours.

The collected snow samples represent the net change in deposition and re-emission of Hg over 12-hour periods. Decreases in THg can be due to Hg^{2+} reduction to Hg^0 and subsequent volatilization and loss from the snowpack. Increases in THg result from Hg deposition to the snowpack or water loss from melting or sublimation of snow. However, during all of the time series, temperatures only reached values above freezing on March 1st, the final day of DTS_3.

The THg measured in fresh snow was similar to snow collected for Hg isotopes from a rooftop in Peterborough, Ontario, Canada (avg. = 1.55±0.82ng/L, 1SD, n=4) (Chen et al., 2012). In contrast, THg measured in fresh snow is significantly lower than THg previously reported for wet precipitation at both Pellston and Dexter ($p<0.05$) (avg. = 14.84±8.96 ng/L, 1SD, n=17) (Gratz et al., 2010; Sherman et al., 2015). It has been suggested that aerosols in rain droplets are more efficient at scavenging Hg from the atmosphere as compared to snow crystals (Mason et al., 1997). Additionally, colder temperatures in the atmosphere could hinder conversion of Hg^0 to Hg^{2+} causing lower THg in snow than wet precipitation (Landis et al., 2002; Mason et al., 2000).

4.3.3 MDF in Snow

Measured values for $\delta^{202}Hg$ in snow are listed in Table 4.2 and plotted versus time since snowfall on Figure 4.2B and Figure 4.2F for Dexter and Pellston, respectively. DTS_1 snow was

deposited with a δ^{202}Hg value of 0.32±0.13‰ and generally decreased to -0.03±0.13‰ at 36 hours before increasing to 0.10±0.10‰ at 48 hours. Both DTS_2 and DTS_3 generally increased through time with deposited values of -0.03±0.13‰ and 0.17±0.10‰, respectively. δ^{202}Hg values increased to 0.52±0.13‰ at 48 hours for DTS_2 and 0.28±0.10‰ at 36 hours for DTS_3. Fresh snow from PTS_1 was deposited with δ^{202}Hg ranging from -0.05±0.10‰ to 0.25±0.13‰. Snow from PTS_2 had a δ^{202}Hg value of 0.16±0.13‰ at 12 hours and then decreased to -0.08±0.13‰ at 24 hours before increasing to 0.14±0.10‰ at 36 hours.

Particles filtered from each snow sample were consistently lower in δ^{202}Hg than their accompanying melted and filtered snow (avg. = -0.38±0.27‰, 1SD, n=23) (Figure 4.3 and Figure 4.4). Due to the short atmospheric lifetime of $Hg^{2+}_{(p)}$, the Hg isotopic composition of the particle Hg may be dominated by local and regional sources, whereas the Hg associated with the snow may reflect long range transport of Hg with a different isotopic composition, similar to previous observations for filtered wet precipitation (S. Yuan et al., 2018). It is also possible that equilibrium fractionation during sorption of Hg^{2+} from the atmosphere onto snow and particles causes the Hg^{2+} sorbed to the particles to have more negative δ^{202}Hg. This is consistent with the experimental observation that when Hg^{2+} in solution is sorbed to thiols and goethite, the sorbed Hg has δ^{202}Hg values that are -0.30 to -0.62‰ lower than those in solution (Jiskra et al., 2012; Wiederhold et al., 2010).

When considering changes in δ^{202}Hg as snow ages for each individual time series, DTS_1 δ^{202}Hg progresses towards generally lower values, whereas all other time series progress towards generally higher values (Figure 4.2B). Based on published Hg isotope fractionation experiments we suggest that photooxidation of Hg^0 by Cl is the only reaction identified that could deplete δ^{202}Hg in the Hg^{2+} product (G. Sun et al., 2016). This suggests that Cl mediated photooxidation is

a more important process in the polar vortex time series than in the other time series. In contrast, the enrichment in δ^{202}Hg as snow ages in all other time series is likely due to photoreduction of Hg^{2+}, which results in the preferential removal of the light isotopes as they are reduced and lost from the snowpack. Other diagnostic isotope ratios including odd-MIF are useful in determining dominant reaction pathways and will be discussed below.

When comparing δ^{202}Hg values of snow from this study to results from previous studies of snow in Peterborough, ON and wet precipitation from Dexter and Pellston, we find that snow from our study (avg. = 0.16±0.17‰,1SD, n=24) has statistically more positive ($p<0.05$) δ^{202}Hg (wet precipitation avg. = -0.28±0.21‰ and Peterborough snow avg. = -0.98±0.66‰, 1SD, n=17 and n=4) (Chen et al., 2012; Gratz et al., 2010; Sherman et al., 2015) (Figure 4.5). Lower δ^{202}Hg measured in atmospheric Hg is often associated with anthropogenic emissions (Demers et al., 2015; Sherman et al., 2012; Sun et al., 2013). Additionally, the previously measured wet precipitation from Dexter and Pellston was not filtered. If the particles in those samples carried negative δ^{202}Hg similar to what we find in this study, the bulk precipitation samples might be shifted toward lower δ^{202}Hg values (Gratz et al., 2010; Sherman et al., 2015).

4.3.4 Odd-MIF in Snow

Measured Δ^{199}Hg values in snow samples are listed in Table 4.2 and plotted versus time since snowfall on Figure 4.2C and Figure 4.2G. DTS_1 snow was deposited with Δ^{199}Hg of 0.55±0.14‰ and then increased to 0.75±0.11‰ at 12 hours. It then decreased to -0.45±0.11‰ at 24 hours, increased to 0.00±0.11‰ at 36 hours before finally decreasing to a final value of -0.85±0.05‰ at 48 hours. Both DTS_2 and DTS_3 generally increased through time with deposited values of 0.88±0.11‰ and 1.20±0.04‰, respectively. Δ^{199}Hg increased to 1.77±0.11‰ at 48 hours for DTS_2 and 2.73±0.05‰ at 36 hours for DTS_3. Fresh snow from

PTS_1 was deposited with Δ^{199}Hg ranging from -0.31±0.11‰ to 1.71±0.11‰. Snow from PTS_2 had a Δ^{199}Hg value of 0.43±0.13‰ at 12 hours and generally increased to 0.85±0.05‰ at 36 hours.

During PTS_1 (a single long duration snow event that encompasses the whole time series) three samples (PTS_1_Snow_1,2,3) displayed negative Δ^{199}Hg (avg. Δ^{199}Hg = -0.27±0.04‰ 1SD, n=3). These samples are statistically different ($p<0.05$) from the two other snow samples collected during this event (PTS_2_Snow_4,5) (avg. Δ^{199}Hg = 1.23±0.67‰ 1SD, n=2). This is likely due to the difference in the origin and trajectory of the air masses prior to arriving at the sample site, described in section 4.3.1 and displayed in Figure 4.1. The differences in air mass origin and trajectory are likely to have different sources of Hg, which may have had distinct isotopic compositions. Air mass trajectories may also control differences in oxidants and ligands associated with Hg within the air masses. Interestingly, the Δ^{199}Hg of PTS_1_Snow_ 1,2,3 are indistinguishable from Hg^0 samples collected at Dexter (avg. Δ^{199}Hg = -0.22±0.05‰ 1SD, n=11). Hg^0 samples reported in this study are isotopically similar to previously measured Hg^0 samples at background sites in the Great Lakes region (avg. δ^{202}Hg = 0.39±0.38‰ and avg. Δ^{199}Hg = -0.16±0.05‰, 1SD, n=9) (Demers et al., 2013; Gratz et al., 2010). Therefore, if we assume that Hg^0 has a similar isotopic composition in Pellston as in Dexter, this may point to a possible influence from Hg^0 deposition to snow by the reactive surface uptake of Hg^0 from the atmosphere. Previous studies have observed an offset in δ^{202}Hg between Hg^0 in the atmosphere and Hg measured in vegetation and snow with little to no associated MIF (Demers et al., 2013; Douglas and Blum, 2019). While the magnitude of the δ^{202}Hg offset observed in this study (-0.52‰) (Figure 4.5) is lower than that observed in previous studies (~2‰), we suggest this may be due to the reaction time as the magnitude of MDF has been shown to increase with increasing

time (W. Yuan et al., 2018). In contrast, the two samples (PTS_1_Snow_4,5) with positive Δ^{199}Hg have drastically different air mass origins and trajectories from PTS_1_Snow_1,2,3 and from each other. Previous studies have suggested positive Δ^{199}Hg in atmospheric samples is likely due to long range transport of Hg and is controlled by photoreduction of Hg^{2+} in the atmosphere prior to deposition (Chen et al., 2012; Yuan et al., 2015). We suggest this process is the most likely cause for the Δ^{199}Hg observed in PTS_1_Snow_4,5. These observations of contrasting Hg isotopic compositions in fresh snow collected during a single long duration snow event highlight the importance of air mass origins and trajectories likely controlling the associated oxidants and binding ligands mediating Hg redox reactions in the atmosphere.

When comparing the Δ^{199}Hg values measured in snow to both previously collected snow from Peterborough, ON and wet precipitation at Dexter and Pellston, most of the snow, both fresh and aged, has either more positive or more negative Δ^{199}Hg (Figure 4.5). However, the average Δ^{199}Hg measured in fresh snow (avg. = 0.54±0.75‰, 1SD, n=8) is statistically indistinguishable from the average for wet precipitation from Dexter and Pellston (Figure 4.5) and snow from Peterborough, ON (wet precipitation avg. = 0.29±0.15‰ and snow = 0.31±0.43‰, n=17 and n=4). The Hg isotopic composition of the snow (in contrast to rain) deposited to the land surface may not reflect the Hg that is eventually incorporated into ecosystem reservoirs as it may undergo further fractionation before melting. This is reflected in the statistical difference between aging snow (avg. = 0.93±0.98‰, 1SD, n=13) and wet precipitation and final snow (avg. = 2.54±1.37‰, 1SD, n=2) as compared to wet precipitation (both $p<0.05$). This is likely due to the additional photoreduction that Hg in the snowpack undergoes after deposition and has important implications for ecosystem endmember characterization (discussed further in Section 4.3.6).

As indicated above, the evolution of Δ^{199}Hg in snow as snow ages is not consistent between time series. The first time series collected at the Dexter site (DTS_1) provided a unique opportunity to collect snow during a polar vortex. This time series differs from all others in that as snow ages, Δ^{199}Hg trends towards more negative values (linear regression slope = -0.03±0.01, r^2=0.70, p<0.05) (Figure 4.2C). The Δ^{199}Hg of snow in all of the other time series trend towards more positive values (all $r^2 > 0.72$ and $p < 0.05$) (Figure 4.2C). We suggest this difference in the direction of odd-MIF fractionation is due to differences in the oxidants and binding ligands in the snow. We further suggest that Hg deposition during the polar vortex is mediated by halogen oxidants similar to Arctic snow, due to the similarity in direction and magnitude of odd-MIF changes observed in the snow (Sherman et al., 2010).

Snow studied previously in Utqiagvik, Alaska acquired unique Hg isotopic compositions during AMDEs (Sherman et al., 2010). In the polar spring time, Hg^0 is stripped from the atmosphere and deposited to the snowpack through photooxidation with Br and BrO (Wang et al., 2019). The initial isotopic signature in this snow is observed to have slightly more negative Δ^{199}Hg than the atmospheric Hg^0. As the snow is exposed to sunlight, Hg^{2+} is photoreduced to Hg^0 and emitted back to the atmosphere and the snow Δ^{199}Hg becomes more negative. This process is unique to coastal areas with an ample supply of atmospheric halogen oxidants. Obrist et al. (2017) sampled snow on a transect from the northern Alaska coast southward, and found that the further from the coast the less influence from AMDEs was observed in the Hg isotopic composition of the snow. The initial isotopic composition of the snow from the polar vortex time series is more positive than Arctic snow deposited during AMDEs, and the magnitude of change is smaller than that observed in the Arctic, but the isotopic trends are similar.

Previous studies have indicated that oxidant concentrations may at times be elevated in the Great Lakes region with sources from Hudson Bay and the Great Lakes (Carignan and Sonke, 2010; May et al., 2018). This may provide an opportunity far from the Arctic coast for similar Hg fractionation trends to be observed in snow at mid-latitudes and is supported by the consistent air mass trajectories originating at the southern tip of Hudson Bay during the polar vortex following initial deposition. When we regressed δ^{202}Hg vs. Δ^{199}Hg for the polar vortex samples (snow, particles, and Hg^0), we calculated a slope of -3.32±1.19 (r^2=0.10, $p<0.05$). This slope is similar to that derived from Sherman et al. (2010) (-3.44±0.70), which is unique to AMDE snow. We therefore suggest that the polar vortex time series reflects halogen mediated redox reactions similar to those observed in Arctic snow based on the evolution of the measured Hg isotopic composition of snow as it ages. However, the r^2 value for the δ^{202}Hg vs. Δ^{199}Hg regression is low, suggesting that the correlation between δ^{202}Hg and Δ^{199}Hg cannot be fully explained by halogen mediated photoreduction and that multiple oxidants, binding ligands, and other processes may be involved. Additionally, Sun et al. (2016) acknowledged that current photooxidation experiments published to date cannot explain the fractionation in AMDE snow and we suggest that additional photooxidation experiments, possibly involving heterogeneous reactions and other oxidants, may be needed to elucidate the fractionation mechanisms involved in the Hg isotopic evolution of AMDE snow.

All other time series collected at Dexter reveal significant increases in Δ^{199}Hg as snow is aged in sunlight (Figure 4.2C), attaining values as high as 3.51±0.14‰. The most likely explanation for the increase in Δ^{199}Hg is photoreduction of Hg^{2+}. When we regressed Δ^{199}Hg vs. Δ^{201}Hg for samples of each individual time series (including the polar vortex time series and both Pellston Time Series), we found a range in slopes with a minimum of 0.87±0.02 for DTS_1 and a

maximum of 1.18±0.02 for DTS_2 (avg. = 1.06±0.13, 1SD, n=5, all $p<0.05$, all $r^2>0.96$), which are indistinguishable from slopes calculated separately for only snow or for only particles. Additionally, when all samples measured in this study were regressed together on a plot of Δ^{199}Hg vs. Δ^{201}Hg (Figure 4.6) we calculated a slope of 1.09±0.01 ($p<0.05$, $r^2=0.99$), which is similar to the experimentally derived slope of 1.00±0.02 and indicates aqueous photochemical reduction of Hg^{2+} (Bergquist and Blum, 2007; Zheng and Hintelmann, 2010). This suggests that while on shorter timescales there are most likely a number of reactions driving the differences in the measured Hg isotopic composition of the snow overall, photochemical reduction of Hg^{2+} drives Hg fractionation in snow through time. Furthermore, a study that varied reaction conditions (pH, oxic/anoxic) and binding ligands in aqueous photochemical reduction experiments found a range in Δ^{199}Hg vs. Δ^{201}Hg slopes (0.85±0.12‰ to 1.34±0.03‰) (Motta et al., 2020). These results could explain the range in Δ^{199}Hg vs. Δ^{201}Hg slopes calculated for individual time series in this study, highlighting the importance of oxidants and binding ligands involved in these reactions and may account for the direction and magnitude of fractionation observed in snow.

4.3.5 Even-MIF in Snow

Measured Δ^{200}Hg values in snow samples are listed in Table 4.2 and plotted versus time since snowfall on Figure 4.2D and Figure 4.2H for Dexter and Pellston, respectively. DTS_1 snow was deposited with a Δ^{200}Hg value of 0.22±0.03‰ and generally decreased with time to 0.03±0.06‰ at 48 hours. DTS_2 snow was deposited with a value of 0.20±0.14‰, reached a maximum of 0.31±0.14‰ at 36 hours and then decreased to 0.12±0.14‰ at 48 hours. DTS_3 snow was deposited with Δ^{200}Hg of 0.15±0.04‰, reached a maximum of 0.30±0.04‰ at 36 hours and then generally decreased to 0.21±0.06‰ at 48 hours. Fresh snow from PTS_1 was

deposited with Δ^{200}Hg ranging from 0.02±0.14‰ to 0.29±0.08‰. Snow from PTS_2 had Δ^{200}Hg of 0.28±0.14‰ at 12 hours, increased to 0.33±0.14‰ at 24 hours and then decreased to 0.22±0.06‰ at 36 hours.

Even-MIF of Hg is thought to originate in the upper atmosphere due to photo-initiated oxidation of Hg^0 (Chen et al., 2012). Even-MIF has been induced experimentally during homogeneous reactions of Hg^0 with Cl, leaving the Hg^{2+} product with positive Δ^{200}Hg and the residual Hg^0 with negative Δ^{200}Hg (G. Sun et al., 2016). It has been suggested that there is no even-MIF produced at the Earth's surface, therefore, Δ^{200}Hg serves as a conservative tracer of upper atmospheric Hg. The low Δ^{200}Hg values observed in PTS_1_Snow_1,2,3 (avg. 0.07±0.04‰, 1SD, n=3) indicate mixing with a Hg source with low Δ^{200}Hg, further supporting the hypothesis that these samples are influenced by reactive surface uptake of Hg^0 from the atmosphere as discussed in section 4.3.4 (Hg^0 avg. Δ^{200}Hg = -0.09±0.04‰, 1SD, n=11). Additionally, the contrasting snow from PTS_1 (PTS_1_Snow_4,5) has statistically more positive Δ^{200}Hg values ($p<0.05$) (avg. 0.24±0.07‰, 1SD, n=2) than PTS_2_Snow_1,2,3. This supports the argument that PTS_1_Snow_4,5 are influenced by long range transport of Hg and highlights the importance of air mass origin and trajectory.

The fresh snow in DTS_1 has a high Δ^{200}Hg (0.22±0.03‰), indicating an upper atmospheric origin. Over time, the Δ^{200}Hg observed in DTS_1 decreased. We suggest this decrease was due to the oxidation of Hg^0 above the snowpack, yielding a Hg^{2+} product with lower Δ^{200}Hg as compared to the snow, and subsequent deposition of this Hg to the snowpack (Figure 4.2D). This further provides evidence for possible halogen mediated redox reactions during the polar vortex time series. None of the other time series indicate increasing or decreasing trends in Δ^{200}Hg as snow ages.

Overall, Δ^{200}Hg measured in snow in this study (avg. = 0.19±0.09‰, 1SD, n=24) is similar to values previously reported in wet precipitation from Dexter and Pellston (avg. = 0.18±0.08‰, n=17) (Gratz et al., 2010; Sherman et al., 2015) but are not similar to snow from Peterborough, ON ($p<0.05$) (avg. = 0.83±0.47‰, n=4) (Chen et al., 2012). Chen et al. (2012) measured Δ^{200}Hg values up to 1.24‰ in snow and suggested that stratospheric incursions caused influence from polar air masses, bringing large Δ^{200}Hg anomalies. Through measurements of Hg^0 in free tropospheric airmasses, Kurz et al. (2020) suggested that these large Δ^{200}Hg anomalies were due to stochastic processes and are rarely captured in measured samples. Results from the current study agree with this hypothesis as Δ^{200}Hg measured during the polar vortex and throughout the entire sampling period reached values only up to 0.33±0.14‰. Our results are consistent with previous wet precipitation measurements and a York regression of Δ^{204}Hg vs. Δ^{200}Hg indicates a slope of -0.73±0.09 (Figure 4.7), similar to the slope for previously measured atmospheric samples (approximately -0.5; Blum and Johnson, 2017). Even-MIF measured in snow indicates a small but discernable contribution of Hg from the upper atmosphere where even-MIF is suggested to occur.

4.3.6 Hg Isotopic Composition of Snow Deposited to Terrestrial and Aquatic Ecosystems

In this study, we characterized the Hg isotopic composition of Hg that is likely to be incorporated through snowfall into natural ecosystem reservoirs as inferred from analyses of two full-snowpack samples. These samples average over multiple snow events and are therefore more likely to be representative of the Hg isotopic composition of seasonal snowmelt. The Hg isotopic characterization of this endmember is as follows: δ^{202}Hg = 0.23±0.21‰, Δ^{199}Hg = 2.54±1.37‰, Δ^{201}Hg = 2.15±1.22‰, Δ^{200}Hg =0.28±0.03‰, and Δ^{204}Hg = -0.36±0.03‰ (1SD, n=2). Douglas and Blum (2019) measured seasonal snowmelt in Alaska and concluded that the

Hg isotopic composition of the meltwater did not reflect the AMDE snow but rather the reactive surface uptake of Hg^0 from the atmosphere. The snowmelt Hg isotopic values were shown to control the isotopic composition added seasonally to the soils and vegetation. This characterization was critical as it allowed for estimation of the amount of AMDE mercury re-emitted to the atmosphere and provided an endmember characterization of the Hg isotopic composition of snowmelt incorporated into natural reservoirs.

In previous ecosystem studies, including one conducted in Pellston (Kwon et al., 2015), measurements of inorganic Hg sources and biota containing a range of MMHg concentrations were analyzed with the goal of better understanding Hg sources to the aquatic and adjacent terrestrial ecosystems. In that study, wet precipitation measured in the Great Lakes region was used to help explain the shift in both $\delta^{202}Hg$ and $\Delta^{199}Hg$ between terrestrial soils and surface lake sediments. Kwon et al. (2015) had no information at the time of the study on the Hg isotopic composition of Hg deposited through snowfall. Considering an endmember of wet precipitation alone could not easily account for the isotopic shift between the soil and lake sediments. We suggest, however, that consideration of the isotopic composition of both wet precipitation (avg. $\delta^{202}Hg$ = -0.08±0.18‰ and avg. $\Delta^{199}Hg$ = 0.32±0.25‰, 1SD, n=4) and snowmelt (PTS_2_Snow_4_SP $\delta^{202}Hg$ = 0.08±0.19‰ and $\Delta^{199}Hg$ = 1.57±0.14‰) at Pellston could explain this isotopic shift and identify an important source of Hg to the aquatic ecosystem. We use rainfall and snowfall amounts and MDN data to estimate that between 20 and 45% of precipitation derived Hg is delivered through snowfall. We therefore estimate an isotopic endmember that, when added to terrestrial soil at Pellston, is better able to explain the isotopic shift between terrestrial soil and lake sediments than precipitation alone. This endmember would be approximately 19-45% snow and 55-81% wet precipitation. This combined precipitation

endmember is plotted on Figure 4.8, where it is evident that the consideration of snowmelt with a high Δ^{199}Hg value in the endmember calculation is specifically useful in explaining the positive shift in Δ^{199}Hg between terrestrial soil and lake sediments. This exercise highlights the utility of characterizing the Hg isotopic composition of snow at mid-latitudes as an input of Hg to terrestrial and aquatic ecosystems.

4.4 Conclusion

This study provides insight into the evolution of the Hg isotopic composition in aging snow at mid-latitudes and during long duration snow events. Fresh snow collected during a 48+ hour snow event revealed a significant range in odd-MIF and indicates sensitivity to air mass origins and the oxidants and binding ligands controlling redox reactions prior to deposition. Many freshly deposited snow samples also have more extreme odd-MIF values as compared to wet precipitation measured in North America. In a time series collected during a polar vortex, we documented progressively more negative odd-MIF, similar to AMDE snow observed in the Arctic, while other measured snow revealed increasing odd-MIF as the snow aged. We suggest that photoreduction of Hg^{2+} drives the observed isotopic fractionation and the differences in oxidants and binding ligands controls the direction and magnitude of fractionation. Finally, this study highlights the importance of snow measurements for the isotopic characterization of Hg that is deposited into forest and aquatic ecosystems and is available for methylation and ultimately the transfer to humans via fish consumption.

Funding

This research was funded by a University of Michigan MCubed Grant and by the John D. MacArthur Professorship.

Acknowledgements

The authors thank Adam Schubel for his assistance in sample collection at the UMBS. The authors gratefully acknowledge the NOAA Air Resources Laboratory (ARL) for the provision of the HYSPLIT transport and dispersion model and READY website (https://www.ready.noaa.gov) used in this publication.

Table 4.1 Summary of Hg isotopic composition results for standard and reference materials.

Run concentration denotes the concentration standard and reference materials were analyzed on the CV-MC-ICP-MS. For UM Almadèn, n1 denotes the number of isotope measurements and n2 denotes the number of analytical sessions. For reference materials, n1 denotes the number of process replicates and n2 represents the number of isotope measurements.

Run Concentration	Standard Reference Material	n1	n2	$\delta^{204}Hg$	2SD	$\delta^{202}Hg$	2SD	$\delta^{201}Hg$	2SD	$\delta^{200}Hg$	2SD	$\delta^{199}Hg$	2SD	$\Delta^{204}Hg$	2SD	$\Delta^{201}Hg$	2SD	$\Delta^{200}Hg$	2SD	$\Delta^{199}Hg$	2SD
0-0.5ppb																					
	Montana Soil	7	2	-0.25	0.20	-0.14	0.17	-0.33	0.26	-0.10	0.07	-0.29	0.21	-0.04	0.46	-0.22	0.13	-0.03	0.16	-0.25	0.16
	Process Almaden	3	1	-0.67	0.30	-0.50	0.21	-0.40	0.09	-0.21	0.07	-0.15	0.16	0.07	0.10	-0.03	0.07	0.04	0.08	-0.03	0.12
0.5-1ppb																					
	Almaden	6	1	-0.82	0.27	-0.53	0.19	-0.41	0.20	-0.25	0.10	-0.15	0.18	-0.03	0.13	-0.01	0.12	0.01	0.03	-0.02	0.14
	Montana Soil	13	2	-0.22	0.10	-0.15	0.07	-0.29	0.07	-0.07	0.03	-0.25	0.05	0.00	0.12	-0.18	0.03	0.00	0.02	-0.21	0.03
1-2ppb																					
	Almaden	6	1	-0.84	0.04	-0.56	0.13	-0.46	0.06	-0.26	0.06	-0.16	0.04	0.00	0.15	-0.04	0.04	0.02	0.03	-0.01	0.04
	Montana Soil	6	1	-0.28	0.06	-0.19	0.05	-0.34	0.08	-0.09	0.04	-0.28	0.05	0.01	0.02	-0.20	0.04	0.01	0.01	-0.23	0.03
	Process Almaden	6	2	-0.63	0.19	-0.41	0.15	-0.38	0.12	-0.19	0.11	-0.13	0.05	-0.01	0.10	-0.07	0.06	0.01	0.06	-0.03	0.06
2-3ppb																					
	Almaden	6	1	-0.80	0.17	-0.53	0.10	-0.44	0.09	-0.27	0.02	-0.16	0.04	0.00	0.05	-0.04	0.04	0.00	0.06	-0.03	0.05

	Process Almaden	1	1	-0.79	0.00	-0.58	0.00	-0.48	0.00	-0.31	0.00	-0.15	0.00	0.07	0.00	-0.04	0.00	-0.01	0.00	-0.01	0.00
	Montana Soil	3	1	-0.15	0.09	-0.13	0.10	-0.31	0.06	-0.11	0.14	-0.29	0.11	0.05	0.07	-0.21	0.06	-0.04	0.12	-0.26	0.11
3-4ppb																					
	Almaden	4	1	-0.80	0.14	-0.54	0.13	-0.44	0.06	-0.27	0.02	-0.16	0.02	0.01	0.12	-0.04	0.05	0.01	0.06	-0.02	0.05
	Process Almaden	1	1	-0.71	0.00	-0.47	0.00	-0.38	0.00	-0.24	0.00	-0.16	0.00	-0.01	0.00	-0.02	0.00	-0.01	0.00	-0.04	0.00
4-5ppb																					
	Almaden	6	1	-0.87	0.15	-0.59	0.10	-0.48	0.07	-0.29	0.04	-0.17	0.04	0.00	0.06	-0.04	0.01	0.00	0.04	-0.02	0.04
	Montana Soil	3	1	-0.25	0.06	-0.17	0.03	-0.31	0.04	-0.09	0.03	-0.27	0.02	0.00	0.06	-0.19	0.02	0.00	0.04	-0.23	0.03

Table 4.2 Sample THg and Hg stable isotope data for all particle (part), snow, and Hg^0 samples analyzed in this study. Hg isotope values are expressed in permil (‰). *Concentration expressed in ng/m^3.

Site/Time Series	Sample	Collection Date	Night/ Day	Min. Ambient Temp. (ºC)	Max. Ambient Temp. (ºC)	THg (ng/L)	$\delta^{204}Hg$	$\delta^{202}Hg$	2SD	$\delta^{201}Hg$	$\delta^{200}Hg$	$\delta^{199}Hg$	$\Delta^{204}Hg$	2SD	$\Delta^{201}Hg$	2SD	$\Delta^{200}Hg$	2SD	$\Delta^{199}Hg$	2SD
Dexter Time Series 1																				
	DTS_1_Part _1	1/28/19	Day			0.23	-0.30	0.05	0.17	0.34	0.25	0.23	-0.38	0.46	0.30	0.13	0.22	0.16	0.21	0.16
	DTS_1_Part_2	1/29/19	Night			0.25	-0.85	-0.49	0.17	-0.51	-0.08	-0.03	-0.12	0.46	-0.14	0.13	0.17	0.16	0.09	0.16
	DTS_1_Part _3	1/29/19	Day			0.77	-1.32	-0.83	0.19	-1.34	-0.33	-0.79	-0.08	0.13	-0.71	0.12	0.08	0.03	-0.58	0.14
	DTS_1_Part_4	1/30/19	Night			0.59	-1.08	-0.67	0.19	-1.18	-0.21	-0.64	-0.08	0.13	-0.68	0.12	0.13	0.03	-0.47	0.14
	DTS_1_Part_5	1/30/19	Day			1.34	-0.94	-0.60	0.13	-1.31	-0.19	-0.93	-0.05	0.15	-0.86	0.04	0.11	0.03	-0.77	0.04
	DTS_1_Snow_ 1	1/28/19	Day	-12.2	-3.2	0.93	0.20	0.32	0.19	0.73	0.38	0.63	-0.28	0.13	0.48	0.12	0.22	0.03	0.55	0.14
	DTS_1_Snow_2	1/29/19	Night	-9.9	-4.3	1.07	-0.25	0.04	0.13	0.63	0.16	0.76	-0.31	0.15	0.60	0.04	0.13	0.14	0.75	0.11
	DTS_1_Snow_3	1/29/19	Day	-14.3	-9.8	1.00	-0.19	0.01	0.13	-0.58	0.15	-0.46	-0.21	0.15	-0.59	0.04	0.14	0.14	-0.46	0.11
	DTS_1_Snow_4	1/30/19	Night	-22.3	-14.3	0.92	-0.25	-0.03	0.13	-0.14	0.14	0.00	-0.21	0.15	-0.12	0.04	0.15	0.14	0.00	0.11
	DTS_1_Snow_5	1/30/19	Day	-23.9	-19.3	1.80	0.08	0.10	0.10	-0.87	0.08	-0.83	-0.07	0.05	-0.95	0.04	0.03	0.06	-0.85	0.05
	DTS_1_Hg^0_ 1	1/28/19	Night			1.12*	0.68	0.38	0.10	0.06	0.08	-0.15	0.10	0.05	-0.23	0.04	-0.11	0.06	-0.24	0.05
	DTS_1_Hg^0_ 2	1/29/19	Day			1.29*	0.77	0.45	0.10	0.16	0.14	-0.10	0.09	0.05	-0.18	0.04	-0.09	0.06	-0.22	0.05
	DTS_1_Hg^0_ 3	1/29/19	Night			1.12*	1.09	0.66	0.10	0.25	0.22	-0.14	0.11	0.05	-0.24	0.04	-0.11	0.06	-0.31	0.05

Dexter Time Series 2																				
	DTS_2_Part _1	2/18/19	Night			0.49	-0.37	-0.02	0.19	0.23	0.20	0.30	-0.34	0.13	0.24	0.12	0.21	0.03	0.30	0.14
	DTS_2_Part_2	2/18/19	Day			0.38	-0.44	-0.15	0.19	-0.06	0.04	0.16	-0.21	0.13	0.06	0.12	0.11	0.03	0.20	0.14
	DTS_2_Part_3	2/19/19	Night			0.33	-0.29	-0.04	0.19	0.11	0.15	0.36	-0.23	0.13	0.14	0.12	0.17	0.03	0.37	0.14
	DTS_2_Part_4	2/19/19	Day			0.33	-0.22	-0.02	0.19	0.03	0.17	0.32	-0.19	0.13	0.04	0.12	0.18	0.03	0.32	0.14
	DTS_2_Part_5	2/20/19	Night			0.40	-0.23	-0.09	0.19	-0.10	0.08	0.15	-0.09	0.13	-0.03	0.12	0.13	0.03	0.18	0.14
	DTS_2_Part_ 6_SP	2/20/19				0.35	-0.24	0.00	0.19	0.27	0.15	0.55	-0.24	0.13	0.27	0.12	0.15	0.03	0.55	0.14
	DTS_2_Snow_1	2/18/19	Night	-8.3	-5.5	0.95	-0.37	-0.04	0.13	0.77	0.18	0.87	-0.31	0.15	0.80	0.04	0.20	0.14	0.88	0.11
	DTS_2_Snow_2	2/18/19	Day	-8.2	-1.9	0.66	0.08	0.26	0.13	1.23	0.36	1.28	-0.31	0.15	1.03	0.04	0.23	0.14	1.22	0.11
	DTS_2_Snow_3	2/19/19	Night	-17.6	-5.8	0.67	0.08	0.36	0.13	2.00	0.37	2.13	-0.46	0.15	1.73	0.04	0.19	0.14	2.04	0.11
	DTS_2_Snow_ 4	2/19/19	Day	-17.3	-0.5	0.57	0.24	0.39	0.13	1.72	0.51	1.82	-0.34	0.15	1.42	0.04	0.31	0.14	1.72	0.11
	DTS_2_Snow_5	2/20/19	Night	-8.8	-3.6	0.59	0.38	0.52	0.13	1.93	0.38	1.91	-0.40	0.15	1.54	0.04	0.12	0.14	1.77	0.11
	DTS_2_Snow_ 6_SP	2/20/19				0.68	0.19	0.38	0.19	3.30	0.45	3.61	-0.38	0.13	3.01	0.12	0.26	0.03	3.51	0.14
	DTS_2_Hg^0_ 1	2/18/19	Day			1.33*	0.77	0.40	0.13	0.13	0.13	-0.14	0.17	0.12	-0.17	0.05	-0.07	0.06	-0.24	0.05
	DTS_2_Hg^0_ 2	2/18/19	Night			1.27*	1.08	0.65	0.10	0.22	0.13	-0.15	0.11	0.05	-0.27	0.04	-0.19	0.06	-0.31	0.05
	DTS_2_Hg^0_ 3	2/19/19	Day			1.26*	0.96	0.57	0.13	0.22	0.20	-0.07	0.11	0.12	-0.20	0.05	-0.08	0.06	-0.22	0.05
	DTS_2_Hg^0_ 4	2/19/19	Night			1.26*	0.69	0.41	0.10	0.19	0.12	-0.09	0.09	0.05	-0.12	0.04	-0.08	0.06	-0.19	0.05
Dexter Time Series 3																				

	DTS_3_Part_1	2/27/19	Day			2.64	-0.24	0.06	0.10	-0.05	0.31	0.00	-0.33	0.06	-0.10	0.02	0.28	0.04	-0.01	0.04
	DTS_3_Part_2	2/28/19	Night			2.37	-0.21	0.11	0.10	-0.01	0.26	0.01	-0.37	0.06	-0.09	0.02	0.21	0.04	-0.01	0.04
	DTS_3_Part_3	2/28/19	Day			1.46	-0.15	0.04	0.13	-0.41	0.29	-0.18	-0.21	0.12	-0.44	0.05	0.27	0.06	-0.19	0.05
	DTS_3_Part_4	3/1/19	Night			2.13	0.06	0.24	0.13	0.00	0.38	0.14	-0.30	0.12	-0.19	0.05	0.26	0.06	0.08	0.05
	DTS_3_Snow_1	2/27/19	Day	-7.5	-3.9	1.60	-0.15	0.17	0.10	1.25	0.24	1.25	-0.40	0.06	1.13	0.01	0.15	0.04	1.20	0.04
	DTS_3_Snow_2	2/28/19	Night	-13.8	-5.8	1.51	-0.19	0.12	0.10	1.50	0.36	1.63	-0.37	0.06	1.41	0.01	0.30	0.04	1.60	0.04
	DTS_3_Snow_3	2/28/19	Day	-10.3	-1.9	0.87	0.13	0.33	0.13	2.35	0.36	2.43	-0.36	0.12	2.10	0.05	0.19	0.06	2.35	0.05
	DTS_3_Snow_4	3/1/19	Night	-12.9	-2.9	1.05	0.00	0.28	0.10	2.57	0.35	2.80	-0.41	0.05	2.36	0.04	0.21	0.06	2.73	0.05
	DTS_3_Hg^0_ 1	2/27/19	Day			1.19*	1.02	0.64	0.10	0.33	0.26	-0.02	0.06	0.05	-0.15	0.04	-0.06	0.06	-0.18	0.05
	DTS_3_Hg^0_ 2	2/28/19	Night			1.36*	0.90	0.55	0.13	0.24	0.20	-0.07	0.08	0.12	-0.18	0.05	-0.08	0.06	-0.21	0.05
	DTS_3_Hg^0_ 3	2/28/19	Day			1.01*	0.85	0.49	0.10	0.22	0.20	-0.06	0.13	0.05	-0.14	0.04	-0.05	0.06	-0.18	0.05
	DTS_3_Hg^0_ 4	3/1/19	Night			1.53*	0.83	0.50	0.13	0.21	0.20	-0.05	0.09	0.12	-0.16	0.05	-0.04	0.06	-0.17	0.05
Pellston Time Series 1																				
	PTS_1_Part_ 1	2/13/19	Night			0.15	0.00	0.25	0.17	-0.06	0.47	0.04	-0.37	0.46	-0.25	0.13	0.34	0.16	-0.03	0.16
	PTS_1_Part_ 2	2/13/19	Day			1.02	-0.62	-0.34	0.13	-0.72	-0.09	-0.53	-0.11	0.15	-0.46	0.04	0.08	0.03	-0.45	0.04
	PTS_1_Part_ 3	2/14/19	Night			0.57	-0.81	-0.37	0.19	-0.87	-0.10	-0.56	-0.25	0.13	-0.59	0.12	0.09	0.03	-0.46	0.14
	PTS_1_Part_5	2/15/19	Night			0.31	-0.69	-0.61	0.17	-0.65	-0.20	-0.44	0.22	0.46	-0.19	0.13	0.11	0.16	-0.28	0.16
	PTS_1_Snow_1	2/13/19	Night	-10.5	-6.5	0.72	-0.07	0.07	0.13	-0.11	0.05	-0.21	-0.17	0.15	-0.17	0.04	0.02	0.14	-0.23	0.11
	PTS_1_Snow_2	2/13/19	Day	-9.9	-7.6	1.17	-0.29	-0.03	0.10	-0.23	0.08	-0.27	-0.24	0.05	-0.20	0.04	0.10	0.06	-0.27	0.05
	PTS_1_Snow_3	2/14/19	Night	-10.4	-5.3	1.10	-0.23	-0.05	0.13	-0.27	0.07	-0.32	-0.16	0.15	-0.24	0.04	0.09	0.14	-0.31	0.11

	PTS_1_Snow_4	2/14/19	Day	-8.2	-0.8	0.88	0.10	0.25	0.13	1.73	0.41	1.77	-0.27	0.15	1.54	0.04	0.29	0.14	1.71	0.11
	PTS_1_Snow_5	2/15/19	Night	-6.8	-0.1	0.63	-0.48	-0.03	0.21	0.52	0.17	0.75	-0.43	0.10	0.55	0.07	0.19	0.08	0.76	0.16
Pellston Time Series 2																				
	PTS_2_Part_1	2/15/19	Day			0.80	-0.98	-0.50	0.13	-0.76	-0.03	-0.34	-0.23	0.15	-0.39	0.04	0.22	0.03	-0.21	0.04
	PTS_2_Part_ 2	2/16/19	Night			1.15	-1.14	-0.59	0.13	-0.95	-0.15	-0.50	-0.26	0.15	-0.51	0.04	0.14	0.03	-0.35	0.04
	PTS_2_Part_3	2/16/19	Day			0.75	-0.90	-0.50	0.13	-0.95	-0.10	-0.51	-0.15	0.15	-0.58	0.04	0.15	0.03	-0.39	0.04
	PTS_2_Part_4	2/17/19	Night			1.11	-0.84	-0.45	0.10	-0.73	-0.01	-0.35	-0.17	0.07	-0.40	0.06	0.21	0.12	-0.24	0.11
	PTS_2_Part_ 5_SP	2/17/19				0.77	-0.61	-0.16	0.13	-0.27	0.01	-0.02	-0.37	0.15	-0.15	0.04	0.10	0.03	0.02	0.04
	PTS_2_Snow_2	2/15/19	Night	-8.1	-4.3	1.28	-0.19	0.16	0.13	0.47	0.36	0.47	-0.43	0.15	0.35	0.04	0.28	0.14	0.43	0.11
	PTS_2_Snow_3	2/16/19	Day	-7.8	-3.2	0.85	-0.49	-0.08	0.13	0.38	0.29	0.64	-0.36	0.15	0.45	0.04	0.33	0.14	0.66	0.11
	PTS_2_Snow_4	2/16/19	Night	-20.7	-5.7	1.14	-0.15	0.14	0.10	0.77	0.28	0.88	-0.36	0.05	0.67	0.04	0.22	0.06	0.85	0.05
	PTS_2_Snow_5_SP	2/17/19				0.45	-0.22	0.08	0.19	1.35	0.34	1.59	-0.34	0.13	1.28	0.12	0.30	0.03	1.57	0.14

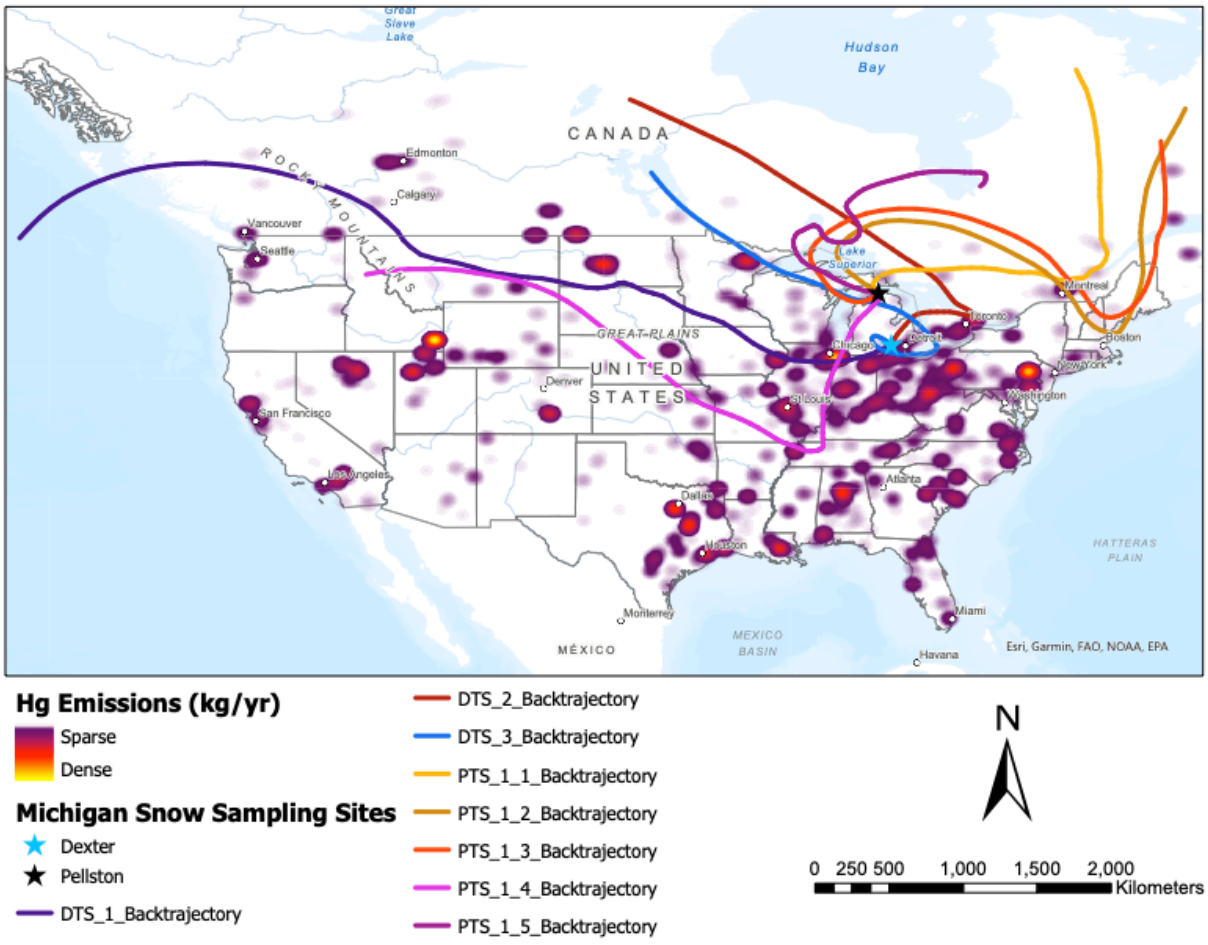

Figure 4.1 Location of Dexter (blue star) and Pellston (black star) sites in Michigan in relation to local and regional Hg sources (USEPA, 2017; NPRI, 2018).

Higher emissions are depicted with pink to white colors while lower emissions are depicted with purples. Back trajectories for fresh snow samples are overlaid on the map.

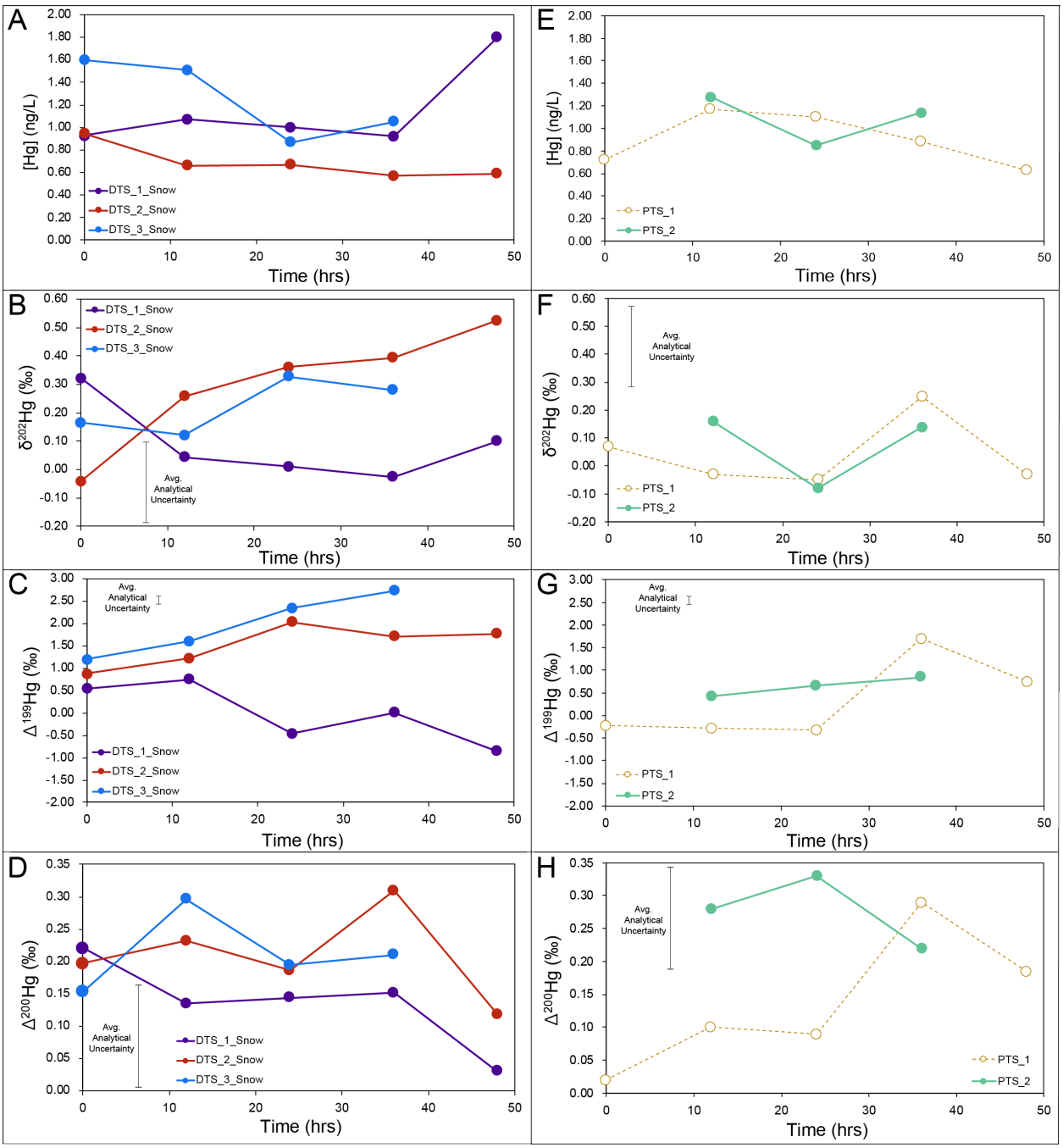

Figure 4.2 Progression of THg, δ^{202}Hg, Δ^{199}Hg and Δ^{200}Hg values in snow for each time series as snow aged in sunlight.

Dexter time series are on the left side and Pellston time series are on the right side. PTS_1 samples were collected during a single snow event so each sample is "fresh snow" and the time for these samples corresponds to the hours after the snow event began. The PTS_2 fresh snow sample was not retained.

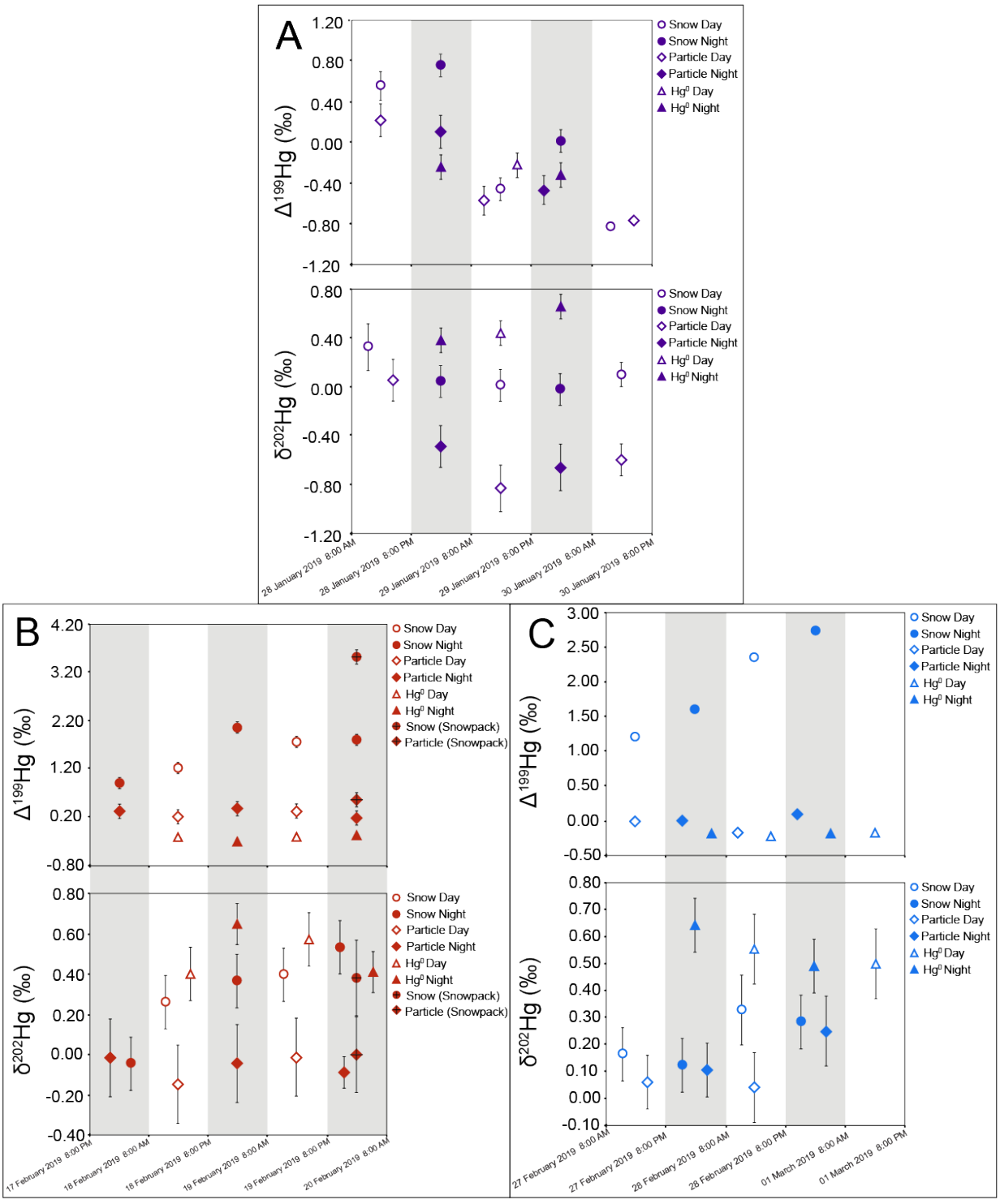

Figure 4.3 Dexter Hg isotope data plotted with δ^{202}Hg and Δ^{199}Hg on separate y-axes while sharing time on the x-axis.

Vertical grey shading represents nighttime periods and white represents daytime. Black bars represent analytical error (2SD). If no black bar is present, the analytical error is smaller than the symbol. Panel A) Time Series 1 (polar vortex), B) Time Series 2, C) Time Series 3.

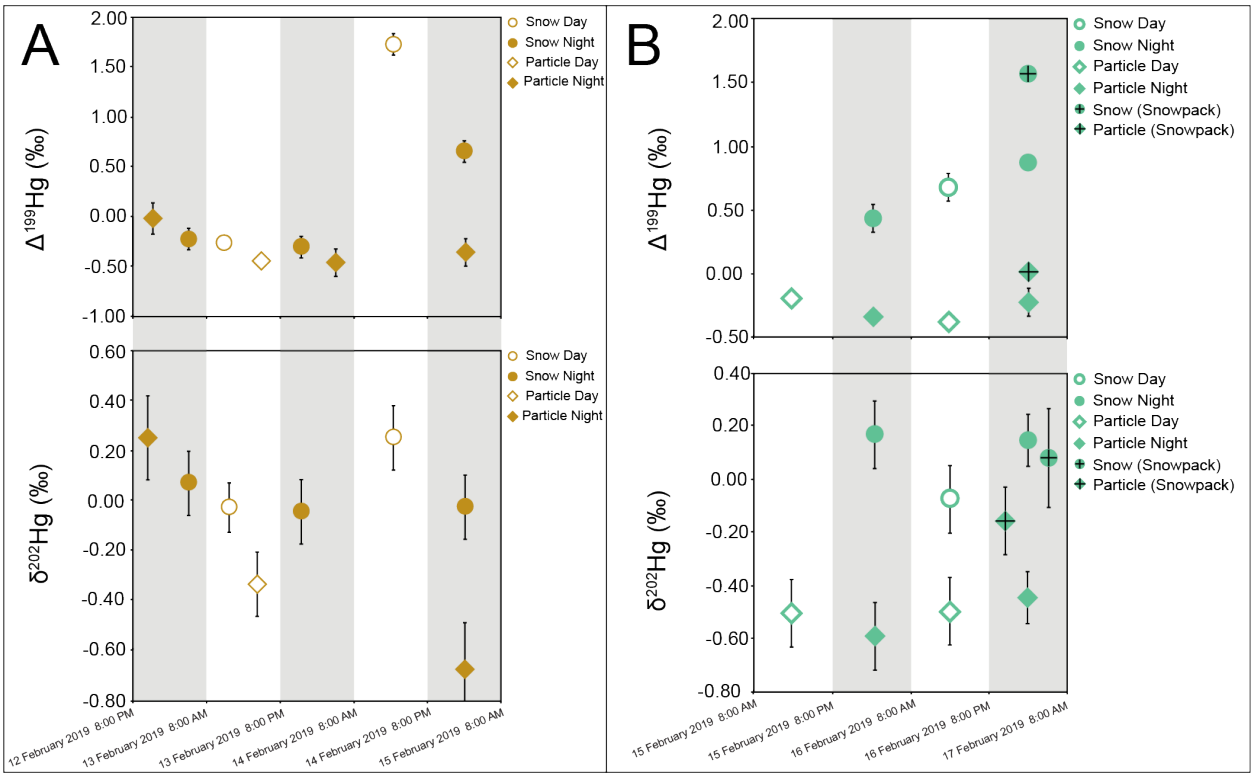

Figure 4.4 Pellston Hg isotope data plotted with $\delta^{202}Hg$ and $\Delta^{199}Hg$ on separate y-axes while sharing time on the x-axis.

Vertical grey shading represents nighttime periods and white represents daytime. Black bars represent analytical error (2SD). Panel A) Time Series 1, B) Time Series 2.

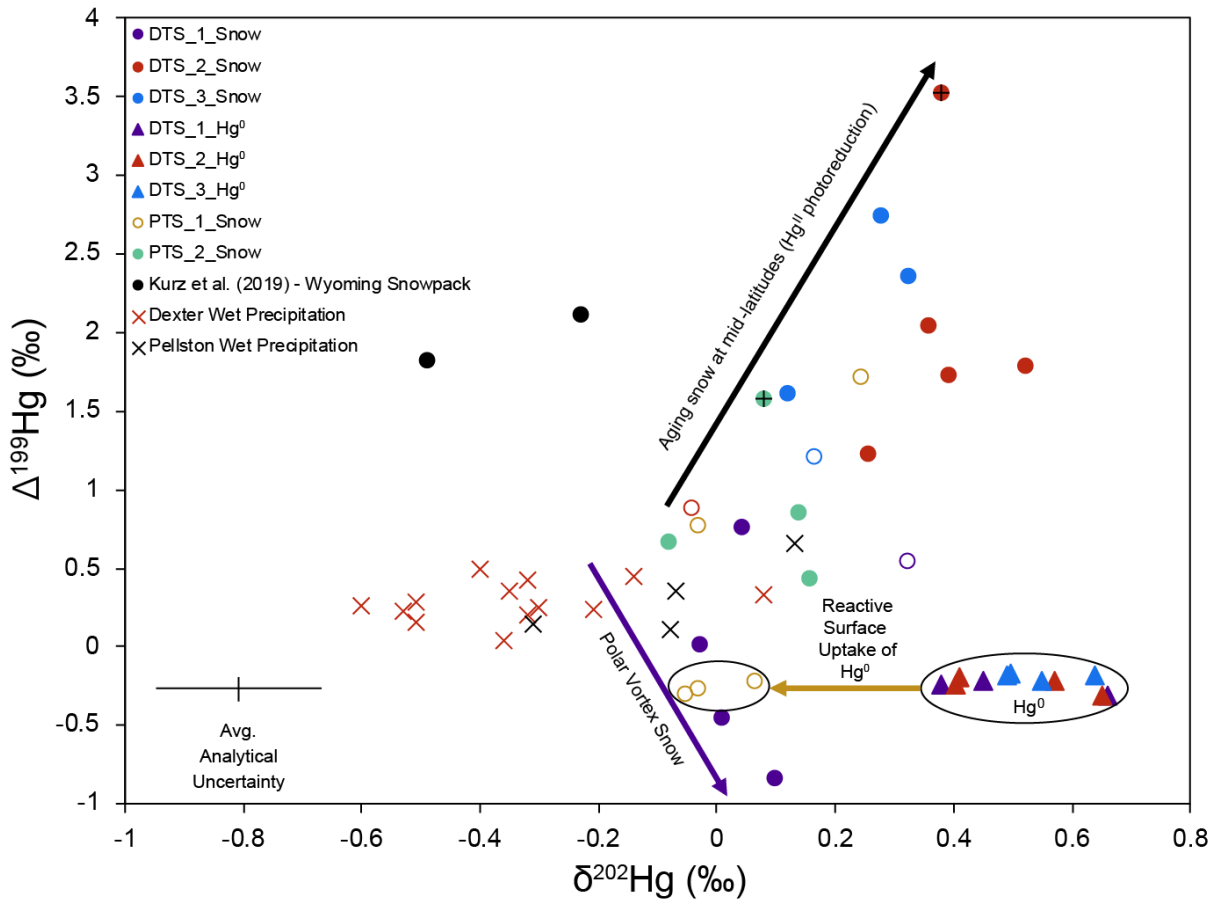

Figure 4.5 All collected snow and Hg^0 samples from this study are plotted as $\delta^{202}Hg$ vs. $\Delta^{199}Hg$ with summertime wet precipitation previously collected at Dexter and Pellston (Gratz et al., 2010; Sherman et al., 2015).

Previously reported snowpack samples (Kurz et al., 2019) from mid-latitudes (Lost Lake, WY) are also included. The polar vortex time series (DTS_1) indicates decreasing $\Delta^{199}Hg$ during aging while all other collected snow samples increased in $\Delta^{199}Hg$. The purple line indicates the general direction of observed fractionation as snow ages during the polar vortex. The black arrow indicates the general direction of observed fractionation as snow ages in all other time series. The brown arrow indicates the direction of fractionation during the reactive surface uptake of Hg^0 and the samples from PTS_1 most likely affected by this process. Open symbols indicate fresh snow and symbols with crosses indicate samples of the entire snowpack.

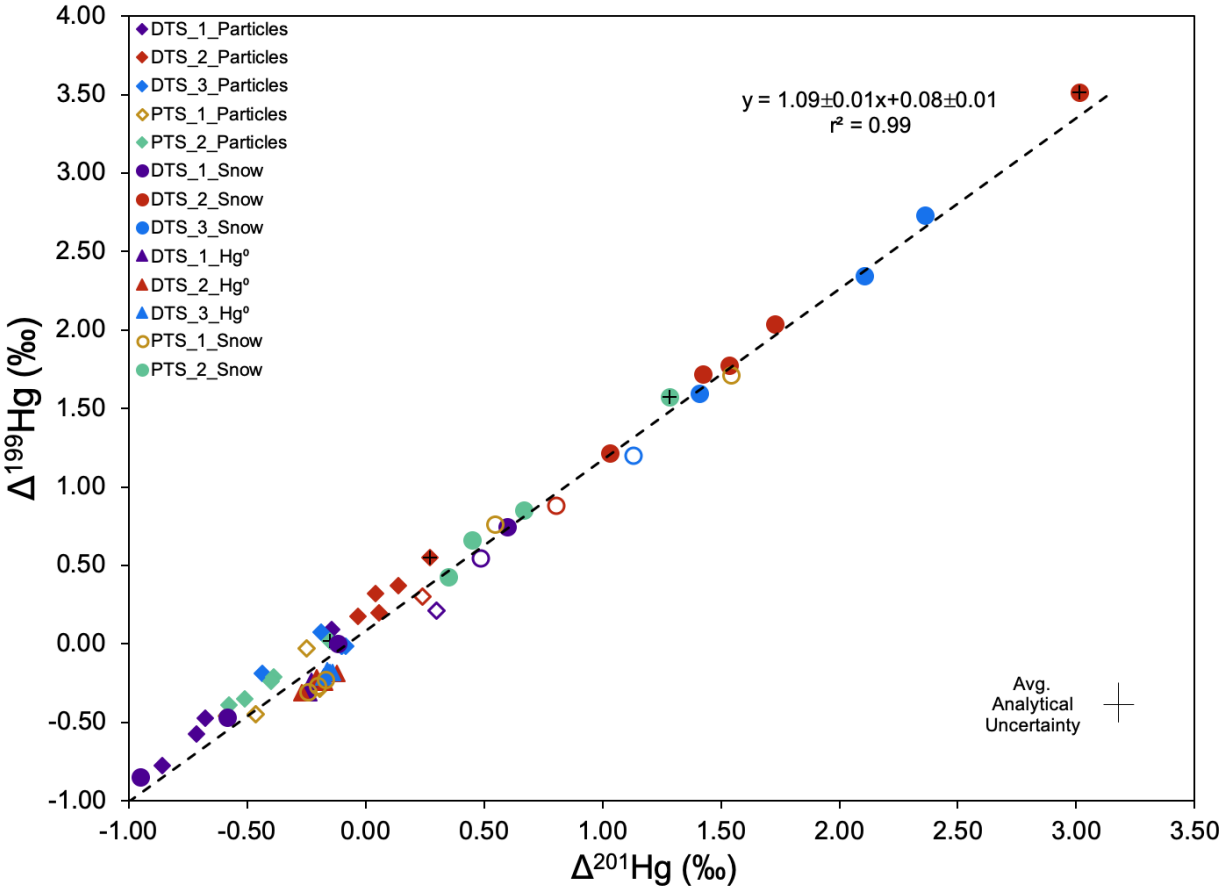

Figure 4.6 All collected samples from both Dexter and Pellston of Δ^{199}Hg vs. Δ^{201}Hg.

A York regression was calculated and yielded a slope with a value of 1.09±0.01, which is similar to the experimentally derived slope of 1.00±0.02 (Bergquist and Blum, 2007; Zheng and Hintelmann, 2010) indicating photoreduction of Hg^{2+}. Open symbols indicate fresh snow and symbols with crosses indicate snowpack samples.

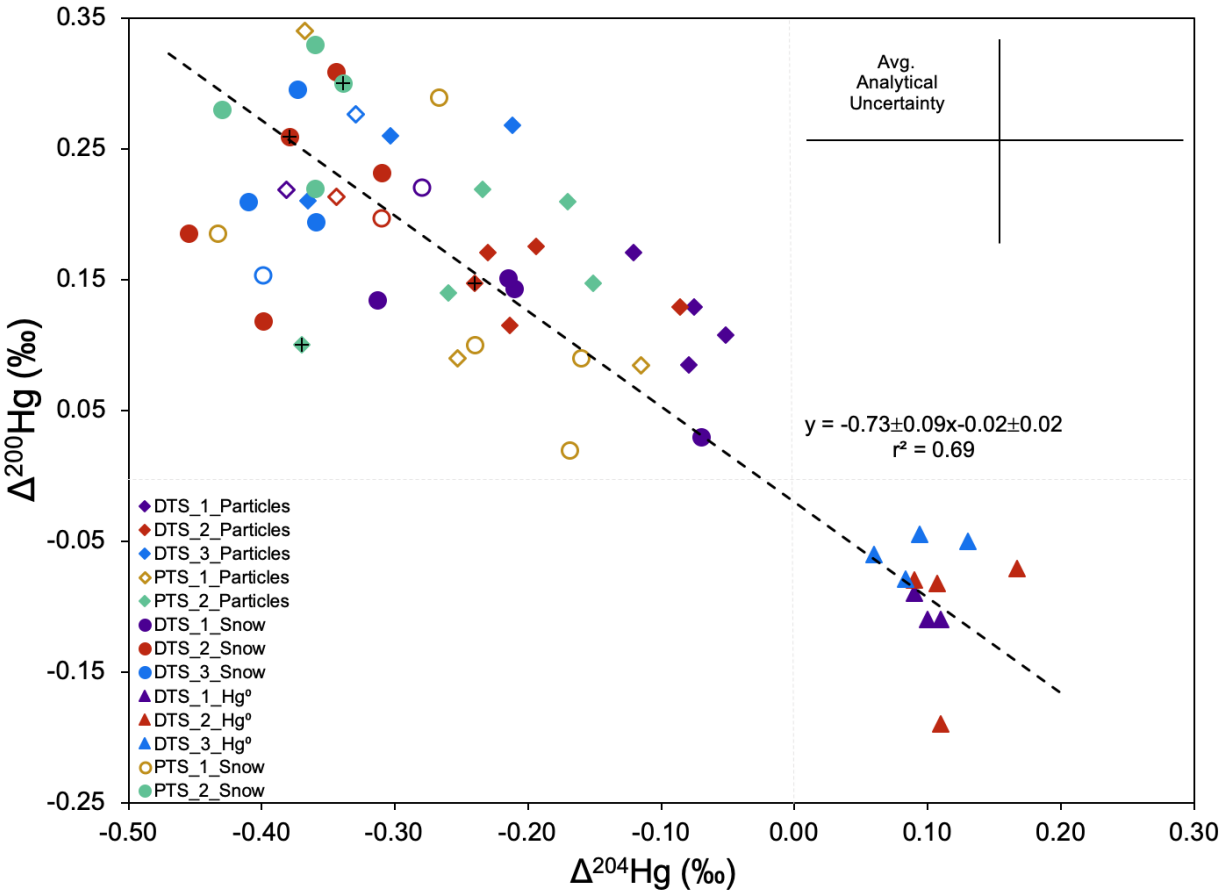

Figure 4.7 All collected samples from both Dexter and Pellston of Δ^{200}Hg vs. Δ^{204}Hg.

A York regression was calculated and yielded a slope with a value of -0.73±0.09, which is similar to the regression of previously reported atmospheric samples (approximately -0.5) (Blum and Johnson, 2017). Open symbols indicate fresh snow and symbols with crosses indicate snowpack samples.

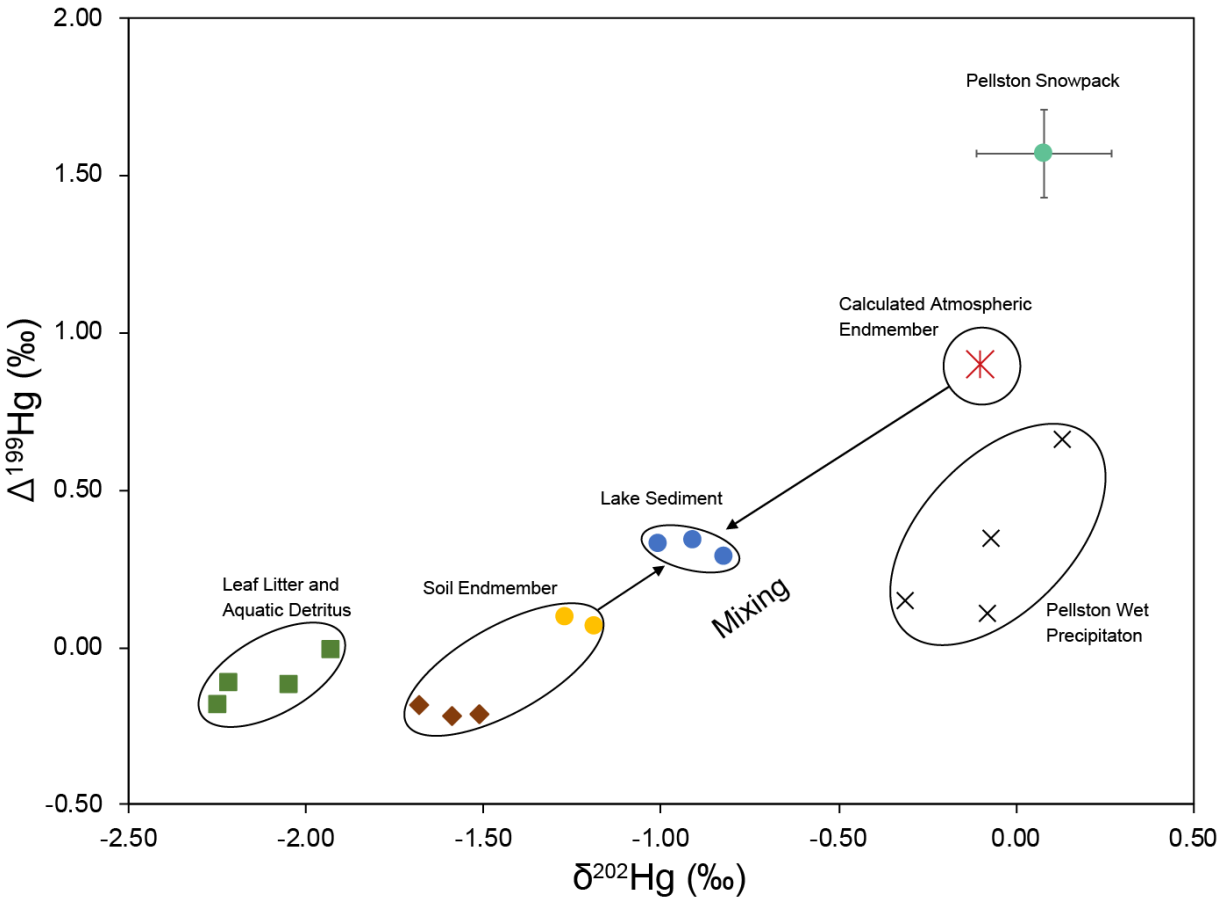

Figure 4.8 Mixing of endmembers on a $\delta^{202}Hg$ vs. $\Delta^{199}Hg$ adapted from Kwon et al. (2015).

Leaf litter and aquatic detritus, soil, and lake sediment are from Kwon et al. (2015). Pellston wet precipitation samples are from Sherman et al. (2015) and Pellston snow is from the current study (PTS_2_Snow_5_SP). The calculated atmospheric endmember consists of 30% Pellston snow and 70% Pellston wet precipitation and can account for the observed Hg isotopic composition of sediments in Douglas Lake by mixing with terrestrial soil.

References

Bergquist, B.A., Blum, J.D., 2007. Mass-dependent and -independent fractionation of Hg isotopes by photoreduction in aquatic systems. Science (80-.). 318, 417–420. https://doi.org/10.1126/science.1148050

Blum, J.D., Bergquist, B.A., 2007. Reporting of variations in the natural isotopic composition of mercury. Anal. Bioanal. Chem. 388, 353–359. https://doi.org/10.1007/s00216-007-1236-9

Blum, J.D., Johnson, M.W., 2017. Recent Developments in Mercury Stable Isotope Analysis. Rev. Mineral. Geochemistry 82, 733–757.

Blum, J.D., Sherman, L.S., Johnson, M.W., 2014. Mercury Isotopes in Earth and Environmental Sciences. Annu. Rev. Earth Planet. Sci. 42, 249–269. https://doi.org/10.1146/annurev-earth-050212-124107

Butler, A.H., Lawrence, Z.D., Lee, S.H., Lillo, S.P., Long, C.S., 2020. Differences between the 2018 and 2019 stratospheric polar vortex split events. Q. J. R. Meteorol. Soc. 146, 3503–3521. https://doi.org/10.1002/qj.3858

Carignan, J., Sonke, J., 2010. The effect of atmospheric mercury depletion events on the net deposition flux around Hudson Bay, Canada. Atmos. Environ. 44, 4372–4379. https://doi.org/10.1016/j.atmosenv.2010.07.052

Chandan, P., Ghosh, S., Bergquist, B.A., 2015. Mercury isotope fractionation during aqueous photoreduction of monomethylmercury in the presence of dissolved organic matter. Environ. Sci. Technol. 49, 259–267. https://doi.org/10.1021/es5034553

Chen, J., Hintelmann, H., Feng, X., Dimock, B., 2012. Unusual fractionation of both odd and even mercury isotopes in precipitation from Peterborough, ON, Canada. Geochim. Cosmochim. Acta 90, 33–46. https://doi.org/10.1016/j.gca.2012.05.005

Demers, J.D., Blum, J.D., Zak, D.R., 2013. Mercury isotopes in a forested ecosystem: Implications for air-surface exchange dynamics and the global mercury cycle. Global Biogeochem. Cycles 27, 222–238. https://doi.org/10.1002/gbc.20021

Demers, J.D., Sherman, L.S., Blum, J.D., Marsik, F.J., Dvonch, J.T., 2015. Coupling atmospheric mercury isotope ratios and meteorology to identify sources of mercury impacting a coastal urban-industrial region near Pensacola, Florida, USA. Global Biogeochem. Cycles 29, 1689–1705. https://doi.org/10.1002/2015GB005146

Donovan, P.M., Blum, J.D., Yee, D., Gehrke, G.E., Singer, M.B., 2013. An isotopic record of mercury in San Francisco Bay sediment. Chem. Geol. 349–350, 87–98. https://doi.org/10.1016/j.chemgeo.2013.04.017

Douglas, T.A., Blum, J.D., 2019. Mercury Isotopes Reveal Atmospheric Gaseous Mercury

Deposition Directly to the Arctic Coastal Snowpack. Environ. Sci. Technol. 6, 235–242. https://doi.org/10.1021/acs.estlett.9b00131

Douglas, T.A., Sturm, M., Simpson, W.R., Blum, J.D., Alvarez-Aviles, L., Keeler, G.J., Perovich, D.K., Biswas, A., Johnson, K., 2008. Influence of snow and ice crystal formation and accumulation on mercury deposition to the arctic. Environ. Sci. Technol. 42, 1542–1551. https://doi.org/10.1021/es070502d

Driscoll, C.T., Mason, R.P., Chan, H.M., Jacob, D.J., Pirrone, N., 2013. Mercury as a global pollutant: Sources, pathways, and effects. Environ. Sci. Technol. 47, 4967–4983. https://doi.org/10.1021/es305071v

Engstrom, D.R., Fitzgerald, W.F., Cooke, C. a., Lamborg, C.H., Drevnick, P.E., Swain, E.B., Balogh, S.J., Balcom, P.H., 2014. Atmospheric Hg emissions from preindustrial gold and silver extraction in the Americas: A reevaluation from lake-sediment archives. Environ. Sci. Technol. 48, 6533–6543. https://doi.org/10.1021/es405558e

Faïn, X., Helmig, D., Hueber, J., Obrist, D., Williams, M.W., 2013. Mercury dynamics in the Rocky Mountain, Colorado, snowpack. Biogeosciences 10, 3793–3807. https://doi.org/10.5194/bg-10-3793-2013

Gratz, L.E., Keeler, G.J., Blum, J.D., Sherman, L.S., 2010. Isotopic composition and fractionation of mercury in Great Lakes precipitation and ambient air. Environ. Sci. Technol. 44, 7764–7770. https://doi.org/10.1021/es100383w

Gustin, M.S., Amos, H.M., Huang, J., Miller, M.B., Heidecorn, K., 2015. Measuring and modeling mercury in the atmosphere : a critical review. Atmos. Chem. Phys. 5697–5713. https://doi.org/10.5194/acp-15-5697-2015

Hammerschmidt, C.R., Fitzgerald, W.F., 2006. Methylmercury in freshwater fish linked to atmospheric mercury deposition. Environ. Sci. Technol. 40, 7764–7770. https://doi.org/10.1021/es061480i

Horowitz, H.M., Jacob, D.J., Amos, H.M., Streets, D.G., Sunderland, E.M., 2014. Historical mercury releases from commercial products: Global environmental implications. Environ. Sci. Technol. 48, 10242–10250. https://doi.org/10.1021/es501337j

Horowitz, H.M., Jacob, D.J., Zhang, Y., Dibble, T.S., Slemr, F., Amos, H.M., Schmidt, J.A., Corbitt, E.S., Marais, E.A., Sunderland, E.M., 2017. A new mechanism for atmospheric mercury redox chemistry : implications for the global mercury budget. Atmos 6353–6371. https://doi.org/10.5194/acp-17-6353-2017

Huang, S., Sun, L., Zhou, T., Yuan, D., Du, B., Sun, X., 2018. Natural stable isotopic compositions of mercury in aerosols and wet precipitations around a coal-fired power plant in Xiamen, southeast China. Atmos. Environ. 173, 72–80. https://doi.org/10.1016/j.atmosenv.2017.11.003

Jiskra, M., Wiederhold, J.G., Bourdon, B., Kretzschmar, R., 2012. Solution speciation controls mercury isotope fractionation of Hg(II) sorption to goethite. Environ. Sci. Technol. 46, 6654–6662. https://doi.org/10.1021/es3008112

Kritee, K., Barkay, T., Blum, J.D., 2009. Mass dependent stable isotope fractionation of mercury during mer mediated microbial degradation of monomethylmercury. Geochim. Cosmochim. Acta 73, 1285–1296. https://doi.org/10.1016/j.gca.2008.11.038

Kritee, K., Blum, J.D., Johnson, M.W., Bergquist, B.A., Barkay, T., 2007. Mercury stable isotope fractionation during reduction of Hg(II) to Hg(0) by Mercury resistant microorganisms. Environ. Sci. Technol. 41, 1889–1895. https://doi.org/10.1021/es062019t

Kurz, A.Y., Blum, J.D., Gratz, L.E., Jaffe, D.A., 2020. Contrasting Controls on the Diel Isotopic Variation of Hg0 at Two High Elevation Sites in the Western United States. Environ. Sci. Technol. 54, 10502–10513. https://doi.org/10.1021/acs.est.0c01918

Kurz, A.Y., Blum, J.D., Washburn, S.J., Baskaran, M., 2019. Changes in the mercury isotopic composition of sediments from a remote alpine lake in Wyoming , USA. Sci. Total Environ. 669, 973–982. https://doi.org/10.1016/j.scitotenv.2019.03.165

Kwon, S.Y., Blum, J.D., Nadelhoffer, K.J., Dvonch, J.T., Tsui, M.T., 2015. Isotopic study of mercury sources and transfer between a freshwater lake and adjacent forest food web. Sci. Total Environ. 532, 220–229. https://doi.org/10.1016/j.scitotenv.2015.06.012

Kwon, S.Y., Blum, J.D., Yin, R., Tsui, M.T.K., Yang, Y.H., Choi, J.W., 2020. Mercury stable isotopes for monitoring the effectiveness of the Minamata Convention on Mercury. Earth-Science Rev. 203, 103111. https://doi.org/10.1016/j.earscirev.2020.103111

Landis, M.S., Vette, A.F., Keeler, G.J., 2002. Atmospheric mercury in the Lake Michigan basin: Influence of the Chicago/Gary urban area. Environ. Sci. Technol. 36, 4508–4517. https://doi.org/10.1021/es011216j

Mason, R.P., Lawson, N.M., Sheu, G.R., 2000. Annual and seasonal trends in mercury deposition in Maryland. Atmos. Environ. 34, 1691–1701. https://doi.org/10.1016/S1352-2310(99)00428-8

Mason, R.P., Lawson, N.M., Sullivan, K.A., 1997. The concentration, speciation and sources of mercury in Chesapeake Bay precipitation. Atmos. Environ. 31, 3541–3550. https://doi.org/10.1016/S1352-2310(97)00206-9

May, N.W., Gunsch, M.J., Olson, N.E., Bondy, A.L., Kirpes, R.M., Bertman, S.B., China, S., Laskin, A., Hopke, P.K., Ault, A.P., Pratt, K.A., 2018. Unexpected Contributions of Sea Spray and Lake Spray Aerosol to Inland Particulate Matter. Environ. Sci. Technol. Lett. 5, 405–412. https://doi.org/10.1021/acs.estlett.8b00254

Motta, L.C., Kritee, K., Blum, J.D., Tsz-Ki Tsui, M., Reinfelder, J.R., 2020. Mercury Isotope Fractionation during the Photochemical Reduction of Hg(II) Coordinated with Organic Ligands. J. Phys. Chem. A. https://doi.org/10.1021/acs.jpca.9b06308

Obrist, D., Agnan, Y., Jiskra, M., Olson, C.L., Dominique, P., 2017. Tundra uptake of atmospheric elemental mercury drives Arctic mercury pollution. Nat. Publ. Gr. 547, 201–204. https://doi.org/10.1038/nature22997

Rodriguez-Gonzalez, P., Tessier, E., Guyoneaud, R., Monperrus, M., 2009. Species-Specific Stable Isotope Fractionation of Mercury during Hg (II) Methylation by an Anaerobic Bacteria (Desulfobulbus propionicus) under Dark Conditions. Environ. Sci. Technol. 43, 9183–9188.

Rose, C.H., Ghosh, S., Blum, J.D., Bergquist, B.A., 2015. Effects of ultraviolet radiation on mercury isotope fractionation during photo-reduction for inorganic and organic mercury species. Chem. Geol. 405, 102–111. https://doi.org/10.1016/j.chemgeo.2015.02.025

Schoeberl, M.R., Lait, R., Newman, P. a, Rosenfield, J.E., 1992. The Structure of the Polar Vortex. J. Geophys. Res. 97, 7859–7882.

Schroeder, W.H., Anlauf, K.G., Barrie, L.A., Lu, J.Y., Steffen, A., 1998. Arctic springtime depletion of Mercury. Nature 394, 331–332.

Sherman, L.S., Blum, J.D., Dvonch, J.T., Gratz, L.E., Landis, M.S., 2015. The use of Pb, Sr, and Hg isotopes in Great Lakes precipitation as a tool for pollution source attribution. Sci. Total Environ. 502, 362–374. https://doi.org/10.1016/j.scitotenv.2014.09.034

Sherman, L.S., Blum, J.D., Johnson, K.P., Keeler, G.J., Barres, J. a., Douglas, T. a., 2010. Mass-independent fractionation of mercury isotopes in Arctic snow driven by sunlight. Nat. Geosci. 3, 173–177. https://doi.org/10.1038/ngeo758

Sherman, L.S., Blum, J.D., Keeler, G.J., Demers, J.D., Dvonch, J.T., 2012. Investigation of local mercury deposition from a coal-fired power plant using mercury isotopes. Environ. Sci. Technol. 46, 382–390. https://doi.org/10.1021/es202793c

Steffen, A., Douglas, T., Amyot, M., Ariya, P., Aspmo, K., Berg, T., Bottenheim, J., Brooks, S., Cobbett, F., Dastoor, A., Dommergue, A., Ebinghaus, R., Ferrari, C., Gardfeldt, K., Goodsite, M.E., Lean, D., Poulain, A.J., Scherz, C., Skov, H., Sommar, J., Temme, C., 2008. A synthesis of atmospheric mercury depletion event chemistry linking atmosphere, snow and water. Atmos. Chem. Phys. 8, 1445–1482. https://doi.org/10.5194/acpd-7-10837-2007

Štrok, M., Hintelmann, H., Dimock, B., 2014. Development of pre-concentration procedure for the determination of Hg isotope ratios in seawater samples. Anal. Chim. Acta 851, 57–63. https://doi.org/10.1016/j.aca.2014.09.005

Sun, G., Sommar, J., Feng, X., Lin, C.-J., Ge, M., Wang, W., Yin, R., Fu, X., Shang, L., 2016.

Mass-Dependent and -Independent Fractionation of Mercury Isotope during Gas-Phase Oxidation of Elemental Mercury Vapor by Atomic Cl and Br. Environ. Sci. Technol. 50, 9232–9241. https://doi.org/10.1021/acs.est.6b01668

Sun, R., Heimbürger, L., Sonke, J.E., Liu, G., Amouroux, D., Berail, S., 2013. Mercury stable isotope fractionation in six utility boilers of two large coal- fi red power plants. Chem. Geol. 336, 103–111. https://doi.org/10.1016/j.chemgeo.2012.10.055

Sunderland, E.M., 2007. Mercury exposure from domestic and imported estuarine and marine fish in the U.S. seafood market. Environ. Health Perspect. 115, 235–242. https://doi.org/10.1289/ehp.9377

U.S. Environmental Protection Agency (USEPA) National Emission Inventory (NEI). https://www.epa.gov/air-emissions-inventories/2017-national-emissions-inventory-nei-data (Accessed February 3rd, 2020).

Wang, S., Mcnamara, S.M., Moore, C.W., Obrist, D., Steffen, A., Shepson, P.B., Staebler, R.M., Raso, A.R.W., Pratt, K.A., Performed, K.A.P., 2019. Direct detection of atmospheric atomic bromine leading to mercury and ozone depletion. Atmos. Planet. Sci. 116. https://doi.org/10.18739/A2D79598P

Wang, X., Luo, J., Yin, R., Yuan, W., Lin, C.J., Sommar, J., Feng, X., Wang, H., Lin, C., 2016. Using mercury isotopes to understand mercury accumulation in the montane forest floor of the Eastern Tibetan Plateau. Environ. Sci. Technol. 51, 801–809. https://doi.org/10.1021/acs.est.6b03806

Washburn, S.J., Blum, J.D., Kurz, A.Y., Pizzuto, J.E., 2018. Spatial and temporal variation in the isotopic composition of mercury in the South River , VA. Chem. Geol. 494, 96–108. https://doi.org/10.1016/j.chemgeo.2018.07.023

Washburn, S.J., Blum, J.D., Motta, L.C., Bergquist, B.A., Weiss-Penzias, P., 2020. Isotopic Composition of Hg in Fogwaters of Coastal California. Environ. Sci. Technol. Lett. https://doi.org/10.1021/acs.estlett.0c00716

Wiederhold, J.G., Cramer, C.J., Daniel, K., Infante, I., Bourdon, B., Kretzschmar, R., 2010. Equilibrium mercury isotope fractionation between dissolved Hg(II) species and thiol-bound Hg. Environ. Sci. Technol. 44, 4191–4197. https://doi.org/10.1021/es100205t

Yin, R., Feng, X., Shi, W., 2010. Application of the stable-isotope system to the study of sources and fate of Hg in the environment: A review. Appl. Geochemistry 25, 1467–1477. https://doi.org/10.1016/j.apgeochem.2010.07.007

York, D., 1968. Least squares fitting of a straight line with correlated errors. Earth Planet. Sci. Lett. 5, 320–324.

Yuan, S., Chen, J., Cai, H., Yuan, W., Wang, Z., Huang, Q., Liu, Y., Wu, X., 2018. Sequential

samples reveal significant variation of mercury isotope ratios during single rainfall events. Sci. Total Environ. 624, 133–144. https://doi.org/10.1016/j.scitotenv.2017.12.082

Yuan, S., Zhang, Y., Chen, J., Kang, S., Zhang, J., 2015. Large variation of mercury isotope composition during a single precipitation event at Lhasa City , Tibetan Plateau , China. Procedia Earth Planet. Sci. 13, 282–286. https://doi.org/10.1016/j.proeps.2015.07.066

Yuan, W., Sommar, J., Lin, C., Wang, X., Li, K., Liu, Y., Zhang, H., Lu, Z., Wu, C., Feng, X., 2018. Stable Isotope Evidence Shows Re-emission of Elemental Mercury Vapor Occurring after Reductive Loss from Foliage. Environ. Sci. Technol. 53, 651–660. https://doi.org/10.1021/acs.est.8b04865

Zheng, W., Hintelmann, H., 2010. Isotope Fractionation of Mercury during Its Photochemical Reduction by Low-Molecular-Weight Organic Compounds. J. Phys. Chem. A 114, 4246–4253.

Chapter 5 Conclusion

Mercury (Hg) is a persistent neurotoxin with a complex biogeochemical cycle that has been the subject of intensive study in a variety of natural media. Researchers have worked to elucidate the processes and mechanisms that result in high levels of monomethylmercury (MMHg) in predatory fish species, the crucial vector for human exposure (Driscoll et al., 2013). In recent decades, advances in multiple-collector inductively-coupled-plasma mass spectrometry have allowed for high precision measurements of Hg stable isotopes. This growing body of analyses has expanded the understanding of environmental processes and biogeochemical conditions that influence the mobility and fate of Hg (Blum et al., 2014; Kwon et al., 2020; Sonke, 2011; Sun et al., 2019; Tsui et al., 2020; Yin et al., 2010). Of particular importance is the ability to analyze background samples with low Hg concentrations, which has contributed to the fundamental of understanding of Hg biogeochemical cycling. While knowledge gaps still remain in our understanding of Hg cycling, the research presented here fills in some of these gaps and invites additional studies to further explore a wide range of aspects of Hg cycling.

5.1 Review of Key Findings

5.1.1 Historical Deposition of Hg to an Aquatic Ecosystem

In Chapter 2, we highlighted the utility of Hg isotopes preserved in natural archives as a tool for exploring the historical atmospheric deposition of Hg. A substantial number of studies have used natural archives to trace the impact of historical Hg releases in the global environment, most have focused on variations in Hg concentrations (Cooke et al., 2013; Engstrom et al., 2014;

Enrico et al., 2017; Schuster et al., 2002; Zdanowicz et al., 2016). Only a few studies have sampled natural archives located in remote regions for Hg stable isotopes analyses (Cooke et al., 2013; Zdanowicz et al., 2016). In the work conducted at Lost Lake, we aimed to identify a lake far from any Hg sources that would preserve direct atmospheric deposition with little to no influence from the surrounding catchment. Analysis of Hg accumulation rates in Lost Lake agree well with previous findings from other lakes, indicating an increase in Hg deposition by 3.8 times since the onset of the Industrial Revolution (Engstrom et al., 2014 and references therein). Similar to other studies, deposition rates in Lost Lake reached a maximum circa 2005 and began to decrease to the present, reflecting the diminishing use and release of Hg (Zhang et al., 2015). Further, measurements of Hg stable isotopes from Lost Lake sediments displayed an increasing trend in δ^{202}Hg, Δ^{199}Hg and Δ^{200}Hg from 1850 to the present. We suggest these trends are indicative of a fundamental shift in the atmospheric chemical processes and reactions controlling the fractionation of Hg in the atmosphere prior to deposition to the Earth's surface (Kurz et al., 2019).

5.1.2 Identifying Contrasting Atmospheric Processes at High Elevation

In Chapter 3, we used measurements of the isotopic composition of Hg^0 to identify the dominant processes controlling Hg isotope fractionation in the atmosphere. Past studies have collected time series of Hg^0 samples at a single site to elucidate the conditions and processes that effect the measured Hg isotopic composition (Demers et al., 2015; Fu et al., 2016a). These studies, however, relied on samples that were integrated over time periods of between 24 hours and 2 weeks due to the low concentration of Hg. We sought to build on these measurements by collecting continuous diurnal Hg^0 samples over seven days at two high elevation sites with contrasting geographic locations and characteristics. At Mount Bachelor, Oregon, a high

elevation site that has been well characterized atmospherically and receives nightly free tropospheric air masses, we found lower THg, δ^{202}Hg, and Δ^{199}Hg nightly in free tropospheric air masses as compared to daytime planetary boundary layer samples. Near the end of the sampling period, a forest fire (the Milli fire) ~31 km NW of Mount Bachelor came to dominate both daytime and nighttime samples, masking the diurnal variation observed at the beginning of the time series. To further explain differences in the measured Hg isotopic composition, we used a three-endmember mixing model to identify a high THg, low δ^{202}Hg, and high Δ^{199}Hg endmember as combusted vegetation from the Milli fire, a low THg, high δ^{202}Hg, and low Δ^{199}Hg endmember as Hg^0 in the free troposphere, and an intermediate THg, intermediate δ^{202}Hg, and high Δ^{199}Hg endmember as a mixture of regional Hg sources (Kurz et al., 2020). At the Camp Davis sampling site near Jackson, Wyoming, we also observed diel variation, however, the trends were different than those observed at Mount Bachelor. Nightly Hg^0 samples at Camp Davis displayed low THg and high δ^{202}Hg as compared to daily samples. We attributed this variation to the nightly uptake of Hg^0 by vegetation, which has been demonstrated to deplete δ^{202}Hg in the residual atmospheric Hg^0 (Demers et al., 2013; W. Yuan et al., 2018). Additionally, to further explain the variation observed at Camp Davis, we employed a three-endmember mixing model. We identified a low THg, high δ^{202}Hg, and intermediate Δ^{199}Hg endmember as the residual Hg^0 in the atmosphere as vegetation preferentially takes up the light isotopes, a high THg, low δ^{202}Hg, and high Δ^{199}Hg endmember as Hg^0 that was re-emitted from vegetation during the day through photoreduction of Hg^{2+}, and an unknown low Δ^{199}Hg endmember.

5.1.3 Characterization of Hg Isotope Fractionation at Mid-Latitudes

In Chapter 4, we presented the first time series of snow samples collected at mid-latitudes to investigate and characterize the progressive fractionation of Hg isotopes i) during a long

duration (48+ hour) snow event and ii) as snow was aged in sunlight. The majority of studies investigating Hg isotopes in snow have been conducted in the Arctic due to intense interest in a phenomenon called atmospheric mercury depletion events (AMDE) (Schroeder et al., 1998; Steffen et al., 2008). During AMDEs, atmospheric Hg^0 is oxidized by Br and BrO and subsequently stripped from the atmosphere and deposited to the snowpack (Wang et al., 2019). As the snow is exposed to sunlight, Hg^{2+} is photoreduced to Hg^0 within the snowpack and released back to the atmosphere, leaving the residual Hg in the snowpack with unprecedented negative $\Delta^{199}Hg$ (Sherman et al., 2010). In Pellston, Michigan, we collected snow samples every 12 hours for a total of 48 hours during a single long-duration snowfall event. The first three snow samples collected during this time series had $\Delta^{199}Hg$ values identical to those measured in Hg^0 samples, but $\delta^{202}Hg$ values that were on average 0.52‰ lower than those measured in Hg^0. We hypothesized this was due to the reactive surface uptake of Hg^0 from the atmosphere prior to deposition (Kurz et al., *in review*). Those three samples contrast with the proceeding two samples, which displayed $\Delta^{199}Hg$ and $\delta^{202}Hg$ values indicative of long-range atmospheric transport of Hg.

The first time series at the Dexter sampling site was collected during a polar vortex. Snow samples from this time series displayed progressively lower $\Delta^{199}Hg$ values after the snow was deposited and exposed to sunlight. A York regression of $\delta^{202}Hg$ vs. $\Delta^{199}Hg$ yielded a slope of -3.32±1.19, similar to the slope calculated for snow samples collected in northern Alaska during an AMDE (Sherman et al., 2010). In contrast, the snow samples collected during the two other time series at Dexter displayed progressively more positive $\Delta^{199}Hg$ values. We hypothesized that this was due to photoreduction of Hg^{2+} from the snowpack. We supported this hypothesis by performing a York regression of $\Delta^{199}Hg$ vs. $\Delta^{201}Hg$ and calculated a slope of

1.09±0.01, which is similar to the experimentally derived slope for the aqueous photoreduction of Hg^{2+} (Bergquist and Blum, 2007). When we regressed each individual time series, we calculated a range of $\Delta^{199}Hg$ vs. $\Delta^{201}Hg$ slopes from 0.87±0.02 to 1.18±0.02. We suggested this range in slopes indicates differences in binding ligands and reaction conditions control the direction and magnitude of fractionation (Kurz et al., *in review*).

5.1.4 Characterization of the Isotopic Composition of Hg Deposited via Snow to Mid-Latitude Ecosystems

In Chapter 4, we estimated the isotopic composition of Hg that is likely to be incorporated into mid-latitude ecosystems based on two vertically integrated snowpack samples (one from each sample site), which average over multiple snowfall events. This endmember was characterized as: $\delta^{202}Hg$ = 0.23±0.21‰, $\Delta^{199}Hg$ = 2.54±1.37‰, $\Delta^{201}Hg$ = 2.15±1.22‰, $\Delta^{200}Hg$ =0.28±0.03‰, and $\Delta^{204}Hg$ = -0.36±0.03‰. Douglas and Blum (2019) demonstrated the importance of characterizing snowmelt in Alaska, estimating the amount of AMDE snow incorporated into ecosystems and concluding that snowmelt reflected the reactive surface uptake of Hg^0 as opposed to AMDE snow. We used the characterization of our snowmelt endmember to better explain inputs into an aquatic ecosystem previously studied in Pellston, MI (Kwon et al., 2015). The addition of the snowmelt endmember to previously measured wet precipitation at Pellston helps explain the difference in Hg isotopic composition between terrestrial soil and lake sediments (Kurz et al., *in review*). This exercise highlights the importance of snowmelt isotopic characterization at mid-latitudes for endmember-mixing and source apportionment calculations.

5.2 Future Directions

The work presented in this dissertation has added to the quickly growing body of work utilizing high precision measurements of Hg stable isotopes to better understand the global biogeochemical cycle, particularly in low concentration samples. The results of this dissertation indicate a number of opportunities for future studies to continue the understanding of Hg isotope dynamics in the environment.

The study of Lost Lake sediments highlights the importance of identifying natural records that record direct atmospheric deposition without influence from secondary processing and catchment inputs. Without fully accounting for deposition of Hg from the catchment to lake sediments, interpretation of the historical deposition of Hg can be misinterpreted. Terrestrial processing of Hg leads to distinct isotopic fractionations and is not reflective of either wet or dry deposition directly to aquatic ecosystems. Therefore, it is necessary to consider all deposition pathways to lake sediments and their influence on Hg isotope fractionation when using natural archives to infer historical atmospheric conditions and processes.

The atmospheric measurements of Hg^0 at both Mount Bachelor and Camp Davis have important implications for atmospheric cycling of Hg. Our observations of contrasting isotopic compositions of Hg^0 in the free troposphere versus the planetary boundary layer implies differences in dominant reaction pathways and processes. Further investigation of processes in the free troposphere are important, especially as anthropogenic Hg emissions decrease in the future. Additionally, the identification of the influence of forest fires on the isotopic composition of Hg^0 will become more important as the prevalence of forest fires increases in the western United States and globally. Finally, confirmation of the previously identified influence of vegetation on the isotopic composition of Hg^0 has global implications for Hg cycling. Further

experimental work would help in elucidation of the identified odd-MIF induced by the uptake of Hg^0 by vegetation. Additionally, as vegetation is a key component of global atmospheric cycling of Hg, future clear-cutting of forests will greatly impact Hg cycling and should therefore be characterized in the present to inform future interpretations of Hg measurements.

We presented the first measurements of Hg stable isotopes in snow at mid-latitudes. We also demonstrated the importance of endmember characterization of snow for understanding inputs to mid-latitude ecosystems. Further measurements of snow at mid-latitudes have become possible with improved Hg separation techniques and are important for understanding inputs of inorganic Hg, which can become available for methylation and ultimately transfer to humans through the consumption of fish. Furthermore, the identification of AMDE type Hg isotope behavior in snow mid-latitudes during a polar vortex is unprecedented.

Future sampling should aim to characterize dominant processes controlling Hg isotopic fractionation in snow at mid-latitudes. This work could involve the assessment of both geographic and elevation controls on the evolution of odd-MIF as snow is exposed to sunlight. Characterization of the specific ligands involved in photoreduction could prove beneficial in the prediction of the magnitude and direction of Hg isotope fractionation in snow, possibly through conducting flux chamber experiments in the snowpack at mid-latitudes. Additionally, current Hg oxidation experiments are not able to fully account for the fractionation observed during AMDEs and we therefore suggest that further laboratory experiments, possibly involving heterogenous reactions and additional oxidants, may provide further insights into the observed Hg isotopic fractionation in both snow and the atmosphere. These experiments would provide a significant contribution to the Hg isotope research community.

References

Bergquist, B.A., Blum, J.D., 2007. Mass-dependent and -independent fractionation of Hg isotopes by photoreduction in aquatic systems. Science (80-.). 318, 417–420. https://doi.org/10.1126/science.1148050

Demers, J.D., Blum, J.D., Zak, D.R., 2013. Mercury isotopes in a forested ecosystem: Implications for air-surface exchange dynamics and the global mercury cycle. Global Biogeochem. Cycles 27, 222–238. https://doi.org/10.1002/gbc.20021

Demers, J.D., Sherman, L.S., Blum, J.D., Marsik, F.J., Dvonch, J.T., 2015. Coupling atmospheric mercury isotope ratios and meteorology to identify sources of mercury impacting a coastal urban-industrial region near Pensacola, Florida, USA. Global Biogeochem. Cycles 29, 1689–1705. https://doi.org/10.1002/2015GB005146

Engstrom, D.R., Fitzgerald, W.F., Cooke, C. a., Lamborg, C.H., Drevnick, P.E., Swain, E.B., Balogh, S.J., Balcom, P.H., 2014. Atmospheric Hg emissions from preindustrial gold and silver extraction in the Americas: A reevaluation from lake-sediment archives. Environ. Sci. Technol. 48, 6533–6543. https://doi.org/10.1021/es405558e

Fu, X., Marusczak, N., Wang, X., Gheusi, F., Sonke, J.E., 2016. Isotopic Composition of Gaseous Elemental Mercury in the Free Troposphere of the Pic du Midi Observatory, France. Environ. Sci. Technol. 50, 5641–5650. https://doi.org/10.1021/acs.est.6b00033

Kurz, A.Y., Blum, J.D., Gratz, L.E., Jaffe, D.A., 2020. Contrasting Controls on the Diel Isotopic Variation of Hg0 at Two High Elevation Sites in the Western United States. Environ. Sci. Technol. 54, 10502–10513. https://doi.org/10.1021/acs.est.0c01918

Kurz, A.Y., Blum, J.D., Washburn, S.J., Baskaran, M., 2019. Changes in the mercury isotopic composition of sediments from a remote alpine lake in Wyoming , USA. Sci. Total Environ. 669, 973–982. https://doi.org/10.1016/j.scitotenv.2019.03.165

Kwon, S.Y., Blum, J.D., Nadelhoffer, K.J., Dvonch, J.T., Tsui, M.T., 2015. Isotopic study of mercury sources and transfer between a freshwater lake and adjacent forest food web. Sci. Total Environ. 532, 220–229. https://doi.org/10.1016/j.scitotenv.2015.06.012

Schroeder, W.H., Anlauf, K.G., Barrie, L.A., Lu, J.Y., Steffen, A., 1998. Arctic springtime depletion of Mercury. Nature 394, 331–332.

Sherman, L.S., Blum, J.D., Johnson, K.P., Keeler, G.J., Barres, J. a., Douglas, T. a., 2010. Mass-independent fractionation of mercury isotopes in Arctic snow driven by sunlight. Nat. Geosci. 3, 173–177. https://doi.org/10.1038/ngeo758

Steffen, A., Douglas, T., Amyot, M., Ariya, P., Aspmo, K., Berg, T., Bottenheim, J., Brooks, S., Cobbett, F., Dastoor, A., Dommergue, A., Ebinghaus, R., Ferrari, C., Gardfeldt, K., Goodsite, M.E., Lean, D., Poulain, A.J., Scherz, C., Skov, H., Sommar, J., Temme, C., 2008. A synthesis of atmospheric mercury depletion event chemistry linking atmosphere, snow and water. Atmos. Chem. Phys. 8, 1445–1482. https://doi.org/10.5194/acpd-7-10837-2007

Wang, S., Mcnamara, S.M., Moore, C.W., Obrist, D., Steffen, A., Shepson, P.B., Staebler, R.M., Raso, A.R.W., Pratt, K.A., Performed, K.A.P., 2019. Direct detection of atmospheric atomic bromine leading to mercury and ozone depletion. Atmos. Planet. Sci. 116. https://doi.org/10.18739/A2D79598P

Yuan, W., Sommar, J., Lin, C., Wang, X., Li, K., Liu, Y., Zhang, H., Lu, Z., Wu, C., Feng, X., 2018. Stable Isotope Evidence Shows Re-emission of Elemental Mercury Vapor Occurring after Reductive Loss from Foliage. Environ. Sci. Technol. 53, 651–660. https://doi.org/10.1021/acs.est.8b04865

Zhang, Y., Jacob, D.J., Horowitz, H.M., Chen, L., Amos, H.M., Krabbenhoft, D.P., Slemr, F., Louis, V.S., Sunderland, E.M., 2015. Observed decrease in atmospheric mercury explained by global decline in anthropogenic emissions. Proc. Natl. Acad. Sci. U. S. A. 113, 526–531. https://doi.org/10.1073/pnas.1516312113

Appendix

Introduction

Even-MIF has been used as a conservative tracer to understand atmospheric deposition pathways. It has been proposed that even-MIF is induced in the tropopause through UV initiated oxidation reactions (Chen et al., 2012). This hypothesis was developed through seasonal observations of precipitation samples collected on a rooftop in Peterborough, Ontario (Chen et al., 2012). The authors reported unprecedented Δ^{200}Hg values, reaching up to 1.24‰, in samples collected during winter months (November-February) that consisted of a mixture of rain and snow. Through the analysis of airmass back trajectories, the authors proposed that the origin of the air masses over the Arctic allowed for increased penetration of UV radiation, therefore inducing the extreme values observed in the collected samples. The authors further suggested that the oxidation of Hg^0 may be occurring on the surfaces of particles and/or snow crystals in the upper troposphere (Chen et al., 2012). These extreme values have not been observed in any other samples collected to date.

To better understand the origin of even-MIF, we analyzed particulate bound mercury (PBM) samples collected from two separate aircraft flights conducted by the National Aeronautics and Space Administration (NASA). We hypothesized that if even-MIF is induced in the tropopause on particle surfaces, it is likely that PBM samples collected within the tropopause would have similarly high even-MIF values to those reported by Chen et al (2012).

Methods

High altitude PBM samples were collected from flights conducted by a NASA DC-8 aircraft as part of the Atmospheric Tomography (ATom) sampling campaign. Two flights were used to collect PBM samples. The first flight was the ATom-3 TF02 which was conducted on September 26th, 2017. The flight followed a path from the Armstrong Flight Research center in Palmdale, California to the East to central Kansas (38°52'49.89" N, 98°23'31.94 W). The return flight followed a similar flight path. The second flight was the ATom-4 TF02 conducted on April 13th, 2018 from Armstrong Flight Research center in Palmdale, California to the west over the Pacific Ocean (23°07'.56" N, 141°56'46.13" W) with the return following a similar flight path.

Samples were collected onto pre-cleaned glass fiber filters (GF/A) that were baked at 450°C for 2 hours to remove any Hg and organic matter from the filters. Atmospheric air was pulled through the filters at a rate of approximately 180 L/min. Sampling was conducted when the aircraft reached an altitude of 8534m and continued as the aircraft reached a max altitude of 12497m. Due to the low concentration of PBM at these altitudes, samples were collected onto 2 individual GFA filters per sample and combined during sample processing.

After the sampling flight was completed, the filters were packaged in acid cleaned (5% HCl) petri dishes and packed into clean polyethylene bags and sent to the University of Michigan for processing. Filters were subjected to a microwave digest in a reverse aqua regia solution (1 part HCl:3 parts HNO_3, v/v) previously described in Gehrke et al. (2009). After microwave digestion, samples were diluted to a 10% acid strength. The solution was then added to a 2 L Pyrex bottle and diluted to a volume of 1 L for Purge and Trap processing. The purge and trap processing protocol has been previously described in Washburn et al. (2017). Briefly, a 10% $SnCl_2$ solution was added to the 2 L Pyrex reservoir bottle over a 30-minute period. The liquid

was bubbled with gold-filtered Hg-free air to purge the Hg^0 from solution. The Hg^0 was then bubbled through a 5.5g liquid trap of 1% $KMnO_4$. Hg concentration was determined for the 1% $KMnO_4$ by partially reducing the sample solution with 2% (w/w) of a 30% $NH_2OH \cdot HCl$ and analyzing an aliquot for total mercury (THg) by cold vapor atomic fluorescence spectroscopy (CV-AFS).

Due to the low run concentrations of the PBM aircraft filter samples, we use the 2SD of UM-Almadèn measurements made at the same run concentration to assign analytical uncertainty to these samples. The analytical uncertainties are as follows: ±0.20‰ for $\delta^{202}Hg$, ±0.32‰ for $\Delta^{204}Hg$, ±0.20‰ for $\Delta^{201}Hg$, ±0.10‰ for $\Delta^{200}Hg$, and ±0.32‰ for $\Delta^{199}Hg$.

Discussion of High Altitude PBM Samples

To assess the differences in $\Delta^{200}Hg$ values within the vertical gradient of the atmosphere, we collected PBM (Hg^{2+}) samples aboard a DC-8 aircraft during the ATom-3 and ATom-4 research flights conducted by NASA. We report for the first time Hg isotopic measurements of PBM collected in the tropopause (Appendix Table 1). The $\Delta^{199}Hg$ values measured in the samples collected from the ATom-4 TF02 flight over the Pacific Ocean are more positive than the $\Delta^{199}Hg$ value from the ATom-3 TF02 flight (ATom-4 TF02 $\Delta^{199}Hg$ avg. = 0.88±0.05‰ and ATom-3 TF02 flight $\Delta^{199}Hg$ = 0.12±0.32‰). The differences in $\Delta^{199}Hg$ values between these two flights may indicate a difference in the exposure to UV radiation as odd-MIF is driven by photochemical reactions (Bergquist and Blum, 2007; Zheng and Hintelmann, 2010). However, similar to observations from Chen et al (2012), $\Delta^{199}Hg$ and $\Delta^{200}Hg$ measured in the PBM samples are not well correlated, likely indicating different reactions controlling these two isotope ratios.

The three Δ^{200}Hg values measured in these samples are 0.01±0.10‰, 0.38±0.10‰, and 0.04±0.10‰. Using a two sided t-test with equal variance at the 95% confidence level, we compared the measured PBM values (avg. Δ^{200}Hg = 0.14±0.21‰, 1SD, n=3) with previously published PBM values (avg. Δ^{200}Hg = 0.08±0.06‰, 1SD, n=215) (Fu et al., 2019; Huang et al., 2019, 2018) and did not find a statistical difference (p=0.084). Additionally, when we compared our measured PBM values with all published precipitation data (avg Δ^{200}Hg = 0.17±0.14‰, 1SD, n=129) (Chen et al., 2012; Demers et al., 2013; Donovan et al., 2013; Gratz et al., 2010; Huang et al., 2018; Sherman et al., 2015, 2012; Wang et al., 2015), which is dominated by Hg^{2+}, we did not find a statistical difference between these two datasets (p=0.77). If the measured Δ^{200}Hg values of the PBM samples collected in the troposphere displayed high magnitude even-MIF, the values would be outside of analytical uncertainty. Our samples did not display this large even-MIF signal, they are comparable to previously published data, and we therefore conclude that it is possible that even-MIF is not being imparted onto samples through reactions in the tropopause or that events that mix Hg with these even-MIF signatures are stochastic and therefore would rarely be captured in measured samples. With these conclusions, we caution the Hg isotope community that the large magnitude even-MIF values measured by Chen et al. (2012) may represent processes occurring under a very limited and specific set of conditions and may not be generally applicable to the atmosphere. Thus, we suggest caution when including the Chen et al. (2012) measured Δ^{200}Hg values as an endmember for the isotopic composition of Hg in the atmosphere when calculating the sources of Hg to various precipitation samples.

Future Work

Additional work is needed to further characterize the isotopic signatures of high altitude atmospheric Hg. This may include direct sampling of PBM, Hg^0, and gaseous oxidized mercury

at high altitudes. Modifications to current sample collection methodology for this type of sampling will be needed due to the extremely low Hg concentrations at high altitudes. Additionally, more experimental work, likely involving heterogeneous Hg^0 photooxidation is needed to either support or refute the hypothesis developed by Chen et al (2012) regarding even-MIF. To date, there is only one study that investigated the Hg isotopic fractionation during photooxidation of Hg^0 by Cl and Br (Sun et al., 2016). While these experiments induced small magnitude even-MIF, they cannot account for the large magnitude $\Delta^{200}Hg$ values observed by Chen et al (2012). These experiments should therefore be expanded upon and would represent a significant contribution to the Hg isotope research community.

Appendix Table 1. Hg isotope ratios from particulate bound mercury samples collected aboard two aircraft flights.

Sample	Flight	Collection Date	Concentration	$\delta^{204}Hg$	$\delta^{202}Hg$	$\delta^{201}Hg$	$\delta^{200}Hg$	$\delta^{199}Hg$	$\Delta^{204}Hg$	$\Delta^{201}Hg$	$\Delta^{200}Hg$	$\Delta^{199}Hg$
			ng/m^3	‰	‰	‰	‰	‰	‰	‰	‰	‰
First Aircraft Filter	ATom-3 TF02	9/26/17	0.16	-0.56	-0.41	-0.07	-0.19	0.01	0.05	0.24	0.01	0.12
A4TFZ_Inboard	ATom-4 TF02	4/13/18	0 .14	1.43	1.05	2.09	0.91	1.17	-0.14	1.30	0.38	0.91
A4TFZ_Outboard	ATom-4 TF02	4/13/18	0.11	0.48	0.56	1.53	0.32	0.99	-0.36	1.10	0.04	0.84

References

Bergquist, B.A., Blum, J.D., 2007. Mass-dependent and -independent fractionation of Hg isotopes by photoreduction in aquatic systems. Science (80-.). 318, 417–420. https://doi.org/10.1126/science.1148050

Chen, J., Hintelmann, H., Feng, X., Dimock, B., 2012. Unusual fractionation of both odd and even mercury isotopes in precipitation from Peterborough, ON, Canada. Geochim. Cosmochim. Acta 90, 33–46. https://doi.org/10.1016/j.gca.2012.05.005

Demers, J.D., Blum, J.D., Zak, D.R., 2013. Mercury isotopes in a forested ecosystem: Implications for air-surface exchange dynamics and the global mercury cycle. Global Biogeochem. Cycles 27, 222–238. https://doi.org/10.1002/gbc.20021

Donovan, P.M., Blum, J.D., Yee, D., Gehrke, G.E., Singer, M.B., 2013. An isotopic record of mercury in San Francisco Bay sediment. Chem. Geol. 349–350, 87–98. https://doi.org/10.1016/j.chemgeo.2013.04.017

Fu, X., Zhang, H., Feng, X., Tan, Q., Ming, L., Liu, C., 2019. Domestic and Transboundary Sources of Atmospheric Particulate Bound Mercury in Remote Areas of China : Evidence from Mercury Isotopes. Environ. Sci. Technol. 53, 1947–1957. https://doi.org/10.1021/acs.est.8b06736

Gratz, L.E., Keeler, G.J., Blum, J.D., Sherman, L.S., 2010. Isotopic composition and fractionation of mercury in Great Lakes precipitation and ambient air. Environ. Sci. Technol. 44, 7764–7770. https://doi.org/10.1021/es100383w

Huang, Q., Chen, J., Huang, W., Reinfelder, J.R., Fu, P., Yuan, S., 2019. Diel variation in mercury stable isotope ratios records photoreduction of PM2.5-bound mercury. Atmos. Chem. Phys. 19, 315–325.

Huang, S., Sun, L., Zhou, T., Yuan, D., Du, B., Sun, X., 2018. Natural stable isotopic compositions of mercury in aerosols and wet precipitations around a coal-fired power plant in Xiamen, southeast China. Atmos. Environ. 173, 72–80. https://doi.org/10.1016/j.atmosenv.2017.11.003

Sherman, L.S., Blum, J.D., Dvonch, J.T., Gratz, L.E., Landis, M.S., 2015. The use of Pb, Sr, and Hg isotopes in Great Lakes precipitation as a tool for pollution source attribution. Sci. Total Environ. 502, 362–374. https://doi.org/10.1016/j.scitotenv.2014.09.034

Sherman, L.S., Blum, J.D., Keeler, G.J., Demers, J.D., Dvonch, J.T., 2012. Investigation of Local Mercury Deposition from a Coal-Fired Power Plant Using Mercury Isotopes. Environ. Sci. Technol. 46, 382–390.

Sun, G., Sommar, J., Feng, X., Lin, C.-J., Ge, M., Wang, W., Yin, R., Fu, X., Shang, L., 2016. Mass-Dependent and -Independent Fractionation of Mercury Isotope during Gas-Phase

Oxidation of Elemental Mercury Vapor by Atomic Cl and Br. Environ. Sci. Technol. 50, 9232–9241. https://doi.org/10.1021/acs.est.6b01668

Wang, Z., Chen, J., Feng, X., Hintelmann, H., Yuan, S., Cai, H., Huang, Q., Wang, S., Wang, F., 2015. Mass-dependent and mass-independent fractionation of mercury isotopes in precipitation from Guiyang, SW China. Comptes Rendus - Geosci. 347, 358–367. https://doi.org/10.1016/j.crte.2015.02.006

Zheng, W., Hintelmann, H., 2010. Isotope Fractionation of Mercury during Its Photochemical Reduction by Low-Molecular-Weight Organic Compounds. J. Phys. Chem. A 114, 4246–4253.